NOTE TO USERS

The Effects of Vortex Profile on Sound Generation and Propagation in Non-Uniform Flows

Tinghui Zheng

A Thesis

in

the Department

Mechanical and Industrial Engineering

Presented in Partial Fulfillment of the Requirements

for the Degree of Doctor of Philosophy at

Concordia University,

Montreal, Quebec, Canada

February 2005

Your file Votre référence
ISBN: 0-494-04064-5
Our file Notre référence
ISBN: 0-494-04064-5

ABSTRACT

The Effects of Vortex Profile on Sound Generation and Propagation in Non-uniform Flow

Tinghui Zheng, Ph.D

Concordia University, 2004

This study was motivated by airframe noise in aircraft and blade-vortex interaction (BVI) noise in helicopters.

In this thesis, the sound generated by vortical disturbances in a subsonic flow around solid surfaces, using different vortex velocity formulations, was investigated by numerically solving the linearized or non-linearized Euler equations. Analytical solutions for this general case are not available because the wavelength of the generated acoustic wave is comparable to the vortex size, which is at variance to the compact source assumption of the acoustic analogy. Numerical errors associated with the discretization and boundary conditions were kept small using a high-order scheme with accurate non-reflecting boundary conditions.

Stagnation flow on a flat plate, flow around a stationary and rotating cylinder, and that about two cylinders were taken as prototypes of real-world flows with strong gradients of mean pressure and velocity. Single and periodic vortices were taken into consideration. In addition, the effect of vortex core size, the street distance, street

frequency, and the Mach number of the mean flow on sound generation and propagation were examined.

The sound wave strength was found to be proportional to the vortex strength. If the acoustic pressure is normalized by the vortex strength, then all the distinct acoustic pressure profiles will collapse into single curve. Sound generation by vortex interaction with a solid surface, as well as its propagation, were found to be totally different between the Taylor's and Vatistas's vortices. The vortex core size and vortex street distance have minor influences on the acoustic pressure profile for sound waves radiated by the Vatistas vortex. Nevertheless, the change of the core size or the distance between the vortex rows significantly affects the sound pressure profile and sound directivity radiated by a Taylor vortex.

The effects of the non-linear terms on sound wave properties were also investigated. The non-linear influence was found to increase with the vortex strength. A lifting cylinder is shown not only to increase the sound wave amplitude, but also to shift its directivity.

The developed methods and computer codes can be used in the future as platforms to more elaborate methods that will predict the noise generated by multi-element airfoils, and the undercarriage of an aircraft. This will help reduce the need of costly, time consuming, wind tunnel and field experiments.

ACKNOWLEDGEMENTS

The author would like to express her greatest gratitude and appreciation to her supervisor Dr. Georgios Vatistas and Dr. Alex Povtisky, for their continuous encouragement and support. Extended thanks are given to Dr. Povistky for initiating this project, his good suggestions, advice, and for always prompting me to think further.

I first must thank Dr. Vatistas, for broadening my vision and always encouraging me to do better. Most importantly, he always exposed me to new ideas, views and concepts that go beyond the present thesis. I still vividly remember Dr. Vatistas saying that there are two groups of researcher in the world. The larger group consists from the explorers, the other from the developers. Every explorer has to start as a developer, and never stops of being a developer. I will try my best to become an explorer like him. I thank Dr. Vatistas from the bottom of my heart for all the encouragement and help he offered me during the studies.

I thank and appreciate Dr. Wahid Ghaly and Dr. Marius Paraschivoiu, for their kindly help and answering my questions.

I would like to express my deepest indebtedness to my husband, my great parents,

and my dear sister who stood by my side all these years. They always kept on encouraging me, offering me their moral support and love all the way from China.

I also would like to thank my very dearest friends for their unconditional friendship and encouragement they gave me and continue to give me.

I would like to thank Mr. Conway Daly, for his great help in my English speaking and writing.

This thesis is dedicated to my parents Daxin Zheng and Chuanxiu Liu.

TABLE OF CONTENTS

CHAPTER 1 INTRODUCTION 1

1.1 RESEARCH MOTIVATION 1

1.2 LITERATURE REVIEW 4

1.2.1 Vortex profiles 4

1.2.2 Computational Aeroacoustics 11

1.3 CONTRIBUTIONS 30

1.4 SIGNIFICANCE OF CONTRIBUTIONS 32

CHAPTER 2 METHODOLOGY 35

2.1 MATHEMATICAL MODEL 35

2.2 MODELS OF VORTEX 38

2.3 NUMERICAL METHOD 43

2.4 BOUNDARY CONDITIONS 48

2.5 CODE VALIDATION AND GRID REFINEMENT STUDY 51

CHAPTER 3 IMPINGEMENT OF SINGLE VORTEX INTO FLAT PLATE 58

3.1 PROBLEM SET UP 58

3.2 BOUNDARY CONDITION COMPARISON 61

3.3 COMPUTATIONAL RESULTS 65

3.4 SUMMARY OF FINDINGS 67

CHAPTER 4 SINGLE VORTEX IMPINGEMENT INTO SOLID CYLINDER 79

4.1 PROBLEM SETUP 80

4.2 BOUNDARY CONDITIONS: 83

4.3 COMPUTATIONAL RESULTS: 86

4.3.1 A. non-zero circulation vortex 87

4.3.2 Zero-circulation vortex and non-zero-circulation vortex 93

4.3.3 Turbulent Vortex Model 98

4.3.4 Non-linearity analysis 99

4.4 SUMMARY OF FINDINGS 101

CHAPTER 5 VORTEX STREET IMPINGEMENT ON A NON-ROTATING CYLINDER 125

5.1 PROBLEM SETUP 126

5.2 BOUNDARY CONDITIONS 128

5.3 COMPUTATIONAL RESULTS 129

5.4 SUMMARY OF FINDINGS 136

CHAPTER 6 VORTEX IMPINGEMENT ON A ROTATING CYLINDER 148

6.1 PROBLEM SETUP 148

6.2 COMPUTATIONAL RESULTS 150

6.2.1 Single vortex impingement into rotating cylinder 150

6.2.2 A vortex street impingement into rotating cylinder 152

6.3 SUMMARY OF FINDINGS 153

CHAPTER 7 ACOUSTIC SOURCES TRAPPED BETWEEN TWO CYLINDERS 163

7.1 PROBLEM SETUP 163

7.2 BIPOLAR SYSTEM 165

7.3 MEAN FLOW AROUND TWO CYLINDERS 168

7.4 BOUNDARY CONDITION: 171

7.5 RESULTS 172

7.6 SUMMARY OF FINDINGS 175

CONCLUSIONS 184

FUTURE WORK 186

REFERENCES 189

LIST OF FIGURES

Figure 1-1 Configuration of vortex–body interaction (VBI): (a) parallel VBI, (b) streamwise VBI, (c) normal VBI. 22

Figure 1-2 Physic space of noise generation and possible hybrid strategies (from Sagaut et al. 2002). 25

Figure 2-1 Vortex velocity distributions with respect to the distance to vortex center: (a) tangential velocity and, (b) radial velocity. 39

Figure 2-2 A representative flow visualization image of a tip vortex emanating from a rotor blade showing three distinct regions: (1) Laminar region, (2) Transitional region, (3) Turbulent region (from Ramasamy & Leishman, 2004). 40

Figure 2-3 Swirl velocity distribution with respect to r. 42

Figure 2-4 Computational domain that combines the Euler and PML domains (from Fang Q. Hu, 2001). 49

Figure 2-5 Log-Log plot of pressure error vs. mesh size (h) for a fixed time step size $\Delta t = 0.001$ 55

Figure 2-6 Log-Log plot of pressure error vs. time step size (Δt) for a fixed mesh size $h = 0.002$ 55

Figure 2-7 Acoustic pressure time history at the point $(0.2,0.2)$. 56

Figure 2-8 The angular distribution of RMS of acoustic pressure for Vatistas one-cell vortex with $n = 2$ 56

Figure 2-9 The RMS of acoustic pressure angular distribution on the left cylinder. 57

Figure 3-1 Case A: Physical set-up of vortex impingement onto flat plate. 59

Figure 3-2 Case A: (a) computational domain, (b) streamlines of the background flow. 59

Figure 3-3 Vortex image system. 61

Figure 3-4 Generation of acoustic waves by: (a, b) the Taylor's Vortex, (c, d) the Vatistas's vortex ($n = 2$), (a, c) using PML boundary, (b, d) using Characteristic boundary. 68

Figure 3-5 Acoustic pressure time history at the point $(0.2,0.2)$: (a) the Taylor's vortex, (b) the Vatistas's vortex ($n = 2$). 69

Figure 3-6 Generation of pressure quadrupole and acoustic waves for Taylor and Vatistas vortices: (a) the Taylor's vortex, (b) the Vatistas's vortex. Negative line represents negative pressure values. 75

Figure 3-7 Generation of pressure quadrupole and acoustic wave for Taylor and Vatistas vortex dipole: (a) the Taylor's vortex, (b) the Vatistas's vortex ($n = 2$). 78

Figure 4-1 Case B, C: an overview of single vortex impingement on cylinder. 80

Figure 4-2 A schematic of the computational problem. 80

Figure 4-3 Background flow around non-rotating cylinder. 81

Figure 4-4 Images of a vortex in a fixed circular cylinder. 83

Figure 4-5 Initial flowfield after the image system is implemented: (a) the Taylor's vortex, (b) the Vatistas's vortex ($n = 2$). 85

Figure 4-6 The RMS of acoustic pressure for one and two- cell vortices by linear simulation by Eq. (55). 88

Figure 4-7 The RMS pressure distribution for linear and non-linear Euler simulations of one-cell vortical disturbances with and without initial radial velocity: (a) linear simulation by Eq. (55), (b) non-linear simulation by Eq. (56) 89

Figure 4-8 The RMS of acoustic pressure distribution for the two-cell vortical disturbances. ... 90

Figure 4-9 Unsteady pressure generated by the two-cell vortical disturbance: (a) the vortex with initial tangential velocity only, (b) the initial two-cell disturbance with the radial velocity component, (c) the full two-cell vortex 104

Figure 4-10 The non-linear terms contribution to RMS of acoustic pressure. 105

Figure 4-11 The flow-field of the two-cell vortical disturbance convected by the mean flow around cylinder at: (a) $M = 0.1$ and, (b) $M = 0.4$. 105

Figure 4-12 The RMS of acoustic pressure generated by two-cell vortices at different Mach numbers of the mean flow around a cylinder: (a) two-cell vortex with initial zero radial velocity, (b) two-cell disturbance with initial zero tangential velocity and, (c) the full two-cell vortex. 106

Figure 4-13 Distorting of the vortex in the flow around the cylinder at times $t = 0.4$, $t = 0.8$, and $t = 1.2$: (a) the Taylor's vortex, (b) the Vatistas's vortex. 109

Figure 4-14 Radial distribution of the sound pressure for a single vortex disturbance propagation in the mean flow around the cylinder: (a) the Taylor's vortex, $\theta = 145°$ and, (b) the Vatistas's model $\theta = 135°$ 110

Figure 4-15 The RMS of acoustic pressure for the mean flow with $M_\infty = 0.1,0.2,0.3,0.4$: (a) the Taylor's vortex and, (b) the Vatistas's vortex . Angle α is measured from the negative x axis. 111

Figure 4-16 The RMS of acoustic pressure for the initial vortex location at $(-0.75,0)$, Notation is the same as in Fig. 4.15. 112

Figure 4-17 Acoustic disturbance velocity field at $t = 0.8$: (a) the Taylor's vortex, (b) the Vatistas's vortex. 113

Figure 4-18 Distorting of the large core vortex in the mean flow around the cylinder at times $t = 0.4$, $t = 0.8$, and $t = 1.2$. (a) the Taylor's vortex, (b) the Vatistas's vortex. 116

Figure 4-19 The RMS of acoustic pressure for the large vortex ($R_c = 0.25$) for a mean flow with $M_\infty = 0.1,...,0.4$: (a) the Taylor's vortex, (b) the Vatistas's vortex. 117

Figure 4-20 Distorting of the small vortex dipole in the mean flow around the cylinder at times $t = 0.4$, $t = 0.8$, and $t = 1.2$. (a) the Taylor's vortex, (b) the Vatistas's vortex. 120

Figure 4-21 The RMS of acoustic pressure for a small vortex dipole for a mean flow with $M_\infty = 0.1,...,0.4$: (a) the Taylor's vortex, (b) the Vatistas's vortex 121

Figure 4-22 The RMS of acoustic pressure distribution on cylinder surface with respect to angle θ 122

Figure 4-23 Sound pressure contributed by non-linear terms at $t = 1.0$. The Solid line denotes positive acoustic pressure; the dotted line denotes negative pressure..... 122

Figure 4-24 The root mean square acoustic pressure distribution $R_c = 0.25, V_{\max} = 0.2$. (a) the Taylor's vortex , (b) the Vatistas's vortex. 123

Figure 4-25 The difference in pressure RMS between the linearized and non-linear Euler equations. 124

Figure 5-1 Scheme of vortex street and cylinder interaction..... 126

Figure 5-2 Vortex deformation in the background flow about the cylinder at (a, c) Vortex street at frequency 1/0.05, (b, d) Vortex street at frequency $f = 1/0.5$, (a, b) the Vatistas vortex street, (c, d) the Taylor vortex street. 138

Figure 5-3 The pressure isoline generated by the Vatistas vortex street at different vortex adding frequency at time $t = 10$: (a) frequency 1/0.0.5, (b) frequency 1/0.5. 139

Figure 5-4 The RMS of acoustic pressure distribution for a single row vortex street: (a) Vatistas vortex street at frequency =1/0.05, (b) Vatistas vortex street at frequency =1/0.5, (c) Taylor vortex street at frequency=1/0.5. 140

Figure 5-5 The RMS of acoustic pressure radiated by (a, b) Vatistas vortex street, (c) Taylor vortex street, and at (a, c) frequency $f = 1/0.05$, (b, d) frequency $f = 1/0.5$. 141

Figure 5-6 Flow-field of two-row Vatistas vortex street of alternating signs at different vortex adding frequency and different vortex street distance at time $t = 10.0$: 142

Figure 5-7 Flow-field of two-row Taylor vortex street of alternating signs at different vortex adding frequency and different vortex street distance at time $t = 10.0$: 143

Figure 5-8 The RMS of acoustic pressure distribution with different vortex adding frequency. (a) the Vatistas vortex street, (b) the Taylor vortex street..... 144

Figure 5-9 The RMS of acoustic pressure radiated by (a) Vatistas vortex street at frequency1/0.05=20, (b) Vatistas vortex street at frequency 1/0.5=2, (c) Taylor vortex street at frequency 1/0.5=2.0, vortex street distance is set to 0.1. 145

Figure 5-10 Normalized RMS of acoustic pressure radiated by (a) Vatistas vortex street at frequency 1/0.05=20, (b) Vatistas vortex street at frequency 1/0.5=2, (c) Taylor vortex street at frequency 1/0.5=2.0, vortex street distance is set to 0.1. 146

Figure 5-11 The RMS of acoustic pressure radiated by (a, b) the Vatistas vortex street, (c) the Taylor vortex street, and at (a, c) (frequency=1/0.05=20, $D = 0.1$), (b) (frequency=1/0.5=2, $D = 0.1$). 147

Figure 6-1 Stagnation points for the lifting flow over a circular cylinder 149

Figure 6-2 Background flow around rotating cylinder with one stagnation point 150

Figure 6-3 Distorting of the small vortex in the mean flow around a rotating cylinder, at times t=0.1 and $t = 1.2$. (a) the Taylor's vortex and, (b) the Vatistas's Vortex. 156

Figure 6-4 The RMS acoustic pressure distribution for rotating cylinder case. (a) the Taylor's vortex, (b) the Vatistas's vortex 157

Figure 6-5 The RMS acoustic pressure distribution at different cylinder Circulation value: (a) the Taylor's vortex (b) the Vatistas's vortex. 158

Figure 6-6 The RMS of acoustic pressure for Vatistas vortex street: (a) at frequency 1/0.05=20, (b) at frequency 1/0.5=2 159

Figure 6-7 Normalized RMS (normalized by vortex strength) of acoustic pressure for Vatistas vortex street at frequency 1/0.5=2. Vortex street distance is set to 0.1. 160

Figure 6-8 RMS of acoustic pressure for Vatistas vortex street: (a) at frequency 1/0.05=20, (b) at frequency 1/0.5=2. 161

Figure 6-9 RMS of acoustic pressure for Vatistas vortex street at: (a) frequency 1/0.05=20, (b) frequency 1/0.5=2.Vortex street distance was set equal to 0.1 162

Figure 7-1 Geometry of acoustic scattering. 164

Figure 7-2 The flow field of mean flow around two cylinders: (a) parallel mean flow, (b) perpendicular mean flow. 170

Figure 7-3 The schematic of computational domain. 172

Figure 7-4 The RMS of acoustic pressure distribution on the right cylinder (computed on the

coarse mesh (300×300) grid). 177

Figure 7-5 The RMS of acoustic pressure distribution on the right cylinder (computed with fine mesh (600×600) grid). 177

Figure 7-6 The RMS of acoustic pressure distribution on the upper half cylinder: (a) left cylinder, (b) right cylinder (solution on (600×600) grid). 178

Figure 7-7 Unsteady pressure generated by the vortical disturbance that trapped between two cylinders (Case D-2) at times: (a) $t = 0.1$ and, (b) $t = 1.2$. 179

Figure 7-8 Unsteady pressure generated by the vortical disturbance that trapped between two cylinders (Case D-3) at times: (a) $t = 0.1$ and, (b) $t = 1.2$. 180

Figure 7-9 The RMS of acoustic pressure distribution on the cylinders (a) left cylinder and (b) –right cylinder, angle θ is measured from the negative x axis and the corresponding cylinder center, Case D-2. 181

Figure 7-10 The RMS of acoustic pressure distribution along the cylinders (a) left cylinder and (b) right cylinder θ is measured from the negative x axis and the corresponding cylinder center , Case D-3. 182

Figure 7-11 The RMS of acoustic pressure far-field distribution with angle θ from the positive x axis and measured from the origin: (a) Case D-2, (b) Case D-3. 183

NOMENCLATURE

U_∞	Mean flow velocity at infinity
$U,\ V$	Mean flow velocity
R	Mean flow density
M_∞	Mean flow Mach number
c	Speed of sound
c_∞	Ambient speed of sound
M_0	Mach number at the reference point
U'	Spatial derivative
u', v'	Acoustic disturbance velocity
p'	Disturbance pressure
ρ'	Disturbance density
ρ_∞	Ambient gas density
L	Characteristic length
t	Time
P_{rms}	Root mean square of disturbance pressure

P_{ave}	Time average distrubance pressure
P_{acous}	Root mean square of acoustic pressure
T_1, T_2	Time limits for integration of disturbance variable
T	Integration time period, $T = T_1 - T_2$
t_f	Running final time for code validation
Γ	Vortex circulation or the circulation of a loaded cylinder
Ω	Vorticity(2-D case)
V_θ	Vortex tangential velocity
V_r	Vortex radial velocity
V_z	Vortex axial velocity
R_e	Vortex Reynolds number
ν	Dynamic viscosity
$V_{\max}$	Maximum tangential velocity
R_c	Vortex core radius where vortex tangential velocity reaches
$\bar{r}$	Radial distance dimensionalized by vortex core
r, z, θ	Polar coordinates
x, y	Cartesian coordinates
ξ, η	Bipolar coordinates

n	A constant value of the exponent for first generation Vatistas
η, k, β, m	Scaling constants for the two-cell Vatistas vortex
C_∞	A coefficient for the two-cell Vatistas vortex
M	Constant angular momentum
R_{cyl}	Cylinder radius
H^M	Intermediate variable for time-marching scheme
h_ζ, h_η	The Lame coefficients
q_1, q_2, q_3	Immediate variable used in perfect matched layer equations
$\sigma_x, \sigma_{y,} \sigma_r, \sigma_m$	Damping coefficient for sponger layer equations
ψ	Stream function
ϕ	Potential function
c_1, c_2	The location of the centers of two cylinders
r_1, r_2	Radius of the cylinders
$\zeta_1, \zeta_2, \eta_1, \eta_2$	The boundaries of domain in bipolar coordinate
ε, a	Arbitrary constants
D_0	Drag of the generating wing
δ	Eddy viscosity coefficient

Chapter I

Introduction

1.1 Research Motivation

Vortices incident to a rigid body can produce vibrations and substantial unsteady aerodynamic loadings. Vortex-Body Interaction (VBI henceforth) is thus of importance to several industrial devices. Although the general theme of VBI has been under scientific scrutiny for many years, much less is known about the noise generated by vortices. In particular, eddies that are convected by a non-uniform flow near the rigid surface may be distorted by the flow, and so radiate sound waves. Furthermore, the emanated waves may be redirected, amplified or weaken while propagating through the non-uniform flow. Because of numerical and experimental impediments, several of the associated aeroacoustic features have not yet been adequately understood.

The problem with airframe noise (the non-propulsive noise of an aircraft in flight), is most prominent in the landing phase of a flight, where the engines do not operate at full thrust. In particular, the deployment of the undercarriage gear (wheels, axles, struts, shafts), along with the high-lift devices such as trailing-edge flaps and leading-edge slats

appear to be a major source of airframe noise. Advances made in reducing engine noise have led to an increased awareness of landing gear noise. Consequently, these have prompted computational studies with an aim to understand the landing gear aeroacoustics. In the past, this area did not receive much attention from researchers. While part of the landing gear noise may be explained by wing and fuselage turbulent boundary layers, shedding of vortices from solid objects (wheels, axles, struts) interacting with downstream rigid surfaces is also an important source of noise production. Periodic vortices, which are deforming in a non-uniform mean flow in the vicinity of a rigid surface, create repeated acoustic disturbances. As a result, the corresponding sound is often stronger than the sound produced by turbulent eddies. Impulsive noise-generation in multi-element airfoils is caused by surface-vortex interaction (SVI), which results from the close proximity of trailing edge flaps to the main airfoil. Trailing edge wakes impinge into an leading edge of the flaps and generate sound. The sound amplifies as it propagates upstream, reflects from the main airfoil surface, and refracts into the mean flow. Noise emitted by the slot (gap) ahead of the leading edge of the flap, becomes the major source of aircraft noise in the landing stage of the flight. Experiments have shown that SVI tonal single-frequency noise exceeds the broadband noise caused by unsteady turbulent boundary layers and wakes. The SVI phenomenon causes vastly different noise patterns when multi-element airfoil design differs even slightly.

The high noise levels produced by aircraft and helicopters (including tiltrotors) are

unacceptable. Their adverse environmental impact, particularly during descent and ascent from airports, has been identified as a major obstacle in receiving civil acceptance. With the anticipated demand for integration the tiltrotors into the civil transport arena, the noise sources of helicopters (including tiltrotors) must be well understood, modeled, and predicted. The high noise levels of helicopters in descending flight operations are mainly caused by an impulsive noise-generating mechanism known as BVI. This occurs because of the close proximity between the main rotor blades and the vortices generated by them during the descent flight (Gervais 2001, Janakiram 2000). The BVI noise is particularly bothersome, because the BVI events commonly occur near the ground as the rotorcraft slows and descends for landing. The frequency of noise introduced by this is in a range that humans are extremely sensitive to (Collis, et al. 2002). Thus, the BVI can substantially increase environmental noise pollution.

Another principal noise source mechanism is due to the recirculating fountain flow phenomenon (Liu et al. 1998, Veigh 1985). Fountain flows occur when the downwash from the rotors strikes the wings, and is redirected laterally toward the centerline of the fuselage. When the flows originated from the opposing rotors meet, the flow is forced upward to form a "fountain".

The above mentioned phenomena are related to vortices distorting in a non-uniform flow, vortex impingement on solid body, sound reflection and sound refraction. The current study will provide a computational insight into the physical mechanisms of sound

generation by VBI and sound propagation in the presence of strong mean flow gradients. The computational methodology implemented in this study allows the prediction of the directivity and strength of sound waves caused by deforming vortices. This study is a necessary step for future noise control efforts.

1.2 Literature review

The literature review contains five sections. In the first section, the vortex profiles used for acoustic modeling are reviewed. In Section 1.2.2 previous computational aeroacoustic approaches are appraised. In Section 1.2.3, the orientation of the vortex and the axis of the body for the VBI phenomena are assessed. Furshermore, the previous research conducted for the parallel vortex body interaction (that is, the focus of our study), is reviewed in detail.

1.2.1 Vortex profiles

In aeroacoustic modeling, the choice of the vortex model influences strongly the predictions (Bhagwat & Leishman 2002). Tip vortex models that accurately predict the aerodynamic loads on helicopter blades are needed. The potential vortices, that are often used, do not take into account viscous effects in the wake. On the other hand, a complete description of a viscous, turbulent, trailing vortex requires a solution of the complete Navier-Stokes equations, which is not feasible. Analytical solutions to these non-linear sets of equations are not possible. Even numerical solutions are deterred by formidable

computational costs and technical difficulties. Various closed form solutions obtained by further simplification of the governing equations are used instead (Burgers, 1948; Taylor, 1918; Vatistas, 1991, 1998).

A. Steady, intense vortices

The most elementary vortex model was proposed by Rankine in 1858. This involves a linear tangential velocity distribution inside the vortex core, and a hyperbolic variation outside. This formulation is an exact solution to a simplified form of the Navier-Stokes equations and it exhibits the main features of a more realistic vortex than a pure potential vortex. However in Rankine's model, the swirl velocity and vorticity distributions are discontinuous at the vortex core boundary. In addition, both the radial and axial velocity components are zero, i.e.,

$$V_\theta = \begin{cases} \dfrac{\Gamma}{2\pi} r & 0 \le r \le R_c \\ \dfrac{\Gamma}{2\pi r} & r > R_c \end{cases}$$
$$V_r = 0 \qquad (1)$$
$$V_z = 0$$

where R_c is the radial distance from the vortex axis to the position of the maximum swirl velocity, and Γ is the maximum vortex circulation.

Taylor (1918), proposed a vortex formula that corresponds to the vortices created by localized stirring for a short period of time. It begins with singular tangential velocity

and vorticity at the origin. Notably, this vortex profile assumes a zero total circulation and constant angular momentum. Also, both the radial and axial velocity components are zero, i.e.

$$\begin{aligned} V_\theta &= V_{\max}\frac{r}{R_c}\exp\left(1-(r/Rc)^2\right)/2 \\ V_r &= 0 \\ V_z &= 0 \end{aligned} \qquad (2)$$

where $V_{\max}$, the maximum tangential velocity, is defined as $V_{\max}=\frac{\Gamma}{2\pi R_c}$. R_e, given as $\Gamma/2\pi\nu$, is the vortex Reynolds number, ν is the kinematic viscosity. Other variables represent the vortex properties as mentioned previously.

Burgers (1948) put forward a vortex formulation which improves on the correlation between the observed and predicted values for the tangential velocity. However, it assumes a linear profile for the radial velocity and a constant axial velocity that makes the flow unbounded, i.e.,

$$\begin{aligned} V_\theta &= \frac{\Gamma}{2\pi}\frac{R_c}{r}\left[1-\exp\left(-1.25643\left(\frac{r}{R_c}\right)^2\right)\right] \\ V_r &= -\frac{\Gamma}{2\pi}\frac{2\times 1.25643}{R_e}\frac{r}{R_c} \\ V_z &= \frac{\Gamma}{2\pi}\frac{4\times 1.25643}{R_e} \end{aligned} \qquad (3)$$

Scully (1975) suggested an empirical tangential velocity distribution, in which the smoothing effects of viscosity in the neighborhood of vortex core were taken into

consideration. However, Scully's vortex model underestimates most of the measured values of the tangential velocity near R_c.

$$
\begin{aligned}
V_\theta &= \frac{\Gamma}{2\pi}\left(\frac{r}{R_c^2 + r^2}\right) \\
V_r &= -\frac{\Gamma}{2\pi}\frac{4}{\mathrm{Re}}\left(\frac{r}{R_c^2 + r^2}\right) \\
V_z &= \frac{\Gamma}{2\pi}\frac{8}{\mathrm{Re}}\frac{R_c^4}{\left(R_c^2 + r^2\right)^2} z
\end{aligned}
\tag{4}
$$

Vatistas (1990) proposed a family of algebraic velocity profiles for stationary vortices, i.e.,

$$
\begin{aligned}
V_\theta &= \frac{\Gamma}{2\pi}\left(\frac{r}{\left(R_c^{2n} + r^{2n}\right)^{1/n}}\right) \\
V_r &= -\frac{\Gamma}{2\pi}\frac{2(n+1)}{R_e}\frac{r^{2n-1}}{R_c^{2n} + r^{2n}} \\
V_z &= \frac{\Gamma}{2\pi}\frac{4n(n+1)}{R_e}\frac{R_c(n-1)}{\left(R_c{}^{2n} + r^{2n}\right)^2}
\end{aligned}
\tag{5}
$$

where n can take values from 1 to ∞. This model is now known as the Vatistas first-generation vortex profile. The $n = 2$ member of this family, has been found to agree well with experiment data (e.g. Bhagwat and Leishman, 2002), and turns out to be a solution of simplified Navier-Stokes equations too. It also exhibits the key features of a viscous vortex: when r goes to ∞ it behaves like a free potential vortex, but when r goes to zero, it becomes a forced vortex. Furthermore, this vortex model appears to be

very versatile; given different values of n other known self-similar vortex models can be obtained.

Vatistas(1998) presented a second-generation vortex model that offers wider latitude. Depending on the choice of the scaling parameters, the flow in the azimuthal plane can assume either a one-cell or two-cell configuration:

$$V_\theta = \frac{\Gamma C_\infty}{2\pi r}\int_0^{r/R_c}\left[\frac{1+\beta r^2}{\left(1+\eta\beta r^2\right)^{(1/\eta k)}}\right]^m rdr$$

$$\frac{V_r R_e k}{2m\beta} = V_{\max} r\left(\frac{kR_c}{R_c{}^2+\beta r^2}-\frac{R_c}{R_c{}^2+\eta\beta r^2}\right) \qquad (6)$$

$$\frac{V_z R_e k}{2m\beta} = V_{\max} r\left(\frac{kR_c}{R_c{}^2+\eta\beta r^2}-\frac{R_c}{R_c{}^2+\beta r^2}\right)$$

where η, β, k and m are the scaling constants that must be chosen in such a way as to allow the tangential velocity to attain its maximum value at $r = R_c$.

According to the boundary condition at infinity ($V_\theta r \to \frac{\Gamma}{2\pi}$ for $r \to \infty$), the constant C_∞ is given by

$$C_\infty = 1\Big/\int_0^\infty\left[\frac{1+\beta r^2}{\left(1+\eta\beta r^2\right)^{(1/\eta k)}}\right]^m rdr \qquad (7)$$

For $k < 1.0$, a one-cell vortex, which is similar to the first-generation Vatistas vortex, will be achieved. Its radial velocity is negative and increases in value as the radius

becomes smaller. For $k = 1.0$, a saddle-like profile for the radial velocity is acquired ($V_r = 0$ at $r = 0$). For $k > 1.0$, a two-celled vortex that is characterized by an alternating sign of the radial velocity at the cell interface is obtained. Until now, the two-cell vortex model is considered up to the scaling constant $k = 1.12$ (Vatistas, 1998).

Adopting the swirl velocity distribution of the Vatistas vortex family when $n = 2$, Bhagwat and Leishman (2002) give vortex velocity profiles that are written in terms of a single integer exponent. The viscous core growth is given by a semi-empirical relation for the turbulent viscosity that scales as a function of the vortex Reynolds number, i.e.,

$$
\begin{aligned}
V_\theta &= \frac{\Gamma}{2\pi}\left(\frac{r}{\left(R_c^{2n} + r^{2n}\right)^{1/n}}\right) \\
V_r &= \frac{-Ar}{2z^2}\left(1 - \frac{r^2}{\left(R_c^{2n} + r^{2n}\right)^{1/n}}\right) \\
V_z &= -\frac{A}{z}\left(1 - \frac{r^2}{\left(R_c^{2n} + r^{2n}\right)^{1/n}}\right)
\end{aligned}
\tag{8}
$$

where A is a constant that may be determined based on the drag of the generating wing, i.e.,

$$
A = \frac{D_0}{4\pi\rho(\delta\nu)} \tag{9}
$$

where D_0 is the drag of the generating wing, ρ is the density, δ is the eddy viscosity coefficient and ν is the kinematics viscosity

B. Unsteady vortex profile

Assuming a constant angular momentum of the eddy, Taylor (1918) proposed a decaying vortex of the form

$$V_\theta(r,t) = \frac{M}{\pi\rho}\frac{r}{4\nu t^2}\exp\left(-r^2/4\nu t\right)$$
$$R_c(t) = \sqrt{2\nu t} \qquad (10)$$

where M is the constant angular momentum, ν is the dynamic viscosity and ρ is the density.

Based on the time dependent Navier-Stokes equations, Oseen (1912) and then Lamb (1932) formulated the decay of an originally potential vortex model using,

$$V_\theta(r,t) = \frac{\Gamma}{2\pi r}\left[1-\exp\left(-\frac{r^2}{4\nu t}\right)\right]$$
$$R_c(t) = \sqrt{4\alpha\nu t} \qquad (11)$$

where $\alpha = 1.25643$, Γ is the maximum vortex circulation, ν is the vortex dynamic viscosity.

Yasser (2003) presented a theoretical study on the decay of strong isolated vortices. Based on the tangential momentum equation and using the standard separation of variables technique, the space-time velocity variation was given in terms of a Fourier-Bessel series.

1.2.2 Computational Aeroacoustics

Computational aeroacoustics, which is the science of noise generation and propagation through airflows, is a relatively young discipline compared to other more classical fields of mechanics. Although the sound equations are a particular form of the equations governing fluid flow, acoustic perturbations are typically at least 10 times weaker than the corresponding hydrodynamic perturbations and a thousand times smaller than the mean flow that carries them. On the other hand, acoustic wavelengths are typically larger than or equal to the corresponding structures in the flow. (Djambazov et al. 1998).

A. Analytical and Computational Approaches in Aeroacoustics

Typically, in aeroacoustics the solutions can be grouped into frequency-domain solution and a natural variables (x,t) solution (which was adopted in this study). Within the aeroacoustics field using natural variables, the different approaches can be categorized into three groups.

The first group makes use of the acoustic analogy. The most renowned acoustic analogy is by Lighthill (1952), who rearranged the mass and momentum equations such that the left-hand side represents an equation that describes the propagation of an acoustic wave, in a medium at rest, i.e.,

$$\left(\frac{1}{c_0^2}\frac{\partial^2}{\partial t^2}-\nabla^2\right)\left[c_0^2(\rho-\rho_0)\right]=\frac{\partial^2 T_{ij}}{\partial x_i \partial x_j} \qquad (12)$$

The forcing function on its right-hand side of Eq. 12 represents a distribution of acoustic sources in the ambient flow at rest, replacing the complex unsteady flow. Ffowcs Williams and Hawkins (1969) proposed the now classical FW-H equations, which generalized Lighthill's acoustic analogy to include the effects of very general types of surfaces and motions. The FW-H equation includes a quadrupole source distribution in the volume, and monopole and dipole sources on the surface. Mohring (1978, 1979), put forward the vortex sound theory for predicting the sound from two and three-dimensional, acoustically compact, compact vortical flows.

In the analysis of the first group, the computation of sound generation and propagation is carried out in two steps. First, the source terms in the near-field are obtained by traditional computational fluid dynamics (CFD) techniques. Next, the aerodynamic results are taken as an input in the acoustic analogy to compute the far-field acoustic field. This group of approaches can compute noise directivity on the ground in an economical way, because in the far field the flow is actually uniform. However, all of the acoustic analogies are based on a variety of assumptions such as compact source and low Mach number. Acoustically compact sources (including a vortex) mean that the size of the acoustic source is much smaller than the wavelength of the acoustic waves. In fact, in many practical cases, the wavelength of generated acoustic waves is comparable to that of the vortices. The advantage of numerical simulation is that this compact source assumption is not needed.

The second group of approaches is to make use of acoustic/viscous splitting method that is based on the expansion about incompressible flow (EIF) approach. In sound propagation problems the effects of viscosity and heat conduction can be neglected and the fluid motion can be determined by solving the linearized or the non-linear Euler Equations. In the EIF method, the instantaneous velocities and density are treated as the summation of the steady mean flow and the unsteady disturbances. Substituting the sums to the Euler equations, the dynamic equations for unsteady disturbance components of mass and momentum fluxes are obtained (Goldstein, 1976). The mean flow can be obtained analytically or numerically using low-order schemes of CFD. However, it is not an easy task to obtain steady state solution for the background flow and the acoustic solution for disturbances simultaneously. Therefore, a multi-stage approach has been implemented by many researchers: (i) to obtain steady state solution using traditional low-order schemes; (ii) to find unsteady wave propagation solution using high-order schemes for space and time to precisely capture the sound pressure. This approach was developed by Hardin and Pope (1992), and later expanded to compressible and unsteady mean flow by Shen and Sorensen (1999).

This approach splits the direct simulation approach into a background flow problem and a perturbation problem, and does not allow for acoustic backscatter into the flow solution. It makes possible computation of aeroacoustic noise generation and propagation by viscous, unsteady, non-uniform flows in complex domains that pose substantial

advantage over the first group of methods. On the other hand, the computing cost required is much smaller than that for the CFD solution of the time-dependent subsonic flowfield. When the radiated noise is originated from deforming relatively large (compared to the size of turbulent eddies) vortices in the flow about the solid surface, the mean velocity gradients are still significant. Therefore, integral methods, which are often used to solve the far-field noise, are not applicable to this domain; only the Euler equations may account for the sound propagation in a non-homogenous flow. Thus, this approach was adopted for the current research although the first stage (viscous vortex generation) was replaced by given initial conditions or forcing term in the Euler equations for the disturbances.

The third group of approaches is to make use of direct numerical simulation (DNS), where both the fluid motion and the generated sound are directly computed by means of the Navier-Stokes equations. One of the advantages of DNS over the methods in the first two groups is its capability to compute the generation and propagation processes of the sound in the near and intermediate fields, without suffering from restrictions such as low Mach number, high Reynolds number and compactness of the source region. DNS methods are specially suited to model broadband noise generated by turbulence and dedicated frequencies that appear from vortex-structure interactions. This approach requires tremendous computational resources. Some authors solve the Euler equations for short-time, high-speed sound-generating phenomena such as shock wave-vortex

interaction and call it Direct Numerical Simulation (e.g., Inoue el al., 2002) although these authors neglect viscosity and turbulence.

B. PDE discretization

The acoustic waves are non-dispersive and non-dissipative in their propagation, and are particularly susceptible to numerical dispersion and numerical dissipation. Numerical dispersion distorts the phase between various waves and numerical dissipation reduces the gradients in the solution (Tam, 1995). One straightforward way to overcome this obstacle is to use a very fine grid along with a standard low-order method. Although such an approach is possible in principle, such calculations are not truly feasible because of such dramatic increase of computational time and memory requirements. To accurately resolve the propagation of the acoustic wave finite difference and time-marching schemes that have low numerical dissipation, and accurately represent the dispersion relation for the inviscid equations are required (Inoue et al, 1999). The following high-order schemes are widely used in computational aeroacoustics.

Lele(1992) analyzed the implicit-in-space high order finite difference scheme, with spectral-like resolution and a compact stencil. This represents accurately the exact result, over the broad range of length scales that can be realized on a given mesh of reasonable size. Choosing different coefficients, forth-order, sixth-order or eighth-order compact schemes can be obtained on a three-point stencil. Furthermore, after the coordinate

transformation, this scheme may be used on non-uniform meshes, and a variety of boundary conditions may be imposed.

Tam & Webb (1993) introduced the now classic explicit DRP (Dispersion-Relation-Preserving) finite difference scheme. The DRP scheme is fourth-order of accurate using a seven point stencil in space and a third-order in time. The DRP approach minimizes the level of dispersion and dissipation by adjusting the central-difference scheme on a wide stencil to match the characteristics of the wave.

In terms of dispersion properties, the fourth-order DRP scheme is similar to the fourth-order compact scheme. The DRP scheme does not need to solve 3-diagonal matrices but a smaller time step is needed for the DRP scheme than that for compact schemes. And a smaller time step is necessary for the stability of a wider stencil. Both compact schemes and DRP explicit schemes require adopting special one-sided near boundary stencils. However, the DRP scheme is less warrant in terms of near-boundary stability of integration in time.

Runge-Kutta (RK) methods are widely used in CFD to discretize the time derivative because of their flexibility, relatively large stability limits, and ease of programming. However, classical Runge-Kutta methods retain both dissipation and dispersion errors. When classical Runge-Kutta schemes are used in wave propagation problems using high-order spatial finite differences, to be time accurate in resolving the

wave propagation, the time steps allowed are much smaller than those dictated by the stability limit analysis.

To satisfy the low dissipation and low dispersion requirements, several Runge-Kutta schemes have been developed by various authors. They may have a slightly different number of stages, memory requirements, and may be explicit or implicit in time. Consequently, they may have moderately different time steps that are given by a von-Neumann analysis. Williamson (1980) conceived a fourth-order, five sub-stage, low storage Runge-Kutta method, which was proven to be low in dissipation and dispersion errors. The schemes are low-storage in the sense that only two storage locations are required for the time advancement; one for the time derivative and one for the variable itself. Hu and co-workers (1996) showed that it is possible to choose the coefficients of the Runge-Kutta schemes, so as to minimize the dissipation and dispersion for the convective wave equation.

C. Boundary condition

Aeroacoustics problems are defined on an infinite or semi-infinite domain. The numerical solution of the discrete equations requires truncation of the infinite domain, and the imposition of artificial numerical boundary conditions at the edges of the computational domain. These artificial boundaries not only must ensure non-reflection of acoustic waves, but must also account for the direction of the mean flow with respect to

the boundary.

The theoretical basis for nonreflecting boundary conditions stems from a paper by Engquist & Majad (1977), which discusses both ideal nonreflecting boundary conditions and a method for constructing approximate forms. Also, a paper by Kreiss(1970) analyzes the well-posedness of initial boundary value problems for hyperbolic systems. Since then, a variety of nonreflecting boundary conditions have been developed.

The most widely used nonreflecting boundary conditions for the Euler equations are the characteristics-based inflow and outflow boundary conditions. These are formed by a generalization of the one-dimensional Euler equations to the multidimensional cases. Thompson (1987) and Giles (1990) proposed a nonreflecting boundary condition for the linearized Euler equations. Watson et al (1991) and Lele (1992) modified Thompson's boundary condition for use with the nonlinear Navier-Stokes computations of open flow problems. The use of characteristic variables is quite straightforward and robust, especially for up-winding schemes. However, the accuracy of characteristic boundary conditions is limited by the one-dimensional assumption of wave propagation, because they usually show the best accuracy when the wave propagation angle is normal to the boundary. When the wave is convected in an arbitrary direction, the performance of a one-directional characteristic based scheme deteriorates.

Another type of widely used nonreflecting boundary condition is based on far-field

asymptotic solutions. Engquist & Majda (1977) proposed a boundary condition that would replace the wave equation at the grid boundary, by the one-way wave equation for acoustic and elastic waves. These boundary conditions are suitable for angles of incidence smaller than 45 degrees. Bayliss & Turkel (1980) obtained a sequence of radiation boundary conditions for the wave equation with axial and spherical symmetries. Keys (1985) and Higdon (1986) independently proposed an improved boundary condition that successfully eliminates the artificial reflections from arbitrary angles of incidence. The asymptotic solution is accurate when it is applicable. However, the asymptotic forms are normally difficult to obtain, this type of boundary condition may not be applicable in many situations. In addition, to implement the asymptotic solution-based boundary condition, the computational boundary has to be placed further in the field to achieve the accuracy, which will mean a great cost of computation.

A third type of widely used nonreflecting boundary condition is the buffer zone technique, in which a non-physical computational domain is introduced to adjoining the physical computational domain, and the governing equations are accordingly modified to absorb the incident waves. The buffer zone solutions serve to prevent contamination of the solution in the physical domain of interest by the reflections from the computational boundaries. Various types of buffer zone techniques have been used in flow simulations. For instance, Israeli and Orszag (1981) tried grid-stretching and numerical damping to damp the numerical solution in the buffer zone. Colonius et al. (1993) used low-pass

filters to filter the numerical solutions in the extra zone. Ta'asan and Nark (1995) modified the governing equations in the buffer zone to change the orientation of the characteristics. The mean flow was accelerated to a supersonic velocity toward the end of the added buffer sub-domain, thus softening the need for perfectly nonreflecting boundary conditions. The accuracy of buffer zone methods depends on the gradualness in which thee different parameters are varied inside the buffer zone. Moreover, the added buffer zone is usually required to be of substantial length for the method to be effective. Because of this, increase in computational cost can be quite significant.

The forth type of nonreflecting boundary condition, called the perfectly matched layer (PML) technique, was first introduced by Berenger (1994) for absorbing electromagnetic waves of the Maxwell equations. Hu (1996) gave PML equations for absorbing acoustic waves of the Euler equations. As a follow-up to Berenger's formulation, Hu first used split variables in the PML domain. However, with split variables numerical instability can occur in the PML domain, and ruin the numerical solution in the computational domain. Hu (2001) proposed to use original physical variables in PML domain, which is proved to be stable and well-posed. The PML technique and the other buffer zone techniques, have an added zone which is the non-physical computational domain to reach the non-reflection boundary condition. Moreover, the equations to be used in the added region in the PML technique, are constructed in such a way that, theoretically, the outgoing waves will not cause any

reflection when entering a PML domain for any frequency and angle of incidence, which the buffer zone technique can not reach.

If there is either still media or uniform background flow, there should be several PML forms available. However, for advective problems with non-uniform flow, no general stable solution is known. Therefore in this study, a considerable effort has been put to implement appropriate boundary conditions.

D. Vortex-body Interaction

Based on the orientation of the incident vortex with respect to the leading edge or surface of the body, vortex body interaction can be categorized into three parts:(a) parallel or two-dimensional blade vortex interaction where vorticity along the axis of the vortex is perpendicular to the x, y plane of the body, (b) streamwise or perpendicular vortex interaction where the axis of the vortex is aligned with the direction of the incident flow and perpendicular to the leading edge of the body, and (c) normal vortex interaction where the axis of the vortex is perpendicular to the direction of the incident flow and nominally orthogonal to the direction of the leading edge of the body (see Fig.1.1).

1. Normal vortex-body interaction

Normal vortex-body interaction is particularly representative of rotorcraft aerodynamic problems. Namely, the impingement of rotor tip vortices on the vehicle empennage, airframe tail section and tail.... during hover and low-speed flight. This BVI

leads to strong impulsive forces and moments on the vehicle (Sheridan & Smith 1980; Bi & Leishman 1990; Bi, Leishman & Crouse 1993). For normal vortex body interaction, some experiments (Harvey & Perry 1971; Barker & Crow 1977; Brand et al. 1989; Krishnamoorthy et al. 1999), and numerical investigations (Harvey & Perry 1971; Affes

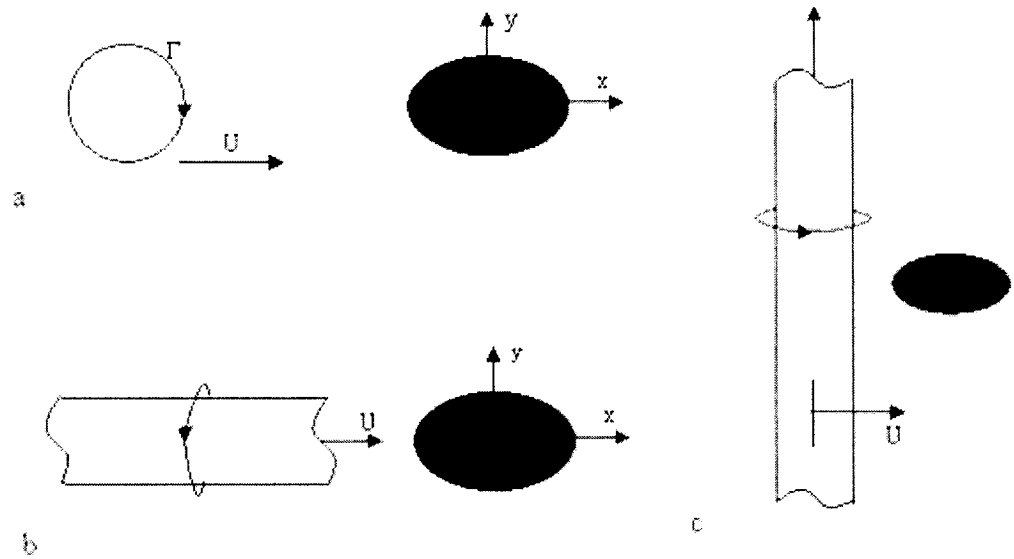

Figure 1-1 Configuration of vortex–body interaction (VBI): (a) parallel VBI, (b) streamwise VBI, (c) normal VBI.

et al. 1993; Marshall & Yalamanchile 1994; Krishnamoorthy et al. 1999; Gossler & Marshall, 2001) have been done. Unlike the movement of the vortex about the body (for parallel or streamwise vortex body interaction), which involves either direct impingement upon the body or a miss, a normal vortex-body interaction involves an unavoidable collision with the leading edge of the body and distortions of the vortex structure are very rapid. Also the separation of the boundary-layer in the adverse pressure gradient region,

leads to the ejection of (secondary) vorticity generated on the body into the surrounding fluid. The secondary vorticity interacts with the original (primary) vortex, and can lead to such consequences as vortex rebound from the surface or a breakup of the vortex into small-scale turbulence (Gossler & Marshall, 2001).

2. Perpendicular vortex-body interaction

The study of the encounter of a streamwise vortex, with a blade or airfoil is mainly motivated by its affect on the lift, and on the blade and acoustic effects, specifically the impulsive noise. Impulsive noise is generated as a consequence of the unsteady lift, experienced, during the subsequent parallel blade vortex interactions. To better predict this noise, the accurate knowledge of the vortex parameters is required, namely, the vortex core size, the strength and the circulation distribution. A perpendicular blade vortex interaction can substantially alter the character and development of a trailing vortex even when the vortex core passes some distance from the blade. Therefore, perpendicular BVIs can substantially influence the BVI noise generated by the subsequent parallel blade vortex interaction.

The experimental studies on perpendicular vortex interaction by Ham (1974, 1975), McAlister & Tung (1984), Rockwell (1993), Mayori & Rockwell (1994), Wittmer & Devenport (1999), and the numerical studies on perpendicular vortex interaction by Rizk & Gee (1992), Gee et al (1995), Kandl et al. (1995), Rizzetta (1996), and Visbal (1994,

1995, 1997), identified some key physical features of the encounter of a streamwise vortex with blade or airfoil. They are: (a) the displacement of the trajectory of the vortex in the spanwise direction arising from image effects and the associated mutual induction, (b) the generation of a local separation zone on the surface of the blade, (c) the onset of a vortex breakdown, and (d) the vortex passes the blade without immediate change in the form and structure of its core (Gossler & Marshall, 2001). However, outside of the core the flow is modified by the blade wake, which contains negative streamwise vorticity. This negative vorticity and the turbulent motions of the blade wake, trigger the turbulent decay of the vortex core resulting in an increase in its size, reduction in its strength, and loss of circulation in the flows.

3. Parallel vortex-body interaction

The investigation of parallel vortex-body interaction (which this study focuses on), is mainly concerned with its impulsive BVI noise. Non-impulsive noise prediction (i.e., thickness and loading noise) can now be accomplished routinely, and with great confidence for a steady rectilinear flight. Since the prediction of the rotor flow field and aerodynamic state is challenging, the prediction of vortex-body-interaction noise is even more difficult. According to extensive experiments on the topic, the nearer the parallel the tip vortex is to the blade at the time of interaction, the greater the noise radiation. In fact, a perpendicular interaction, results in little noise (Widnall, 1971).

The problem of the numerical simulation of VBI noise is still beyond the capabilities of direct numerical simulation, so hybrid methods are used in most practical cases. The idea is to divide the physical space of sound into three domains, in which specific physical mechanisms are simulated using the most adequate set of equations with the cheapest discretization strategy (see Fig. 1.2).

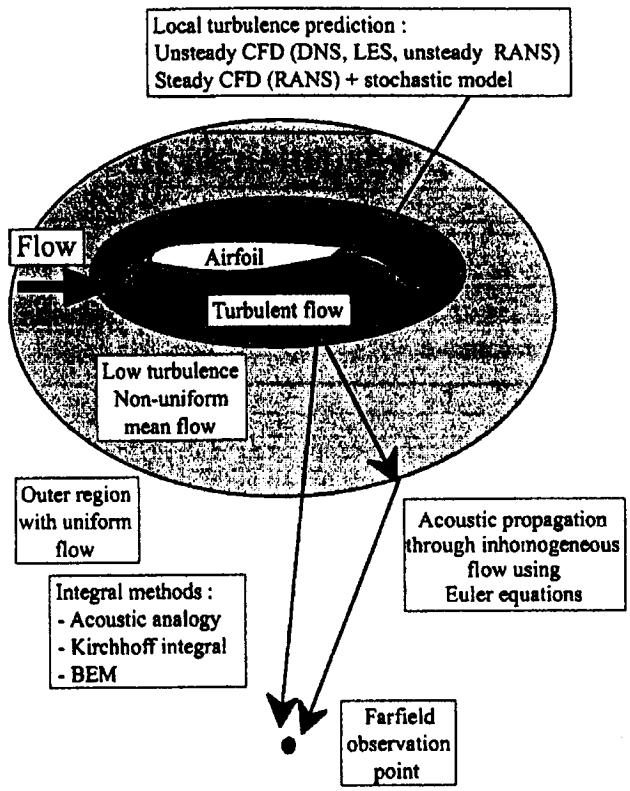

Figure 1-2 Physic space of noise generation and possible hybrid strategies (from Sagaut et al. 2002).

The wake and boundary layer, which are either turbulent or highly viscous, serves as a nursery of vortices. The thickness is of the order of the airfoil thickness – say 0.1 m. In this stage, the fluid dynamics of the vortex and the aerodynamics of the blade are the

main concern. Ziada & Rockwell (1982) visualized the deformation of the vortex structure, during direct and nearly-direct BVI in inviscid flow. Straus et al. (1988) measured airfoil surface-pressure variations during parallel BVI (including near head-on cases), and reported a large flow separation caused by BVI. Wilder et al. (1990) visualized a sequence of interactions of a blade with the oncoming vorticity and reported that a secondary vortex is induced by the incident vortex. Tucker & Conlisk (1992) assumed inviscid flow and employed a large-scale vortex with constant vorticity to determine the initial stages of vortex deformation. By incorporating the viscous effect, Lee & Bershader (1991) clearly demonstrated severe vortex distortion during parallel BVI. Lee & Bershade (1994) calculated the tangential velocity profile of a convecting vortex from measurements and independently obtained the density and pressure distribution of the vortex, and the flow separation arose in both the experiment and the computations. Howe (1995) provided a basis for relating the unsteady loading to the distortion of the incident vortical structures in incompressible viscous flow. Additional information can be found in the article by Rockwell (1998).

The non-uniform mean flow around multi-element airfoil, landing gear etc., where the viscous effects are minor. Deformation of vortices, propagation and refraction of sound waves occur in this domain. The thickness of this area is 1 to 5 chords lengths =1 to 10m.

In the near field, the mean flow velocity gradients are still significant. The FW-H or

Kichroff acoustic analogies do not account for the non-linear convection, so these methods are not suitable for near-field noise prediction. The linearized Euler equations can handle refraction and reflection of the sound waves in non-uniform mean flows in the presence of a rigid surface. Therefore, this means that they are capable accounting for sound propagation in non-homogeneous flow. In comparison, much less work has been done concerning near-field noise prediction. The amplification or weakening of sound propagating in non-uniform flows, has attracted considerable researchers, but the researches are mainly restricted to one-dimensional mean flow. Howe (1976) demonstrated the downstream amplification, which is a result of the Doppler effect. Atassi & Grzedzinsky (1989) considered the propagation of unsteady disturbances in incompressible potential mean flows, that is, around bodies with a stagnation point. They suggested a single Poisson equation of wave propagation for each single source to replace all of the governing equations. This significantly simplifies the governing equations. However, their approach is limited to the immediate vicinity of the stagnation point, and is not applicable to two-dimensional flows. An integral equation of the Fredholm-type for the acoustic velocity potential is also used for the acoustic problem, in which additional assumptions and simplifications are needed to perform the integration. Howe (1989) studied the noise generation due to interactions of a mean flow with vorticity regions in the presence of rigid boundaries. He made use of Lightill's acoustic analogy to solve the propagation of sound through the mean flow, with a steady vorticity given in advance. Lee et al. (1994) conducted an experimental and computational study of head-on parallel

blade-vortex interaction. In this study, the detailed structure of a convecting vortex was analyzed through independent measurements of density and pressure distribution across the vortex center, and where viscous effects were thought to play a significant role in head-on BVIs. Povitsky (2001, 2002) simulated the propagation of acoustic waves originating from cylindrical and spherical pulses and single vortices (the Taylor vortex) convected in a non-uniform mean flow in the presence of a rigid wall or a circular cylinder. In recent study (Povitsky, Zheng &Vatistas, 2004), the influence of the vortex profile on sound generation, propagation and directivity was investigated using the linearized Euler equations. The zero-circulation Taylor vortex model, and the non-zero-circulation Vatistas' vortex model with $n=2$ were considered. It was discovered that the strength, directivity, profile and sector of influence for acoustic waves coming out of the Vatistas vortex were quite different from the ones generated by the Taylor vortex model.

Far field noise is at very long distance from the sound source, where the flow can be assumed uniform. The distance is around 10 m to 100 m. At this location, the effects of landscape, wind, and buildings on the ground should be taken into consideration.

In the last twenty years, considerable progress has been made to understand, as well as to predict, BVI far field noise. Many experiments have been performed to obtain the blade airloads and noise data on the ground (Lee & Mosher, 1979; Maisel &Harris, 1981; Conner & Wellman, 1994; Mosher & Light, 1994; Polak & George, 1996; Polak &

George, 1998; Boyd & Burley, 2001). These experiments concluded that the intensity of BVI noise is strongly dependent on the following factors:(i) tip vortex strength and structure, (ii) distance between the shed vortex and the subsequent blade, (iii) blade loading at the time the vortex is generated, and (iv) blade loading during BVI.

For the numerical simulation of far field noise, a variety of indicial, boundary-element and CFD methods has been used to predict the aerodynamics. These are combined with FW-H or Kirchhoff methods for predicting the far-field acoustics. Howe (1976) provided a framework for assessing the generation of sound by parallel vortex-airfoil interaction. Widnall & Wolf (1980) pointed out that the tip vortex structure can significantly affect the magnitude, of both the unsteady lift and the transient acoustic signal. Brentner & Farassat (1994) have reviewed the acoustic theory and the development in BVI noise prediction. Rahier & Delrieux (1997) used a rotor wake roll-up model and the FW-H equation for BVI noise prediction. They concluded that a rotor wake roll-up model is better for BVI noise prediction. Lily (2001) discussed the several sources of airframe noise and their major characteristics, and pointed out that the prediction of airframe noise depends on the availability of a space/time accurate unsteady flow database for the flow over the complete aircraft and its components. Caradonna et al. (2000) have reviewed the methods for the prediction of blade-vortex interaction noise. One of the outcomes of the computational work was the TRAC code, which was specifically developed by NASA to predict the noise far field of tiltrotor aircrafts. The

TRAC system is found to very accurately predict, the peak value of the BVI sound pulse and its general shape. However, the two side peaks are not evident in the computations, and the computed pulse width is approximately double that of the experimental data (Kitaplioglu & Johnson, 2002).

In the current study, the radiated noise results from sources located near solid walls, where velocity gradients are still significant. In this case, the discretised Euler equations, which may account for the propagation in non-homogeneous flows, was adopted as the governing equations for the sound generation by VBI and sound propagation in non-uniform flow.

1.3 Contributions

In summary, because of the numerical and experimental obstacles involved, many aspects of the aeroacoustics phenomena related to airframe noise or blade vortex interaction noise have not yet been understood. Specifically, compared with the far-field noise prediction, much less is known about the noise generation and propagation in non-uniform flows.

To simulate numerically the sound generation and propagation in a non-uniform flow, it is important to have computational tools with high-order numerical schemes, high-order time integration methods and elaborate artificial boundary conditions. To understand the mechanisms of vortex-body interaction noise, we should be able to predict

the pressure quadrupole generation and the radiation of acoustic waves.

The objective of this research is to develop high-performance computing tools for aeroacoustic predictions. The developed tool will then help provide insi ght into the physical mechanisms and the influence that the strong mean flow gradients have on the directivity and strength of sound waves generated by a deforming vortex while propagating in such a flow. This research is are aiming at to numerically examine the effect that the various vortex profiles have on the generated sound wave.

The sound generation, propagation, and refraction in a non-uniform flow around a solid surface were analyzed in the current study for a sequence of increasingly complex configurations of rigid elements. The work includes:

The modeling of noise generation and propagation when the mean potential stagnation flow carries a single vortex that impinges on a flat plate (Case A). This is a simplified set-up to approximate the impingement of vortices, which are shed by multi-element airfoils or by the landing gear, into the fuselage surface.

The numerical simulation of the interaction between either a convected single vortex or a vortex-street and a stationary cylinder (Case B). This set-up represents a simplification of the blade-vortex and airfoil-vortex interaction problem. Both weak and strong vortices were modeled and the nonlinear effects were also investigated.

The impingement effects of the mean flow, carrying a single vortex or vortex street,

into the flow around rotating cylinder (Case C), which satisfies the Kutta condition.

Sound generated by a periodic acoustic pulse or vortex trapped between two cylinders (Case D), is considered as the prototype of sound generation by several bodies in close proximity to each other, such as a multi-element airfoil.

1.4 Significance of Contributions

The uniqueness and significance of this research is as follows:

1. For the first time, single and periodic vortices combined with various vortex velocity profiles were considered in the same computational framework. This provided a computational insight into the physical mechanisms of the influence of mean flow gradients on the directivity and strength of sound waves.

2. The role that the vortex strength, vortex core size, vortex street frequency, the Mach number of mean flow, and the vortex profile play on the sound radiation were examined, and simple scaling laws were obtained where possible.

3. The effects of the non-linear terms in the Euler equations (in terms of disturbances) were investigated. Several crucial features of the acoustic field obtained by non-linear simulations were shown to be different from those obtained by linear simulations. While linear predictions have suggested a zone of silence around the centerline, the non-linear simulation results reveal that the acoustic pressure was

actually far from zero on the centerline.

4. Sound generation and propagation by a turbulence vortex model was investigated. It was found that consideration of the turbulence in the vortex would not change the sound directivity but would enhance the sound strength of the radiated noise by VBI .

5. The strength and directivity of acoustic wave patterns were found to be similar for all one-cell non-zero-circulation vortex models. The influence of the radial velocity on the sound generation and propagation was investigated. For the first time, sound waves radiated by a two–cell vortex were investigated.

6. The mean flow around a lifting cylinder, which was a prototype of a loaded airfoil, was considered. Computations revealed that the sound was amplified and the directivity was shifted.

7. Multi-body vortex interactions were examined as prototypes of noise generated by several bodies in close proximity to each other. In this case, bipolar and elliptic coordinate transformations were used.

8. In terms of tool development, this research centered on a single-grid approach and implements the corresponding transformation of coordinates. The advantage of single-grid approach over multi-zone or unstructured grid approaches is that it requires less strict stability constraints and reduces the time required to run and develop the codes.

9. The developed codes can be used as a core part of software that effectively predicts the noise of deploying multi-element airfoil and undercarriage noise. They will reduce the need for costly wind tunnel and field aeroacoustic experiments for the future design of multi-element airfoils.

Chapter II

Methodology

In this section, the methodology developed for this study will be introduced. In Section 2.1, the mathematical methodology is outlined. In Section 2.2, the vortex models used are introduced. The high-order spatial derivatives and time-marching scheme are provided in Section 2.3. The boundary conditions are provided in Section 2.4.

2.1 Mathematical Model

In sound propagation problems, the effects of viscosity and heat conduction can be neglected and the fluid motion can be determined by solving the linearized Euler Equations. To solve the governing unsteady Euler equations, the expansion about incompressible flow (EIF) method, which was proposed by Hardin & Pope (1992), was implemented. The EIF approach splits the direct simulation approach into a mean flow problem, and a perturbation problem. It does not allow for the acoustic perturbation problem to backscatter into the flow solution. In the near field, the perturbation quantities are the differences between the unsteady compressible and steady incompressible flowfield variables, e.g., pressure quadrupoles. The perturbation quantities are equivalent

to the acoustic quantities in the far field. The variable split used in the EIF, reduces the difficulties associated with:(a) the small amplitude resolution of the acoustic wave fluctuations relative to the mean flow quantities, (b) the long propagation distance of acoustic waves to the far field, and (c) the large acoustic temporal scales, a characteristic for periodic vortices. The EIF approach provides an effective method of predicting acoustic fields resulting from low Mach number noncompact source region (Slimon et. al.1990).

Introducing a disturbance, the instantaneous velocities and density are treated as sums of the given steady mean flow and the unsteady disturbances, i.e.,

$$u = U + u', v = V + v', p = P + p', \rho = R + \rho' \tag{1 3}$$

where u', v', p', ρ' are acoustic disturbances, U, V, P, R are background steady mean flow components. This may be given, either analytically or numerically. Upon substitutions of the sums to the Euler equations, the dynamic equations for the unsteady disturbance components of mass and momentum fluxes yield in Cartesian coordinates:

$$\begin{aligned}
(R+\rho')\frac{\partial(U+u')}{\partial t} &= -\frac{\partial(P+p')}{\partial x} - (U+u')(R+\rho')\frac{\partial(U+u')}{\partial x} - (V+v')(R+\rho')\frac{\partial(U+u')}{\partial y} \\
(R+\rho')\frac{\partial(V+v')}{\partial t} &= -\frac{\partial(P+p')}{\partial y} - (U+u')(R+\rho')\frac{\partial(V+v')}{\partial y} - (V+v')(R+\rho')\frac{\partial(V+v')}{\partial y} \\
\frac{\partial(R+\rho')}{\partial t} &= -\frac{\partial(U+u')(R+\rho')}{\partial x} - \frac{\partial(V+v')(R+\rho')}{\partial y}
\end{aligned} \tag{14}$$

The fluctuating quantities have been non-dimensionalized by the following scales:

Length scale = Characteristic length, L

Velocity scale = ambient speed of sound, c_∞

Time scale = $\frac{L}{c_\infty}$

Density scale = ambient gas density, ρ_∞

Pressure scale = $\rho_\infty c_\infty^2$

Neglecting the second or higher order, after subtracting the mean flow equations, the linearized Euler equations for disturbance are obtained as

$$\begin{aligned}
\frac{\partial p'}{\partial t} &= -R\left(\frac{\partial u'}{\partial x}+\frac{\partial v'}{\partial y}\right)-U\frac{\partial p'}{\partial x}-V\frac{\partial p'}{\partial y}-u'\frac{\partial R}{\partial x}-v'\frac{\partial R}{\partial y}-p'\left(\frac{\partial U}{\partial x}+\frac{\partial V}{\partial y}\right)\\
\frac{\partial u'}{\partial t} &= -\frac{1}{R}\frac{\partial p'}{\partial x}-U\frac{\partial v'}{\partial y}-V\frac{\partial u'}{\partial y}-\frac{\partial U}{\partial x}u'-\frac{\partial U}{\partial y}v'-\left(U\frac{\partial U}{\partial x}+V\frac{\partial U}{\partial y}\right)\frac{p'}{R}\\
\frac{\partial v'}{\partial t} &= -\frac{1}{R}\frac{\partial p'}{\partial y}-V\frac{\partial v'}{\partial y}-U\frac{\partial v'}{\partial x}-\frac{\partial V}{\partial x}u'-\frac{\partial V}{\partial y}v'-\left(U\frac{\partial V}{\partial x}+V\frac{\partial V}{\partial y}\right)\frac{p'}{R}
\end{aligned} \tag{15}$$

If the compressibility of the background flow is considered, the local density R and the local speed of sound are given by:

$$\begin{aligned}
R &= \left(1-\frac{\gamma-1}{2}\left(U^2+V^2-M_0^2\right)^{1/(\gamma-1)}\right)\\
c &= \left(1-\frac{\gamma-1}{2}\left(U^2+V^2-M_0^2\right)^{1/2}\right)
\end{aligned} \tag{1 6}$$

where M_0 is the Mach number in the reference point where the speed of sound and the density of mean flow are set equal to unity. Povitsky (2002) demonstrated the

accounts for the compressibility in the mean flow (i.e., variable density and speed of sound) for $M < 0.4$ leads to modest changes in the directivity of sound. In our study, incompressible background flow is assumed, and the equation is normalized in such a way that $c = 1$ and $R = 1$, therefore the normalized disturbance pressure and density are identical. The governing equations for the pressure p' and density ρ', will be the same and only one of them is required to be solved.

2.2 Models of vortex

As mentioned in the literature review, different vortex profiles have been developed by different authors. Those vortices can be categorized into two groups in accordance with the total circulation of the vortex, $\Gamma = \int \Omega dA$ (where Ω is the vorticity in the 2-D flow). The first group includes zero-circulation vortex model such as the Taylor (1918) vortex, in which the tangential velocity decays exponentially fast. The non-zero-circulation vortex models include: the Scully (1975) vortex, and a family of Vatistas (1991, 1998) vortices in which the tangential velocity decays proportional to $\Gamma/(2\pi r)$, and where r is the distance away from the vortex center. The velocity distribution of different vortex models is presented in Fig. 2.1.

Taylor's vortex, a representative zero-circulation vortex, is compact. This means that, the tangential velocity decays exponentially outside the vortex core, as shown in Fig. 2.1. The tangential velocity is negligibly small for $r/Rc \geq 3.5$. For non-zero circulation vortex models, the tangential velocity decreases proportionally to $\Gamma/(2\pi r)$ outside the vortex

core. The radial velocity is several orders of magnitude smaller than the tangential velocity. The radial distribution of the vortical disturbance has the same sign everywhere and reach zero at the vortex center for the one-cell vortices. For a two-cell vortex model, the radial velocity experiences a direction reversal at the cell interface.

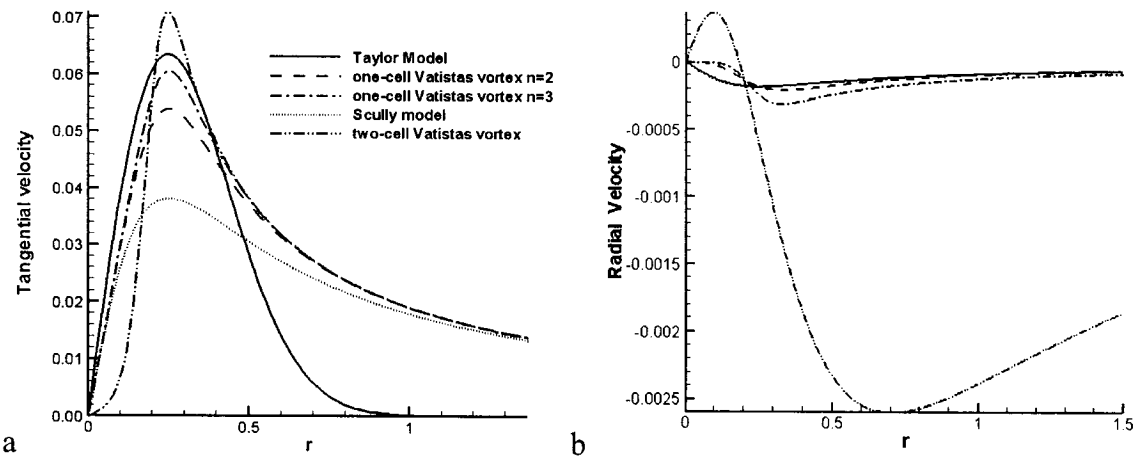

Figure 2-1 Vortex velocity distributions with respect to the distance to vortex center: (a) tangential velocity and, (b) radial velocity.

All the vortex models that were considered above assume that the vortex is laminar, which only occurs when Reynolds number is low. In reality, many wings operate at conditions where the vortex Reynolds number is in the intermediate (transitional) regime where the vortex is neither fully laminar nor fully turbulent (see Fig. 2.2).

The following vortex model takes into consideration the effects of turbulence and is formulated by curve-fitting the experimental results of Leishman (2004) and Ramasamy & Leishman (2003). The assumed velocity profile used to approximate the data via the least-Squares method is:

$$V = \frac{r(a+4)^{1/m}}{\left(a+r^2+r^4+r^6+r^8\right)^{1/m}} \qquad (17)$$

Figure 2-2 A representative flow visualization image of a tip vortex emanating from a rotor blade showing three distinct regions: (1) Laminar region, (2) Transitional region, (3) Turbulent region (from Ramasamy & Leishman, 2004).

Where a and m are constants that are to be determined. The requirement that V must be maximum at $r = 1$ yields,

$$m = \frac{20}{a+4} \qquad (18)$$

The value of a is then found by minimizing the square error E, i.e.,

$$E = \sum_{j=1}^{N} \left[V(r_j) - f(r_j)\right]^2 \qquad (19)$$

where f_j and V_j are the experimental and theoretical values of the velocity respectively.

For minimum E the above equation must satisfy:

$$\frac{\partial E}{\partial a} = \sum_{j=1}^{N} \left[V(r_j) - f(r_j) \right] \frac{\partial}{\partial a} V(r_j) = 0 \qquad (20)$$

The value of a is then determined finding the root of the following equation,

$$\sum_{j=1}^{N} \left[\frac{r_j \beta \gamma}{\left(a + r_j^2 + r_j^4 + r_j^6 + r_j^8 \right)^{\gamma}} - f(r_j) \right] (A_j + B_j) = 0 \qquad (21)$$

where

$$\beta = a + 4$$
$$\gamma = \frac{\beta}{20} \qquad (22)$$
$$A_j = \frac{r_j \beta \gamma}{\left(a + r_j^2 + r_j^4 + r_j^6 + r_j^8 \right)^{\gamma}} \left(\frac{1}{20} + \ln[\beta] \right)$$

and

$$B_j = \frac{r_j \beta \gamma \left(\dfrac{\gamma}{a + r_j^2 + r_j^4 + r_j^6 + r_j^8} + \ln\left[a + r_j^2 + r_j^4 + r_j^6 + r_j^8 \right] \right)}{\left(a + r_j^2 + r_j^4 + r_j^6 + r_j^8 \right)^{\gamma}} \qquad (23)$$

The zero may be obtained numerically using, say, the secant method. This gave $a = 0.3993330202959833$. The value of m then is 4.546136783752

Finally, the swirl velocity distribution is approximated well by,

$$V_\theta = \frac{\Gamma}{2\pi R_c} \frac{\bar{r}}{\left(0.399 + \bar{r}^2 + \bar{r}^4 + \bar{r}^6 + \bar{r}^8 \right)^{\frac{1}{4.54}}} \qquad (24)$$

Where $\bar{r}$ is dimensionalized by R_c, the vortex core radius.

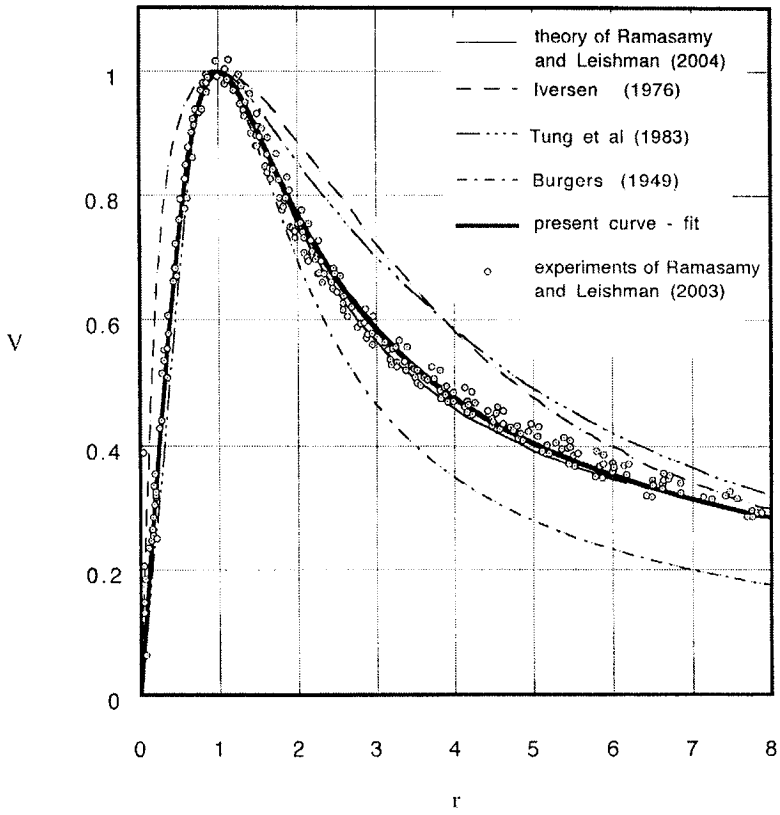

Figure 2-3 Swirl velocity distribution with respect to r.

The tangential velocities for different turbulent vortex models are presented in Fig. 2.3. It must be noted that in this model the vortex Reynolds number is high $R_e = 48{,}000$. Within the vortex core, the vortex is still laminar, outside the core however, the vortex is fully turbulent.

In the present study, the interaction of a single vortex, a vortex dipole, and a vortex street with a solid body, in which, a vortex dipole is composed of a pair of vortices with same strength but counter-spinning, were investigated. Two types of vortices were used,

the weak or small vortex, which has a vortex core of 0.04 and a circulation of 0.00005. The other is the strong or large vortex, which has a vortex core of 0.25 and a circulation of 0.12. If not specified, the Vatistas vortex represents the one-cell Vatistas vortex with $n = 2$, which formula is given in Eq. 5.

2.3 Numerical method

To accurately resolve the propagation of acoustic waves, finite difference and time-marching schemes that have low numerical dissipation and represent accurately the dispersion relation are required (Tam, 1995). In this study, the forth-order-accurate central-difference compact scheme of Lele (1992), which is characterized by low dissipation, and near spectral representation of the dispersion relationship, was chosen for the numerical approximation of the spatial derivatives in the Euler equations.

If the values of a function on a set of nodes are given, the finite difference approximation to the derivative may be expressed as a linear combination of the given function values. The finite difference approximation U_i' of the first derivative $\frac{dU}{dx}(x_i)$ at the node i, depends on the function values at nodes near i, i.e.,

$$\beta U'_{i-2} + \alpha U'_{i-1} + U'_i + \alpha U'_{i+1} + \beta U'_{i+2} = c\frac{U_{i+3} - U_{i-3}}{6\Delta x} + b\frac{U_{i+2} - U_{i-2}}{4\Delta x} + a\frac{U_{i+1} - U_{i-1}}{2\Delta x} \qquad (25)$$

where U is the function value. In this study u', v', p'. U' represent the spatial derivative of U and Δx is th e grid step.

The relations between the coefficients a,b,c and α,β, are derived by matching the Taylor's series coefficients of various orders. The first unmatched coefficient, determines the formal truncation error in the approximation of Eq. 25

The constraint for fourth order scheme is:

$$a+2^2b+3^2c=2\frac{3!}{2!}\left(\alpha+2^2\beta\right) \qquad (26)$$

If the dependent variables are periodic in x, then the system of relations (25) written for each node, can be solved together as a linear system of equations for the unknown derivative values. This linear system is a cyclic tridiagonal when β is zero. If $c=0$ is made, a one-parameter (α) family of fourth-order tridiagonal schemes is obtained. For these schemes

$$\beta=0,\quad a=\frac{2}{3}(\alpha+2),\quad b=\frac{1}{3}(4\alpha-1),\quad c=0 \qquad (27)$$

If $\alpha=\frac{1}{4}$ is chosen, thus $a=\frac{3}{2}$ and $b=0$

Substitute the above values into Eq. 25 and the classical Pade scheme is obtained:

$$\frac{1}{4}U'_{i-1}+U'_i+\frac{1}{4}U'_{i+1}=\frac{3}{4\Delta x}\left(U_{i+1}-U_{i-1}\right) \qquad (28)$$

At the boundary of computational domain, the first derivative at node $i=1$ may be obtained from a relation of the form (Lele, 1992):

$$U'_1+\alpha U'_2=\frac{1}{\Delta x}\left(aU_1+bU_2+cU_3+dU_4\right) \qquad (29)$$

If a third-order-accurate scheme is desired, the coefficients must satisfy the following constrains:

$$a=-\frac{11+2\alpha}{6},\quad b=\frac{6-\alpha}{2},\quad c=\frac{2\alpha-3}{2},\quad d=\frac{2-\alpha}{6} \tag{30}$$

If $d=0$ is given, then $a=-\frac{5}{2},\quad b=2,\quad c=\frac{1}{2}$

Thus, a third-order-accurate compact scheme biased toward the interior nodes is obtained:

$$\begin{aligned} U_1'+2U_2' &= \frac{1}{\Delta x}\left(-\frac{5}{2}U_1+2U_2+\frac{1}{2}U_3\right) \\ U_n'+2U_{n-1}' &= \frac{1}{\Delta x}\left(-\frac{5}{2}U_n+2U_{n-1}+\frac{1}{2}U_{n-2}\right) \end{aligned} \tag{31}$$

Classical Runge-Kutta schemes not only provide relatively large stability limits, but also include low storage requirements. This is important for computational acoustics applications, where large memory use is expected. However, Runge-Kutta schemes retain both dissipation and dispersion errors, the time step is limited by the tolerable dissipation and dispersion errors in computing acoustic waves. A family of low-storage schemes which is proposed by Williamson (Williamson, 1980) and implemented by Wilson et al. (Wilson, 1998), gives low amplitude and phase errors of traveling wave solutions.

To simplify this discussion, consider the following convective wave equation:

$$\frac{\partial U}{\partial t}+\frac{\partial U}{\partial x}+\frac{\partial U}{\partial y}=0 \tag{32}$$

The equation is advanced from time level, n, to $n+1$ in Q substag es. The advancement from substage M to $M+1$, is defined by:

$$U^{M+1} = U^{M} + b^{M+1}\Delta t H^{M} \qquad (33)$$

where M =1,...,5 is the particular stage number; Δt i s the time step, b^{M} is the coefficient, and U^{M} represents the U value at the M_{th} sub -stage. The term H^{M} is given as the sum of all the right-hand side terms of Eq. 24, and the accumulation from the previous sub-stage or from the initial conditions at $t = 0$:

$$H^{M} = S_x \frac{\partial U^{M}}{\partial x} + S_y \frac{\partial U^{M}}{\partial y} + a^{M} H^{M-1} \qquad (34)$$

The low-storage requirement is accomplished by continuously overwriting the storage location for the time derivatives and unknown variables at each sub-stage:

$$\begin{aligned} a^{M} H^{M-1} &\rightarrow H^{M} \\ U^{M} + b^{M+1}\Delta t H^{M} &\rightarrow U^{M+1} \end{aligned} \qquad (35)$$

The notation $\rightarrow$ is used to indicate that the storage locations, H^{M-1}, U^{M} are overwritten by H^{M}, U^{M+1} at each time, respectively.

For a fourth-order, five sub-stage Runge-Kutta low storage scheme, the coefficients a^{M} and b^{M} are given in (Wilson, 1998) as:

$$a^{1} = 0; a^{2} = -0.41789047; a^{3} = -1.19215169; a^{4} = -1.69778469; a^{5} = -1.51418344$$

$$b^1 = 0.14965602; b^2 = 0.37921031; b^3 = 0.82295502; b^4 = 0.69945045; b^5 = 0.15305724$$

(36)

In the current study, the conservative schemes which precisely satisfy the continuity equations, and non-conservative scheme, which satisfy the continuity equations with the error of $O(\Delta x^n)$, were both used.

For a conservative scheme, the time marching of the Runge-Kutta scheme is done by the following formulas:

$$H^M = -\frac{1}{h_\zeta h_\eta}\left(\frac{\partial(h_\eta u)^M}{\partial\xi} + \frac{\partial(h_\xi v)^M}{\partial\eta}\right) + a^M H^{M-1} \qquad (37)$$
$$U^{M+1} = U^M + b^{M+1}\Delta t H^M,$$

where the spatial derivatives of $\frac{\partial(h_\eta u)}{\partial\zeta}$ and $\frac{\partial(h_\zeta v)}{\partial\eta}$ are computed by compact scheme

For a non-conservative scheme, the time marching of the Runge-Kutta scheme is done as follows

$$H^M = -\frac{1}{h_\zeta h_\eta}\left(u^M \frac{\partial(h_\eta)^M}{\partial\xi} + v^M \frac{\partial(h_\xi)^M}{\partial\eta}\right) - -\frac{1}{h_\zeta}\frac{\partial u^M}{\partial\xi} - \frac{1}{h_\eta}\frac{\partial v^M}{\partial\eta} + a^M H$$
$$U^{M+1} = U^M + b^{M+1}\Delta t H^M \qquad (38)$$

The computer code was tested using available analytical and numerical solutions (Colonius et al. 1994).

2.4 Boundary conditions

When the vortex field is implemented as an initial condition, it may violate the non-penetrating boundary condition if its core reaches the rigid wall. On the solid surface (flat plate and cylinder wall), to satisfy the zero normal velocity boundary condition, a vortex image system is employed at $t = 0$.

For disturbance variables, the reflection boundary conditions $dp/dn = 0$ and $dv/dn = 0$ are used for pressure disturbance and for the tangential component of velocity. The normal to rigid surface component of velocity is set equal to zero. Discretization of spatial derivatives in the direction perpendicular to a rigid boundary is computed by one-sided finite differences at all boundaries (Povitsky, 2002).

In Case B, C, D, special attention is paid to coinciding points $\theta = -\pi$ and $\theta = \pi$ in polar coordinates. For $\theta = -\pi$, all disturbance components are computed directly by solving the dynamical equations. For $\theta = \pi$, periodic boundaries are employed, namely $u, v, p_{\theta=-\pi} = u, v, p_{\theta=\pi}$. Spatial derivatives for the $\theta = -\pi$ boundary are taken as the average of one-sided spatial derivatives of $\theta = -\pi$ and $\theta = \pi$.

At the outer boundary, artificial boundary conditions (ABC) should be set-up to eliminate reflections of acoustic energy back into the computational domain. First the Characteristic boundary condition, which have been proposed by Thompson (1987) and improved by Giles (1990), was tried. The characteristic boundary-based ABC is

satisfactory for Case A, however, unacceptable numerical reflections are observed in cases B, C and D.

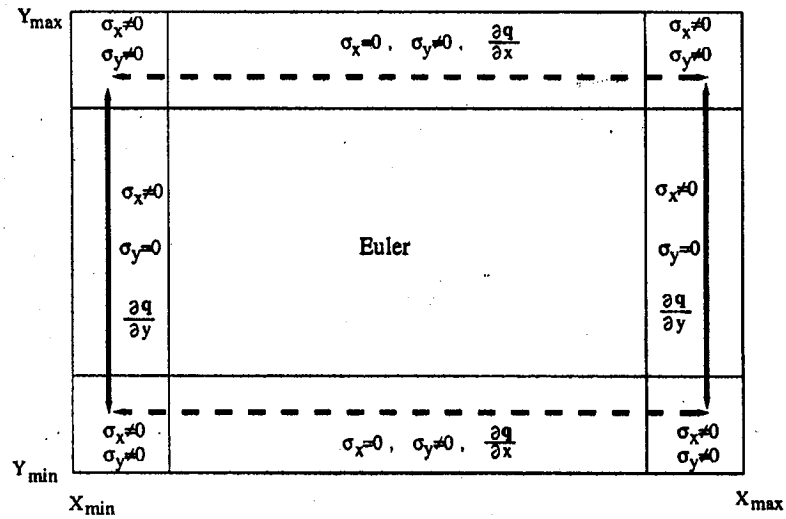

Figure 2-4 Computational domain that combines the Euler and PML domains (from Fang Q. Hu, 2001).

To guarantee the non-reflection boundary condition, the perfect matched layer at the artificial boundary proposed by Hu (1996, 2000) was implemented in the current study, which substantially reduces the numerical reflections at the outer boundary. By introducing a non-physical domain adjacent to artificial boundaries, the Euler equations are solved in the interior field, and the proposed PML equations are solved in the PML domain, thus absorbing all outgoing waves.

Considering the linearized Euler equations in a vector form:

$$\frac{\partial \vec{u}}{\partial t} + A\frac{\partial \vec{u}}{\partial x} + B\frac{\partial \vec{u}}{\partial y} = 0 \tag{39}$$

Two absorption coefficients σ_x, σ_y and one auxiliary variable q are introduced into the PML equations:

$$\begin{aligned} &\frac{\partial \vec{u}}{\partial t} + A\frac{\partial \vec{u}}{\partial x} + B\frac{\partial \vec{u}}{\partial y} + \sigma_y A\frac{\partial \vec{q}}{\partial x} + \sigma_x B\frac{\partial \vec{q}}{\partial y} + (\sigma_x + \sigma_y)\vec{u} + \sigma_x\sigma_y\vec{q} = 0 \\ &\frac{\partial \vec{q}}{\partial t} = \vec{u} \end{aligned} \tag{40}$$

where the coefficients σ_x and σ_y are chosen so that σ_y is the same across an interface normal to x, and σ_x is the same normal to y so as σ_x or σ_y will be zero across an interface normal to x or y between an interior domain and a PML domain. The auxiliary variable q is needed only inside the PML domains; it is neither computed nor stored inside the Euler domain (see Fig. 2.4).

The absorption coefficients used in this study are given by:

$$\sigma_x = \sigma_m \left|\frac{x - x_l}{D}\right|^{\beta}, \quad \sigma_y = \sigma_m \left|\frac{y - x_l}{D}\right|^{\beta} \tag{41}$$

Where x_l or y_l denotes the location where the PML starts, and D is the width of the PML. To compute σ, the relations $\sigma_m \Delta x = 2$, where Δx is the grid size, and $\beta = 2$ are used for all computations.

A simple damping term in the near-boundary layer (so-called sponge layer) was employed as a simplified alternative to the perfect matched layer technique:

$$\frac{\partial \vec{u}}{\partial t} + A\frac{\partial \vec{u}}{\partial x} + B\frac{\partial \vec{u}}{\partial y} + \sigma\vec{u} = 0, \tag{42}$$

where σ is the damping t erm.

To test the effect of non-reflecting boundary conditions and near-boundary damping layer, computations were compared using different size of computational domains and various grid step sizes.

The computational procedure for this numerical method is as follows:

1. Compute the right-hand side of Eq. 42, using values of the governing variable U from the previous time step.

2. Compute the spatial derivatives solving tridiagonal systems in x and y spatial directions.

3. Compute the right-hand side of Eq. 34 using the spatial derivatives computed on Step 2 and update governing variables using the Runge-Kutta scheme.

4. Compute boundary values of governing variables using non-reflecting boundary conditions.

5. Repeat computational steps 1—4 for all stages of the Runge-Kutta scheme.

6. Repeat computational steps 1—5 for all time steps.

2.5 Code Validation and Grid Refinement Study

In this study, the computer of Dell Dimension 4550, Pentium (R)4, CPU 2.53GHZ,

1.00GB of RAM are used and Microsoft Visual C++ 6.0 is taken as the compiler.

To validate the code, the computations were performed on a set of numerical grids where the wave spreads under static ambient conditions and in presence of the flat plate. For the given initial conditions for the acoustic pressure pulse

$$p = \varepsilon \exp\left[-\frac{x^2 + y^2}{a}\right] \tag{43}$$

where ε and a are constants.

The analytic solution for the acoustic pressure in case of the infinite 3D domain is given by

$$p = \frac{\varepsilon}{2r}\left\{(r-t)\exp\left[-a(r-t)^2\right] + (r+t)\exp\left[-a(r+t)^2\right]\right\} \tag{44}$$

where r is the location of the pulse center at $t = 0$. The solution for the semi-infinite domain is obtained by the use of the image pulse located at $-r$, i.e.,

$$p = p(r) + p(-r). \tag{45}$$

The code was run with a fixed time step size, $\Delta t = 0.001$ an d final time $t_f = 1.0$. Varying the mesh size from $h = 0.012$ to $h = 0.004$. The time step size is chosen small enough in such a way that it does not corrupt the results for spatial convergence. At the final time, the solution fields are compared to the analytical solution using a L_2 error norm. The result is presented in Fig. 2.5, and m is the slope of the fitting line. The

expected $O(h^4)$ spatial accuracy is achieved.

Then the mesh size is fixed to $h = 0.006$, while the time step size is varied from $t_f = 0.1$ to $t_f = 0.001$. And the expected $O(\Delta t^4)$ time accuracy is also achieved (see Fig. 2.6).

A Grid refinement study was conducted using the Vatistas vortex model for each case.

For Case A, the computational domain $\Omega = [0 < x < 1.0] \times [-0.5 < y < 0.5]$ is covered with 150×150, 250×250, 350×350 and 400×400 uniform numerical grids.

The acoustic pressure time history at the point $(0.2,0.2)$ is presented in Fig. 2.7. The maximum of acoustic pressure (sound directivity beam) is directed through this point. For the coarse grid of 150×150, there is an obvious difference between the results compared to the results of the 400×400 grid. The acoustic pressure profiles for the 350×350 and 400×400 grids are almost overlapped with each other with the maximum difference below 1%. Therefore, the 350×350 uniform numerical grid is used in this study. The time step is computed by $\Delta t = C\Delta x$, where the Courant numer, C, is taken equal to 0.25.

For Cases B and C the computational domain $\Omega = [0.5 < r < 3.0] \times [-\pi < \theta < \pi]$ is covered with 360×360, 540×540 and 720×720 uniform numerical grids.

The RMS of acoustic pressure is shown in Fig. 2.8 with respect to angle θ from the centerline. It was discovered that the RMS of acoustic pressure profiles for the 540×540 and 720×720 grids were almost the same (the maximum difference was within 1%). Therefore, the 540×540 uniform numerical grid was used. The time step is computed by $\Delta t = C\Delta x$, where the Courant number, C, is taken equal to 0.25.

For Case D, the computational domain $\Omega = [0.5 < r < 3.0]\times[0 < \zeta < 2\pi]$ is covered with the 200×200 and 300×300 uniform numerical grids.

The RMS of acoustic pressure is shown in Fig. 2.9 with respect to angle θ from the centerline. It was discovered that the RMS of acoustic pressure profiles for the 200×200 and 300×300 grids were almost the same. Therefore, the 200×200 uniform numerical grid was used.

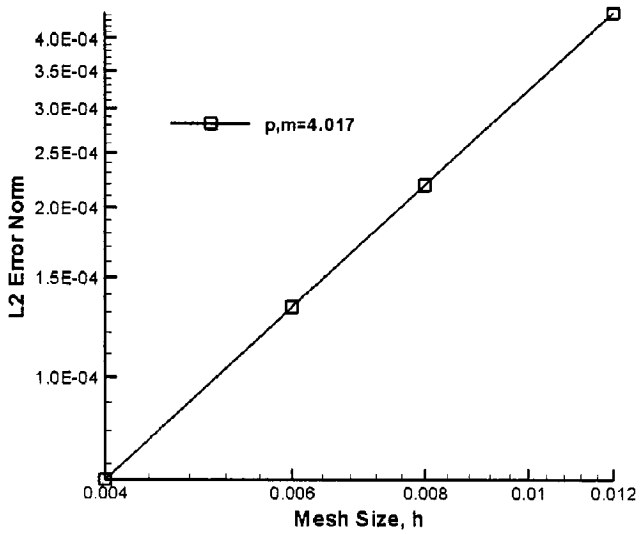

Figure 2-5 Log-Log plot of pressure error vs. mesh size (h) for a fixed time step size $\Delta t = 0.001$.

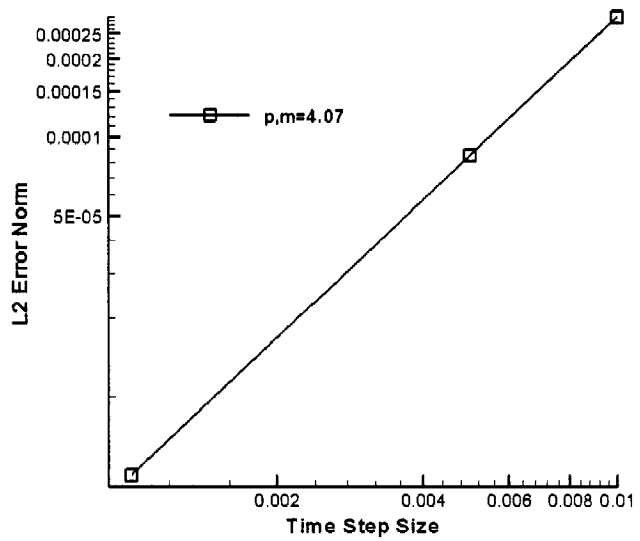

Figure 2-6 Log-Log plot of pressure error vs. time step size (Δt) for a fixed mesh size $h = 0.002$.

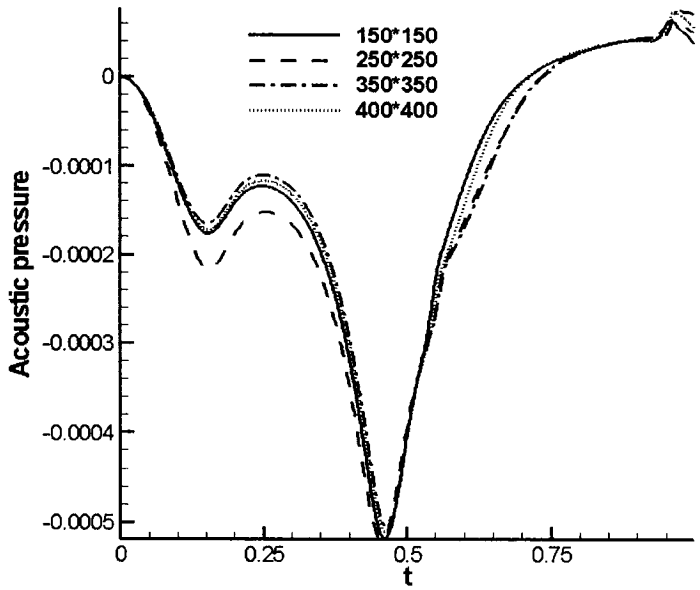

Figure 2-7 Acoustic pressure time history at the point (0.2,0.2).

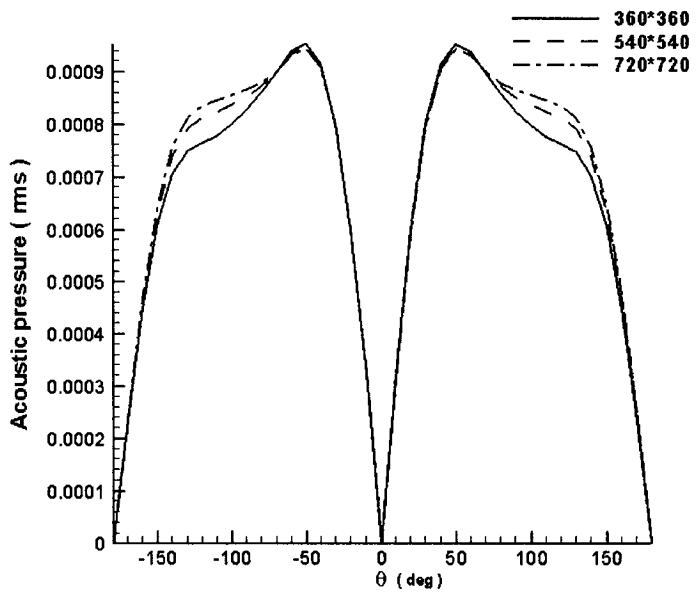

Figure 2-8 The angular distribution of RMS of acoustic pressure for Vatistas one-cell vortex with $n = 2$.

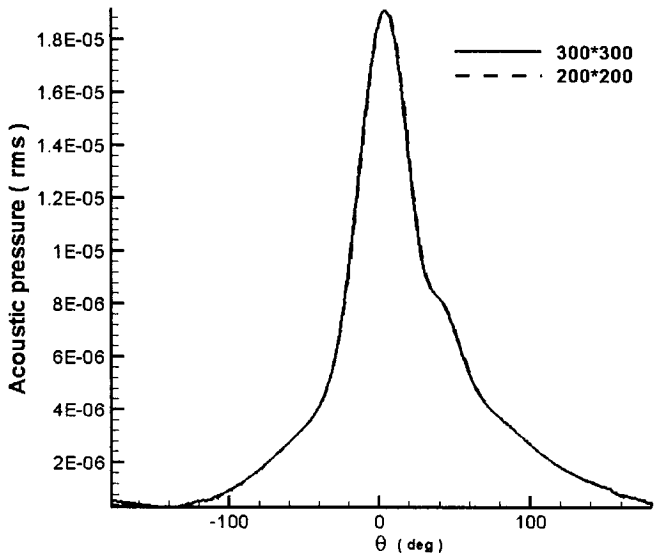

Figure 2-9 The RMS of acoustic pressure angular distribution on the left cylinder.

Chapter III

Impingement of Single Vortex into Flat Plate

The ratio of the vortex core size to the downstream rigid bod may vary from zero to infinity. If the vortex shed by the multi-element airfoil or landing gear impinges into the fuselage, the vortex core diameter is much smaller than the size of the fuselage. Impingement of the mean flow carrying the vortex toward the flat plate may appear to be a reasonably simplified model of such an interaction.

The profile of the flow in a vortex depends on the geometry of the upstream rigid body, the "age" of the vortex when it impinges into the downstream surface, initial vortex-to-core ratio, and many other factors. In the current study, the strength and directivity of the produced sound waves are compared keeping the core size and the maximum circulation for Vatistas model ($n = 2$) and Taylor model the same ($R_c = 0.04$ and $\Gamma = 0.00005$).

3.1 Problem Set Up

Figure 3.1 shows an overview of the vortex impingement on a flat plate framework.

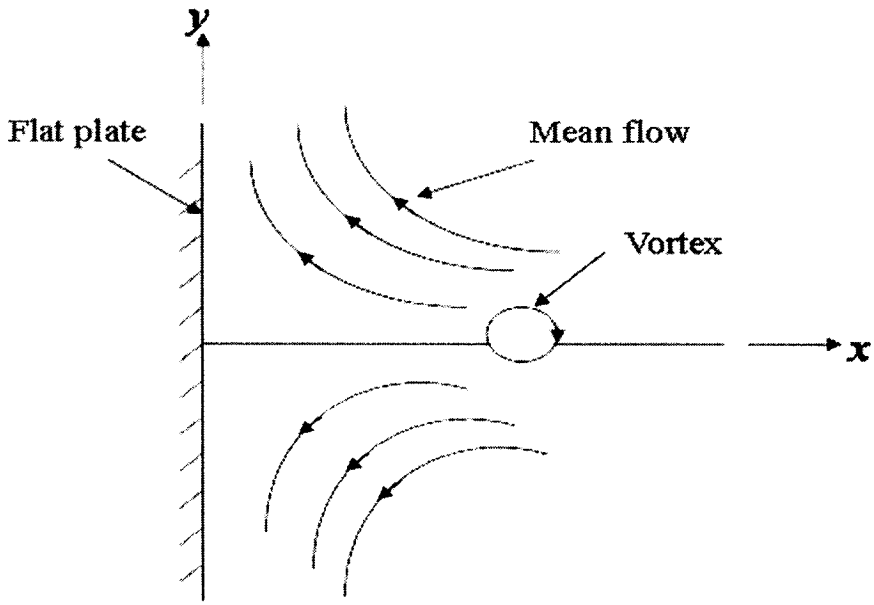

Figure 3-1 Case A: Physical set-up of vortex impingement onto flat plate.

A schematic diagram of the computational domain is presented in Fig. 3.2a

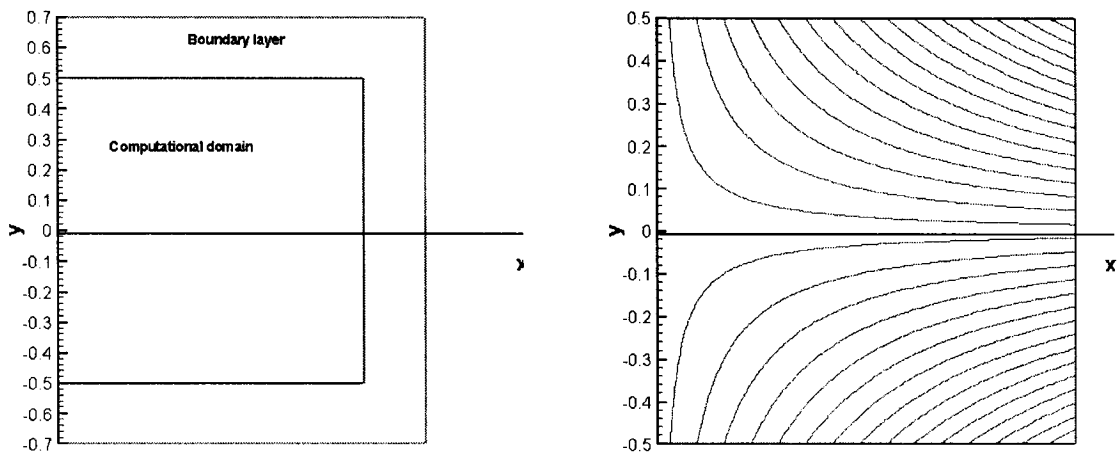

(a)

(b)

Figure 3-2 C ase A: (a) computational domain, (b) streamlines of the background flow.

The boundaries of the computational domain are given as follows:

Upstream boundary $x_{up} = 1.0$;

Flat plate at $x_{down} = 0.0$;

Exit boundaries for impingement flow: $\pm y_b = \pm 0.5$.

If a PML boundary layer is implemented, the thickness of the PML domain is twenty grid nodes. Initial location of the vortices are $x_v = 0.25, y_v = 0$ for a single vortex; and $x_v = 0.25, y_v = \pm 0.1$ for a vortical dipole.

The background flow (see Fig. 3.2b the flowfield) is analytically given in the Cartesian coordinate system and the stagnation flow velocity has been normalized in such a way that

$$U = -x, \quad V = y \tag{46}$$

The linearized Euler equations for unsteady disturbance components of mass and momentum fluxes in Cartesian coordinates are:

$$\begin{aligned}
\frac{\partial p'}{\partial t} &= -\left(\frac{\partial u'}{\partial x} + \frac{\partial v'}{\partial y}\right) + x\frac{\partial p'}{\partial x} - y\frac{\partial p'}{\partial y} \\
\frac{\partial u'}{\partial t} &= -\frac{\partial p'}{\partial x} + x\frac{\partial v'}{\partial y} - y\frac{\partial u'}{\partial y} + u' - xp' \\
\frac{\partial v'}{\partial t} &= -\frac{\partial p'}{\partial y} - y\frac{\partial v'}{\partial y} + x\frac{\partial v'}{\partial x} - v' - yp'
\end{aligned} \tag{47}$$

where p', u', v' are the disturbance components.

3.2 Boundary Condition Comparison

When the vortex flowfield is implemented as an initial condition of the disturbance, it might violate the non-penetrating boundary condition if the non-zero tangential velocity of vortex reaches the rigid wall. On the flat plate, to satisfy the zero normal velocity boundary conditions, a vortex image system is employed at $t = 0$.

An oppositely spinning vortex of equal strength is put at its mirror image location O' (see Fig. 3.3).

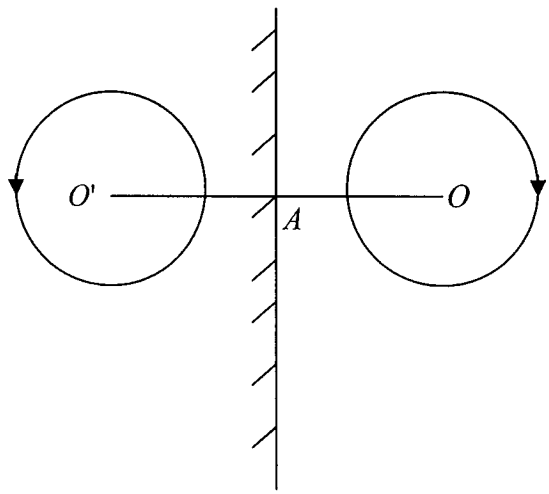

Figure 3-3 Vortex image system.

The inverse point O and O' lie on a line OAO', which is normal to the flat plate, and satisfies

$$OA = O'A$$

On the outer boundary, to satisfy the non-reflecting wave coming back to the

computational domain, two boundary conditions were respectively used to guarantee that no waves are reflected from the artificial boundary: one is the characteristic boundary condition (Gele, 1990); the other is the PML boundary condition (Hu, 1996, 2001).

First the characteristic boundary condition, which was proposed by Thompson (1987) and improved by Giles (1990), was implemented. The basic idea of the characteristic boundary condition is to decompose the hyperbolic Euler equations into quasi-linear characteristic wave modes of definite velocities. The direction normal to the computational boundary and the amplitudes of outgoing waves could be defined entirely from the variables inside the computational domain. Whereas, those of incoming waves should be specified by proper characteristic boundary conditions (Kim & Lee, 2004).

Assuming one-directional background flow perpendicular to the boundary with constant speed u and constant pressure, the Riemanm invariants are

$$\begin{aligned} w_1 &= 0.5(u'+p') \\ w_2 &= 0.5(u'-p') \end{aligned} \tag{48}$$

where the velocity component u' is perpendicular to the boundary. For the right boundary, the invariant w_1 belongs to the incoming characteristic while the invariant w_2 corresponds to the outcoming characteristic. And the disturbance v' is approximated using a one-sided difference.

The acoustic pressures generated by Taylor's vortex and Vatistas' vortex distorting

in the flow are shown at time moment $t = 1.0$ in Fig. 3.4 (a) (c). It is clear that the characteristic boundary conditions are appropriate with the local-in-space Taylor's vortex, however, for the Vatistas vortex there are oscillations of the pressure.

In order to obtain a better non-reflection boundary condition for Vatistas' vortex, the perfect matched layer at the artificial boundary, proposed by Hu (1996, 2000), was implemented.

In introducing a non-physical (PML) domain, adjacent to artificial boundaries, the Euler equations are solved in the interior field, and the proposed PML equations are solved within the PML domain to absorb all outgoing waves.

In the horizontal layer (that is, perpendicular to the y direction):

$$\begin{aligned}
\frac{\partial p'}{\partial t} &= -\left(\frac{\partial u'}{\partial x}+\frac{\partial v'}{\partial y}\right)+x\frac{\partial p'}{\partial x}-y\frac{\partial p'}{\partial y}-\sigma_y\left(x\frac{dq_3}{dx}+\frac{dq_1}{dx}\right)-\sigma_y p' \\
\frac{\partial u'}{\partial t} &= -\frac{\partial p'}{\partial x}+x\frac{\partial v'}{\partial y}-y\frac{\partial u'}{\partial y}+u'-xp'-\sigma_y\left(x\frac{dq_1}{dx}+\frac{dq_3}{dx}\right)-\sigma_y u' \\
\frac{\partial v'}{\partial t} &= -\frac{\partial p'}{\partial y}-y\frac{\partial v'}{\partial y}+x\frac{\partial v'}{\partial x}-v'-yp'+\sigma_y\frac{dq_2}{dx}x-\sigma_y v'
\end{aligned} \tag{49}$$

In the vertical layer (that is, perpendicular to the x direction):

$$\begin{aligned}
\frac{\partial p'}{\partial t} &= -\left(\frac{\partial u'}{\partial x}+\frac{\partial v'}{\partial y}\right)+x\frac{\partial p'}{\partial x}-y\frac{\partial p'}{\partial y}-\sigma_x\left(V\frac{dq_3}{dy}+\frac{dq_2}{dy}\right)-\sigma_x p' \\
\frac{\partial u'}{\partial t} &= -\frac{\partial p'}{\partial x}+x\frac{\partial v'}{\partial y}-y\frac{\partial u'}{\partial y}+u'-xp'-\sigma_x y\frac{dq_1}{dy}-\sigma_x u' \\
\frac{\partial v'}{\partial t} &= -\frac{\partial p'}{\partial y}-y\frac{\partial v'}{\partial y}+x\frac{\partial v'}{\partial x}-v'-yp'-\sigma_x\left(y\frac{dq_2}{dy}-\frac{dq_3}{dy}\right)-\sigma_x v'
\end{aligned} \tag{50}$$

In the corner intersection of two sponge layers:

$$\frac{\partial p'}{\partial t} = -\left(\frac{\partial u'}{\partial x} + \frac{\partial v'}{\partial y}\right) + x\frac{\partial p'}{\partial x} - y\frac{\partial p'}{\partial y} - \sigma_y\left(-U\frac{dq_3}{dx} + \frac{dq_1}{dx}\right) - \sigma_x\left(V\frac{dq_2}{dy} + \frac{dq_3}{dy}\right) - (\sigma_x + \sigma_y)p'$$

$$\frac{\partial u'}{\partial t} = -\frac{\partial p'}{\partial x} + x\frac{\partial v'}{\partial y} - y\frac{\partial u'}{\partial y} + u' - xp' - \sigma_y\left(x\frac{dq_1}{dx} + \frac{dq_3}{dx}\right) + \sigma_x y\frac{dq_1}{dy} - (\sigma_x + \sigma_y)u'$$

$$\frac{\partial v'}{\partial t} = -\frac{\partial p'}{\partial y} - y\frac{\partial v'}{\partial y} + x\frac{\partial v'}{\partial x} - v' - yp' - \sigma_Y\left(y\frac{dq_2}{dx} + \frac{dq_1}{dx}\right) - \sigma_x y\frac{dq_1}{dy}(\sigma_x + \sigma_y)v' \tag{51}$$

and

$$\begin{aligned}\frac{dq_1}{dt} &= u' \\ \frac{dq_2}{dt} &= v' \\ \frac{dq_3}{dt} &= p'\end{aligned} \tag{52}$$

Two absorption coefficients σ_x, σ_y and one auxiliary variable q are introduced into the PML equations.

The auxiliary variable $\vec{q}$ is needed only inside the PML domains; it is neither computed nor stored inside the Euler domain.

The absorption coefficients used in this study are

$$\sigma_x = \sigma_m\left|\frac{x - x_l}{D}\right|^\beta, \quad \sigma_y = \sigma_m\left|\frac{y - x_l}{D}\right|^\beta, \tag{53}$$

where x_l or y_l denotes the location where the PML starts, and D is the width of the PML. To compute σ, the relations $\sigma_m \Delta x = 2$, where Δx is the grid size, and $\beta = 2$ are used for all computations.

The pressure iso-line at time $t = 1.0$ under the PML boundary conditions are presented in Figs. 3.4 (c) and (d). The pressure iso-lines for both vortices turn out to be very smooth, which shows that there are no waves coming back from the boundary into the computational domain. The PML boundary layer performs perfectly, for both Taylor's and Vatistas's vortices.

For the Taylor's vortex, the two boundary conditions produce a minor difference (within 1%) in terms of disturbance pressure. For Vatistas vortex with the adopted PML boundary condition, the acoustic pressure history curve is smooth. However, the curve corresponding to the characteristic boundary is oscillatory and produces noticeable difference in the acoustic pressure amplitude (see Fig 3.5). Therefore, the PML boundary conditions have been adopted for the current study.

The acoustic pressure, as a function of time at locations $(0.2,0.2)$, is presented in Fig. 3.5.

3.3 Computational Results

While an acoustic pulse travels with the speed of sound relative to a mean flow, the vortices travel with the mean flow. When a vortex is convected with a uniform speed, it

does not contribute to aeroacoustic noise. In study, the initial vortex is strongly distorted by the non-uniform stagnation flow; four pressure spots of alternating sign amplitude (quadrupoles) are clearly seen. These spots elongate and generate pressure waves. The influence of the mean flow appears to be very different for the Vatistas's and Taylor's vortices.

Sound waves emanating from a distorting Taylor's vortex develop faster than that for a Vatistas's vortex. For example at $t = 0.5$, for former vortex the pressure waves are separated from the quadrupole and are propagating outwards, whereas for the latter vortex the pressure waves are not separated from the quadrupole (see Fig. 3.7). Later on, Vatistas' vortex becomes more distorted and its quadrupole becomes more spatially distributed than that for a Taylor's vortex. Sound waves emanating from the Vatistas' vortex covers a larger domain with significantly smaller zone of silence at the centerline. Although the vortex core size and vortex circulation was the same for both vortices, the results of the numerical simulations show that the amplitude of acoustic pressure is approximately one and a half times larger for the Vatistas' model than that of Taylor's. The directivity of propagation of sound for Vatistas' vortex is close to $45°$; while for the Taylor's vortex the locus of maximum acoustic pressure corresponds to $30°$.

Acoustic radiation from a vortex dipole in the stagnation flow was studied, and the results for the two models are shown in Fig. 3.8. Each of the vortices is distorted along the wall producing a quadrupole. Waves of the same sign merge near the centerline are

seen to propagate upstream of the stagnation flow. In the dipole cases, the acoustic pressure distribution looks more alike for both vortices than that of a monopole vortex. The maximum acoustic pressure for sound waves emanating from the Vatistas's formulation is almost twice larger than that for Taylor's.

3.4 Summary of Findings

The propagation of acoustic waves, originating from the distortion of vortices in a non-uniform base flow, was presented. The flow around flat plate was taken as the prototype. Non-reflecting boundary conditions were tested, and the perfect matched layer boundary condition proved to work adequatelly for both vortex models. When the vortex is convected by the non-uniform stagnation flow towards the rigid surface, the vortex is strongly distorted. As a result of this deformation, the pressure field becomes non-circular, producing a quadrupole. As the vortex deformation proceeds, pressure waves are formed. The intensity and directivity of acoustic wave pattern appear to be quite different for the Vatistas's and Taylor's vortex models. The sound wave pressure fields generated by a vortex dipole with Vatistas' and Taylor's velocity profiles have more similarities than the wave generated by a monopole vortex with the same strength. The mutual cancellation of outgoing sound waves made the wave pattern similar.

The impingement onto the flat plate model for the mean flow has a deficiency related to the fact that $U_\infty \to \infty$. Therefore, the flow about cylinder with fixed U_∞ represents a more appropriate model.

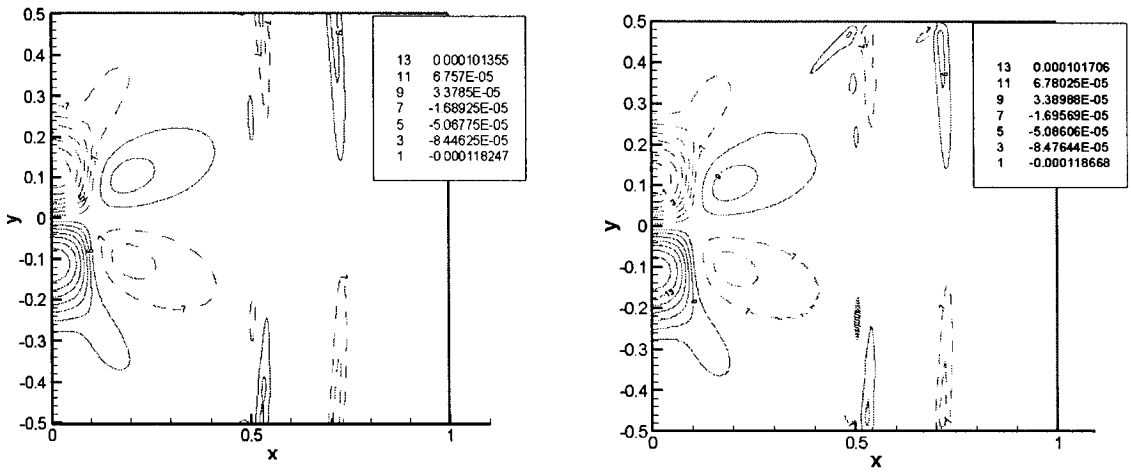

(a) (b)

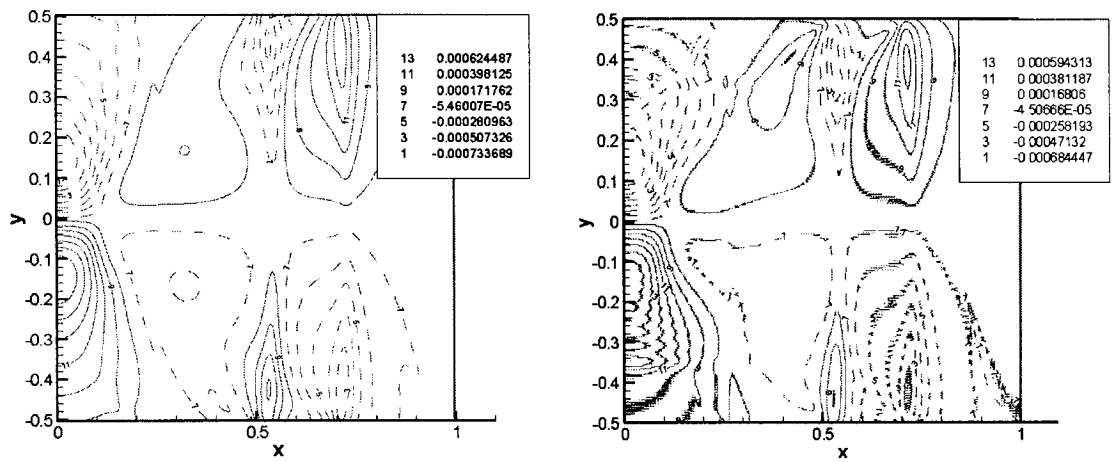

(c) (d)

Figure 3-4 Generation of acoustic waves by: (a, b) the Taylor's Vortex, (c, d) the Vatistas's vortex ($n = 2$), (a, c) using PML boundary, (b, d) using Characteristic boundary.

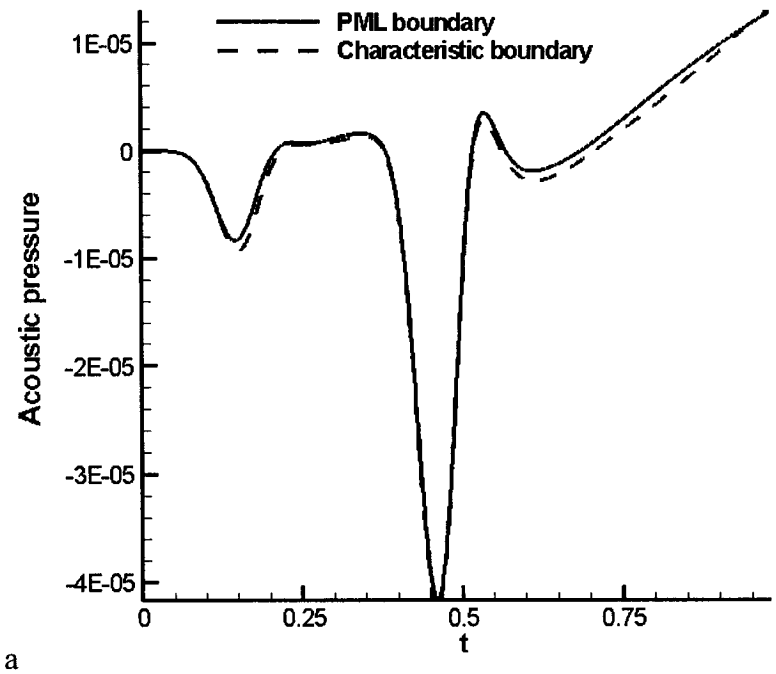

a

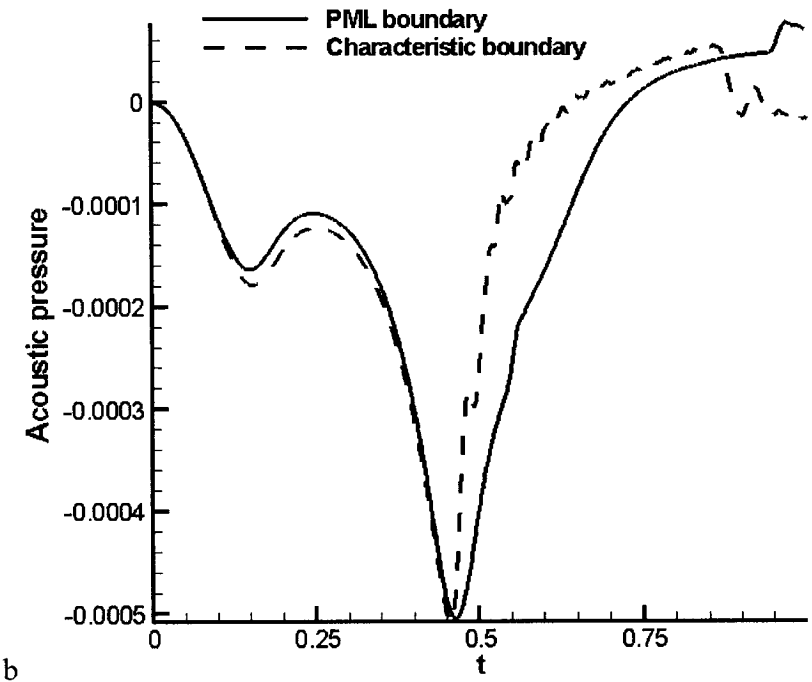

b

Figure 3-5 Acoustic pressure time history at the point $(0.2,0.2)$: (a) the Taylor's vortex, (b) the Vatistas's vortex ($n = 2$).

$t = 0.1$

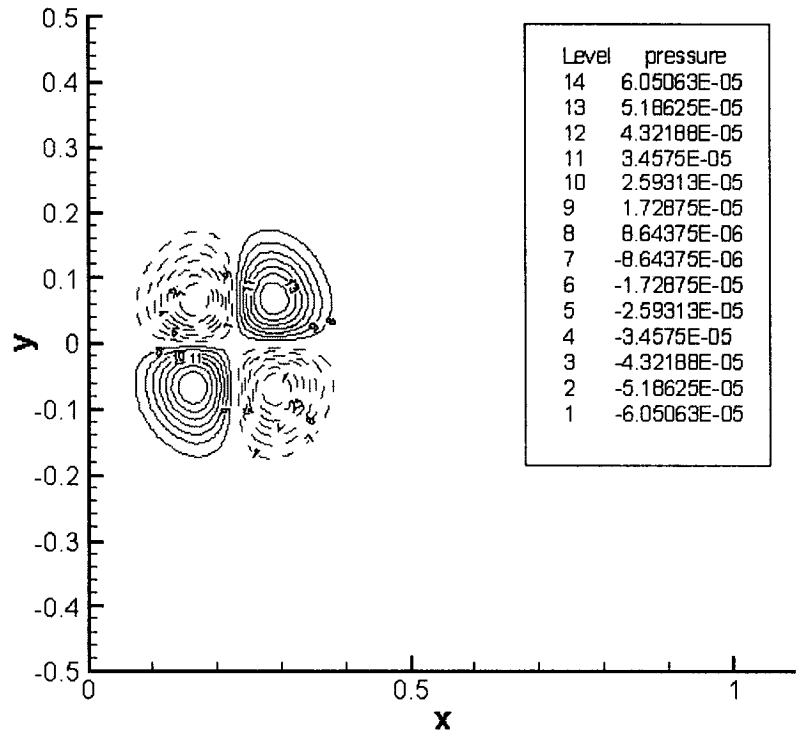
Level pressure
14 6.05063E-05
13 5.18625E-05
12 4.32188E-05
11 3.4575E-05
10 2.59313E-05
9 1.72875E-05
8 8.64375E-06
7 -8.64375E-06
6 -1.72875E-05
5 -2.59313E-05
4 -3.4575E-05
3 -4.32188E-05
2 -5.18625E-05
1 -6.05063E-05
0.5
0.4
0.3
0.2
0.1
0
-0.1
-0.2
-0.3
-0.4
-0.5
y
0
0.5
1
x

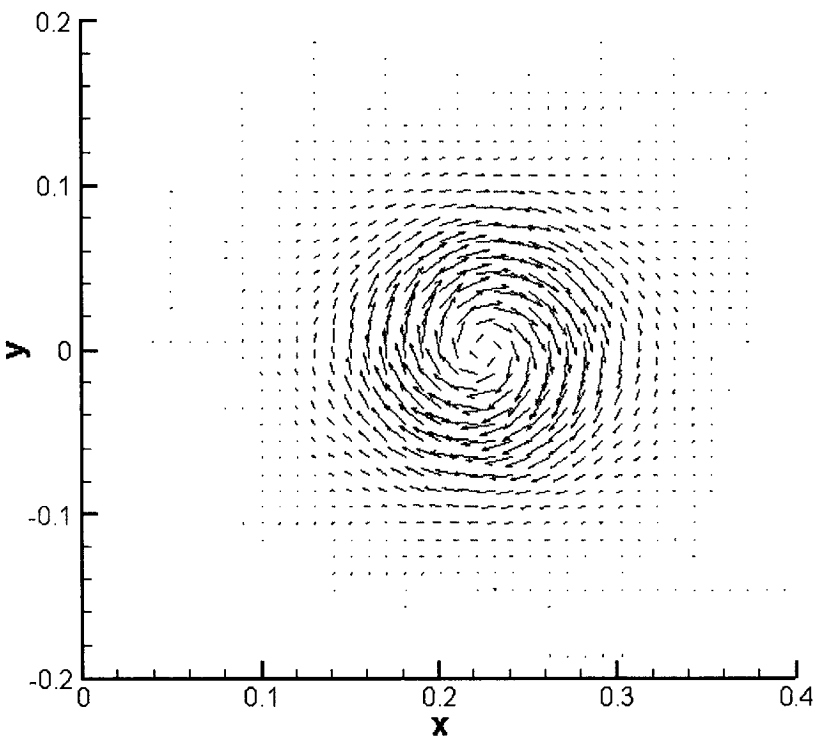
0.2
0.1
0
-0.1
-0.2
y
0
0.1
0.2
0.3
0.4
x

$t = 0.5$

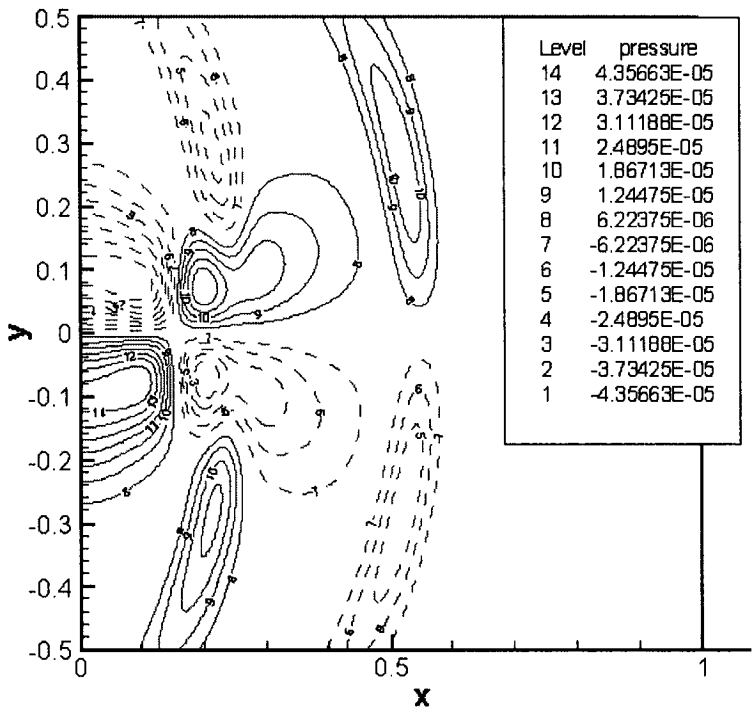
Level pressure
14 4.35663E-05
13 3.73425E-05
12 3.11188E-05
11 2.4895E-05
10 1.86713E-05
9 1.24475E-05
8 6.22375E-06
7 -6.22375E-06
6 -1.24475E-05
5 -1.86713E-05
4 -2.4895E-05
3 -3.11188E-05
2 -3.73425E-05
1 -4.35663E-05
0.5
0.4
0.3
0.2
0.1
0
-0.1
-0.2
-0.3
-0.4
-0.5
y
0
0.5
1
x

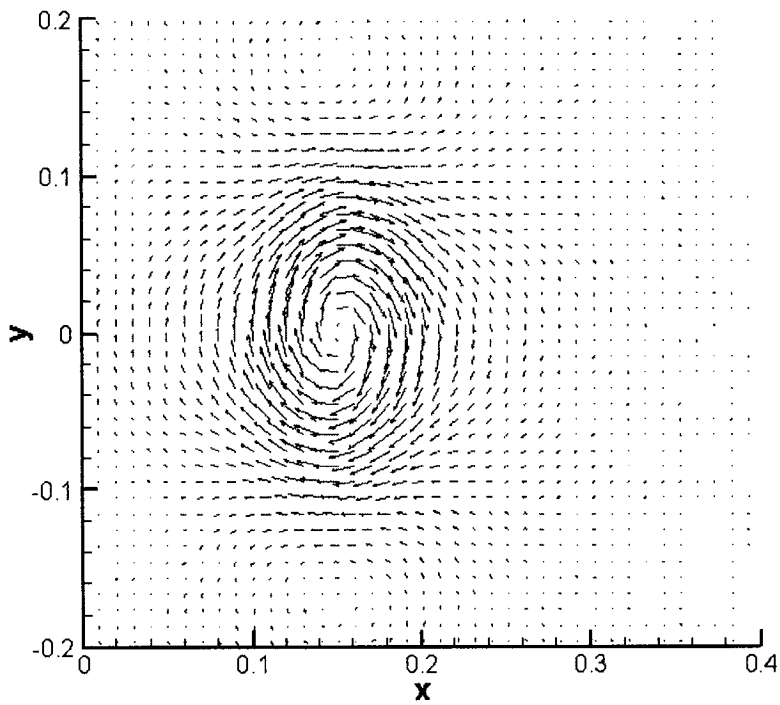
0.2
0.1
0
-0.1
-0.2
y
0
0.1
0.2
0.3
0.4
x

$t = 1.0$

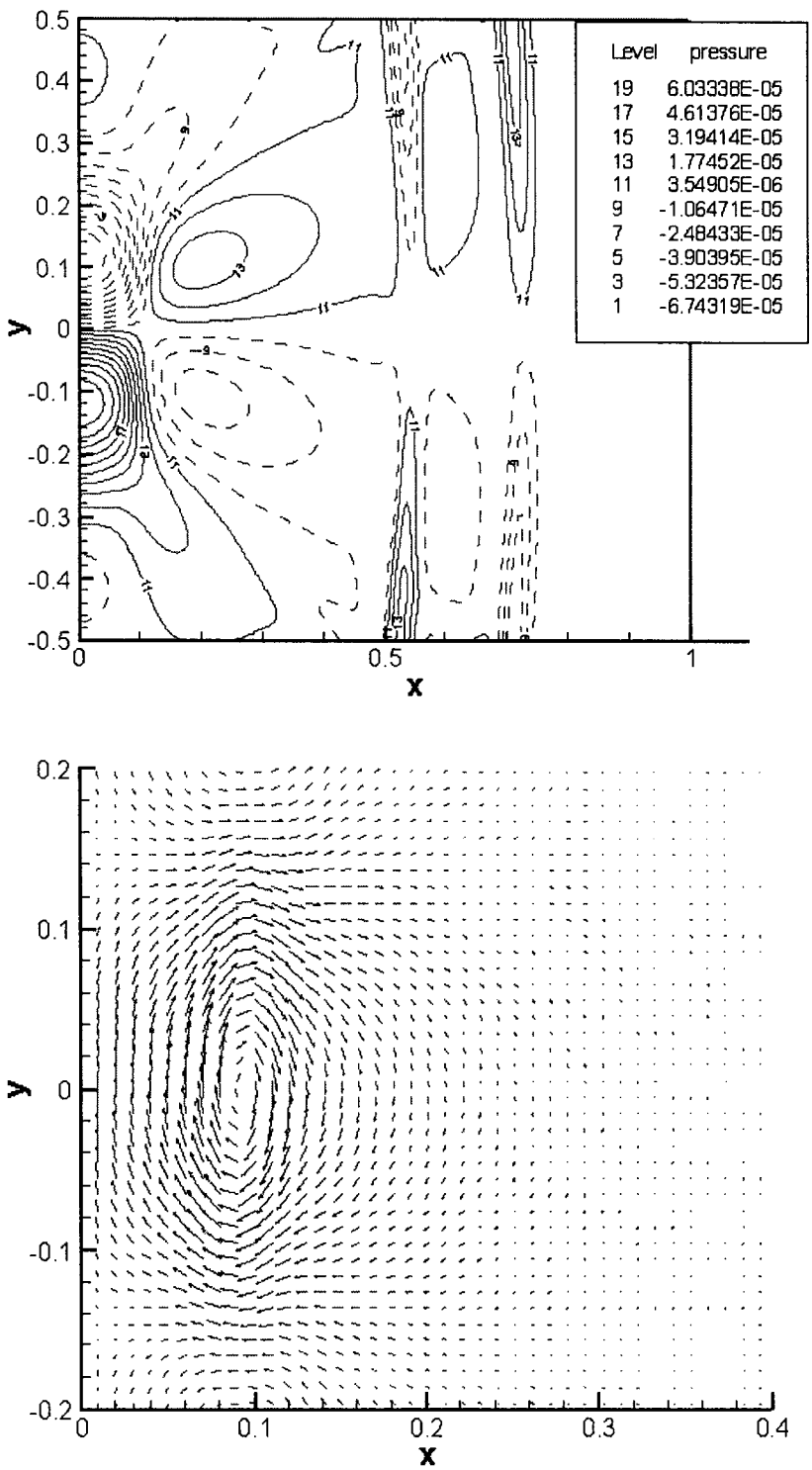
Level pressure
19 6.03338E-05
17 4.61376E-05
15 3.19414E-05
13 1.77452E-05
11 3.54905E-06
9 -1.06471E-05
7 -2.48433E-05
5 -3.90395E-05
3 -5.32357E-05
1 -6.74319E-05
0.5
0.4
0.3
0.2
0.1
0
-0.1
-0.2
-0.3
-0.4
-0.5
y
0
0.5
1
x
0.2
0.1
0
-0.1
-0.2
y
0
0.1
0.2
0.3
0.4
x

(a)

$t = 0.1$

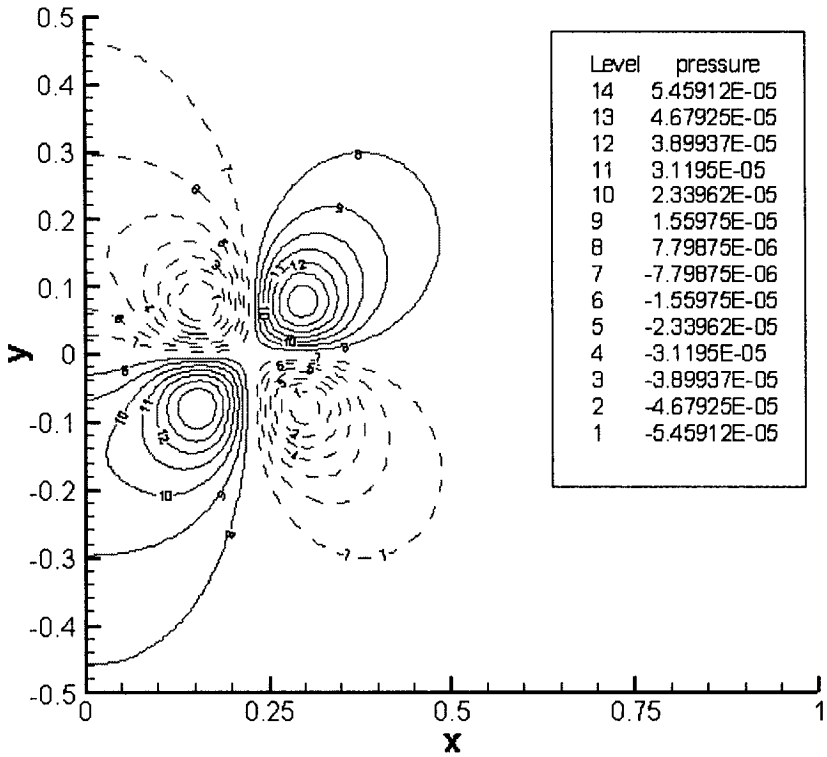
Level pressure
14 5.45912E-05
13 4.67925E-05
12 3.89937E-05
11 3.1195E-05
10 2.33962E-05
9 1.55975E-05
8 7.79875E-06
7 -7.79875E-06
6 -1.55975E-05
5 -2.33962E-05
4 -3.1195E-05
3 -3.89937E-05
2 -4.67925E-05
1 -5.45912E-05
0.5
0.4
0.3
0.2
0.1
0
-0.1
-0.2
-0.3
-0.4
-0.5
y
0
0.25
0.5
0.75
1
x

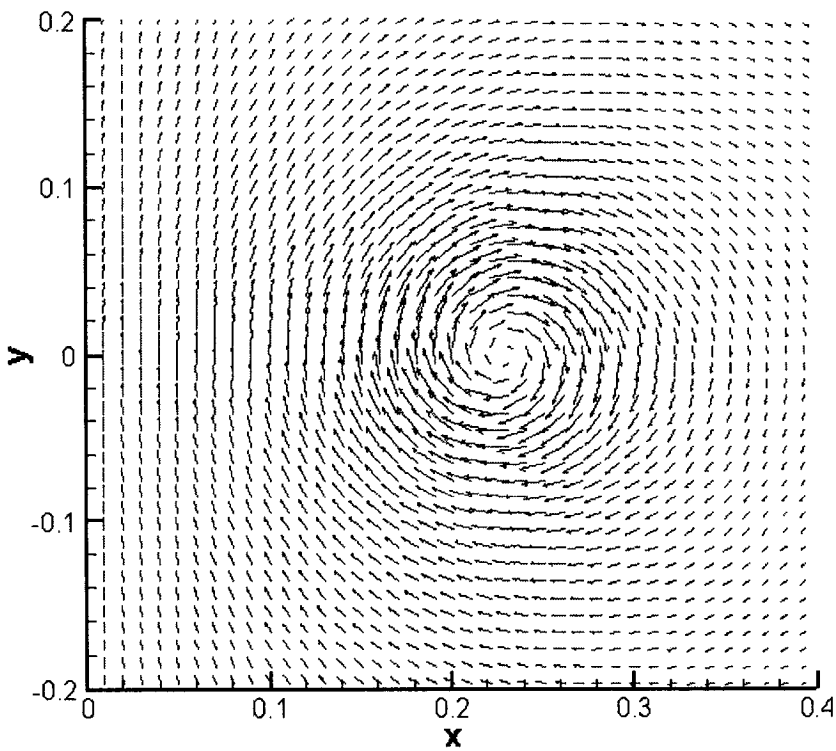
0.2
0.1
0
-0.1
-0.2
y
0
0.1
0.2
0.3
0.4
x

$t = 0.5$

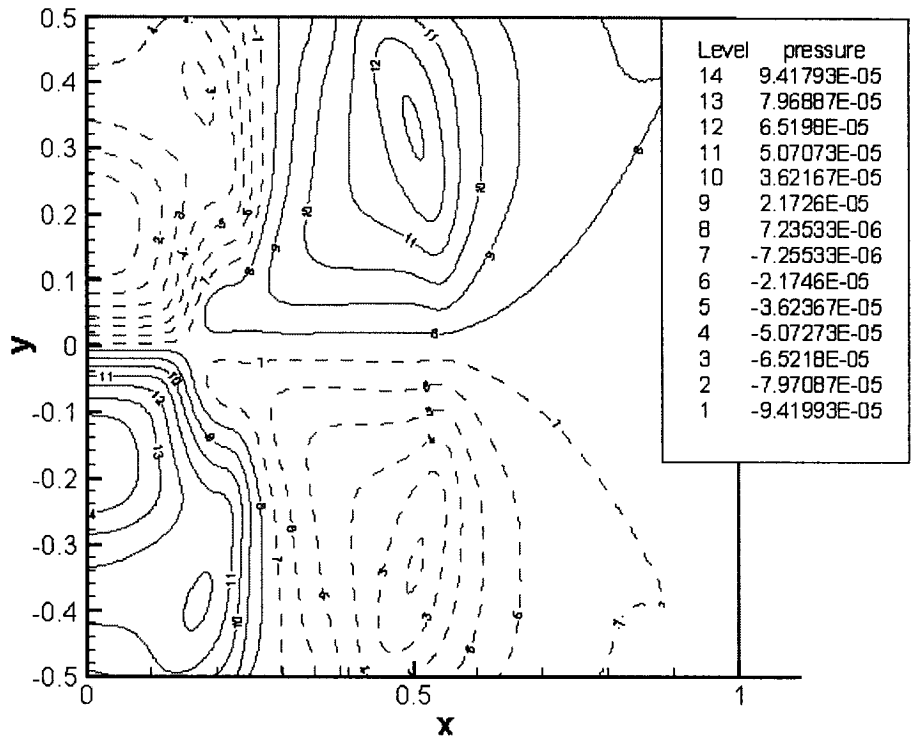
Level pressure
14 9.41793E-05
13 7.96887E-05
12 6.5198E-05
11 5.07073E-05
10 3.62167E-05
9 2.1726E-05
8 7.23533E-06
7 -7.25533E-06
6 -2.1746E-05
5 -3.62367E-05
4 -5.07273E-05
3 -6.5218E-05
2 -7.97087E-05
1 -9.41993E-05
0.5
0.4
0.3
0.2
0.1
0
-0.1
-0.2
-0.3
-0.4
-0.5
y
0
0.5
1
x

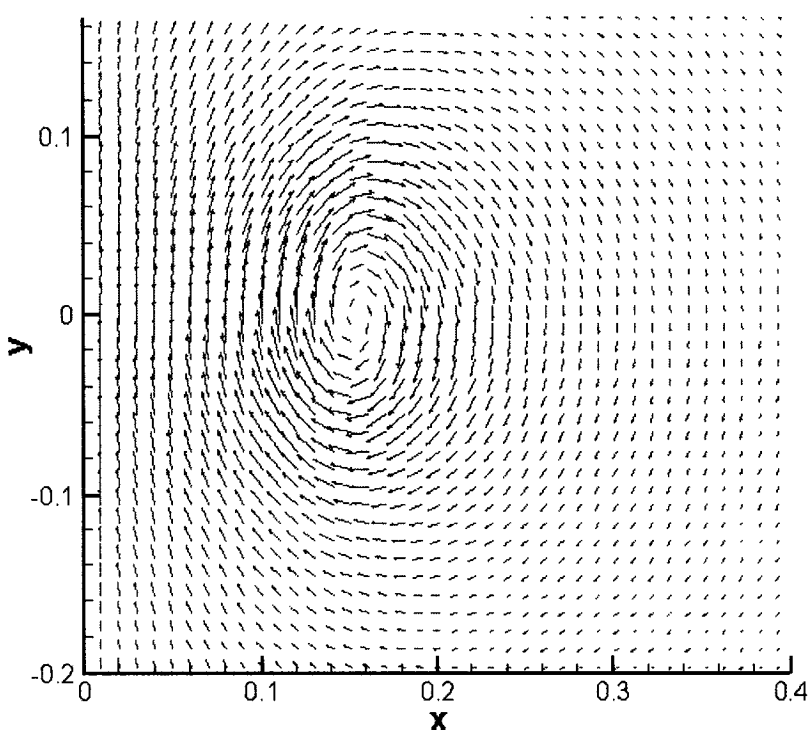
0.1
0
-0.1
-0.2
y
0
0.1
0.2
0.3
0.4
x

$t = 1.0$

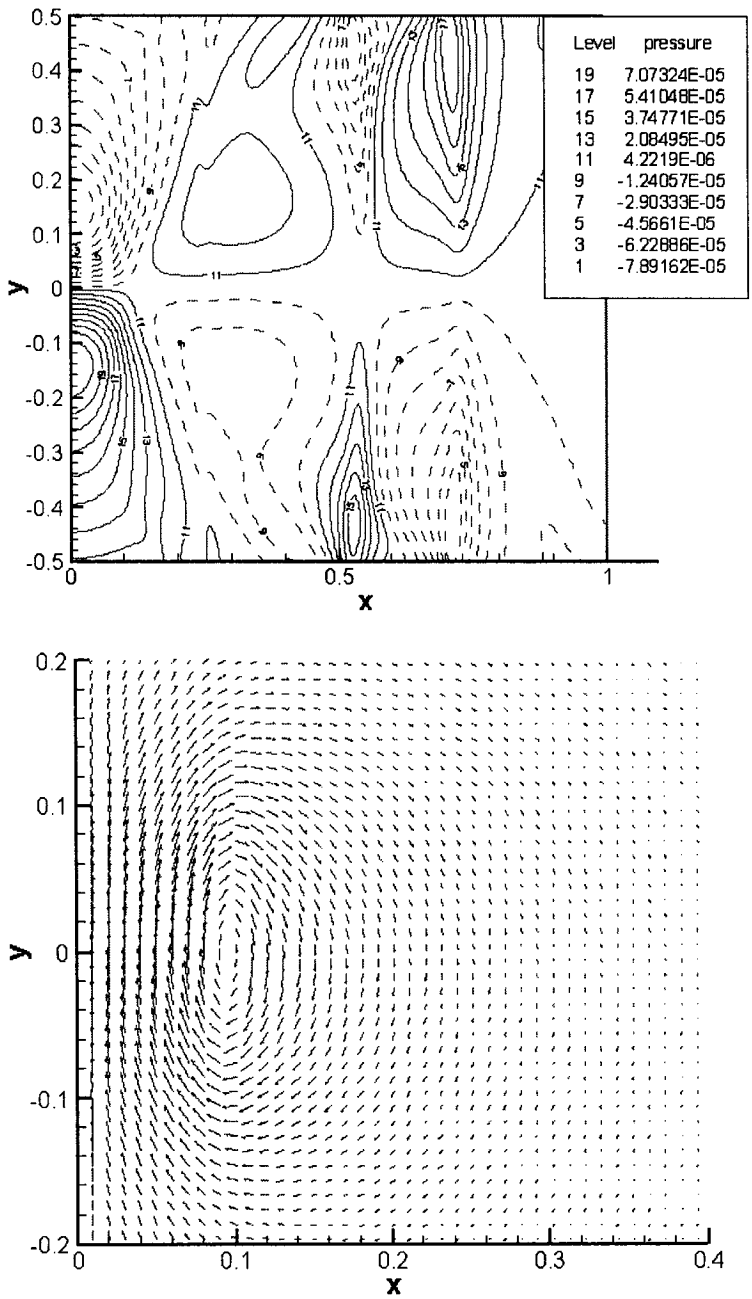

Figure 3-6 Generation of pressure quadrupole and acoustic waves for Taylor and Vatistas vortices: (a) the Taylor's vortex, (b) the Vatistas's vortex. Negative line represents negative pressure values.

$t = 0.4$

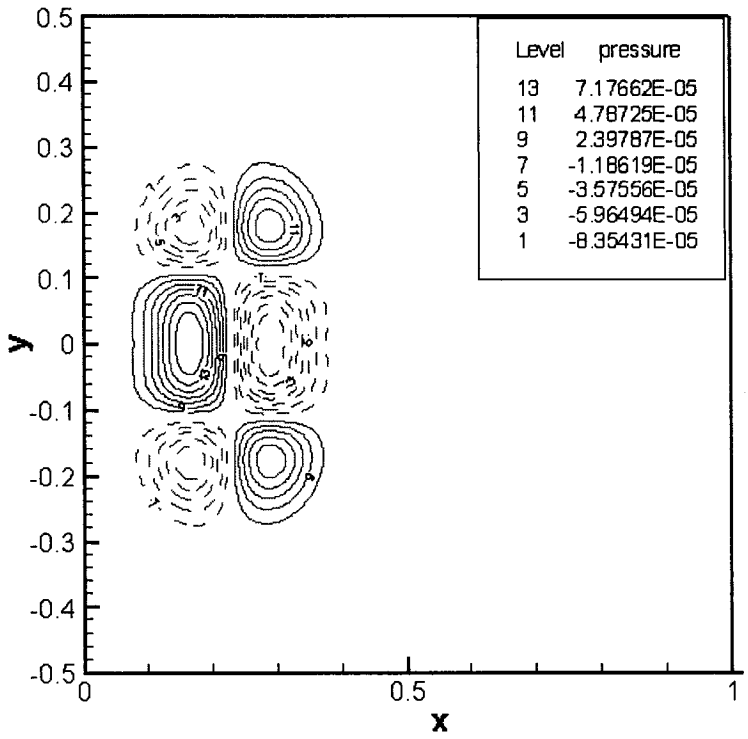
Level pressure
13 7.17662E-05
11 4.78725E-05
9 2.39787E-05
7 -1.18619E-05
5 -3.57556E-05
3 -5.96494E-05
1 -8.35431E-05
0.5
0.4
0.3
0.2
0.1
0
-0.1
-0.2
-0.3
-0.4
-0.5
y
0
0.5
1
x

a

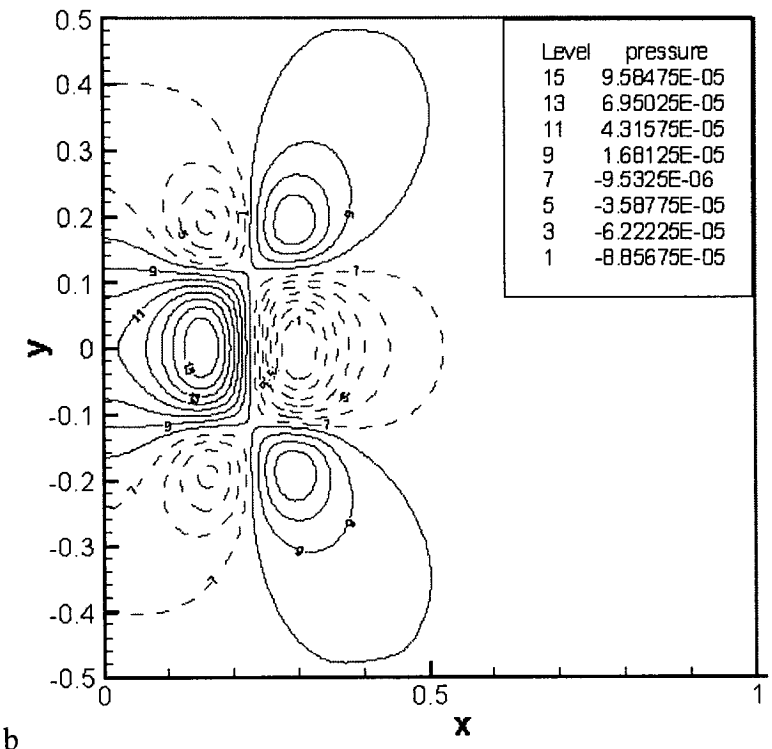
Level pressure
15 9.58475E-05
13 6.95025E-05
11 4.31575E-05
9 1.68125E-05
7 -9.5325E-06
5 -3.58775E-05
3 -6.22225E-05
1 -8.85675E-05
0.5
0.4
0.3
0.2
0.1
0
-0.1
-0.2
-0.3
-0.4
-0.5
y
0
0.5
1
x

b

$t = 0.8$

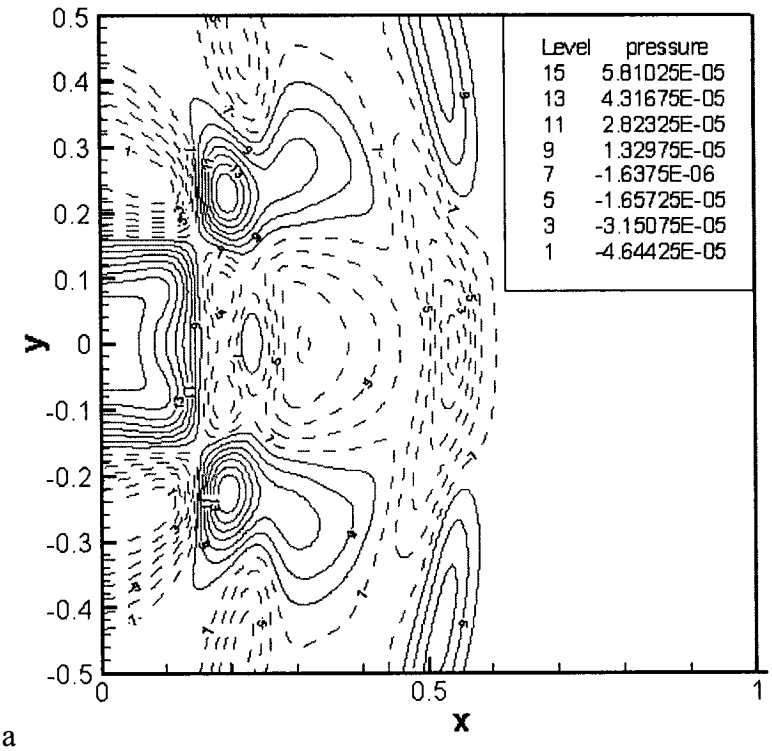
Level pressure
15 5.81025E-05
13 4.31675E-05
11 2.82325E-05
9 1.32975E-05
7 -1.6375E-06
5 -1.65725E-05
3 -3.15075E-05
1 -4.64425E-05
0.5
0.4
0.3
0.2
0.1
0
-0.1
-0.2
-0.3
-0.4
-0.5
y
0
0.5
1
x

a

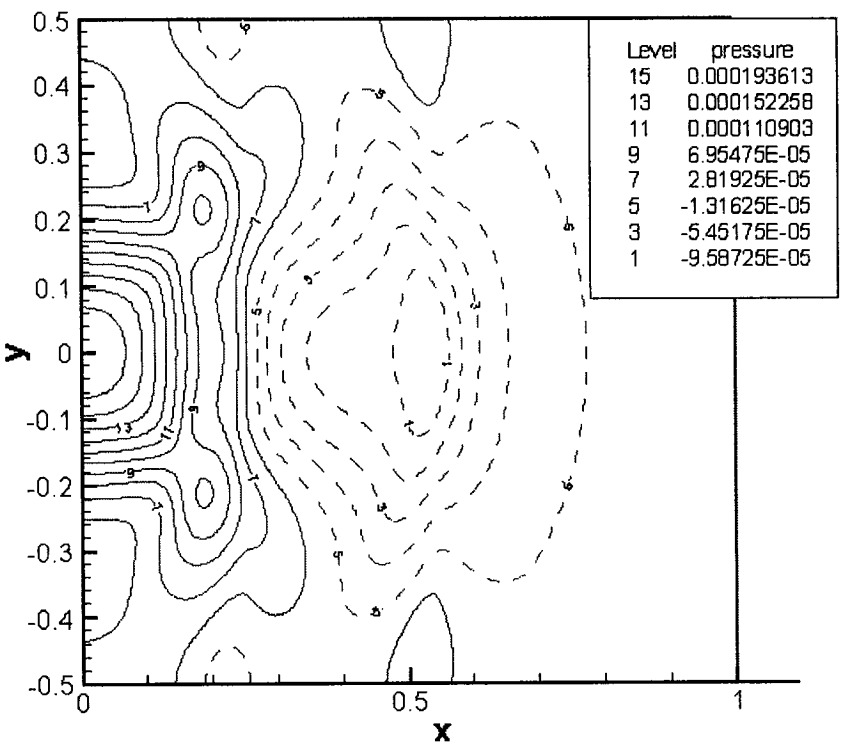
Level pressure
15 0.000193613
13 0.000152258
11 0.000110903
9 6.95475E-05
7 2.81925E-05
5 -1.31625E-05
3 -5.45175E-05
1 -9.58725E-05
0.5
0.4
0.3
0.2
0.1
0
-0.1
-0.2
-0.3
-0.4
-0.5
y
0
0.5
1
x

b

$t = 1.2$

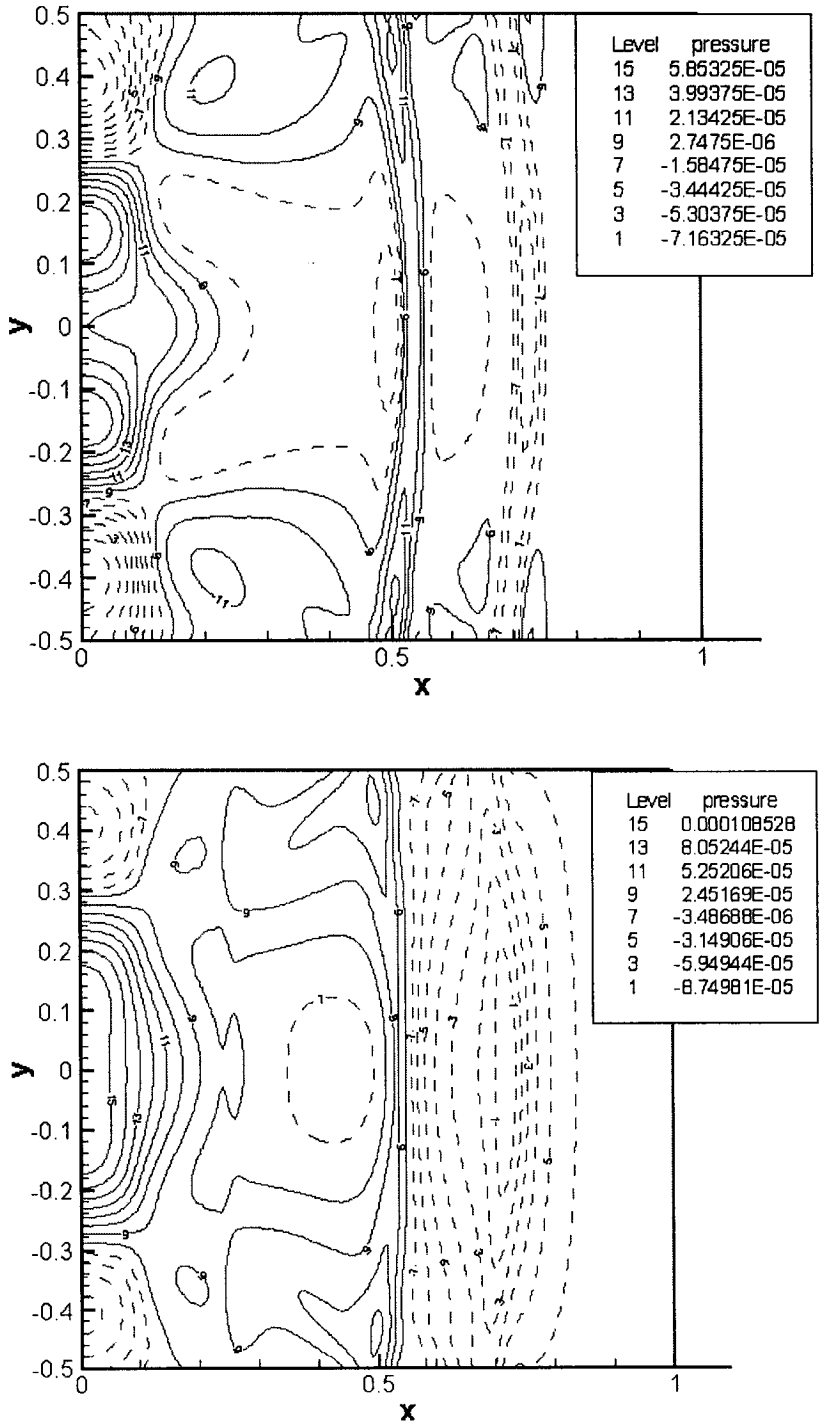

Figure 3-7 Generation of pressure quadrupole and acoustic wave for Taylor and Vatistas vortex dipole: (a) the Taylor's vortex, (b) the Vatistas's vortex ($n = 2$).

Chapter IV

Single Vortex Impingement into Solid Cylinder

Vortex interaction with a blade or airfoil is often complicated by three-dimensionality of the problem. Depending on the flight trajectory of a helicopter, or the operating conditions of a propulsion system, the blade-vortex interaction may involve an oblique vortex, a relatively simpler but challenging parallel vortex, or in the extreme case, either a normal or a streamwise vortex incident upon the leading edge of the blade. According to experiments (Windnall, 1971), the more parallel the tip vortex is to the blade at the time of interaction, the greater the noise radiation. Therefore, the sound generated by a head-on two-dimensional parallel vortex interaction, can be taken as a basic prototype case.

Nakamura (1981) pointed out the importance of the blunt leading-edge of the blade in the vortex and blade surface interaction process. Because blades have blunt leading edges, flows around the circular cylinder with either zero or non-zero circulation are used as prototypes for flow around the leading edge region of a blade.

4.1 Problem Setup

An overview of the vortex impingement on a cylinder is presented in Fig. 4.1.

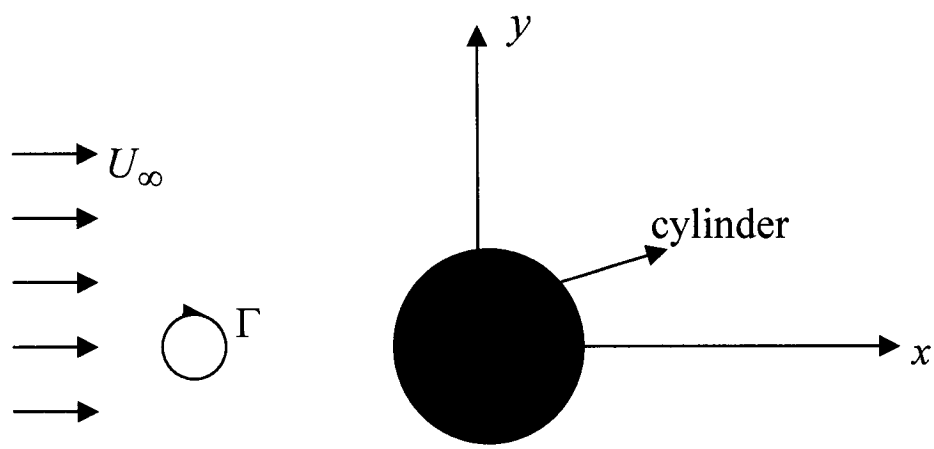

Figure 4-1 C ase B, C: an overview of single vortex impingement on cylinder.

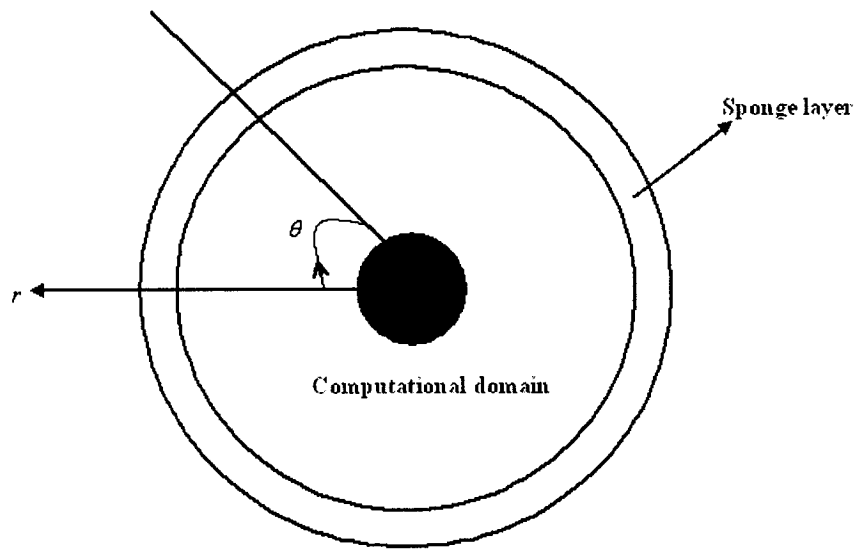

Figure 4-2 A schematic of the computational problem.

The vortex moves near the 2-D cylinder and the computational domain is given as

the space between two circles, where the outer boundary is $r_{up} = 2.5$, the inner boundary coincides with the cylinder surface $r_{down} = 0.5$, and in an angular direction $-\pi < \theta < \pi$ (see Fig. 4.2). A sponge layer was set up to eliminate reflections of acoustic energy back into the computational domain.

The mean flow around a non-rotating cylinder is analytically given in a polar system as follows:

$$U = U_\infty \cos\theta(1 - \frac{R_{cyl}^2}{r^2})$$
$$V = -U_\infty \sin\theta(1 + \frac{R_{cyl}^2}{r^2}) \qquad (54)$$

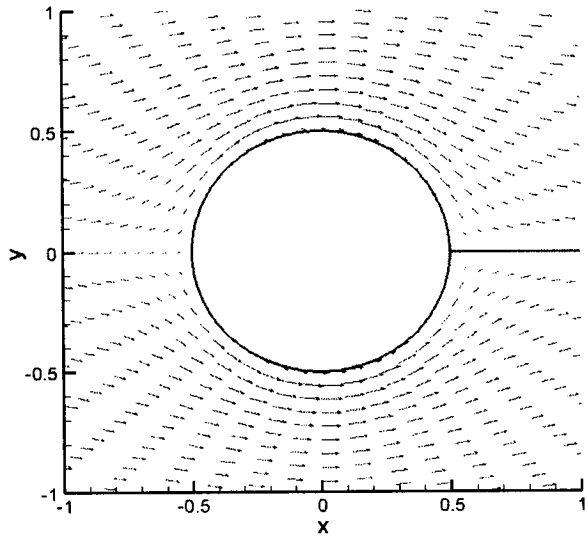

Figure 4-3 Background flow around non-rotating cylinder.

Where U_∞ is the flow velocity in the infinity, R_{cyl} is the radius of the circular cylinder, and r, θ are the polar coordinates. The flow field around the solid cylinder is presented in Fig. 4.3

The linearized mass and momentum flux equations in polar coordinate are:

$$\frac{\partial \rho'}{\partial t} = -\left(\frac{\partial u'}{\partial r} + \frac{u'}{r} + \frac{1}{r}\frac{\partial v'}{\partial \theta}\right) - U\frac{\partial \rho'}{\partial r} - \frac{1}{r}V\frac{\partial \rho'}{\partial \theta}$$

$$\frac{\partial u'}{\partial t} = -\frac{\partial p'}{\partial r} - U\frac{\partial u'}{\partial r} - \frac{\partial U}{\partial r}u' - \frac{1}{r}\left(V\frac{\partial u'}{\partial \theta} + \frac{\partial U}{\partial \theta}v' - 2Vv'\right) - \left(U\frac{\partial U}{\partial r} + \frac{1}{r}V\frac{\partial U}{\partial \theta} - \frac{1}{r}V^2\right)\rho'$$

$$\frac{\partial v'}{\partial t} = -\frac{1}{r}\frac{\partial p'}{\partial \theta} - U\frac{\partial v'}{\partial r} - \frac{\partial V}{\partial r}u' - \frac{1}{r}\left(V\frac{\partial v'}{\partial \theta} + \frac{\partial V}{\partial \theta}v' + Uv' + Vu'\right) - \left(U\frac{\partial V}{\partial r} + \frac{1}{r}V\frac{\partial V}{\partial \theta} + \frac{1}{r}UV\right)$$

(55)

For moderate and small vortex strength, the second-order products of velocity disturbances are often neglected, and linearized Euler equations are used to determine the unknown disturbance variables. However, as the vortex circulation increases, the contribution to the sound generation by non-linear terms becomes non-negligible, and should be accounted for by the following mathematical description:

$$(1+\rho')\frac{\partial u'}{\partial t} = -\frac{\partial p'}{\partial r} - U\frac{\partial u'}{\partial r} - u'\frac{\partial U}{\partial r} - \rho' U\frac{\partial U}{\partial r} - V\frac{\partial u'}{r\partial \theta} - v'\frac{\partial U}{r\partial \theta} - \rho' V\frac{\partial U}{r\partial \theta} + \frac{2Vv'}{r} + \rho'\frac{V^2}{r}$$

$$\begin{aligned}(1+\rho')\frac{\partial u'}{\partial t} = {} & -\frac{\partial p'}{\partial r} - U\frac{\partial u'}{\partial r} - u'\frac{\partial U}{\partial r} - \rho' U\frac{\partial U}{\partial r} - V\frac{\partial u'}{r\partial \theta} - v'\frac{\partial U}{r\partial \theta} - \rho' V\frac{\partial U}{r\partial \theta} + \frac{2Vv'}{r} \\ & + \rho'\frac{V^2}{r} - (u' + \rho' U + \rho' u')\frac{\partial u'}{\partial r} - \rho' u'\frac{\partial U}{\partial r} - (v' + \rho' V + \rho' v')\frac{\partial u'}{r\partial \theta} \\ & - \rho' v'\frac{\partial U}{r\partial \theta} + \frac{v'^2}{r} + \rho'\frac{2Vv'}{r} + \rho'\frac{v'^2}{r}\end{aligned}$$

$$\begin{aligned}(1+\rho')\frac{\partial v'}{\partial t} = {} & -\frac{\partial p'}{r\partial \theta} - U\frac{\partial v'}{\partial r} - u'\frac{\partial V}{\partial r} - \rho' U\frac{\partial V}{\partial r} - V\frac{\partial v'}{r\partial \theta} - v'\frac{\partial V}{r\partial \theta} - \rho' V\frac{\partial V}{r\partial \theta} - \frac{u'V}{r} - \frac{v'U}{r} \\ & - \rho'\frac{UV}{r} - (u' + \rho' U + \rho' u')\frac{\partial v'}{\partial r} - (v' + \rho' V + \rho' v')\frac{\partial v'}{r\partial \theta} \\ & - \rho' u'\frac{\partial V}{\partial r} - \rho' v'\frac{\partial V}{r\partial \theta} - \frac{u'v'}{r} - \rho'\left(\frac{u'V}{r} + \frac{v'U}{r} + \frac{u'v'}{r}\right)\end{aligned}$$

(56)

where u', v', p', ρ' are acoustic disturbances and U, V, P, R are background

steady mean flow components.

4.2 Boundary Conditions:

When the vortex flowfield is implemented as an initial condition, it might violate the non-penetrating boundary condition if its core reaches the rigid wall. On the cylinder wall, to satisfy the zero normal velocity boundary condition, a vortex image system is employed at $t = 0$.

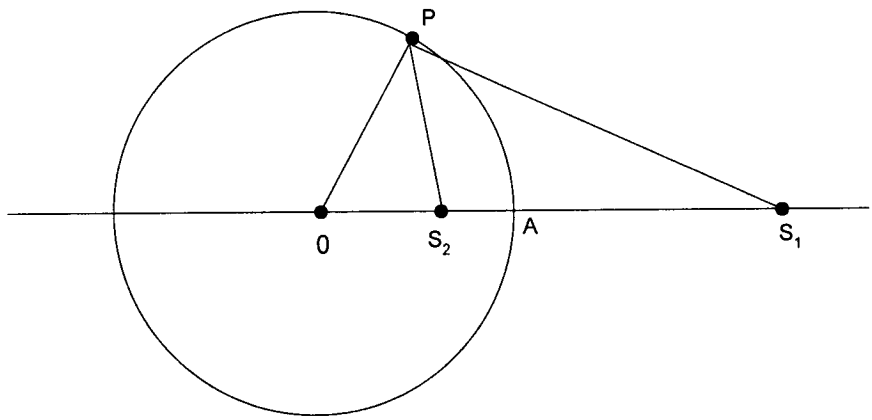

Figure 4-4 Images of a vortex in a fixed circular cylinder.

The inverse points S_1 and S_2, lie on a line OA through the centre O of the circle (see Fig. 4.4) and satisfy:

$OS_1 \bullet OS_2 = OA^2$ Triangle OPS_1 and triangle OPS_2 are similar. Because of this property the following ratio holds true:

$$S_2P : S_1P = OP : OS_1 = \text{constant} \qquad (57)$$

The stream function for a pair of vortices with equal circulation Γ but opposite rotation, situated at S_1, and S_2 respectivel y, is given by:

$$\varphi = \frac{\Gamma}{2\pi}(\ln r_1 - \ln r_2) = \frac{\Gamma}{2\pi}\ln\frac{r_1}{r_2} \qquad (58)$$

where r_1 and r_2 are the distances of a point from S_1 and S_2 respectively.

On the cylinder surface the stream function becomes:

$$\varphi = \frac{\Gamma}{2\pi}\ln\frac{S_2P}{S_1P} = \text{constant} \qquad (59)$$

Hence, the cylinder surface is a streamline, and a fixed boundary can be placed there without altering the flow. However, the vortices located at S_1 and S_2 give zero circulation at infinity. This is because of the fact that the sum of their strengths is zero, where S_1 alone gives the circulation Γ at infinity. To restore this circulation a vortex equal to S_1 is placed at the origin. To sum up, the image system consists of an equal but oppositely spinning vortex at the inverse point, and an equal vortex with same rotation at the origin (Duncan et al., 1970) (see Fig. 4.4).

The initial vortical field after the image vortex system was employed is presented in Fig 4.5. The Taylor vortex (Figure 4.5a) velocity field was not affected by the image vortex combination because of its localized velocity distribution. On the contrary, the one-cell Vatistas $n = 2$ vortex image system, produces a non-trivial flowfield that is

different from the original Vatistas's vortex in infinite space, see Fig. 4.5b. The non-zero flow rear the side of the cylinder causes a downstream sound propagation that will be discussed in this chapter.

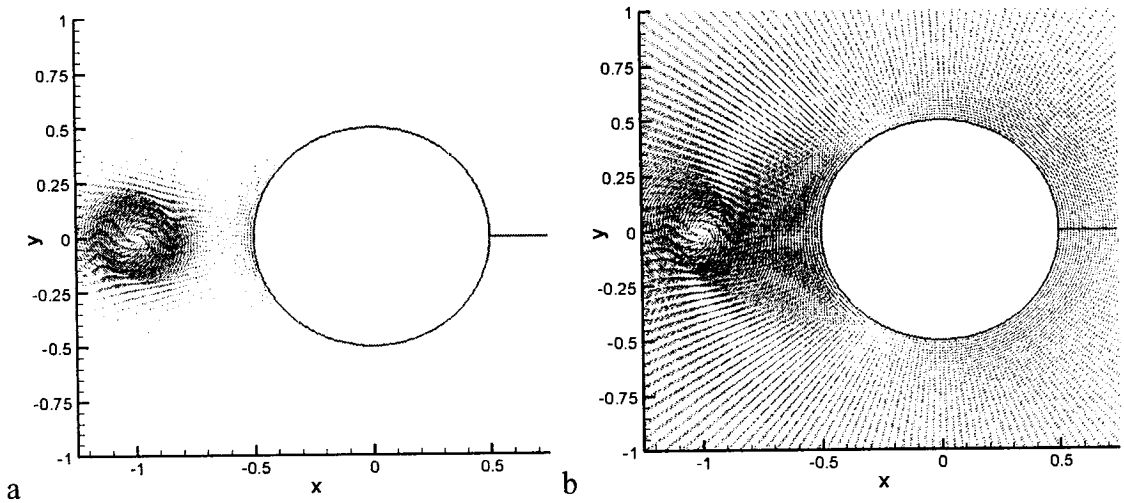

Figure 4-5 Initial flowfield after the image system is implemented: (a) the Taylor's vortex, (b) the Vatistas's vortex ($n = 2$).

Special attention is paid to coinciding points $\theta = -\pi$ and $\theta = \pi$ in the polar coordinates. For $\theta = -\pi$, all disturbance components are computed directly by solving the dynamical equations. For $\theta = \pi$, periodic boundaries are employed, namely $u, v, p_{\theta=-\pi} = u, v, p_{\theta=\pi}$. Spatial derivatives for the $\theta = -\pi$ boundary are taken as the average of one-sided spatial derivatives, $\theta = -\pi$ and $\theta = \pi$.

At the outer boundary, artificial boundary conditions (ABC) are set-up to eliminate reflections of acoustic energy back into the computational domain. The characteristic boundary conditions produce excessive reflected waves in this case. Instead, a simple

damping term in near-boundary layer (so-called sponge layer) was employed as a simplified alternative to the perfect matched layer technique. In ABC, the mean flow was switched off, and the equations used in the ABC were:

$$\begin{aligned}
\frac{\partial p'}{\partial t} &= -\left(\frac{\partial u'}{\partial r} + \frac{u'}{r} + \frac{1}{r}\frac{\partial v'}{\partial \theta}\right) - \sigma_r p' \\
\frac{\partial u'}{\partial t} &= -\frac{\partial p'}{\partial r} - \sigma_r u' \\
\frac{\partial v'}{\partial t} &= -\frac{1}{r}\frac{\partial p'}{\partial \theta} - \sigma_r v'
\end{aligned} \tag{60}$$

where the damping term is given as:

$$\sigma_r = \sigma_m \left|\frac{r - r_l}{D}\right|^{\beta} \tag{61}$$

where r_l denotes the location where the PML starts, and D is the width of the PML. To compute σ_m the relations $\sigma_m \Delta r = 2$, where Δr is the grid size and $\beta = 2$ are used for all computations.

4.3 Computational Results:

The results are composed as follows. In Section 4.1, a noise generation by interaction of cylinder with a convected single vortex was investigated for the zero-circulation Taylor vortex model and the non-zero circulation Vatistas vortex model. In Section 4.2, a turbulence-generated vortex was considered as a source of sound generation. In Section 4.3, the nonlinearity effect on sound generation and propagation

was investigated.

The averaged-in-time, root mean square of acoustic pressure (RMS) is usually measured by experimenters as an indicator of noise intensity:

$$p_{rms} = \sqrt{\int_0^T p^2 \, dt/T} \qquad (62)$$

where p is the instantaneous acoustic pressure and T is the time period of integration which needs to cover the passing of transmitted and reflected waves. In this study the RMS acoustic pressure distributions with respect to angle θ from the centerline were presented to show the sound strength and directivity. In the following RMS computations, if not specified, the RMS acoustic pressure was computed at various angular locations. Also $r = 5R_{cyl} = 2.0$, and T is given equal to 3.5 to cover the passing of transmitted and reflected waves.

4.3.1 Non-zero circulation vortex

First, the influence on the sound generation and propagation in a non-uniform flow of different vortex profiles which belong to the same non-zero-circulation vortex family, were investigated. The effects of the radial velocity that are often neglected on sound prediction were studied in detail. Also a two-cell deforming vortex as a source of sound was examined.

A. One-cell vortex

The computational results were obtained by solving the linearized Euler equations adopting different non-zero circulation vortices. To make a fair comparison of sound generation, all considered vortices have the same vortex core size ($R_c = 0.25$), the same maximum circulation ($\Gamma_{max} = 0.15$) and the background mean flow has the same Mach number $(M_\infty = 0.2)$. In Fig. 4.6 $p_{rms}(r,\theta)$ is shown as a function of angle θ from the centerline. Although there is some difference between the RMS profiles produced by the different vortices, the maximum intensity difference is within 5% for all vortices. The maximum acoustic pressure occurs at 45° from the centerline. To summarize, the sound directivity and intensity for all vortices, are similar to each other for all considered one-cell vortices.

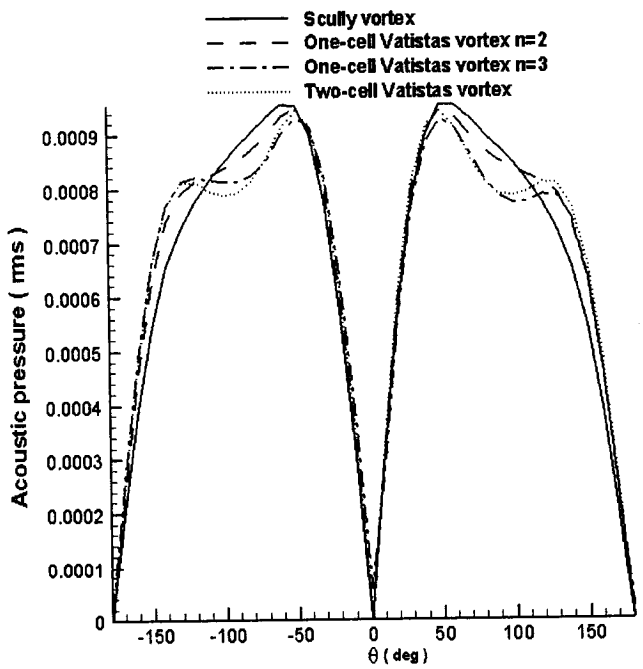

Figure 4-6 The RMS of acoustic pressure for one and two- cell vortices by linear simulation by Eq. (55).

The Vatistas vortex with $n=2$, given in Eq. 5, is chosen as a representative of one-cell non-zero-circulation vortex models, to investigate the influence of vortex radial velocity on sound generation. In Figs 4.7a and 4.7b, $p_{rms}(r,\theta)$ is shown as a function of angle θ from the centerline. If the radial velocity is taken into account, the sound pressure is not equal to zero at the centerline for both linearized and non-linear Euler simulations. Nevertheless, the maximum RMS acoustic pressure difference is within 5% for the linearized and non-linear Euler equations. Therefore, it is justified to neglect the radial velocity influence for predicting sound generated by one-cell vortices.

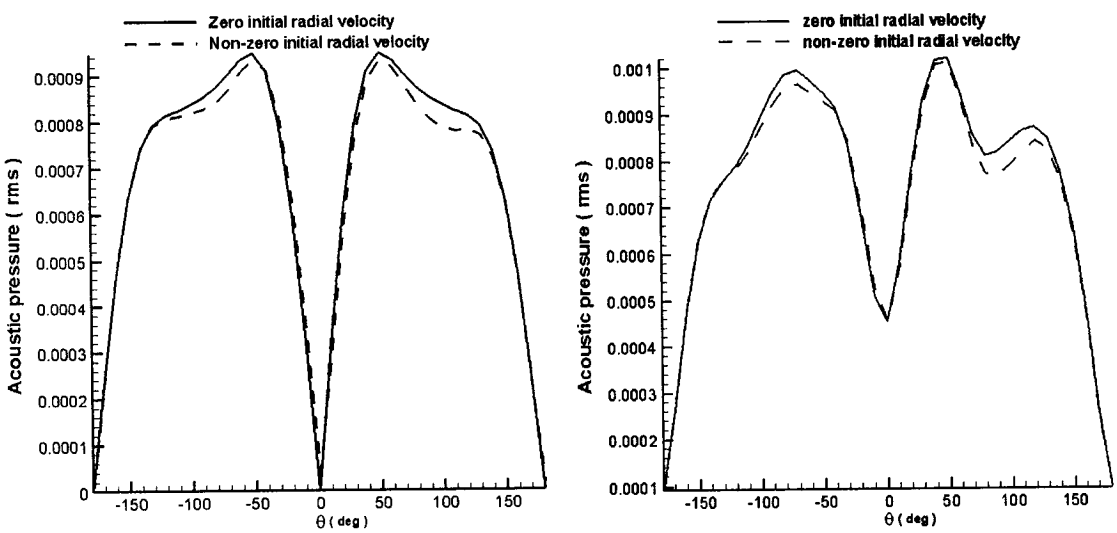

(a) (b)

Figure 4-7 The RMS pressure distribution for linear and non-linear Euler simulations of one-cell vortical disturbances with and without initial radial velocity: (a) linear simulation by Eq. (55), (b) non-linear simulation by Eq. (56).

B. Two-cell vortex

For the two-cell vortical disturbance, it is important to examine how the radial velocity affects the sound generation and propagation in a non-uniform flow. The RMS of acoustic pressure generated by deforming of the two-cell vortex in a flow about a 2-D cylinder is shown in Fig. 4.8.

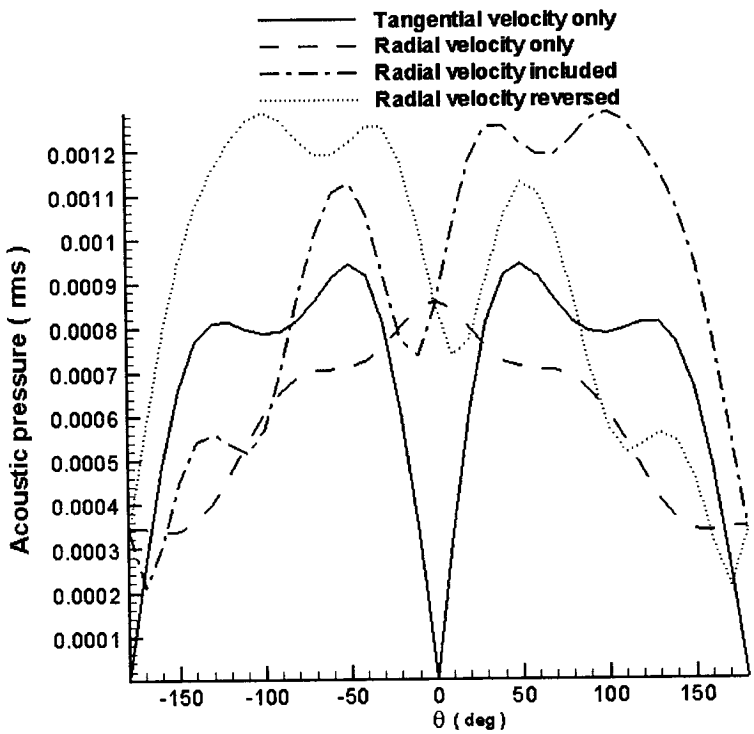

Figure 4-8 The RMS of acoustic pressure distribution for the two-cell vortical disturbances.

The consideration of radial velocity notably changes the angular distribution of acoustic pressure. Although the radial velocity is still much smaller than the tangential velocity, its contribution to acoustic pressure is not negligible for two-cell vortices. The presence of radial velocity has not only strengthened the RMS acoustic pressure level, but

has also changed the angular noise directivity. To confirm that the non-zero radial velocity is the reason for the non-symmetry of acoustic pressure with respect to the centerline, the radial velocity has been reversed. If the radial velocity direction is reversed, then the non-symmetry around the centerline is also reversed (see Fig. 4.8).

To further investigate the effect of radial velocity on the non-symmetrical angular distribution of the RMS pressure, the acoustic pressure isoline generated by reduced two-cell vortical disturbances with (i) the initial tangential velocity only and (ii) the initial radial velocity only, is presented in Figs 4.9 a, b, c, respectively. The generation of sound by the two-cell vortex can be viewed as a combination of sound generation by these two simplified vortices. In Fig. 4.9a, four alternating sign of pressure spots (quardrupole) produced by the convected disturbance (i) are clearly seen. To produce the sound wave, the pressure quardrupole is elongated and the pressure waves are generated. In Figure 4.9b, the pressure wave generated by the convected disturbance (ii) is symmetrical around the centerline, i.e., the acoustic pressure has the same sign on both sides of the centerline. Finally, the two-cell vortex with both components of initial velocity (iii) is considered. The most striking feature of the generated sound wave is the non-symmetric distribution of the RMS of acoustic pressure with respect to the centerline (see Fig. 4.9c).

The linearized Eq. (55) have the same coefficients for all three cases considered in Fig. 4.9 Therefore, the solution for the initial conditions (iii) is a sum of solutions

obtained for initial conditions (i) and (ii). When two pressure disturbance solutions originated from initial conditions (i) and (ii) are added, the total disturbance pressure becomes non-symmetrical about the centerline.

To investigate the influence of the Mach number of a mean flow, the flow-fields of a two-cell vortex in a mean flow, with $M = 0.1$ and $M = 0.4$ at the time $t = 1.5$ are presented in Fig. 4.11. The vortex is convected by the non-uniform mean flow and is deformed by the mean flow. For $M = 0.4$, not only is the vortex center located closer to the cylinder, but the vortex will also be more deformed along the spanwise direction.

To further investigate the influence of the Mach number of background mean flow on the sound generation and propagation by deformation of the two-cell vortex, the acoustic pressure has been computed for Mach numbers, M_∞, from 0.1 to 0.4. For higher Mach numbers, the mean flow becomes transonic, and the adopted mean flow model becomes invalid. The reduced two-cell disturbances (i) and (ii), and the two-cell initial vortex (iii), were submerged in the background flow with different Mach numbers. The computational results are presented in Figs. 4.12a, b, c, respectively. If the reduced two-cell vortex is considered, the sound level increases with the Mach number of the mean flow. The maximum sound level is reached at an angle of $45°$ from the centerline for the considered range of Mach numbers of the mean flow. No simple power law of the dependence of the RMS of acoustic pressure with Mach number has been found. If the initial two-cell vortex is considered, the Mach number of the background flow does not

only change the amplitude of the RMS acoustic pressure, but also affects its angular directivity. The sound profile of the RMS is substantially non-symmetrical (see Fig. 4.12c). For all Mach numbers considered, the RMS has maximums at both lower and upper half-planes with a substantial difference in the maximum amplitude. For M=0.1, the lower half-plane maximum, is approximately 2.5 times larger than the upper half-plane maximum. As the Mach number increases, the maximum RMS acoustic pressure is shifted to the upper half-plane.

4.3.2 Zero-circulation vortex and non-zero-circulation vortex

The profile of flow in a vortex depends on the geometry of the upstream rigid body (which shed vortices), the "age" of the vortex when it impinges into the downstream surface, the initial vortex-to-its-core ratio et.. In this part, the effect of the vortex velocity profile on the amplitude and directivity of sound wave generated by the distorting vortex were studied. The Taylor's vortex, which has localized core and zero total circulation and the Vatistas's vortex with non-zero total circulation are adopted as examples of two different types of vortices. To make fair comparison, the radius corresponding to the maximum tangential velocity and the maximum circulation of the two vortices were made equal.

A. Comparatively weak vortex in non-uniform flow around cylinder

In real terms, the ratio of the vortex core size to the size of downstream rigid body

may increase to the order of one-tenth when the vortex impinges perpendicular to the chord of the blade. The vortex core and the size of rigid body may be similar. For instance, the vortex shed by the main airfoil has a core size comparable to the airfoil thickness (Bhagwat & Leishman, 2002). And its core size is also comparable to the diameter of the flap's leading edge.

First, a relatively weak vortex with circulation $\Gamma = 0.00005$, and a core radius of $R_c = 0.04$, was superimposed in the flow with $M_\infty = 0.2$ at location $(-1.,0)$, i.e., at the distance of one radius upstream of the cylinder surface.

In Fig. 4.13, the acoustic disturbance propagation at different times are presented. Similar to Case A, the vortex is distorted, quadrupoles are produced, and the sound wave propagates outward. From the beginning, the interaction between the vortex and the cylinder show substantial differences for the Taylor and Vatistas models, For the Taylor model, the pressure quadrupole is focused near the upstream centerline at an earlier time, whereas at a later time the sound wave propagates upstream of the cylinder. For the Vatistas vortex, the pressure disturbance is developed circumferentially around the cylinder, and later the sound propagates upstream and downstream. This is indeed a result of the initial imposition of image vortices, which create a non-trivial flowfield downstream of the cylinder. Nevertheless, in reality, as a result of the interaction of a slowly decaying vortex and bluff body such a flowfield must appear.

In Fig. 4.14, the radial acoustic pressure distributions are presented for the Taylor

and Vatistas vortices. Where the angle to the negative x axis are taken equal to $35°$ and $45°$, corresponds to the area of maximum acoustic pressure. The sound wave for the Taylor vortex has a shorter wavelength and develops faster than that for a Vatistas model. For the Taylor vortex, acoustic pressure reaches its maximum at t=0.8, and then starts to weaken. Sound waves generated by the Vatistas vortex have almost three times larger acoustic pressure amplitudes than that of the Taylor model.

To investigate the influence of the mean flow speed, the RMS of acoustic pressure was computed at various angular locations at $r = 5R_{cyl}$. Results of the computations are presented in Fig. 4.15. To test the effect of the initial proximity of a vortex to a cylinder on sound generation, the RMS acoustic pressure is shown in Fig. 4.16, with the initial position of the vortex at $(-0.75,0)$.

When the Mach number of the mean flow increases, the vortex is more distorted, and the generated sound wave becomes stronger. For the conditions in Figs 4.15 and 4.16. the RMS of acoustic pressure radiated by the distorting Taylor vortex has two maxima: (i) at $\theta = 30^{o}$ from the negative x axis; and (ii) $\theta = 110°$ to $\theta = 120°$. The level of RMS for closer location of vortex to the surface (Fig. 4.16a), is more than twice larger than that for more distant location (Fig. 4.15a). This enhancement of acoustic pressure is fully attributed to stronger vortex distorting in the latter case. There is no influence of imaginary vortices even if the vortex is initially located at $(-0.75,0)$ because the Taylor vortex fully decays at a distance of 0.15 from its origin.

When the Vatistas vortex is located at $(-1.,0)$, the first RMS pressure maximum is substantially larger than the subsequent maxima corresponding to the larger values of α. If the Vatistas vortex is initially located closer to the rigid cylinder surface, then the RMS has two maxima with almost the same amplitude (Fig. 4.16b). When the Mach number of mean flow increases, the second maximum pressure exceeds the first maximum pressure as a result of higher distorting of the peripheral part of the vortex. The sound directivity for the Vatistas vortex shifts with an increase of the Mach number. For the lower Mach number, the upstream sound directivity corresponds to $\theta = 45^o$, while the second maximum is located at $\theta = 110^o$. Compared to the Taylor vortex, the level of RMS pressure for the closer proximity of the vortex to the cylinder is only 25% larger than that of a farther location.

In Fig. 4.17, the acoustic disturbance velocity distributions corresponding to the Taylor model and Vatistas model, are presented for $t = 0.8$. Location of stagnation points of acoustic velocity for both vortices are consistent with the maximum sound directivity. The disturbance velocity patterns are quite different for the Taylor and Vatistas vortices. While two counter-rotating vortices appear on the opposite sides of the main Taylor vortex, that is not the case for the Vatistas vortex.

B. Vortex comparable with the cylinder diameter

A relatively strong vortex of circulation $\Gamma = 0.012$ and the core radius $R_c = 0.25$

was superimposed in the flow with $M_\infty = 0.2$ at location $(-1.,0)$.

In Fig 4.18, simulation results are shown for $M_\infty = 0.2$, and the initial vortex location $(-1.,0)$ upstream of the cylinder. Compared to the small core vortices (see Section 4.2.1), the generated pressure quadrupole is more spatially distributed in the angular direction. For the Taylor vortex, the sound wave from the downstream surface of the cylinder encircles the sound wave from the upstream surface. For the Vatistas vortex, the four alternating sign spots are evenly distributed at the cylinder surface. As it was for small core vortices, the RMS pressure is measured at $r = 5R_{cyl}$, and the time period T is equal to 3.5. For the Vatistas vortex, the RMS pressure shapes are similar to those obtained in the previous section for the small core vortex with the maximum sound directivity around $\theta = 45^0$. For the Taylor vortex, the sound directivity is shifted from $\theta = 30°$ for the small core vortex to about $\theta = 80°$ for the large vortex. Compared to acoustic pressure for small core vortices, the sound pressure level for large Taylor and Vatistas vortices are approximately at the same level. If the vortex core size is comparable to the size of the rigid body downstream, the vortex distorting to lesser degree depends on the velocity profile.

C. Acoustic radiation from vortex dipole

In this section, numerical results related to radiation of sound by a pair of distorting counter-rotating small vortices in a flow around the cylinder are presented. Vortices have

a small core $(R_c = 0.04, \Gamma = 0.000053)$, and are initially located at $(x_v = -1.0, y_v = \pm 0.1)$ upstream of the cylinder. For both vortices the pressure quadrupole is concentrated at the centerline (Figs. 4.19, 20), where the same signs of quadrupoles merge. While sound waves propagate upstream of the stagnation flow, the centerline wave is surrounded by two waves of the sign of acoustic pressure, opposite to that of the centerline wave. For the Taylor vortex the peripheral waves are located upstream, while for the Vatistas vortex the peripheral waves are directed downstream, and are weakened by the mean flow. For the Vatistas vortex, the maximum RMS occurs at the centerlines, whereas for the Taylor vortex, the maximum RMS shifts from $\theta = 30^0$ to $\theta = 60^0$ with an increase of the Mach number.

4.3.3 Turbulent Vortex Model

The sound strength and sound directivity corresponding to the sound wave generated by Vatistas's vortex model, a representative of laminar vortex model and the new turbulent vortex model were compared. To make a fair comparison, the vortex core size and the maximum tangential velocity were made equal for the two models.

The RMS of acoustic pressure is presented in Fig. 4.22. It is clear that the sound directivity for the sound wave generated by both models is 45° away from the centerline. However, the sound strength for the turbulence model has increased by about 50% in comparison to the laminar vortex model. In other words, turbulence will not

change the sound directivity but will enhance the sound strength.

4.3.4 Non-linearity analysis

For moderate and small vortex strengths, the second-order products of velocity disturbances are often neglected, and linearized Euler equations are used to determine the unknown disturbance variables. As the vortex circulation increases, the contribution to the sound generation by non-linear terms becomes non-negligible, and should be accounted for by a mathematical description. In this section, the effect of non-linear terms on sound generation and propagation will be investigated.

The Vaitsas vortex, with a vortex core equal to 0.25 and a maximum circulation corresponding to 0.15, are superimposed in the flow with $M_\infty = 0.2$ at the axial location $(-1.,0)$. The sound generation and propagation simulated by the linearized Euler equations, non-linearized Euler equations, and the contribution by the non-linear terms to acoustic pressure, are presented in Fig. 4.23. Whereas the non-linear terms is a modest contribution. Overall some important features of the acoustic field obtained by non-linear simulations are different from those obtained by linear simulations. From the linear simulation result, it can be clearly seen that the sound wave generated is absolutely symmetrical around the centerline. There is an obvious zone of silence near the centerline, which means that an observer standing in this area will not hear the noise. However, from the non-linear simulation, the sound pressure is not only revealed to be asymmetrical to

the centerline, but there is no zone of silence near the centerline. The non-symmetry of sound wave is due to the sound contributed by the non-linear terms, and is strictly symmetrical to the centerline not only in its amplitude but also in its sign. Therefore when it is added to the sound produced by linear terms, the result turns to be non-symmetrical.

Results of computations in terms of the acoustic pressure RMS are presented in Fig. 4.24. The sound directivity remains the same for linear and non-linear simulations and the maximum amplitude of the RMS acoustic pressure computed by the non-linear simulations is a modest 10 per cent higher than that obtained by the linear simulations, which also holds true for the Taylor vortex. The non-linear effect near the centerline is most prominent, so it could be that non-linear effects are important near the centerline in the vicinity of stagnation points where $u' du'/dr$ become s larger than $U du'/dr$, where U is the local mean velocity. In a linearized model, $u' du'/dr$ is neglected in comparison to $U du'/dr$. This may be not applicable near stagnation points and a non-linear model may be needed.

To further investigate non-linear effects, the vortex core size is kept fixed, the vortex Mach number (which is defined as $\Gamma/2\pi R_c$, where Γ is the maximum circulation and R_c is the vortex core) is changed in such a way that its ratio to the far-field uniform Mach number α, becomes equal to one of the following values: 0.05, 0.1, 0.5, or 1.0. The percentage of RMS pressure, obtained by the non-linear simulation and linear simulation,

is presented in Fig. 4.25. When α=0.05, the percentage of RMS pressure is equal to zero except around the centerline. This means that the sound pressure that is solved by the non-linear Euler equations and linear Euler equations are practically the same. However, as the ratio rises to 0.5, the percentage becomes significant, and the contribution by the non-linear terms turns out to be non-negligible. Finally, when the ratio rises to 1.0, it is clear that a non-linear simulation is needed for accurate prediction of the sound generation and propagation.

4.4 Summary of Findings

The effect of the vortex velocity profile on the amplitude and directivity of sound waves generated by the distorting vortex has been studied in this chapter. First, the non-zero-circulation vortex family was investigated. It was found that the sound directivity and intensity for all vortices was similar to each other for one-cell vortices. If the radial velocity is taken into consideration for sound prediction, for a single-cell vortex there would be no substantial changes to the acoustic waves. On the contrary, for the two-cell vortex the presence of the radial velocity, which is still much smaller than the tangential velocity, affected the intensity and directivity of the propagating sound wave. The non-symmetrical directivity of sound with respect to the centerline was much more prominent for the two-cell vortical disturbance than that for the one-cell vortical disturbance.

Secondly, the Taylor vortex, with its localized core and zero total circulation and

the gradually decaying Vatistas vortex with non-zero total circulation were adopted as examples of two different types of vortices. To make the two vortices comparable, the vortex core and maximum circulation were taken to be equal for the Taylor and Vatistas vortices. Stagnation flow of the flow around the 2-D infinite cylinder was taken as the prototype of real world non-uniform flows about a rigid body. All the vortices of two representative core sizes were considered: (i) small-core vortex with $R/R_c = 0.1$, and (ii) large-core vortex with $R/R_c = 0.5$.

For small vortex-core vortices, the strength of the sound wave radiated by Taylor vortex was three times weaker than those radiated by Vatistas vortex if the cylinder is non-rotating. For the large-core vortex, the sound wave strength generated by the Taylor and Vatistas vortices was of the same level. The sound directivity was also quite different for these two vortices. For the Vatistas vortex, the maximum sound directivity was around $\theta = 45°$ to the centerline. This holds for a small-core and large-core vortex for flow around a non-rotating cylinder. On the contrary, for the Taylor vortex the maximum sound directivity increased from $\theta = 30°$ for a small core vortex to $\theta = 80°$ for a large core vortex.

For the Vatistas vortex, the downstream propagating sound waves were observed at an earlier time. Later, these waves were weakened since they propagated downstream, and because the pressure quadrupole source was substantially weaker in the downstream part of the flow. For the Taylor small-core vortex the amplitude of emanating sound

wave increased substantially when the vortex was put closer to the rigid cylinder. However, this was not the case for Vatistas vortex.

When vortex dipoles were convected by the non-uniform mean flow, the sound wave pressure field tended to look more alike for the Vatistas and Taylor models than it did for the monopole vortex. The mutual cancellation of outgoing sound waves made the wave pattern similar. However, the maximum RMS pressure for the Vatistas vortex was at the centerline, while for the Taylor vortex the maximum RMS pressure increased from 30° to 60° with increasing Mach number.

Finally, a non-linear analysis was investigated. The effect of non-linear terms to the sound pressure was controlled by the vortex strength, which was introduced as the ratio of the Mach number of vortex to the Mach number of far-field mean flow. The non-linear effects increased with the growing strength of the vortex. When the vortex was weak, the results obtained by the linearized and non-linearized Euler equations were practically the same. However, as the vortex strength increased, the contribution of the second-order non-linear terms became non-negligible. Several crucial features of the acoustic field obtained by the non-linear simulations were shown to be different from those obtained by linear simulations. While linear predictions have suggested a zone of around the centerline, the non-linear simulation results reveal that the acoustic pressure is far from zero on the centerline

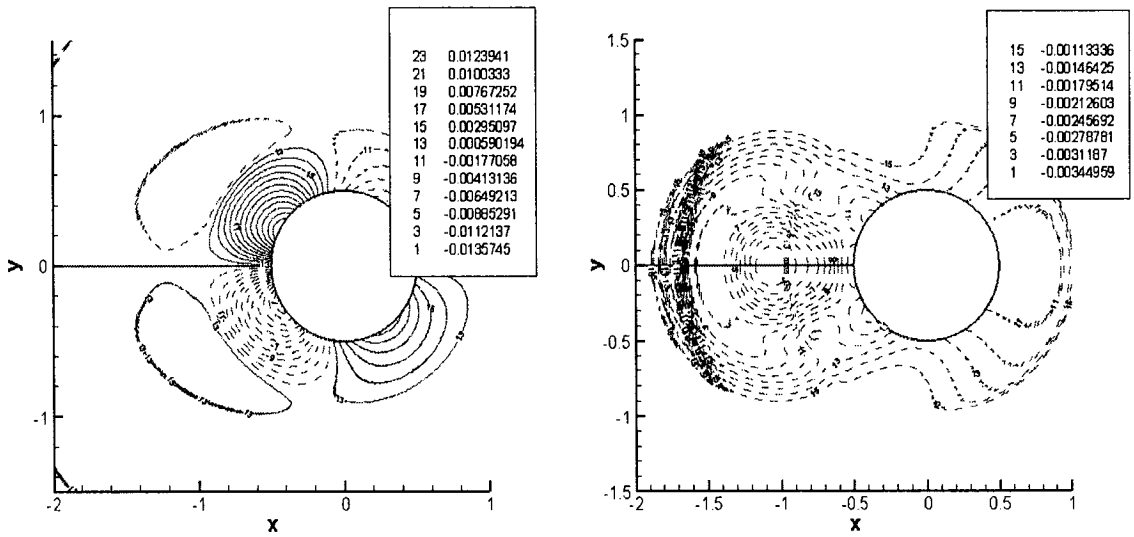

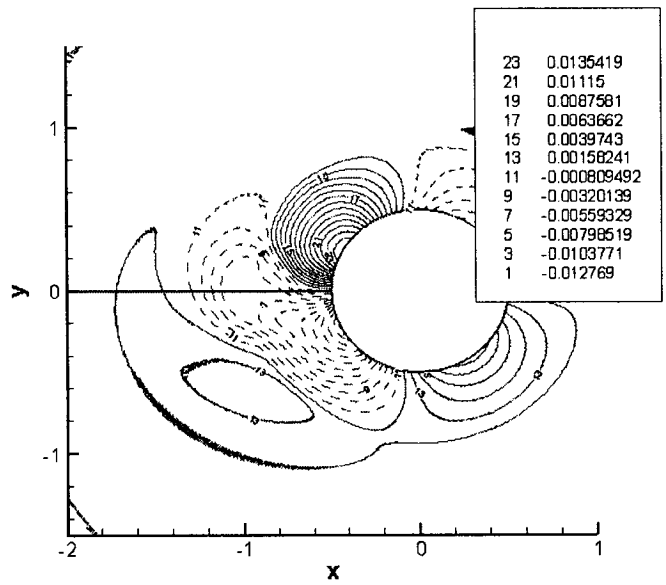

Figure 4-9 Unsteady pressure generated by the two-cell vortical disturbance: (a) the vortex with initial tangential velocity only, (b) the initial two-cell disturbance with the radial velocity component, (c) the full two-cell vortex.

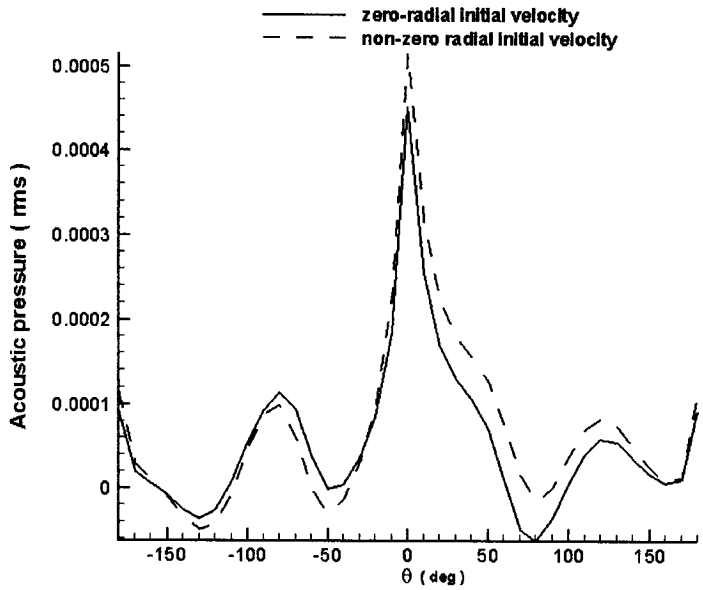

Figure 4-10 The non-linear terms contribution to RMS of acoustic pressure.

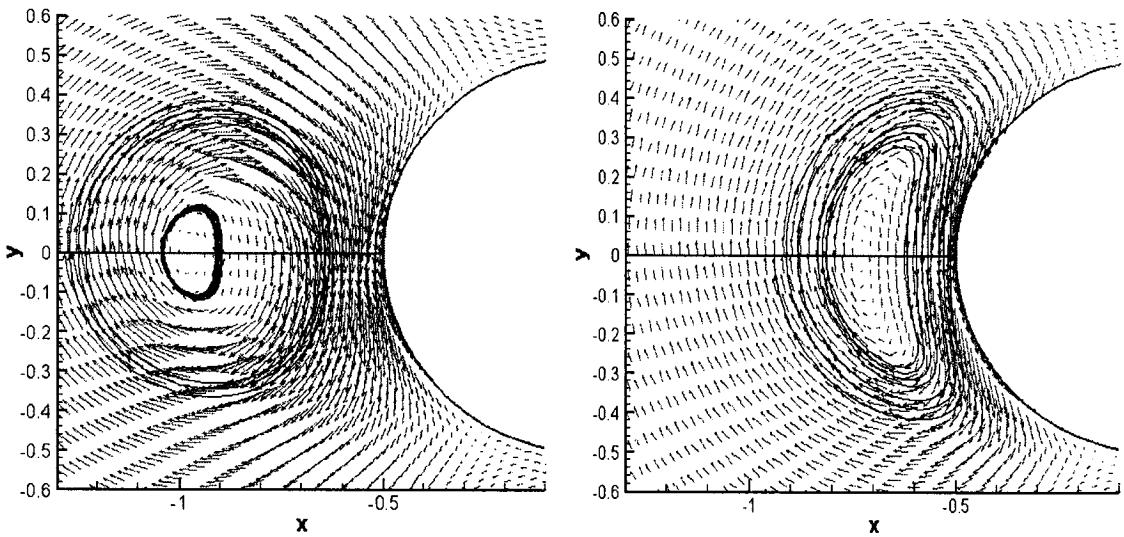

(a) (b)

Figure 4-11 The flow-field of the two-cell vortical disturbance convected by the mean flow around cylinder at: (a) $M = 0.1$ and, (b) $M = 0.4$.

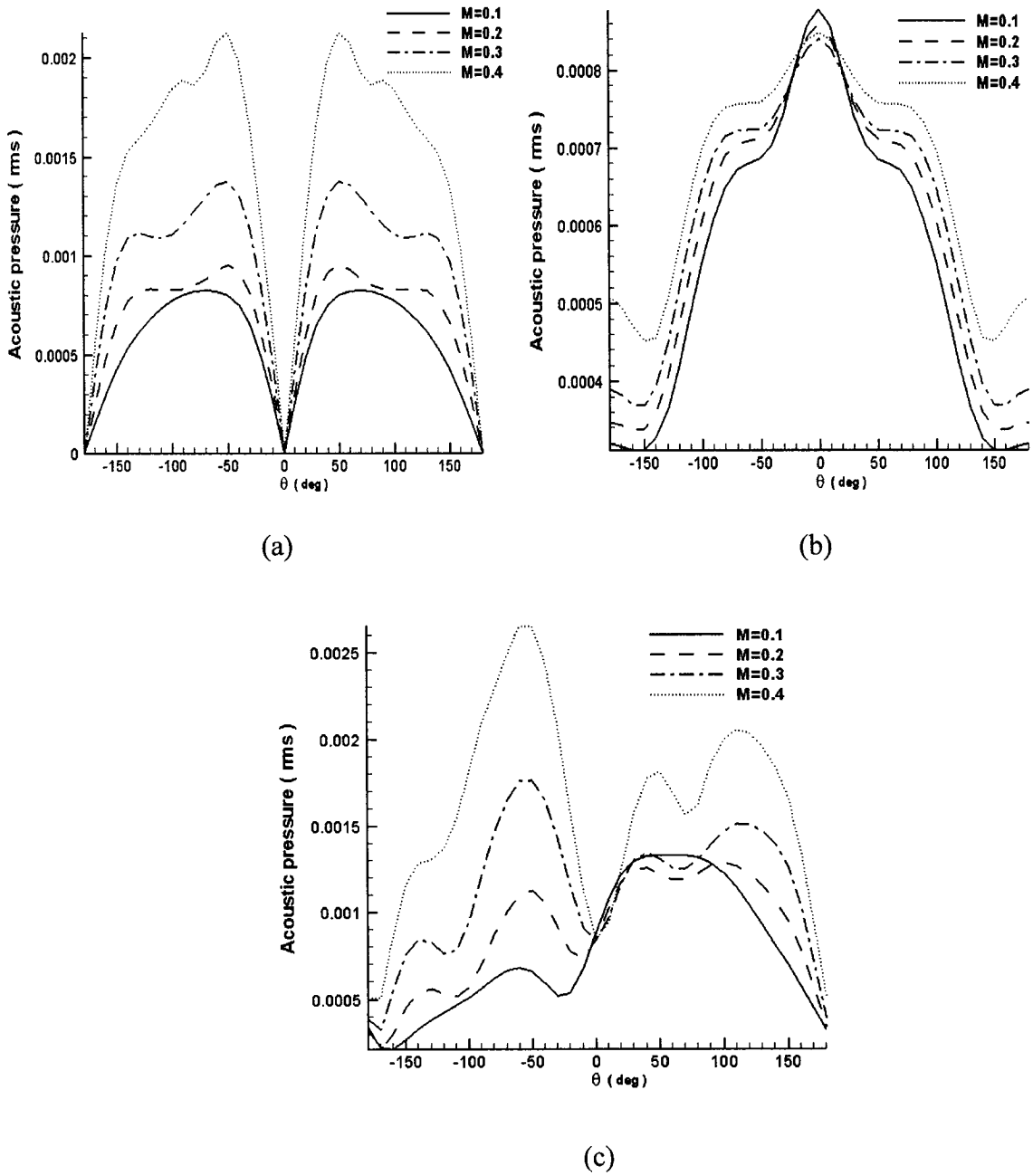

Figure 4-12 The RMS of acoustic pressure generated by two-cell vortices at different Mach numbers of the mean flow around a cylinder: (a) two-cell vortex with initial zero radial velocity, (b) two-cell disturbance with initial zero tangential velocity and, (c) the full two-cell vortex.

$t = 0.4$

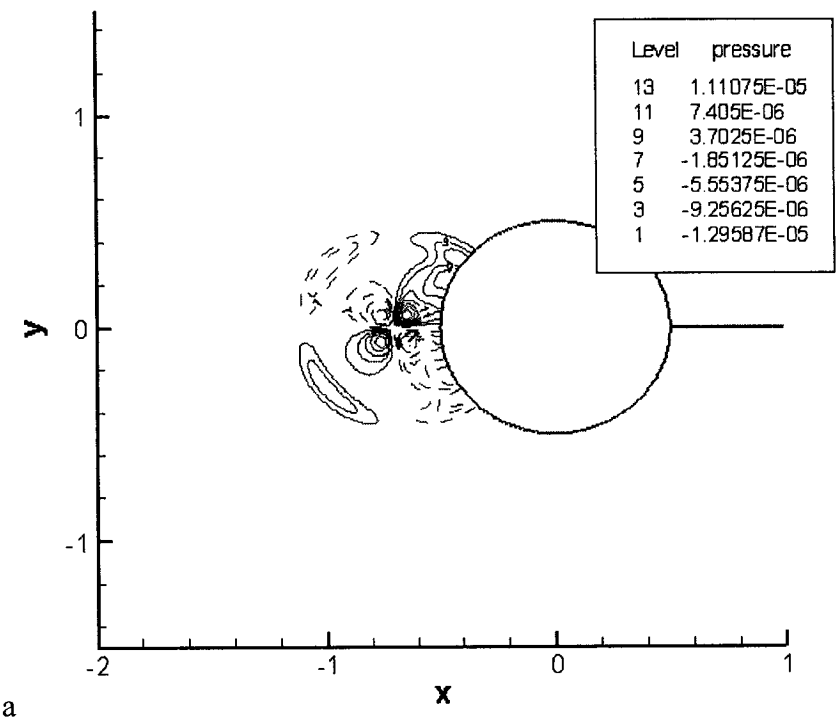
Level pressure
13 1.11075E-05
11 7.405E-06
9 3.7025E-06
7 -1.85125E-06
5 -5.55375E-06
3 -9.25625E-06
1 -1.29587E-05
y
x
1
0
-1
-2
-1
0
1

a

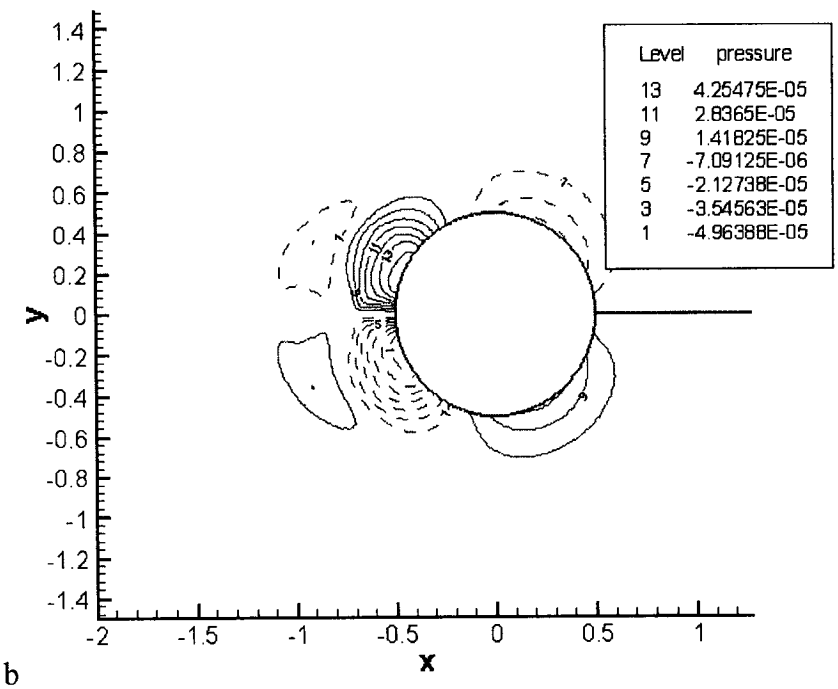
Level pressure
13 4.25475E-05
11 2.8365E-05
9 1.41825E-05
7 -7.09125E-06
5 -2.12738E-05
3 -3.54563E-05
1 -4.96388E-05
y
x
1.4
1.2
1
0.8
0.6
0.4
0.2
0
-0.2
-0.4
-0.6
-0.8
-1
-1.2
-1.4
-2
-1.5
-1
-0.5
0
0.5
1

b

$t = 0.8$

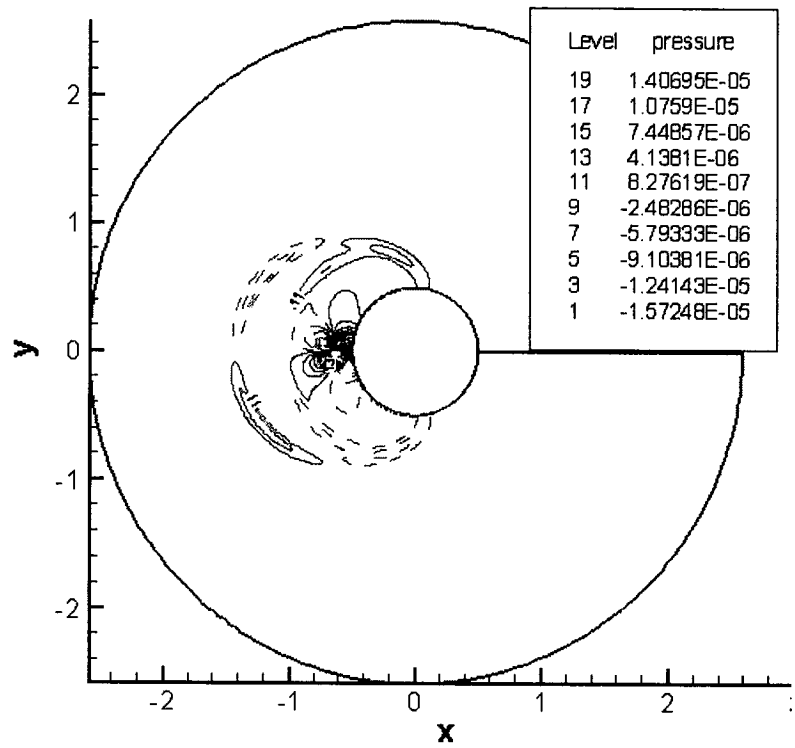
Level pressure
19 1.40695E-05
17 1.0759E-05
15 7.44857E-06
13 4.1381E-06
11 8.27619E-07
9 -2.48286E-06
7 -5.79333E-06
5 -9.10381E-06
3 -1.24143E-05
1 -1.57248E-05
y
x
2
1
0
-1
-2
-2
-1
0
1
2

a

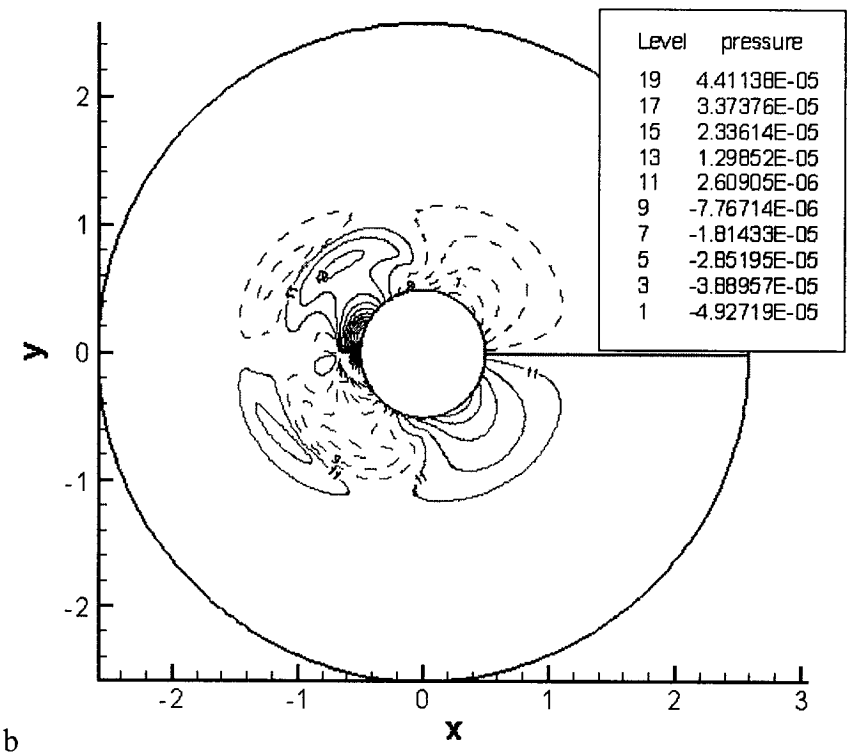
Level pressure
19 4.41138E-05
17 3.37376E-05
15 2.33614E-05
13 1.29852E-05
11 2.60905E-06
9 -7.76714E-06
7 -1.81433E-05
5 -2.85195E-05
3 -3.88957E-05
1 -4.92719E-05
y
x
2
1
0
-1
-2
-2
-1
0
1
2
3

b

$t = 1.2$

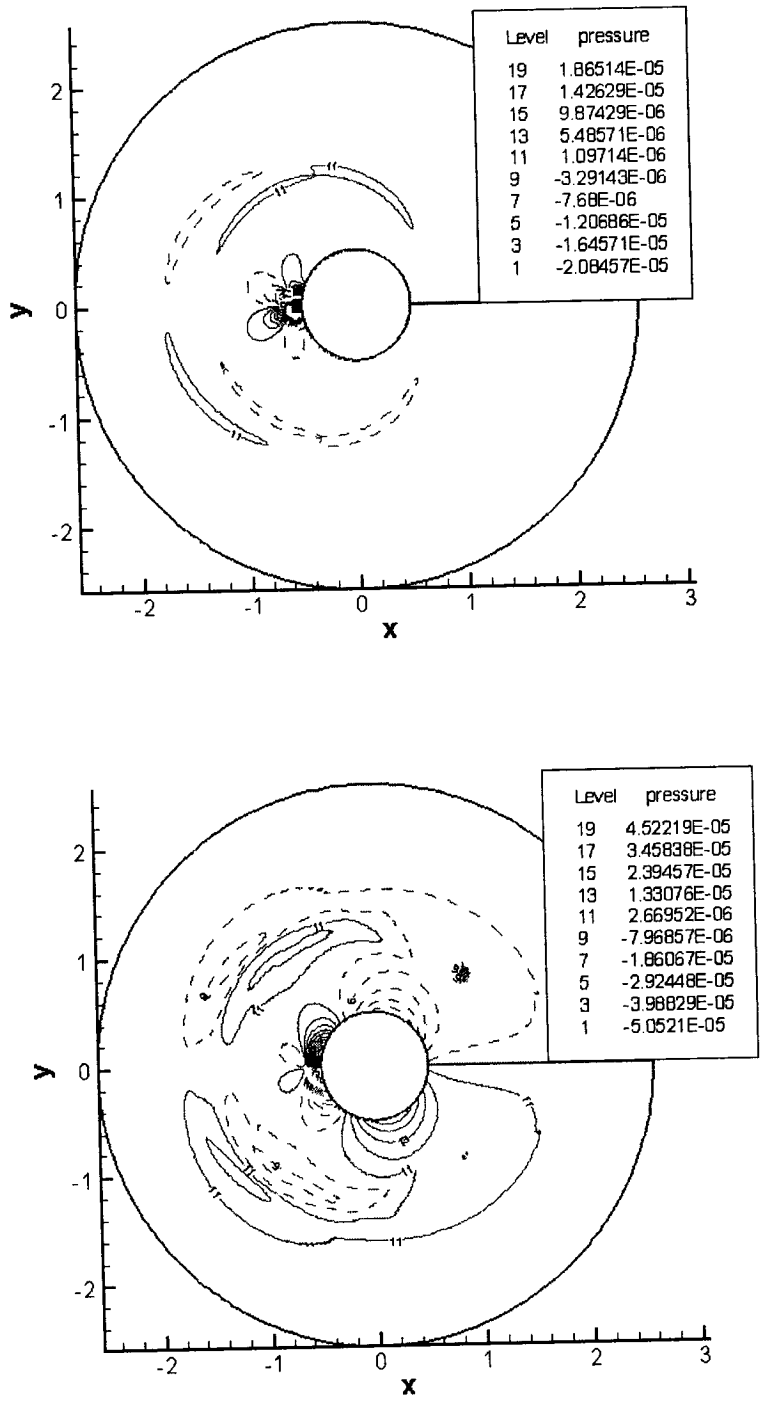

Figure 4-13 Distorting of the vortex in the flow around the cylinder at times $t = 0.4$, $t = 0.8$, and $t = 1.2$: (a) the Taylor's vortex, (b) the Vatistas's vortex.

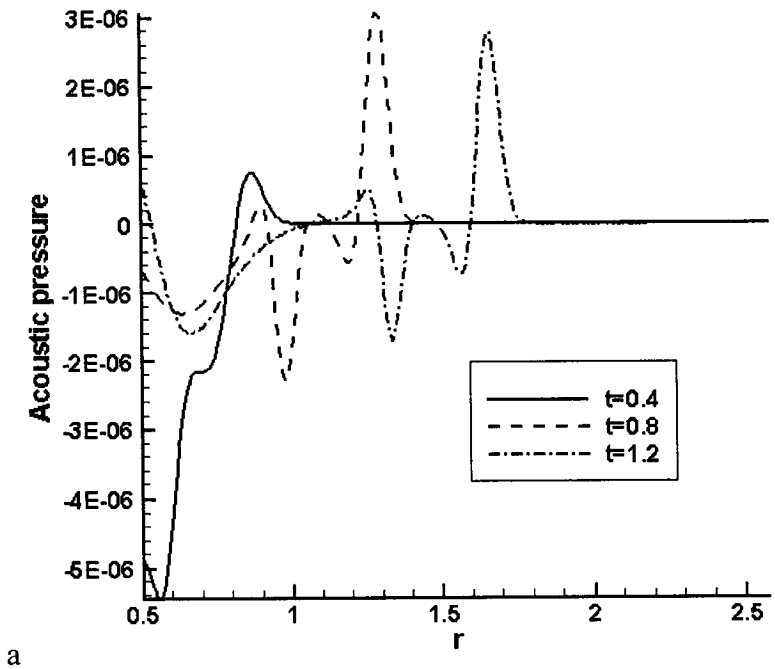

a

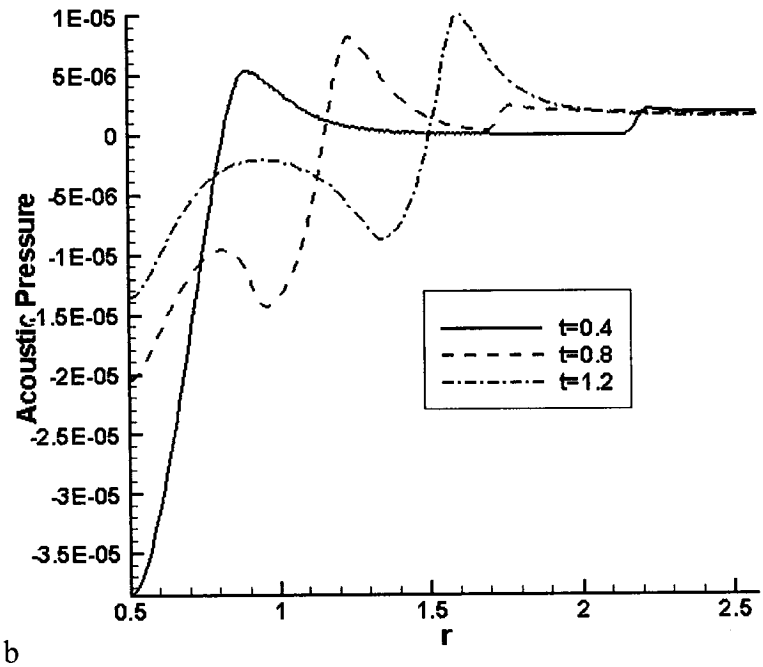

b

Figure 4-14 R adial distribution of the sound pressure for a single vortex disturbance propagation in the mean flow around the cylinder: (a) the Taylor's vortex, $\theta = 145°$ and , (b) the Vatistas's model $\theta = 135°$.

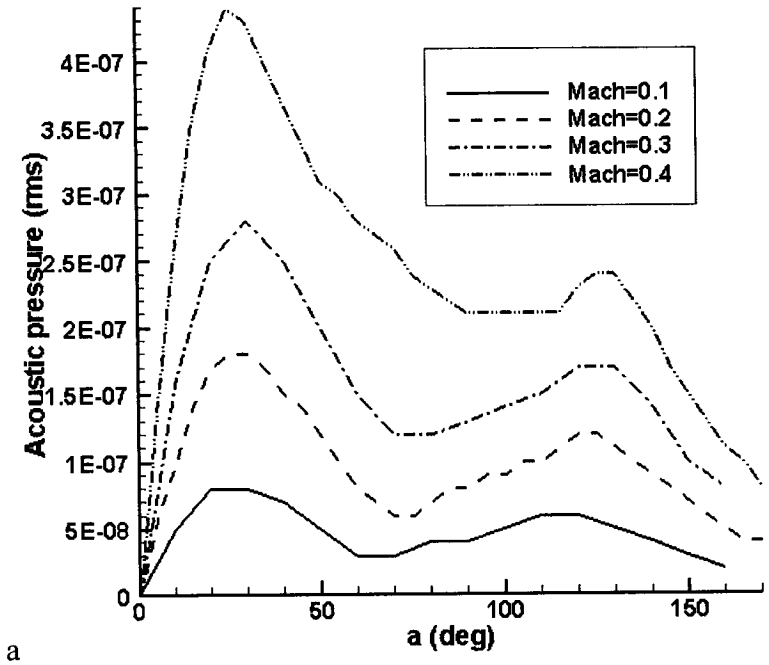

a

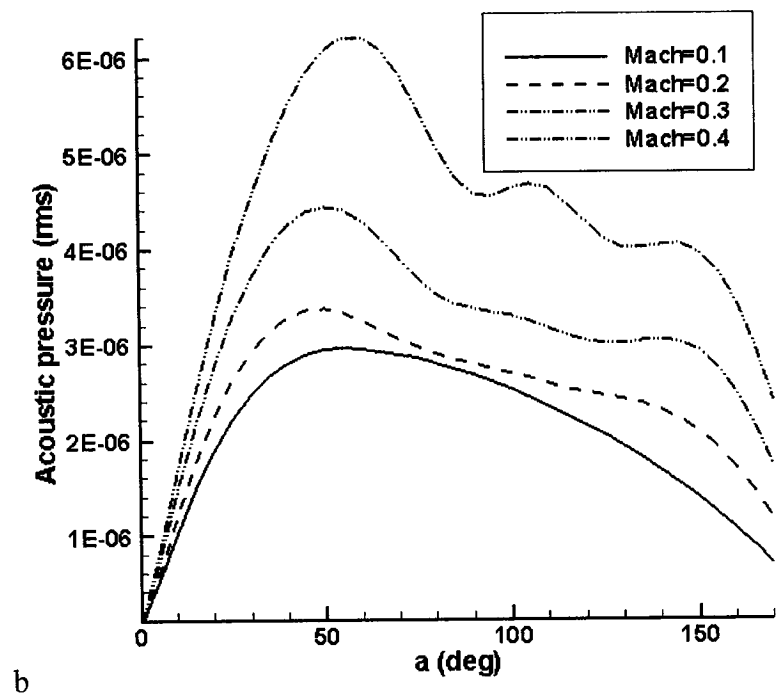

b

Figure 4-15 The RMS of acoustic pressure for the mean flow with $M_\infty = 0.1,0.2,0.3,0.4$: (a) the Taylor's vortex and, (b) the Vatistas's vortex . Angle α is measured from the negative x axis.

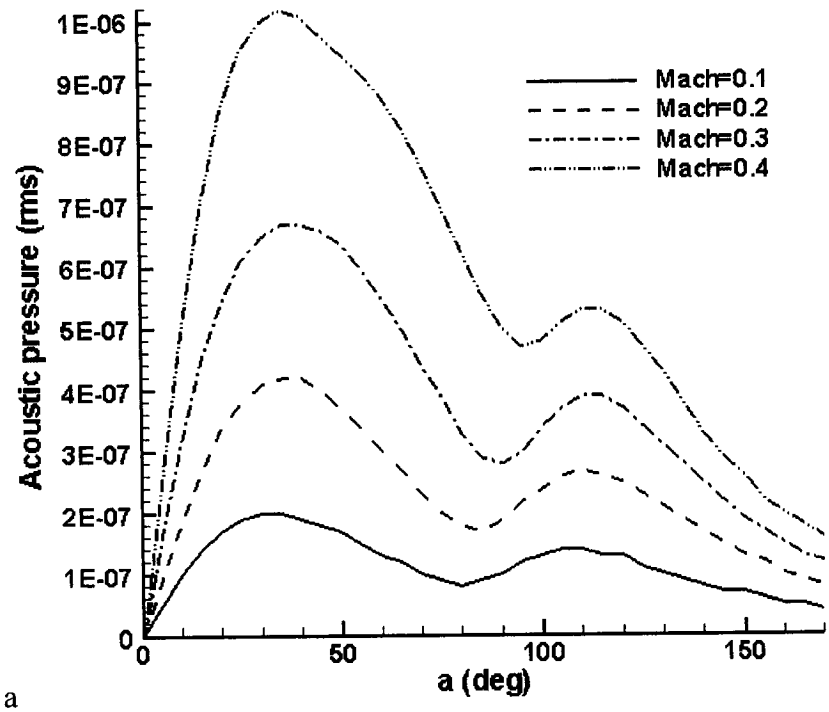

a

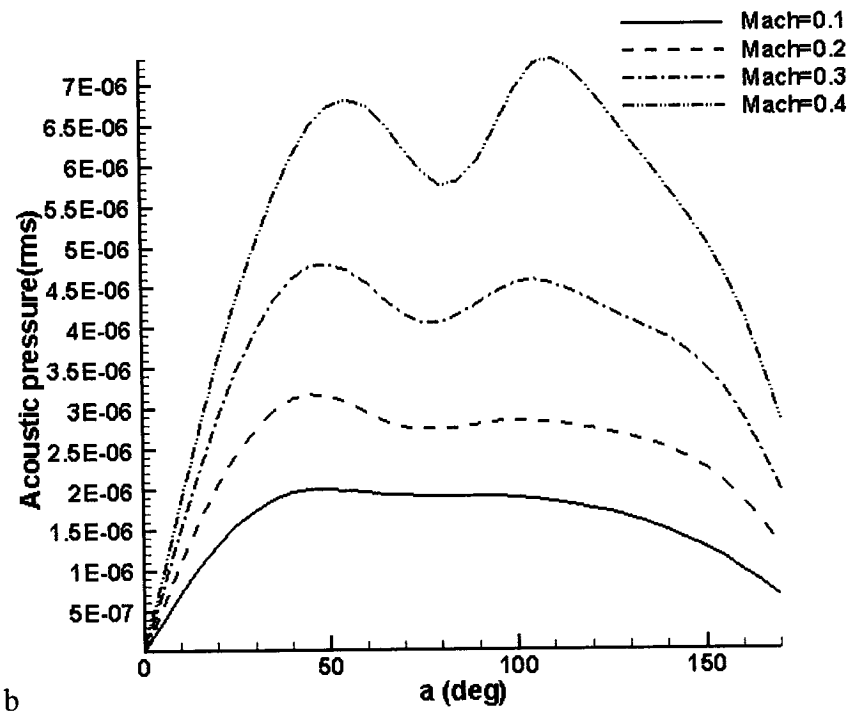

b

Figure 4-16 The RMS of acoustic pressure for the initial vortex location at $(-0.75,0)$,

Notation is the same as in Fig. 4.15.

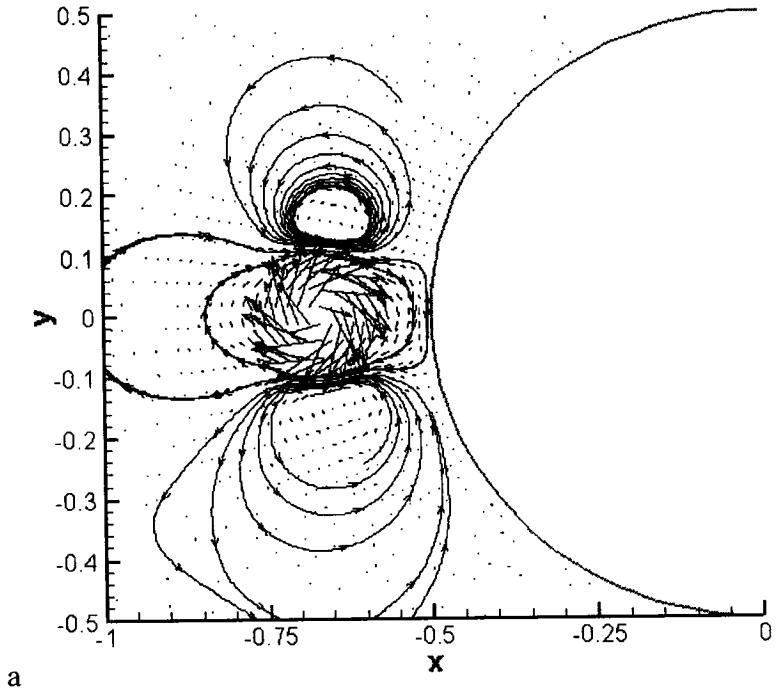

a

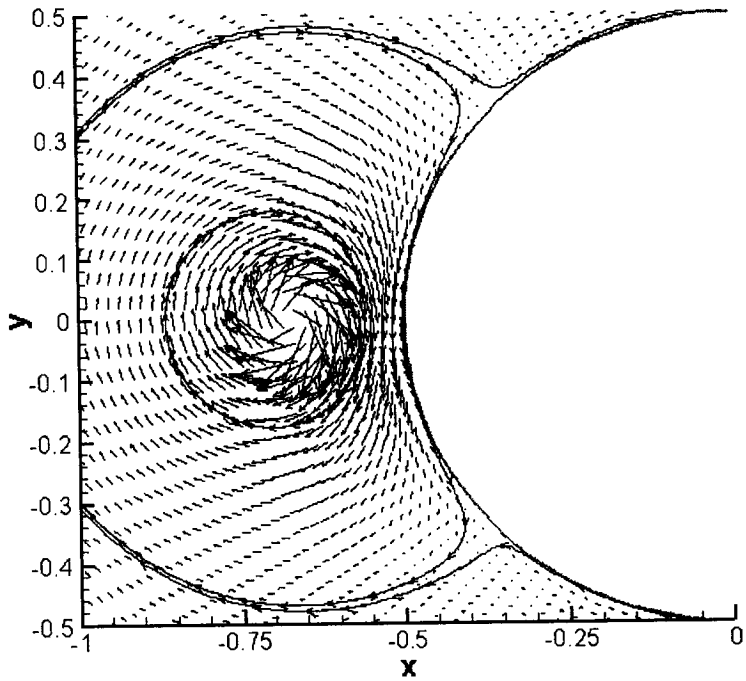

b

Figure 4-17 Acoustic disturbance velocity field at $t = 0.8$: (a) the Taylor's vortex, (b) the Vatistas's vortex.

$t = 0.4$

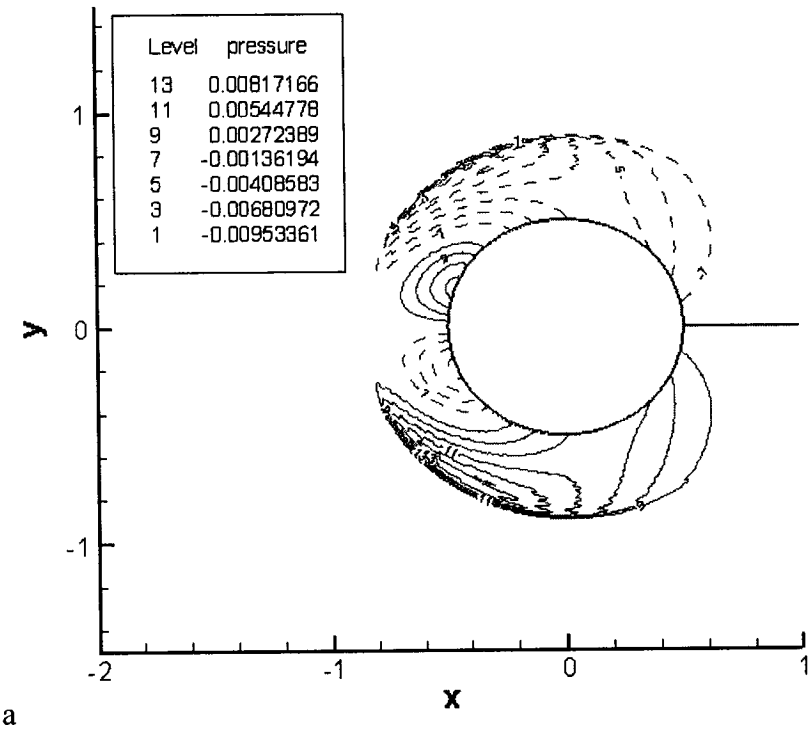
Level pressure
13 0.00817166
11 0.00544778
9 0.00272389
7 -0.00136194
5 -0.00408583
3 -0.00680972
1 -0.00953361
1
0
-1
y
-2
-1
0
1
x

a

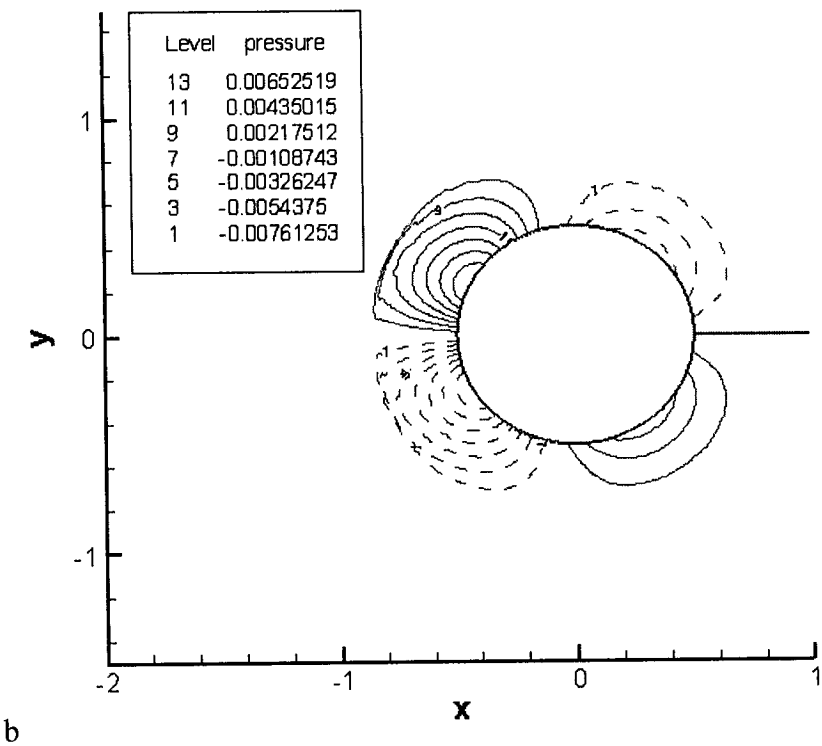
Level pressure
13 0.00652519
11 0.00435015
9 0.00217512
7 -0.00108743
5 -0.00326247
3 -0.0054375
1 -0.00761253
1
0
-1
y
-2
-1
0
1
x

b

$t = 0.8$

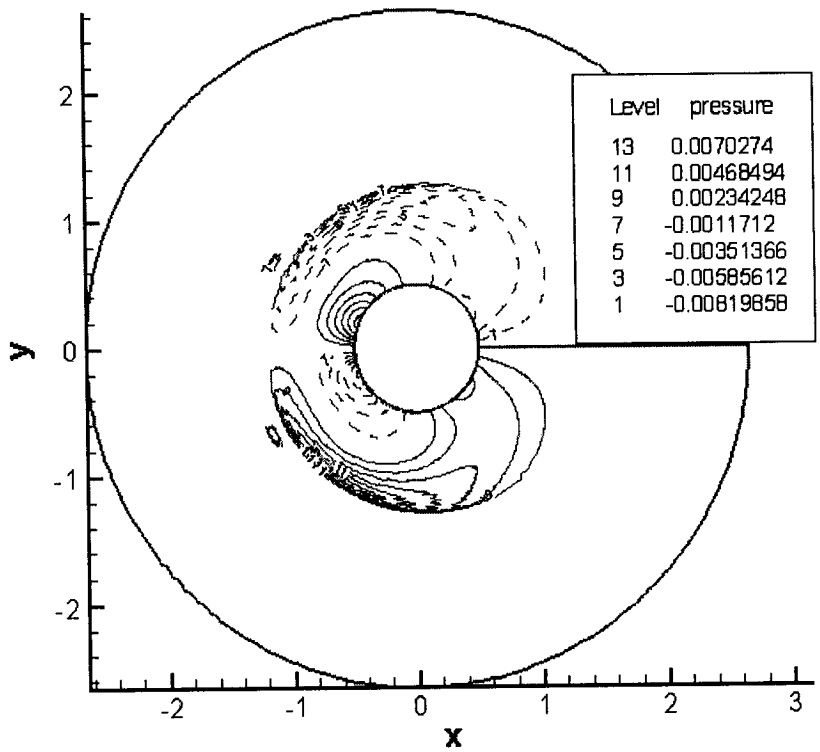
Level pressure
13 0.0070274
11 0.00468494
9 0.00234248
7 -0.0011712
5 -0.00351366
3 -0.00585612
1 -0.00819858
y
x
2
1
0
-1
-2
-2
-1
0
1
2
3

a

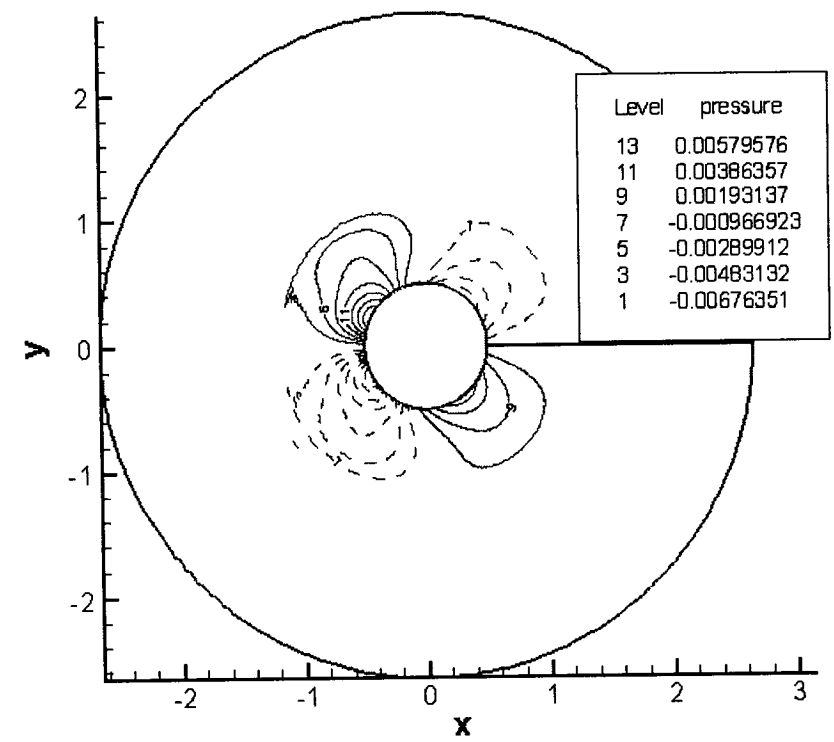
Level pressure
13 0.00579576
11 0.00386357
9 0.00193137
7 -0.000966923
5 -0.00289912
3 -0.00483132
1 -0.00676351
y
x
2
1
0
-1
-2
-2
-1
0
1
2
3

b

$t = 1.2$

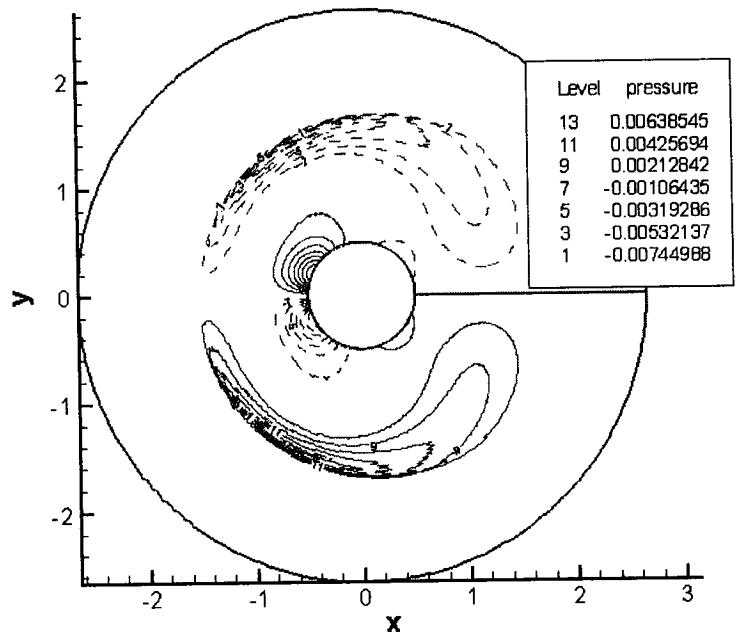

a

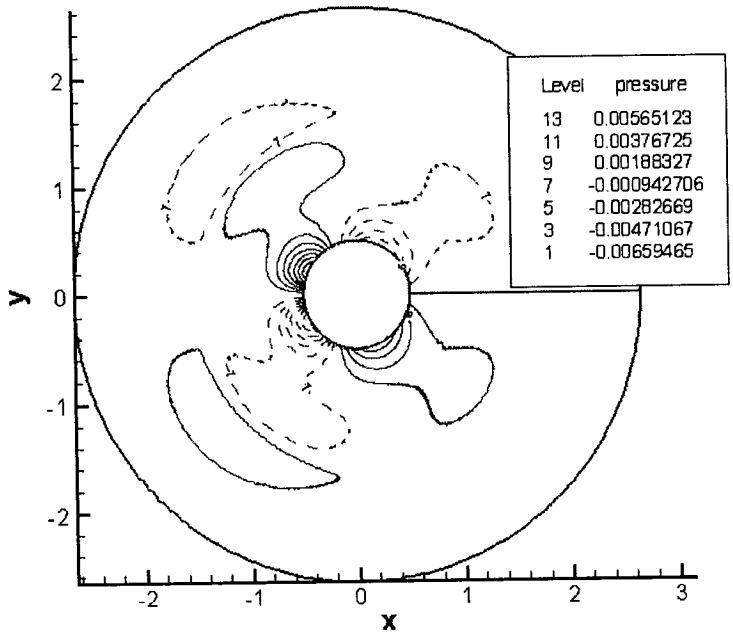

b

Figure 4-18 Distorting of the large core vortex in the mean flow around the cylinder at times $t = 0.4$, $t = 0.8$, and $t = 1.2$. (a) the Taylor's vortex, (b) the Vatistas's vortex.

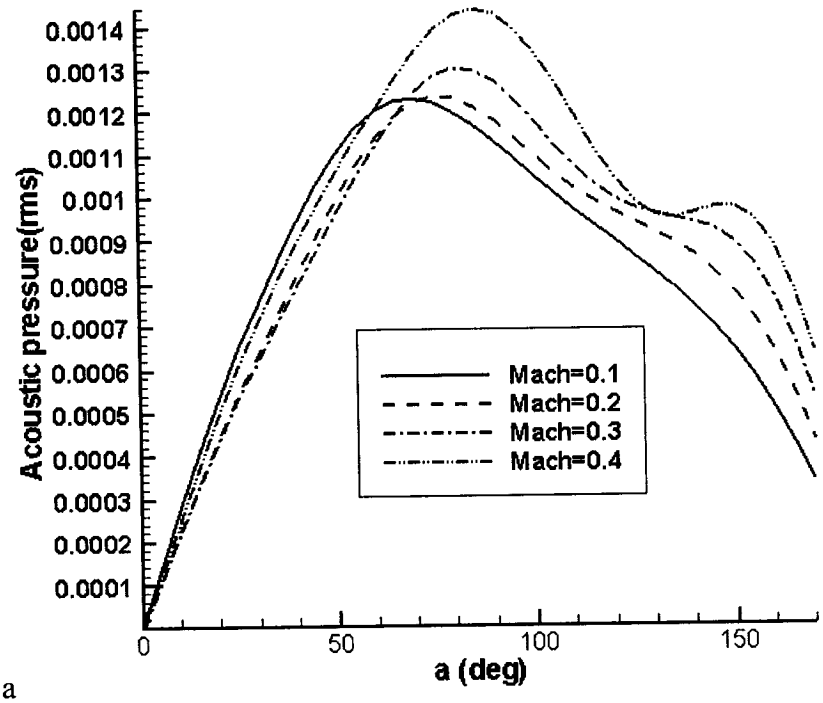

a

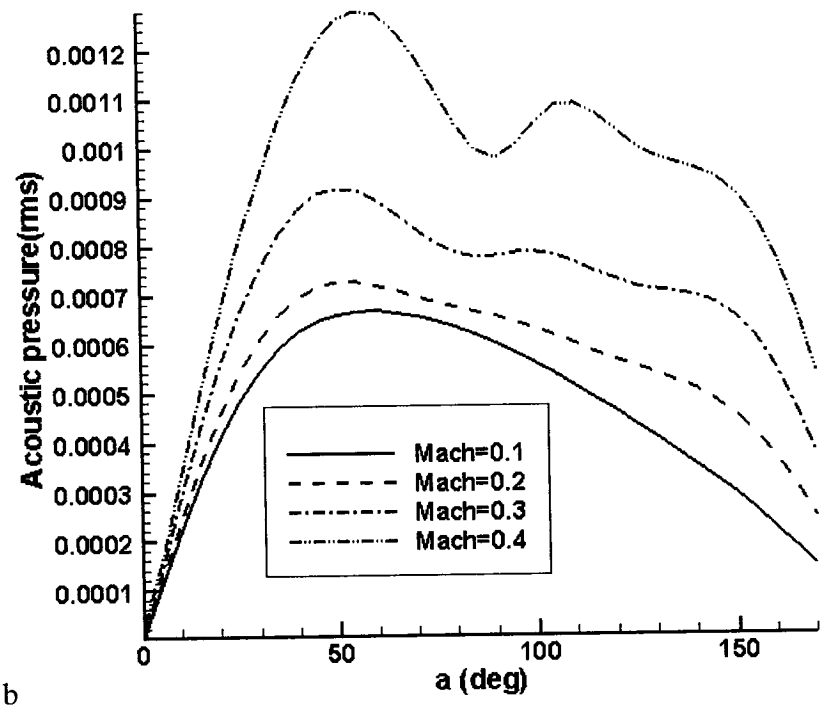

b

Figure 4-19 The RMS of acoustic pressure for the large vortex ($R_c = 0.25$) for a mean flow with $M_\infty = 0.1,...,0.4$: (a) the Taylor's vortex, (b) the Vatistas's vortex.

$t = 0.4$

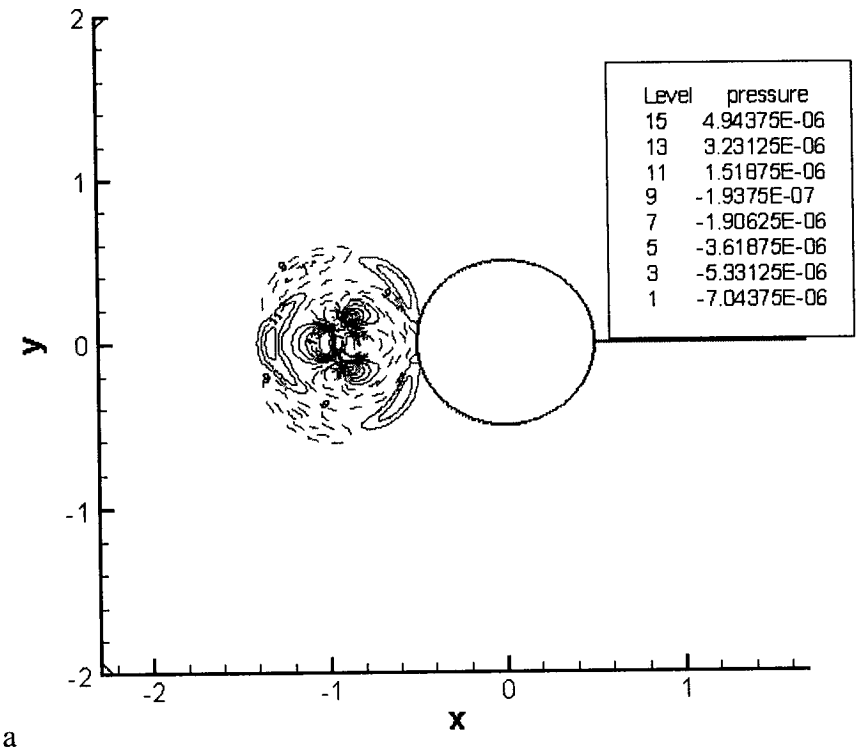
Level pressure
15 4.94375E-06
13 3.23125E-06
11 1.51875E-06
9 -1.9375E-07
7 -1.90625E-06
5 -3.61875E-06
3 -5.33125E-06
1 -7.04375E-06
2
1
0
-1
-2
y
-2
-1
0
1
x

a

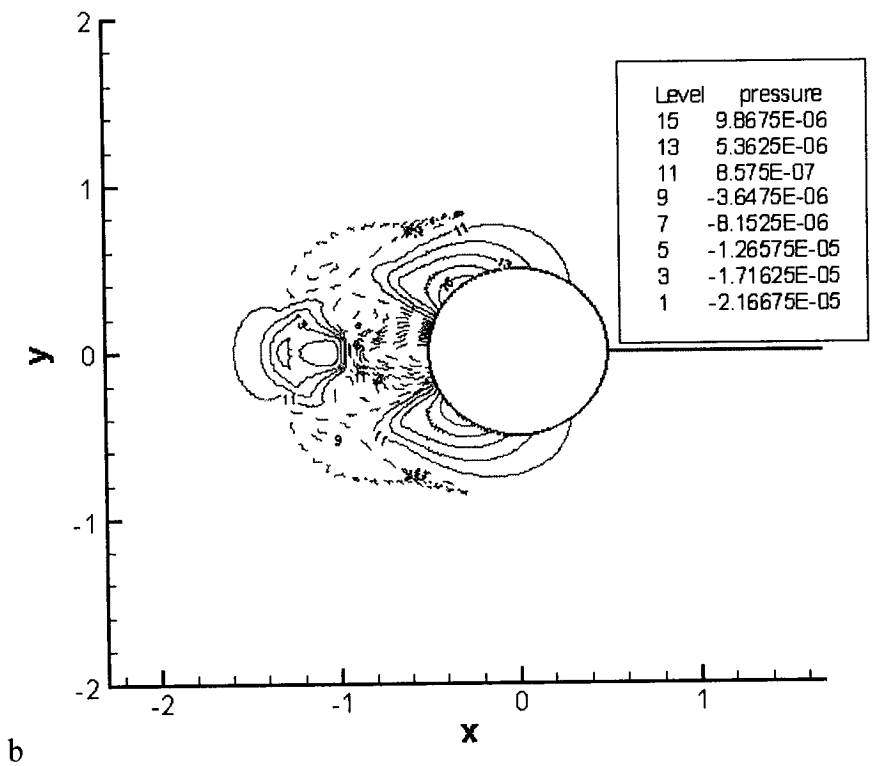
Level pressure
15 9.8675E-06
13 5.3625E-06
11 8.575E-07
9 -3.6475E-06
7 -8.1525E-06
5 -1.26575E-05
3 -1.71625E-05
1 -2.16675E-05
2
1
0
-1
-2
y
-2
-1
0
1
x

b

$t = 0.8$

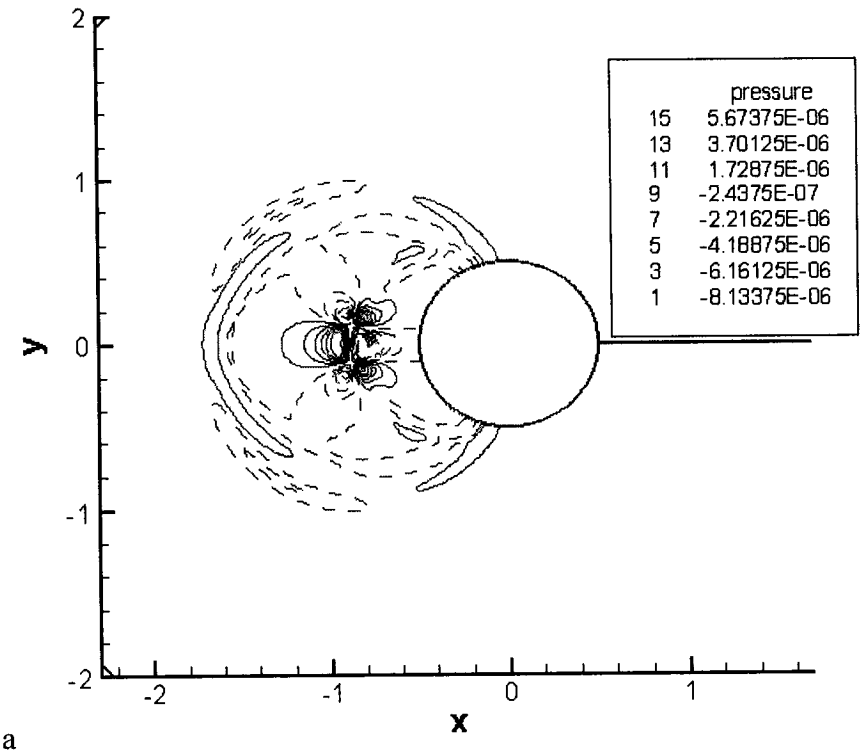
pressure
15 5.67375E-06
13 3.70125E-06
11 1.72875E-06
9 -2.4375E-07
7 -2.21625E-06
5 -4.18875E-06
3 -6.16125E-06
1 -8.13375E-06
2
1
0
-1
-2
y
-2
-1
0
1
x

a

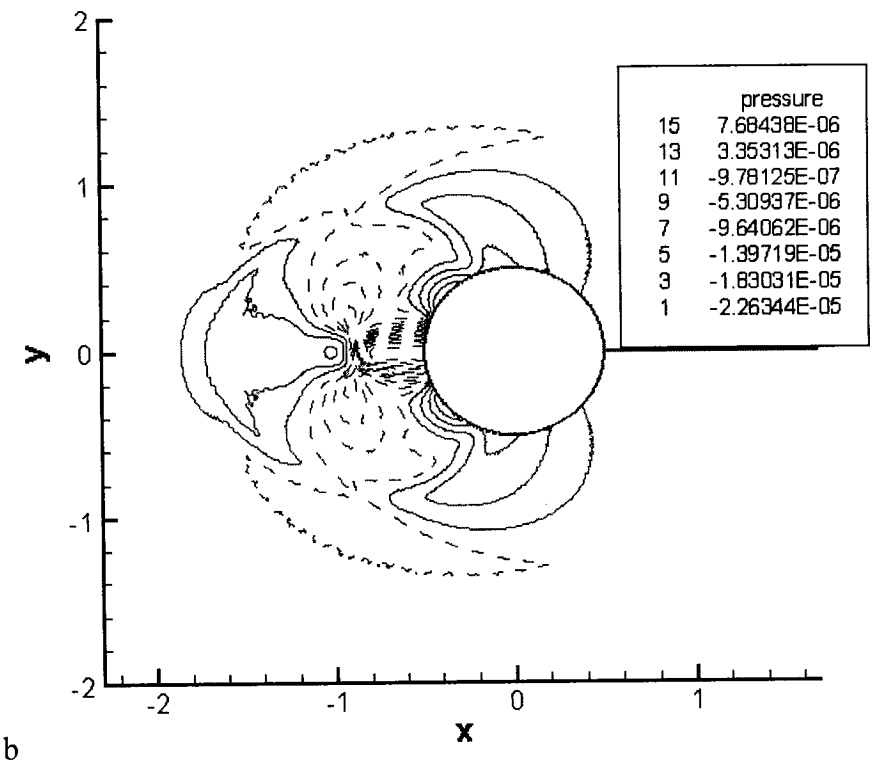
pressure
15 7.68438E-06
13 3.35313E-06
11 -9.78125E-07
9 -5.30937E-06
7 -9.64062E-06
5 -1.39719E-05
3 -1.83031E-05
1 -2.26344E-05
2
1
0
-1
-2
y
-2
-1
0
1
x

b

$t = 1.2$

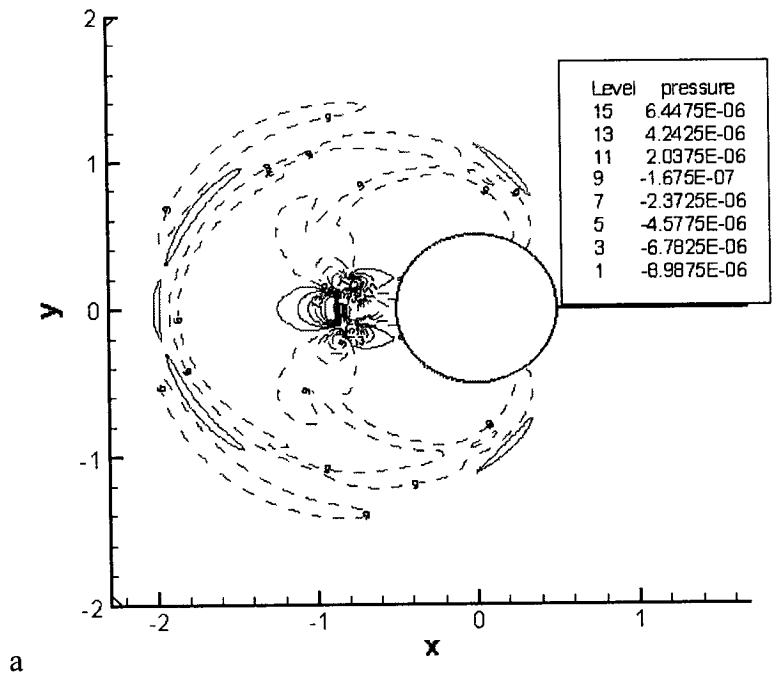

a

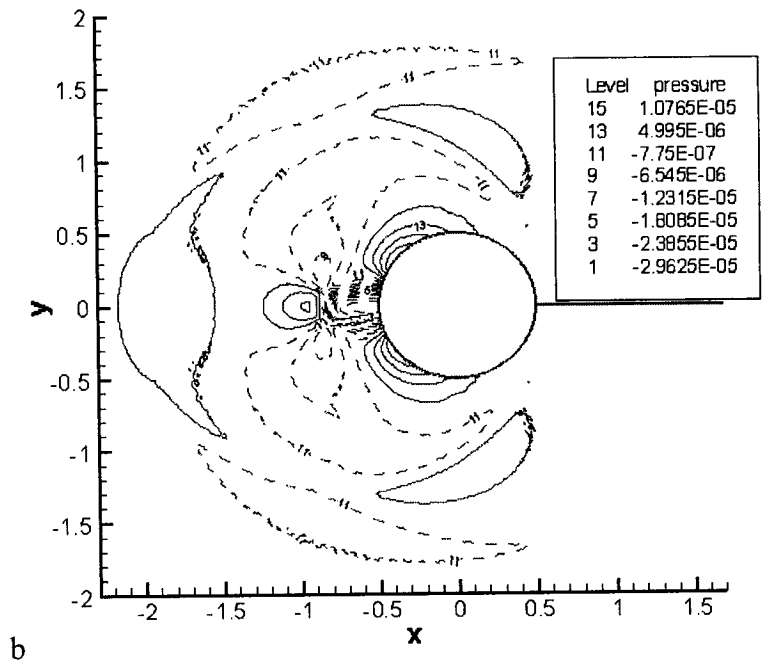

b

Figure 4-20 Distorting of the small vortex dipole in the mean flow around the cylinder at times $t = 0.4$, $t = 0.8$, and $t = 1.2$. (a) the Taylor's vortex, (b) the Vatistas's vortex.

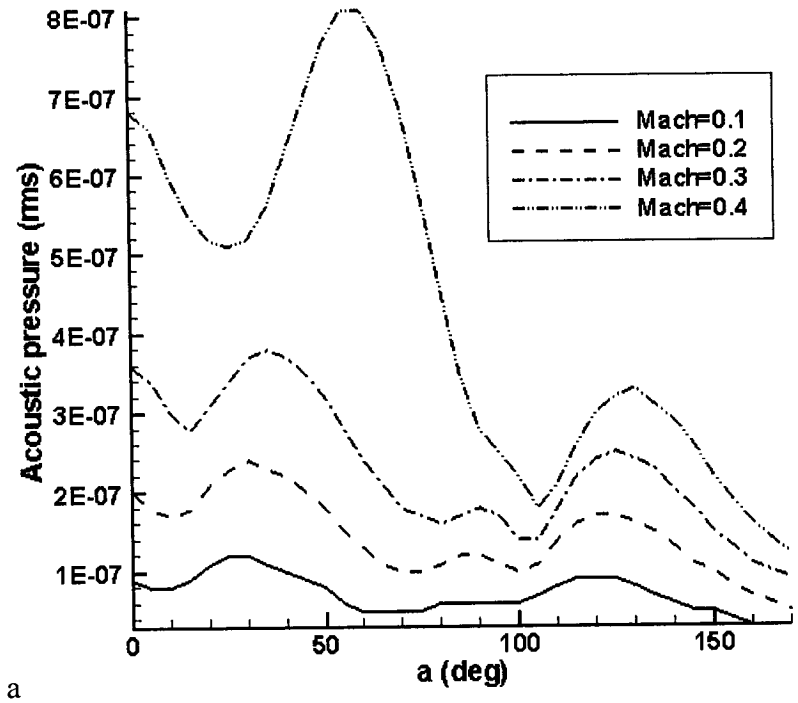

a

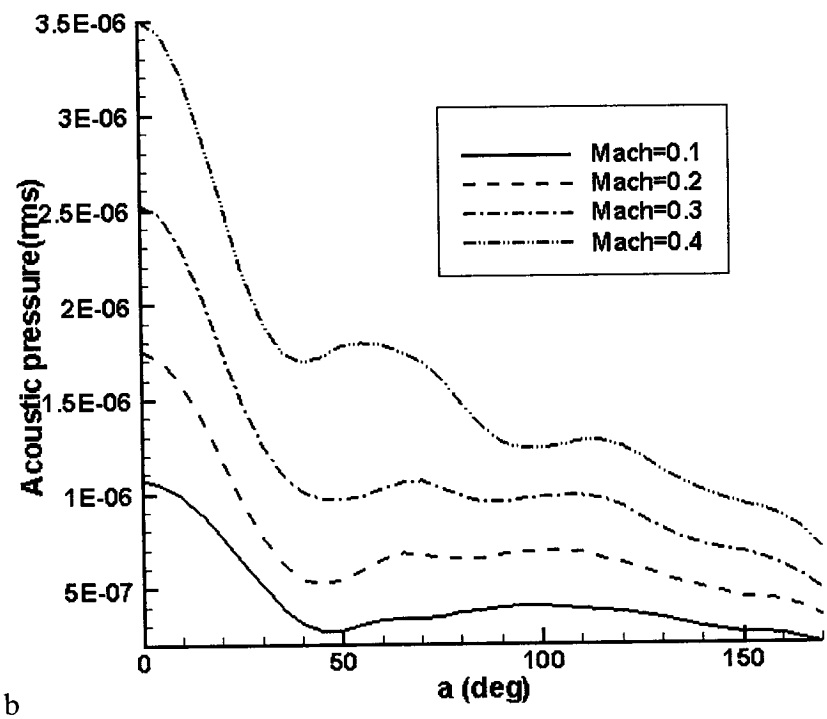

b

Figure 4-21 The RMS of acoustic pressure for a small vortex dipole for a mean flow with $M_\infty = 0.1,...,0.4$: (a) the Taylor's vortex, (b) the Vatistas's vortex.

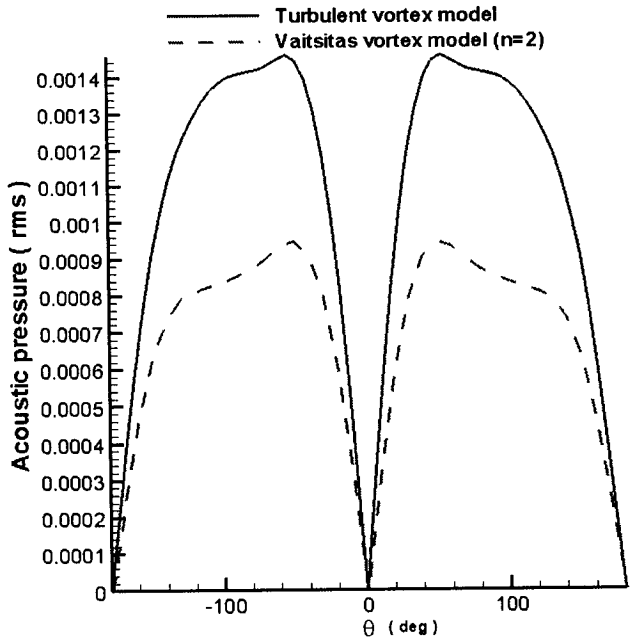

Figure 4-22 The RMS of acoustic pressure distribution on cylinder surface with respect to angle θ.

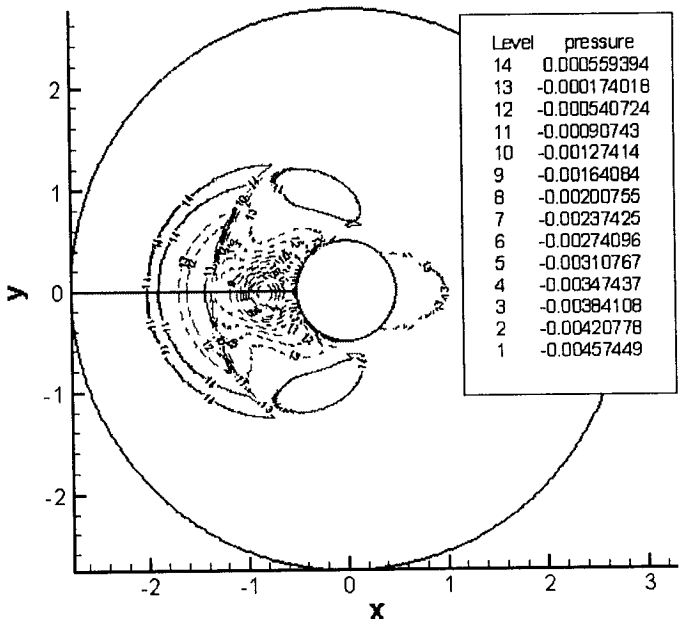

Figure 4-23 Sound pressure contributed by non-linear terms at $t = 1.0$. The Solid line denotes positive acoustic pressure; the dotted line denotes negative pressure.

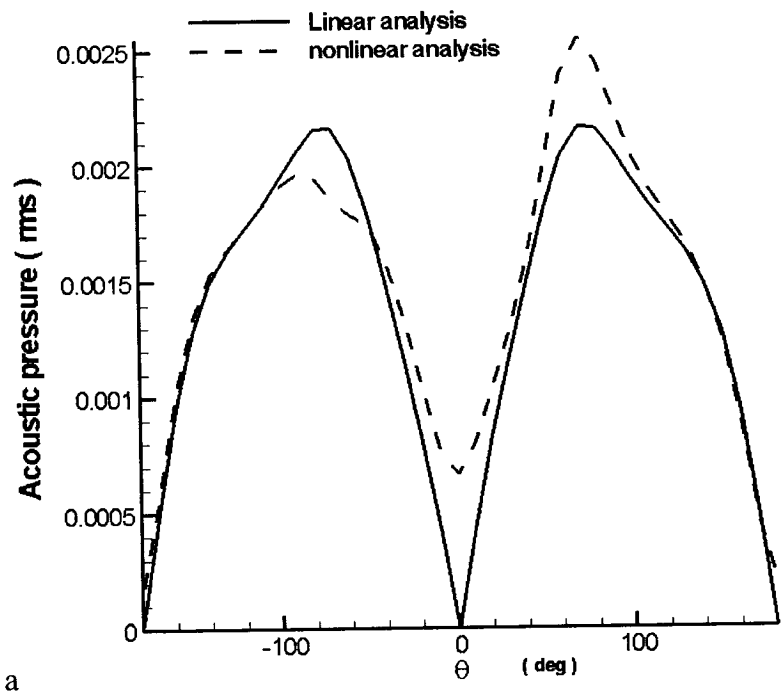

a

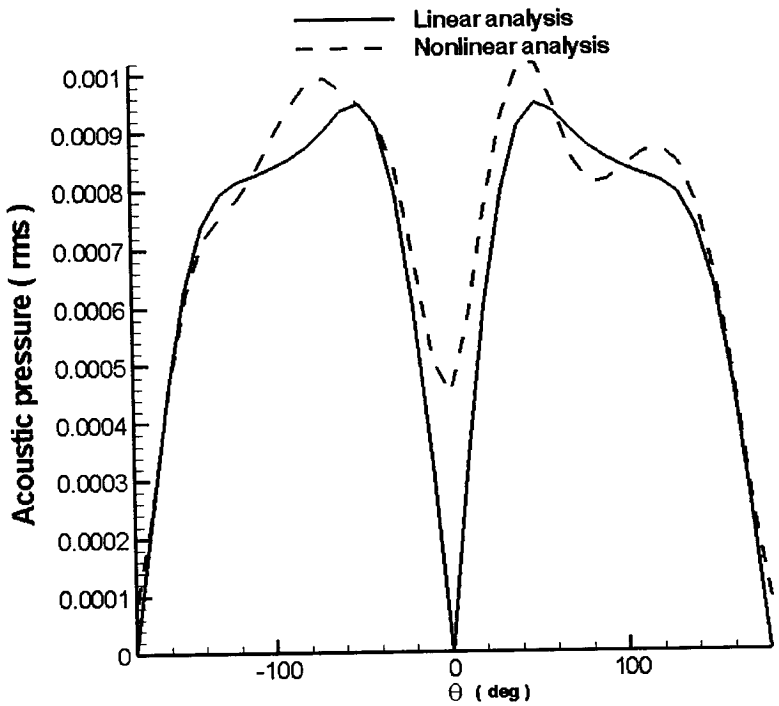

Figure 4-24 The root mean square acoustic pressure distribution $R_c = 0.25, V_{\max} = 0.2$.

(a) the Taylor's vortex , (b) the Vatistas's vortex.

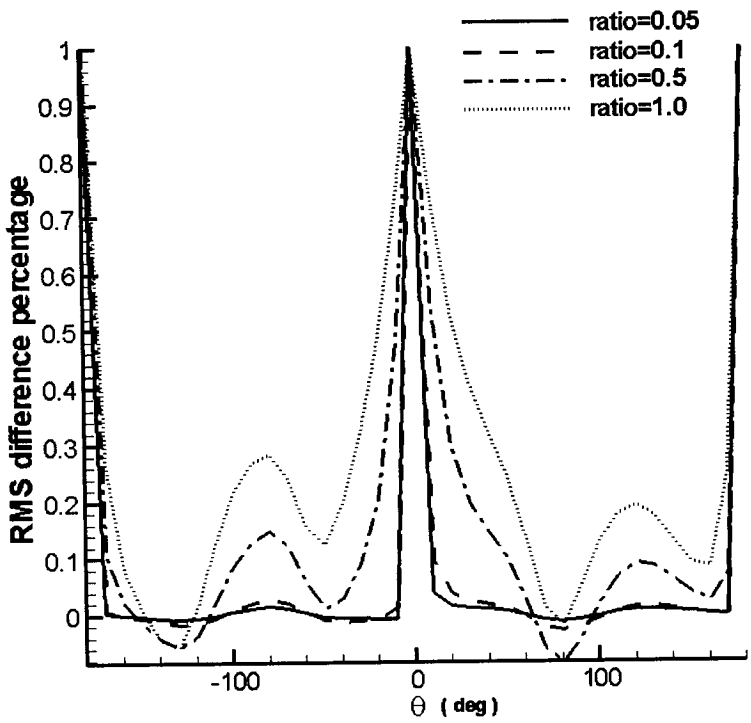

Figure 4-25 The difference in pressure RMS between the linearized and non-linear Euler equations.

Chapter V

Vortex Street Impingement on a Non-Rotating Cylinder

Vortex-body interactions are important in the areas of flow-induced vibration and sound generation. Among the several types of vortex body interactions, the case of a body in the wake of another body is of fundamental importance. Examples include, tip vortices shed by helicopter rotor blades and interacting with the following blade, rotor blades passing through the wakes of stator blades in turbomachinery, tubes in the wakes of upstream tubes in a heat exchanger bank, and a flap in a multi-element airfoil in the wake of the main airfoil (Gursul & D. Rockwall, 1990).

To expand the previous research about noise generated by a single vortex-cylinder interaction, the influence of a vortex street on a cylinder was investigated. The goal of the study was to find out how vortices are deformed in the mean flow about the cylinder. The differences between the sound generation by periodic vortices and a single vortex, what differentiates the sound radiated by the Taylor vortex street from the sound radiated by the Vatistas vortex ($n = 2$) street, as well as how the sound directivity and strength profile can be affected by the vortex street frequency, strength and size, were of prime

concern. The frequency of vortex appearance in the street, the distance between vortices, the vortex core size, the vortex strength, and the mean flow Mach number, were taken as parameters in numerical simulations, and their effect on the sound amplitude and directivity were evaluated.

5.1 Problem Setup

Figure 5.1 shows an overview of the vortex street-cylinder framework.

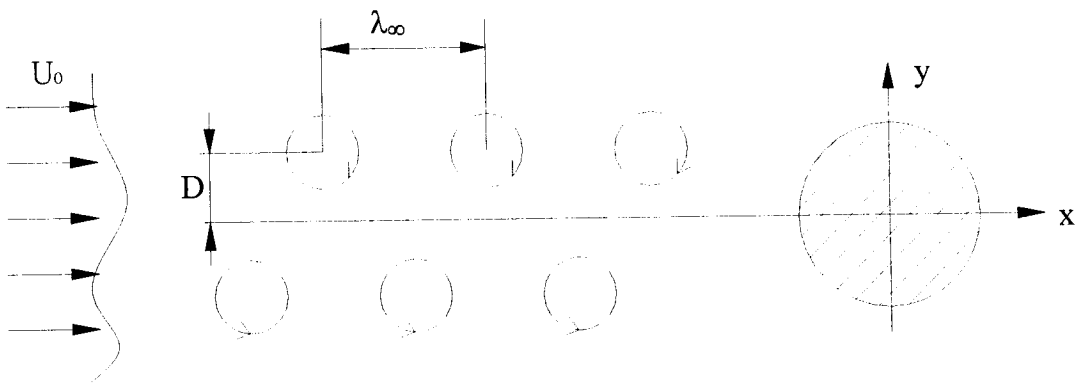

Figure 5-1 Sch eme of vortex street and cylinder interaction.

The vortex velocity is periodicly added to the background mean flow with the constant period T, and the vortices are convected by the mean flow about the 2-D cylinder. The vortex velocity which is equal to 0.00014 is very small compared to the background mean flow velocity (0.2). The vortices are periodicly superimposed on the flow at the axial location $(-1,\pm D)$, i.e., at a distance of one radius upstream of the cylinder surface where the local mean velocity is $U = 0.75U_\infty$. The vortices convect with

the mean flow, so the wavelength λ_∞ of the undisturbed vortex street is determined by $\lambda_\infty = 2TU_\infty$, where U_∞ represents the free stream velocity. According to Cursul (1990), in vortex dynamics research the vortex street flow-cylinder interactions can be classified based on the length scale of the flow as represented by λ_∞, which is reflected by the added vortex frequency in this study. The sound generation and propagation by the vortex street-cylinder interaction was categorized into two groups based on the vortex street frequency $1/T$ in this investigation. One group of typical frequency at $f = 1/0.5 = 2$, represents the 'low'-frequency vortex street; the other group of typical frequency at $f = 1/0.05 = 20$, represents the 'high-frequency' vortex street. In the earlier case λ_∞ is bigger than the distance between two neighboring vortex centers, while in the latter case λ_∞ is smaller than the distance between two neighboring vortex centers.

The time averaged root-mean-square (RMS) of acoustic pressure, which is a standard indication of sound strength and sound directivity, is defined as:

$$p_{rms} = \sqrt{\int_{T_1}^{T_2} p^2(t)dt/T} \tag{63}$$

Local-in-space averaged acoustic pressure is defined as:

$$P_{ave} = \int_{T_1}^{T_2} p^2(t)dt \Big/ T \tag{64}$$

Where $p(t)$ is the instantaneous acoustic pressure and T is the time period of integration $T = T_2 - T_1$. To guarantee that the periodicity is established, the integration

time was taken from $T_1 = 5.0$, to $T_2 = 10.0$

In the investigation a non-zero averaged acoustic pressure was observed. Humans respond to fluctuations of acoustic pressure (which may be named "clean" RMS of acoustic pressure), as opposed to the elevated averaged value of RMS acoustic pressure. To obtain the clean RMS of acoustic pressure, the average acoustic pressure is needed to subtract from the local RMS acoustic pressure.

We have:

$$P_{rms}^2 = (P_{ave} + P_{acous})^2$$

$$P_{rms}^2 = P_{ave}^2 + 2P_{ave}P_{acous} + P_{acous}^2 \qquad (65)$$

$$\text{if } P_{ave} = 0, \quad P_{acous} = P_{rms} \qquad (66)$$

If $P_{ave} \neq 0$, due to the integration $\int_{T_1}^{T_2} P_{acous} dt \Big/ T$ gives zero, so finally we have:

$$P_{acous} = \sqrt{P_{rms}^2 - P_{ave}^2} \qquad (67)$$

In the following investigation P_{acous} instead of P_{rms} will be presented.

5.2 Boundary Conditions

The computational domain (see Fig. 4.2a) is the same as the one for the single vortex impingement on cylinders discussed in Chapter 4. This study used the vortex

image system (Duncan et al., 1970), in which an equal and oppositely spinning vortex was put at the inverse point inside the cylinder and an equal vortex was placed at the origin to satisfy the non-penetrating boundary condition (see Fig. 4.3). The vortex image system was switched-on at any moment when the vortex was added. For the rest of the time, the non-penetrating boundary condition is satisfied by $dp/dn = 0, dv/dn = 0$. The artificial boundary condition, which was verified in chapter 4, was implemented in this study.

5.3 Computational Results

The free-stream velocity, U_∞, if not specified otherwise, was kept equal to a constant of value 0.2, i.e. the Mach number in the far-field was equal to 0.2 in this investigation. Small vortices were considered with core size equal to 0.04, and a circulation of 0.00005.

When the vortex is convected by the flow near the rigid surface of the cylinder, the vortex is strongly distorted by the non-uniform stagnation flow (see Fig. 5.2). As a result of its deformation, the pressure field becomes non-circular, producing four pressure spots of alternating sign amplitude (quadrupole). As the vortex deformation continues, these spots elongate and generate pressure waves (see Fig. 4.4). It is shown in Fig. 5.2, that the embedded vortices are distorted in the streamwise direction in such a way that their shape becomes elliptical, and the longer axis of the elliptical shape becomes parallel to the flow centerline. This effect was also observed for a single vortex interaction with a cylinder.

For the high-frequency case, the vortices are merged and the longer axes of the ellipse become more inclined to the centerline. For the low-frequency case, the vortices keep their independence and it is clear that each vortex is distorted. The extent of distortion is decided by the vortex's location in the mean flow. For the Taylor vortex street, two counter rotating vortices were observed, but this was not the case for the Vatistas vortex street.

First, the single small vortex street of alternating signs was investigated. This is the limit case of a two-row vortex street when the distance between the rows tends to zero. In Fig. 5.3 the acoustic pressure isolines, generated by the vortex street at frequency 1/0.05 and 1/0.5, are presented at time $t = 10.0$. Silence zones near the centerline were observed for all cases. Strong sound pressure propagating downstream was found for the Taylor vortex street; this was not found for its single vortex case. It is interesting to note that, although there are ten times more vortices involved in sound generation by a high-frequency vortex street at 1/0.05 compared with a vortex street at frequency 1/0.5 per the same time interval, the amplitude of sound wave radiated by the two different frequency vortex streets did not show such a large difference. For the Vatistas vortex street, the pressure amplitude corresponding to the high-frequency street is only about two times larger than the one corresponding to the low-frequency street. For the Taylor vortex street, the pressure amplitude is only one and a half times larger.

The P_{rms} and P_{acous} distribution are presented as a function of angle θ from the

centerline in Fig. 5.4. It was observed in this case that the P_{rms} is very close to P_{acous}; that is, the pressure build-up is small to negligible. The modest asymmetry of sound profile with respect to the centerline was observed because of the time delay of the opposite-spinning vortex couples for both vortex streets. The acoustic pressure profile generated by the low-frequency vortex street (frequency = 2), appears to be quite different from that generated by the high-frequency vortex street (frequency = 20). For the low-frequency Vatistas vortex street, the RMS of acoustic pressure has two clear pikes, and the sound directivity forms an angle of 45° to the centerline. For the high frequency Vatistas vortex street, the sound profile becomes strongly non-monotonic with angle θ, although there is still obvious maximum amplitude at about 10° with the centerline. For the low-frequency Taylor vortex street, the sound profile turned out to be non-monotonic and had a larger zone of silence near the centerline.

The effect that the vortex street distance D have on sound generation and propagation was investigated by setting the distances equal to 0, 0.05, 0.1, 0.15 and 0.3, respectively. The value of P_{acous} are presented as a function of the angle θ in Fig. 5.5 For the Vatistas vortex street, as the distance between the rows of vortices increases, the asymmetry appears to be more noticeable (see Figs. 6a,b). The sound pressure on the upper half of the cylinder is larger than the sound pressure on the lower half of the cylinder (note that the maximum amplitude of acoustic RMS increases slightly with the distance). Nevertheless, the sound wave profile quantitatively looks the same for all

different distances at the same vortex street frequency. The sound directivity is almost invariant with the vortex street distance. In other words, there is no difference for the cylinder-vortex interaction mechanism and the sound wave produced by Vatistas vortex row at different distances. However, for the low-frequency Taylor vortex street, it appears that when the vortex street distance was increased to 0.05 from zero, a non-silence zone near the centerline was observed. The change of the vortex street distance did not bring about a large change in sound amplitude, although the sound directivity was shifted. It is justified to say that the vortex row distance is one of the key coefficients for the cylinder-Taylor vortex interaction mechanism, as well as the sound pressure generation and propagation.

The generated sound wave and its directivity are closely related to the deformation of vortices and their angular position. The vortex street flowfield is shown for $D=0.1$ and $D=0.3$ in Figs. 5.6 and 5.7. It is worth noting that at the time moment t=10.0, vortices were found in the downstream. This indicates that after the vortex impingement on the cylinder, the vortex doesn't disappear, but rather it moves down the stream (this was also observed by Cursul (1991)). The flowfields of the Vaitistas vortex street and the Taylor vortex street turn out to display some very prominent differences. For the Vatistas vortex street, the original round vortical disturbance turns out to be a multi-cell vortex at low-frequency. Whereas the high-frequency vortex street forms a couple of one-cell deformed vortices from the merger of the oncoming vortices. Also, the vortices are more

widely distributed and the axis of the ellipse is more inclined to the centerline, at vortex street distance $D = 0.3$, compared to the case of vortex street distance $D = 0.1$. (Compare Figs. 5.6c,d with Figs. 5.6 a,b). In general, for the Vatistas vortex street, the vortices will be more deformed in cases of a larger distance between the vortices. For the Taylor vortex street, counter-rotating vortices were found near the front centerline for all cases. It is interesting to see that the two counter rotating vortices in the back cylinder appear outside the original vortex street, at a high frequency street whereas the counter-rotating vortices appear inside the original vortex street, at a low frequency street. Furthermore at low frequency the Taylor vortex street with a distance of $D = 0.3$, counter rotating vortices appear in between the original vortices when they move to up or down cylinders. For the Taylor vortex street with a high frequency street, there will be more deformation in cases with a larger distance between the vortices. However, for a low frequency street, the vortices will be less deformed and the axis of the ellipse will be less inclined to the centerline in cases of larger distances between the vortices.

In the following investigation the vortex street with distance $D = 0.1$, was taken as a representative case. In Fig. 5.8, P_{acous} is presented with respect to angle θ at different vortex street frequencies. For both the Vatistas vortex street and the Taylor vortex street, the sound pressure amplitude is observed to increase with frequency (see Fig. 5.8). This is because for each time unit more vortices are embedded in the mean flow and impinge into the cylinder surface.

For a low-frequency Vatistas vortex street, a distinct maximum sound directivity was observed. However, the sound directivity is different for each frequency and changes from 30° to 40° when the frequency varies from 1/1.00 to 1/0.5. For the high frequency Vatistas vortex street, the amplitude change with the frequency is quite moderate and the sound profile becomes non-monotonic. As the frequency rises, the sound profile becomes more non-monotonic. For the vortex street at high frequency, there is a well-defined maximum sound directivity at around 10° with the centerline (see Fig. 5.8a).

Silence zones are observed near the centerline for the low-frequency Taylor vortex street compared with the Vatistas vortex street, the sound pressure amplitude is almost ten times smaller (even though they are for the same vortex core size and vortex strength). Moreover, a prominent sound level in the back centerline of the cylinder is observed for the low frequency Taylor vortex street, as well the higher the frequency is, the higher the sound level in the back centerline of cylinder will be.

Next, the effect of the mean flow Mach number was investigated. It was observed that as the mean flow Mach number increases, the vortices become more deformed and appear closer to the cylinder surface. In turn, the RMS acoustic pressure will increase in amplitude and the RMS acoustic pressure pike will become much larger (see Fig. 5.9). For the low frequency Vatistas vortex street, as the Mach number of mean flow increases its sound directivity is shifted slightly toward the centerline. That is, the sound directivity

shifts from 10° for $M_\infty = 0.1$ to 70° for $M_\infty = 0.4$ (see Fig. 5.9b). For the high frequency Vatistas vortex street the mean flow Mach number has a moderate effect on the sound wave profile compared to the low-frequency vortex street (see Fig.5.9a). For the low frequency Taylor vortex street, the Mach number of mean flow greatly affects the sound pressure level. This means that the higher the Mach number, the higher the sound pressure will be (including the back centerline sound pressure). For the low-frequency Taylor vortex street, the sound directivity will shift from the centerline for $M_\infty = 0.1$ to 60° for $M_\infty = 0.4$ (see Fig 5.9c).

It has been found in the current study (see Fig. 5.10), that the RMS acoustic pressure strength is proportional to the vortex strength (circulation) for both the Vatistas vortex street and the Taylor vortex street. This means that, the RMS of acoustic pressure can be normalized by the vortex strength, and the normalized RMS curves collapse into the same curve. In other words, the RMS acoustic pressure amplitude is linearly proportional to the vortex strength. In Fig. 5.9 the vortex core size is equal to 0.04, and the vortex circulation equals to 0.001 and 0.0005, respectively.

The effect that the vortex core size has on the sound generation and propagation was investigated. The RMS of acoustic pressure corresponding to high-frequency and low-frequency vortex streets was presented using vortices of different core sizes for the Vatistas vortex street and the Taylor vortex street respectively. Each vortex was kept at the same vortex strength with 0.0005, but the vortex core size was set at 0.04, 0.10 and

0.20, respectively. It was observed that the variation of the vortex core size, had a totally different effect on the Vatistas vortex from the Taylor vortex. For the Vatistas vortex street, as the vortex core size increases, the amplitude of acoustic pressure RMS also slightly increased, although the sound directivity did not change with the vortex core size. In general, the variation of the vortex core size has a very modest effect on the Vatistas vortex. Therefore for the Taylor vortex street, the variation of the vortex core size not only changed the sound amplitude abruptly, but also changed the generated sound profile. In other words, a moderate increase of the vortex core size will greatly amplify the sound level even at the same vortex strength. Also the sound directivity will shift closer to the centerline with the increase of vortex core size. The above phenomenon is also observed from a single vortex impingement on the cylinder (Povitsky, Zheng & Vatistas, 2004)

5.4 Summary of Findings

The propagation of acoustic waves originating from self-similar periodic vortices deforming in the non-uniform flow were studied numerically using high-order compact finite differences approximation of Euler equations. The vortex streets were categorized as low-frequency vortex streets and high-frequency vortex streets. It was discovered that the interaction mechanism, and sound generation and propagation in a non-uniform flow, are totally different for the Taylor vortex street and Vatistas vortex street.

For the low-frequency vortex street, the original round vortical disturbance turned out to be multi-cell vortex, whereas the high-frequency vortex street formed a couple of

one-cell deformed vortices. Also, counter rotating vortices were found in the Taylor vortex street cylinder interaction, which greatly affected the sound profile generated by the Taylor vortex street. For the low-frequency Vatistas vortex street, the RMS of acoustic pressure had monotonic sound directivity, and the sound amplitude and directivity were greatly affected by the Mach number of the mean flow. For the high frequency Vatistas vortex street, the RMS of acoustic pressure became highly non-monotonic, and the Mach number of mean flow had a very moderate effect on its profile. For low-frequency Taylor vortex street, the RMS of acoustic pressure was monotonic, and the Mach number of mean flow greatly affected its sound amplitude and directivity.

It was found in all cases that the angular maximum of RMS of acoustic pressure was proportional to the vortex strength (circulation), i.e. the RMS of acoustic pressure can be normalized by the vortex strength, and the normalized RMS curves collapse into one single curve. The vortex core size and vortex street distance were found to have a minor effect on the acoustic pressure amplitude for the Vatistas vortex street. Nevertheless, the vortex core size and the distance between vortex rows, significantly affected the sound pressure profile, and sound directivity for the Taylor vortex street.

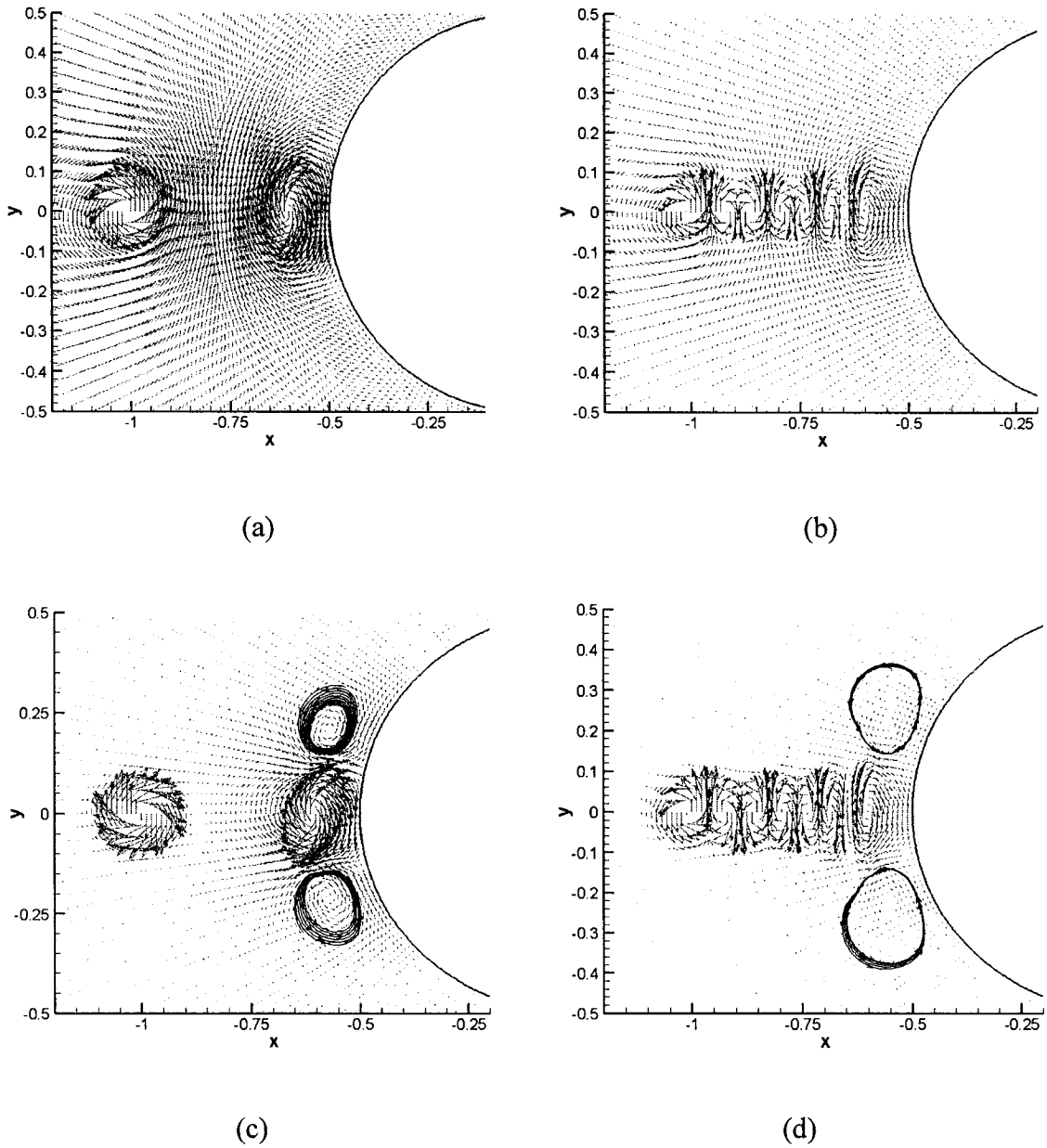

Figure 5-2 Vortex deformation in the background flow about the cylinder at (a, c) Vortex street at frequency 1/0.05, (b, d) Vortex street at frequency $f = 1/0.5$, (a, b) the Vatistas vortex street, (c, d) the Taylor vortex street.

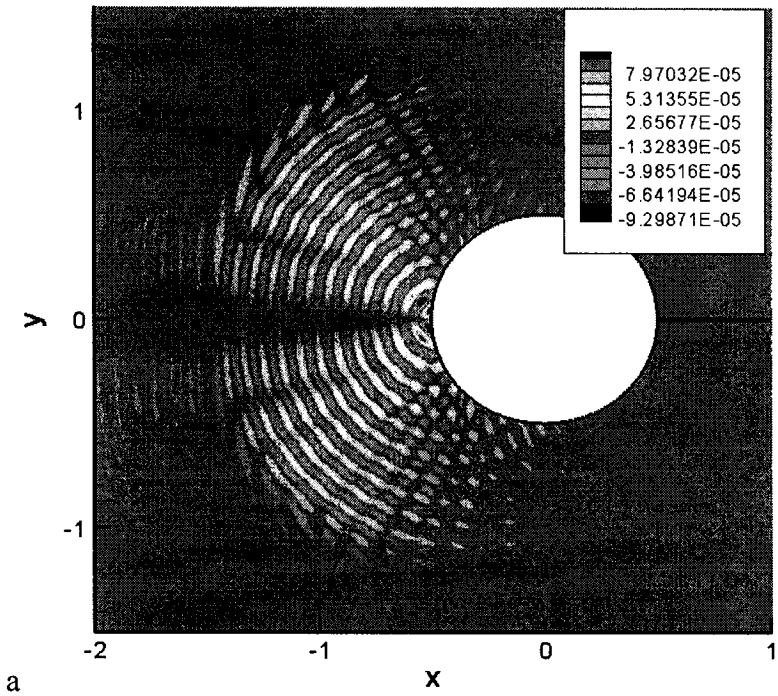

a

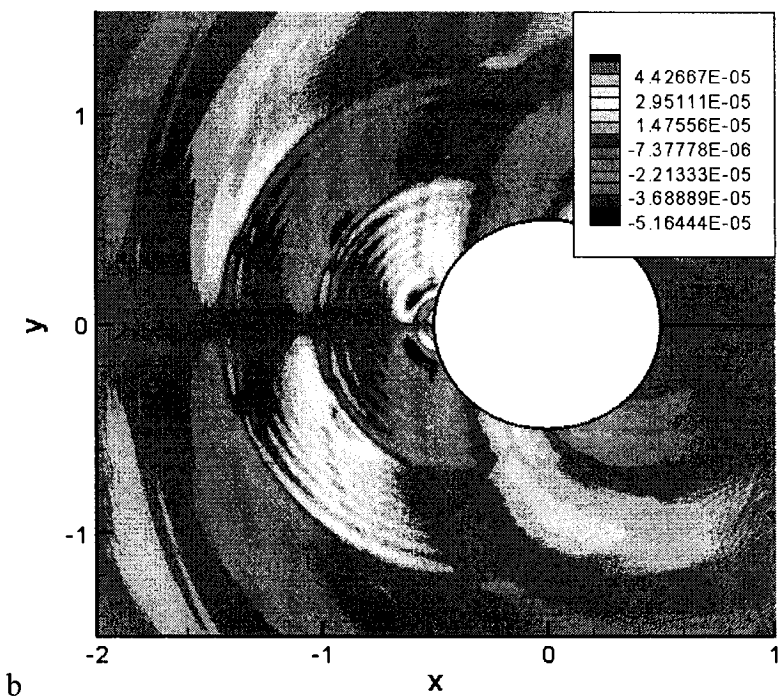

b

Figure 5-3 The pressure isoline generated by the Vatistas vortex street at different vortex adding frequency at time $t = 10$: (a) frequency 1/0.0.5, (b) frequency 1/0.5.

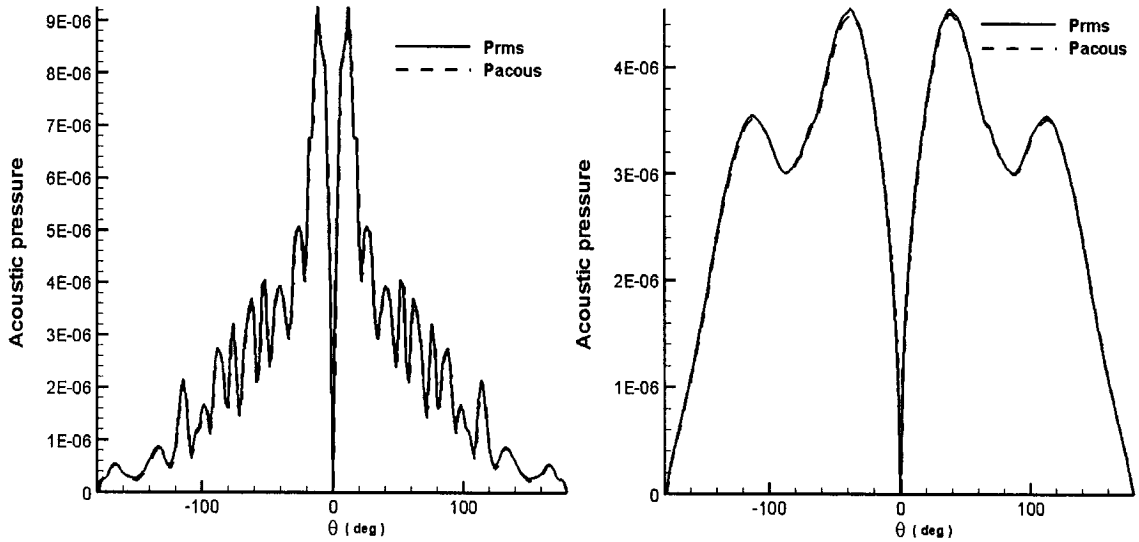

(a)

(b)

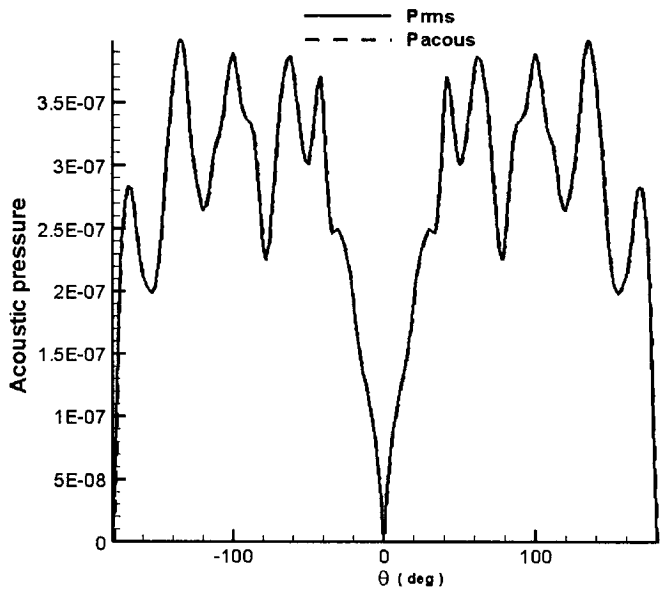

(c)

Figure 5-4 The RMS of acoustic pressure distribution for a single row vortex street: (a) Vatistas vortex street at frequency =1/0.05, (b) Vatistas vortex street at frequency =1/0.5, (c) Taylor vortex street at frequency=1/0.5.

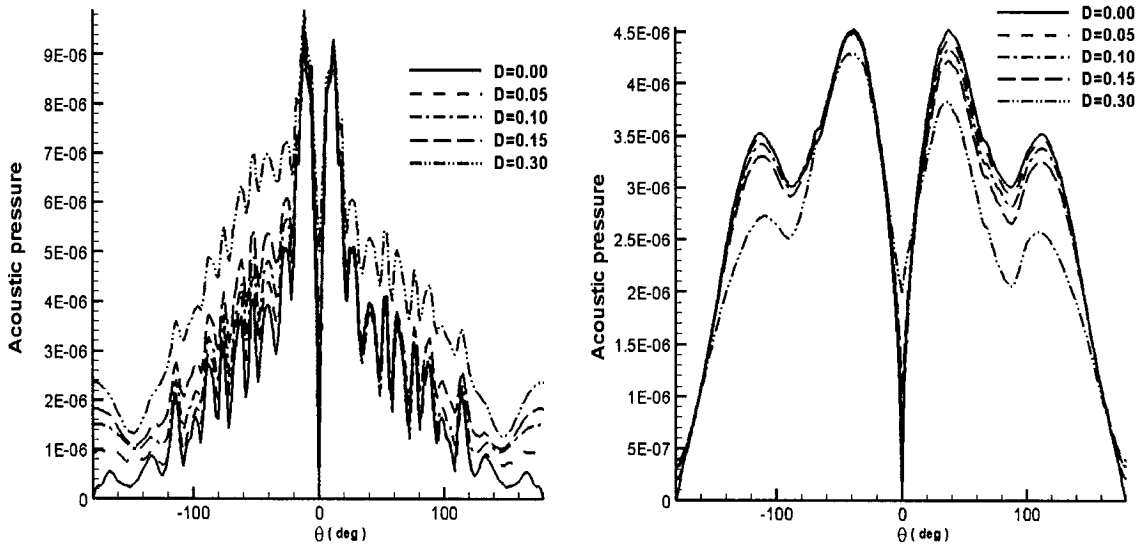

(a) (b)

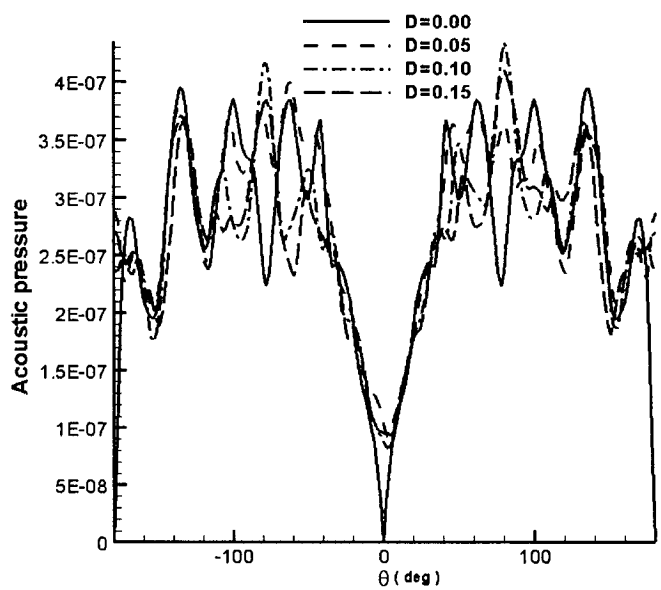

(c)

Figure 5-5 The RMS of acoustic pressure radiated by (a, b) Vatistas vortex street, (c) Taylor vortex street, and at (a, c) frequency $f = 1/0.05$, (b, d) frequency $f = 1/0.5$.

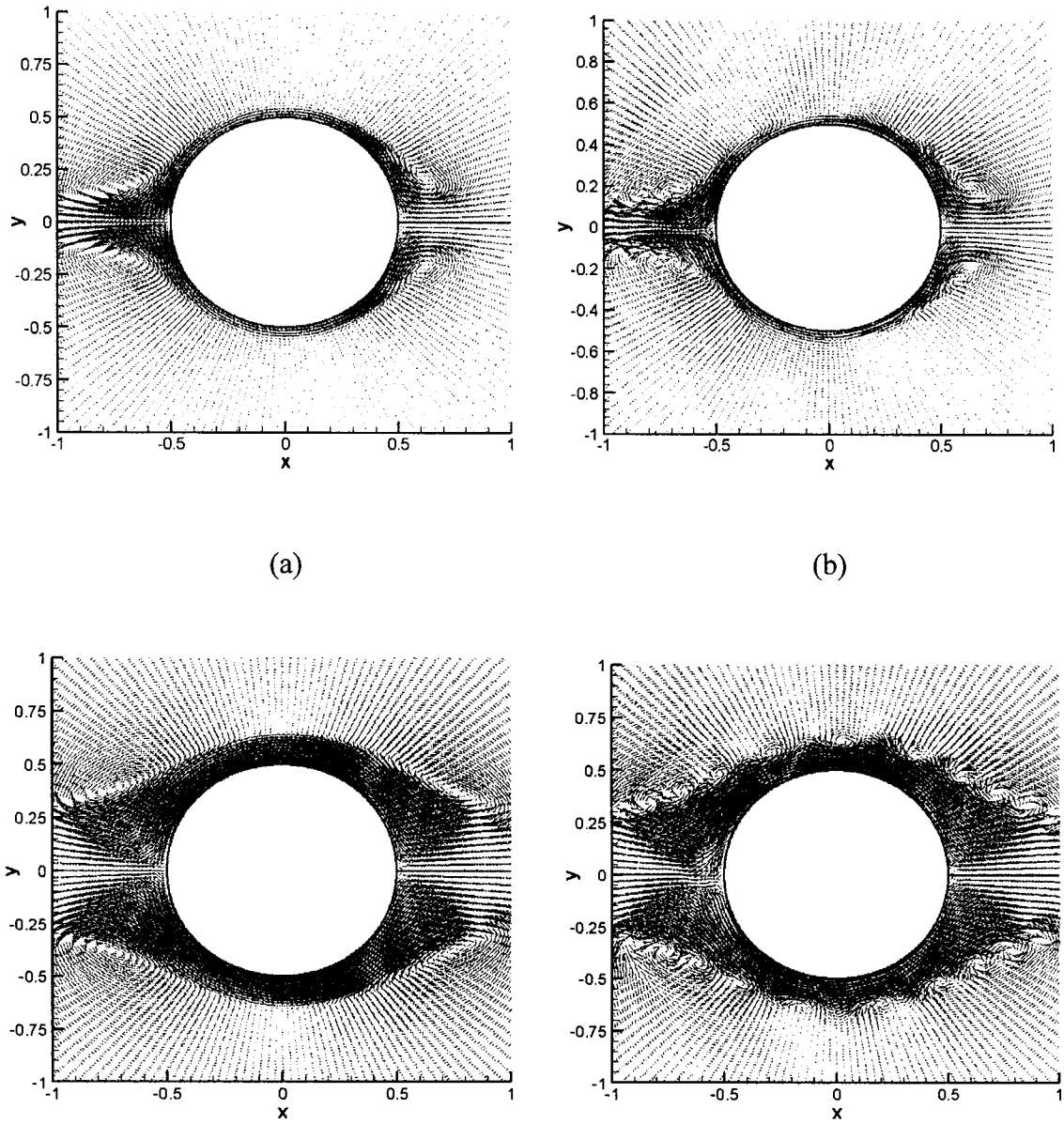

Figure 5-6 Flow-field of two-row Vatistas vortex street of alternating signs at different vortex adding frequency and different vortex street distance at time $t = 10.0$:

(a, c) $f = 1/0.050$, (b, d) $f = 1/0.50$, (a, b) $D = 0.10$, (c, d) $D = 0.30$

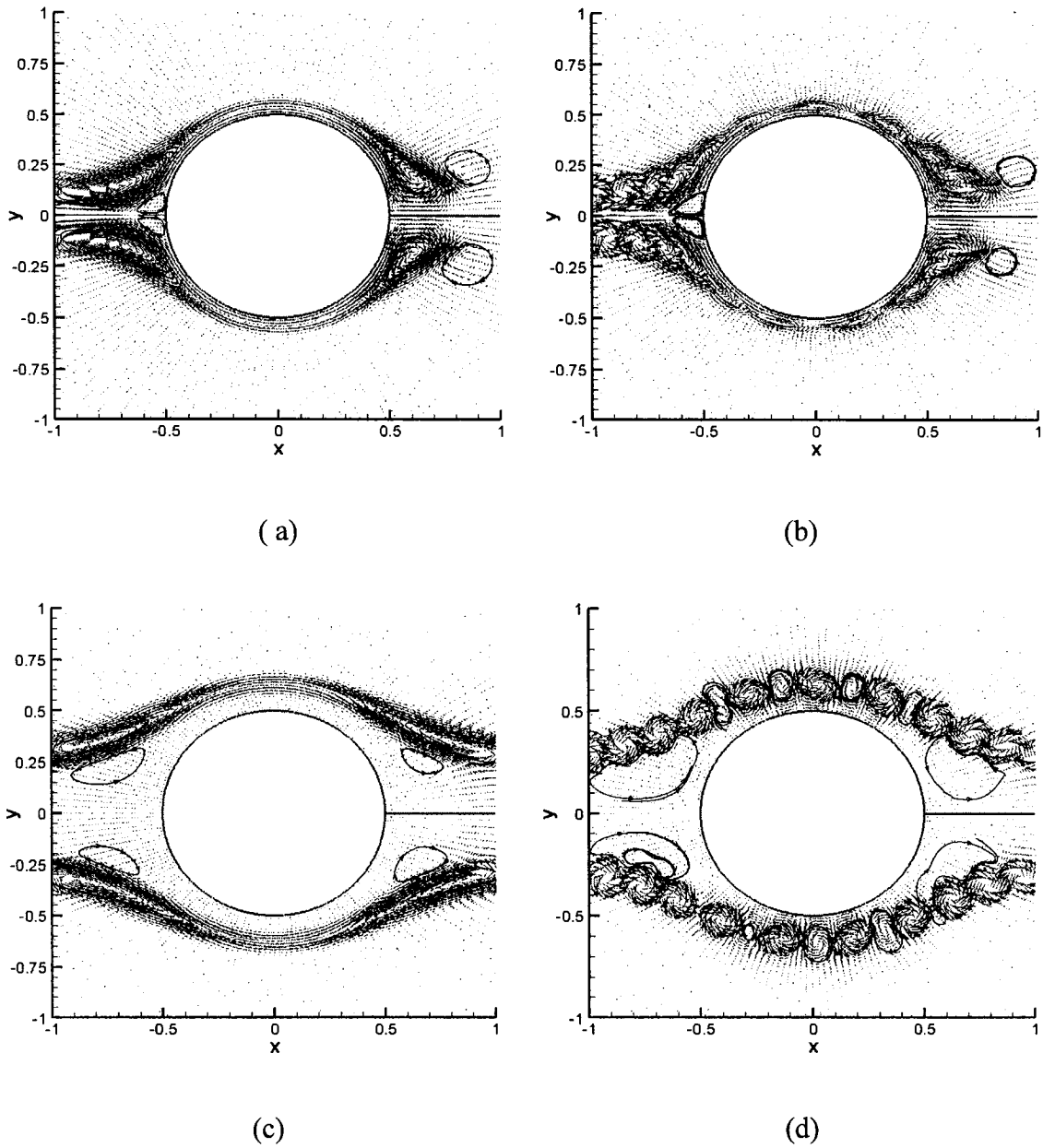

Figure 5-7 Flow-field of two-row Taylor vortex street of alternating signs at different vortex adding frequency and different vortex street distance at time $t = 10.0$:

(a, c) $f = 1/0.050$, (b, d) $f = 1/0.50$, (a, b) $D = 0.10$, (c, d) $D = 0.30$

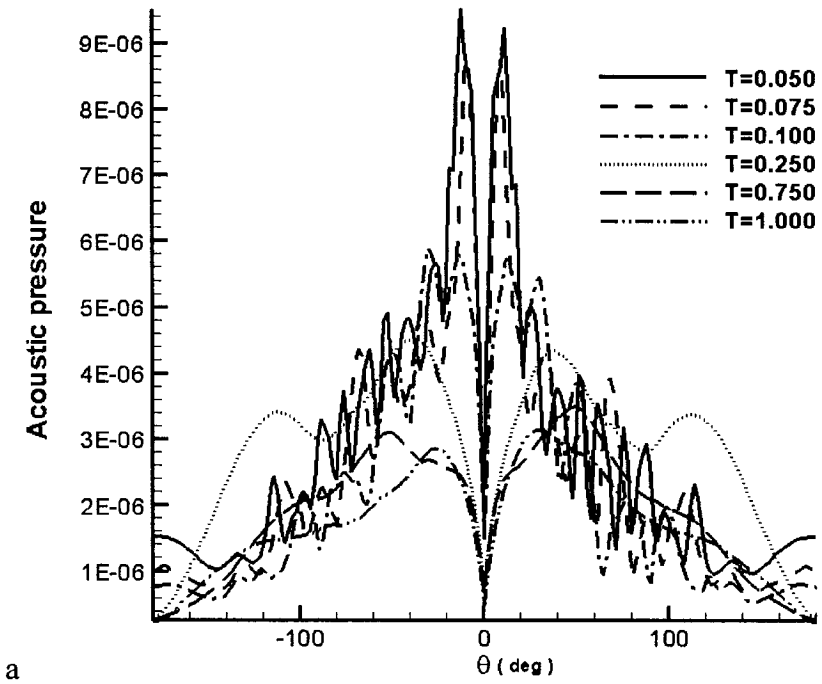

a

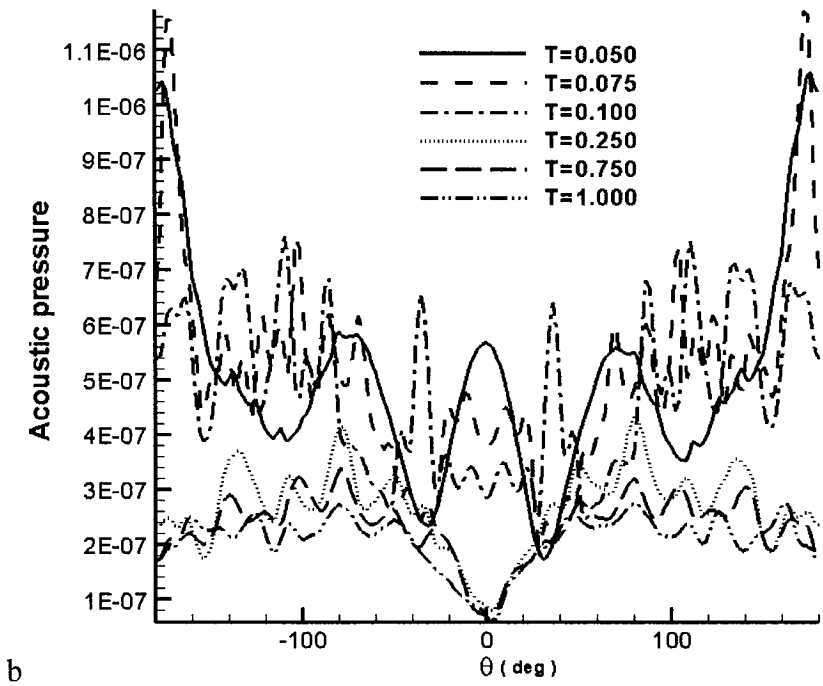

b

Figure 5-8 The RMS of acoustic pressure distribution with different vortex adding frequency. (a) the Vatistas vortex street, (b) the Taylor vortex street.

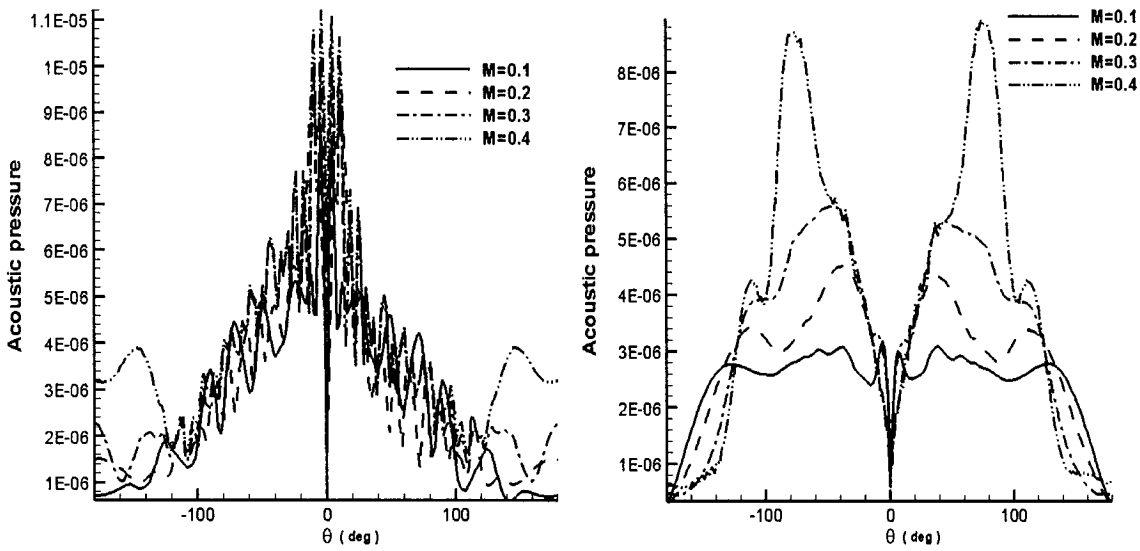

(a)

(b)

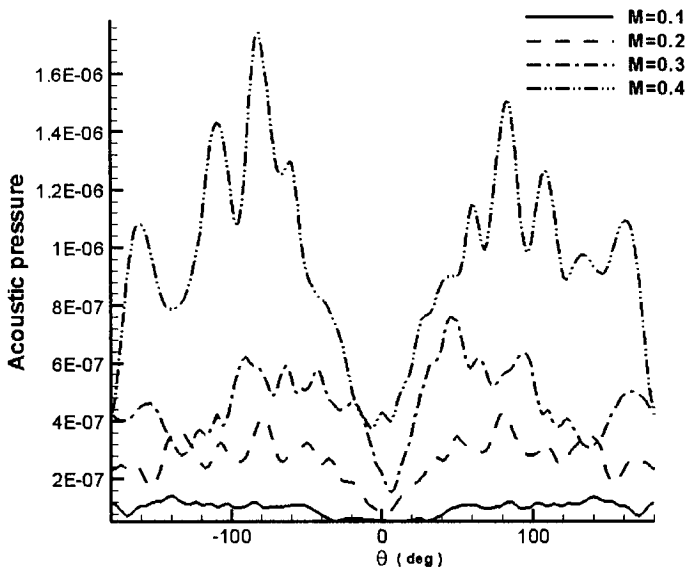

(c)

Figure 5-9 The RMS of acoustic pressure radiated by (a) Vatistas vortex street at frequency1/0.05=20, (b) Vatistas vortex street at frequency 1/0.5=2, (c) Taylor vortex street at frequency 1/0.5=2.0, vortex street distance is set to 0.1.

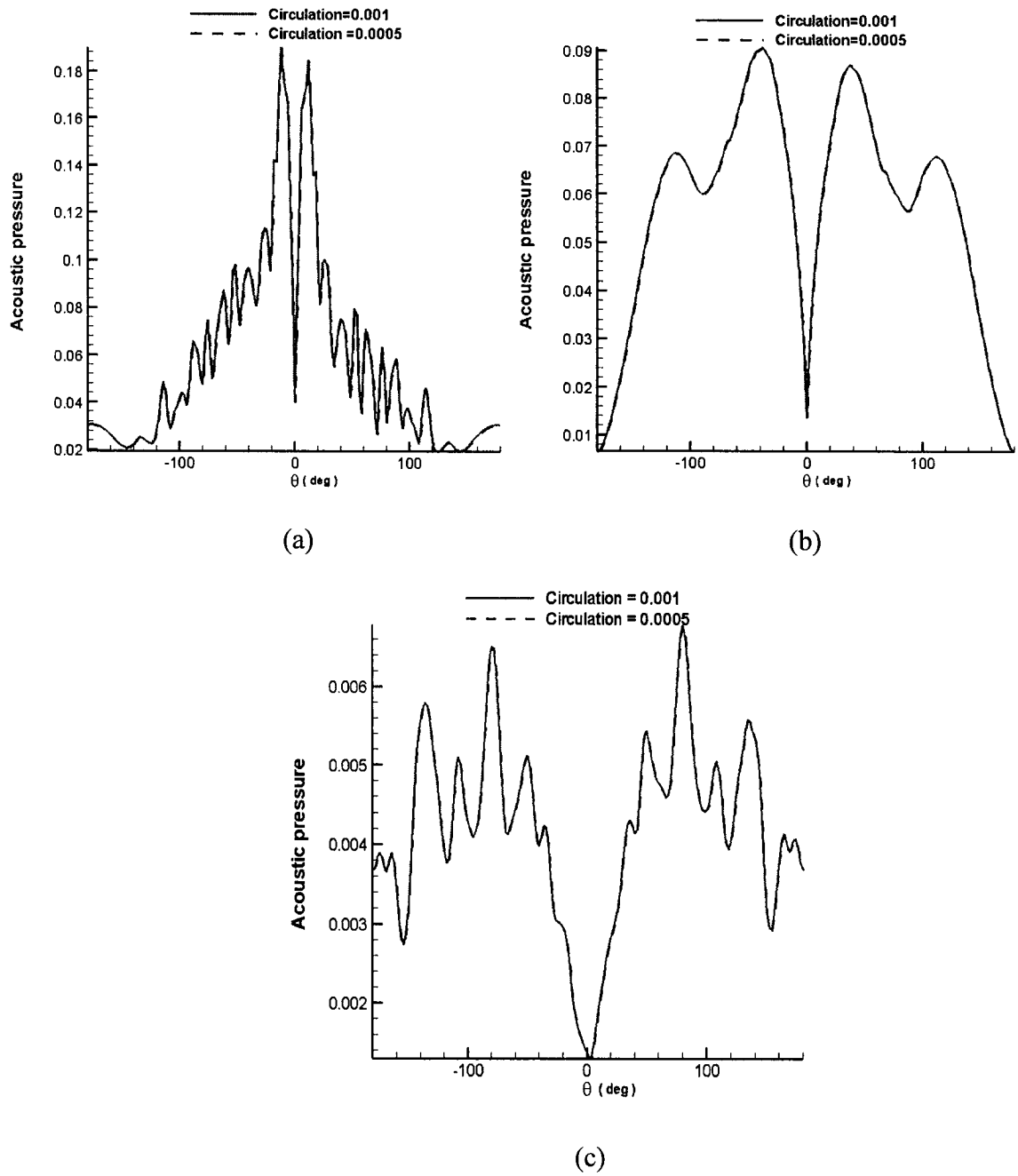

Figure 5-10 Normalized RMS of acoustic pressure radiated by (a) Vatistas vortex street at frequency 1/0.05=20, (b) Vatistas vortex street at frequency 1/0.5=2, (c) Taylor vortex street at frequency 1/0.5=2.0, vortex street distance is set to 0.1.

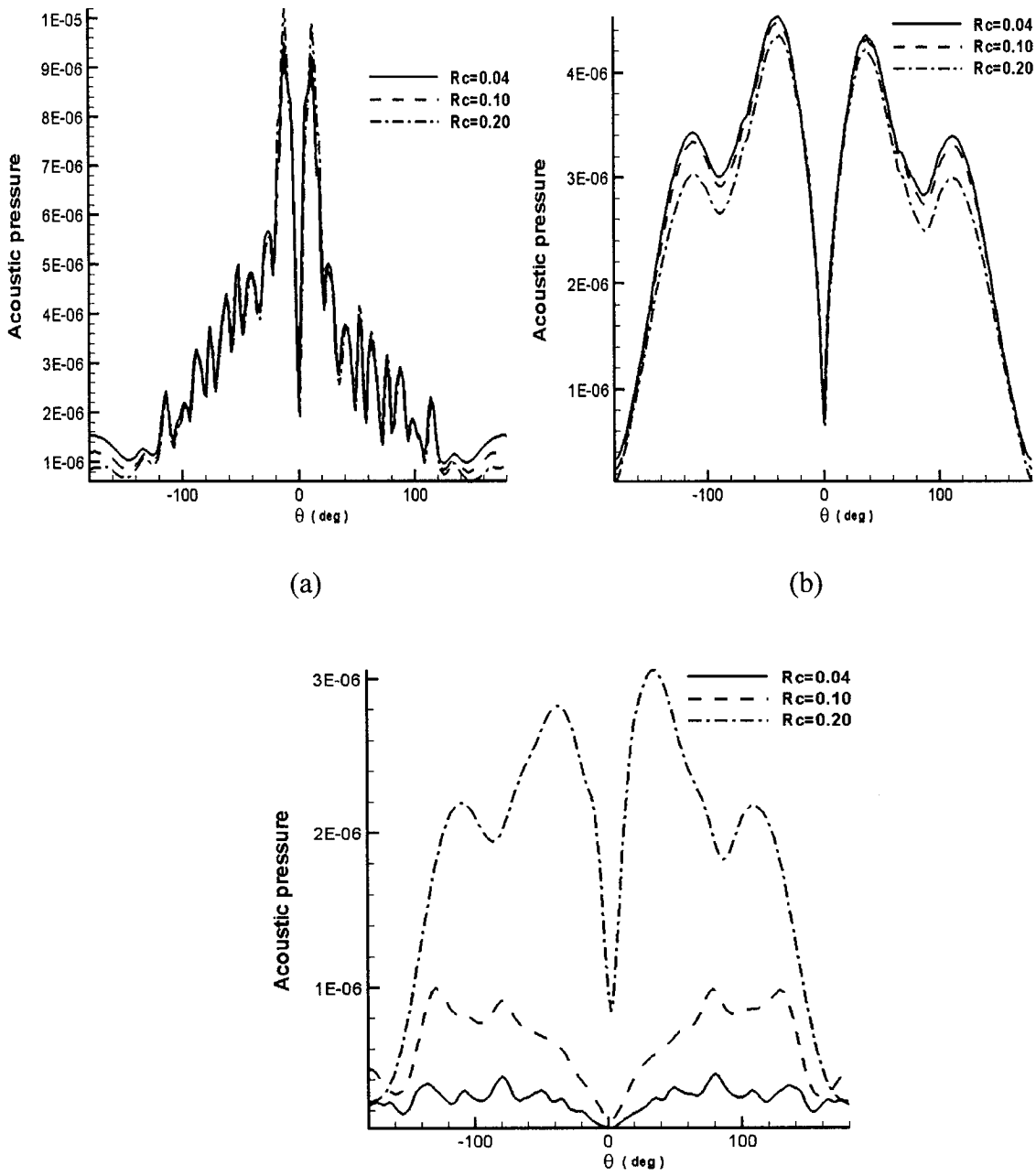

Figure 5-11 The RMS of acoustic pressure radiated by (a, b) the Vatistas vortex street, (c) the Taylor vortex street, and at (a, c) (frequency=1/0.05=20, $D = 0.1$), (b) (frequency=1/0.5=2, $D = 0.1$).

Chapter VI

Vortex Impingement on a Rotating Cylinder

For an airfoil at a given angle of attack, nature adopts a particular value for circulation which results in the flow leaving smoothly at the trailing edge (Anderson, 2001). In other words, the trailing edge is a stagnation point. Therefore, we adopt as a case of wave propagation over a lifting body and the flow about rotating cylinder with one stagnation point on its envelope.

6.1 Problem Setup

The computational domain for this situation is the same as that of Case B (see Fig. 4.2). The governing equations are similar to those in Case B (Eq. 55). Nevertheless, the background flow will be the flow around a lifting cylinder.

For a given circulation, Γ, the following relationships are known:

$\Gamma < 4\pi U_\infty R_{cyl}$ There are two stagnation points on the cylinder

$\Gamma = 4\pi U_\infty R_{cyl}$ There is one stagnation point on the cylinder

$\Gamma > 4\pi U_\infty R_{cyl}$ There is no sta gnation point on the cylinder

See Fig. 6.1 for a sketch of the stagnation points for the lifting flow over a circular cylinder.

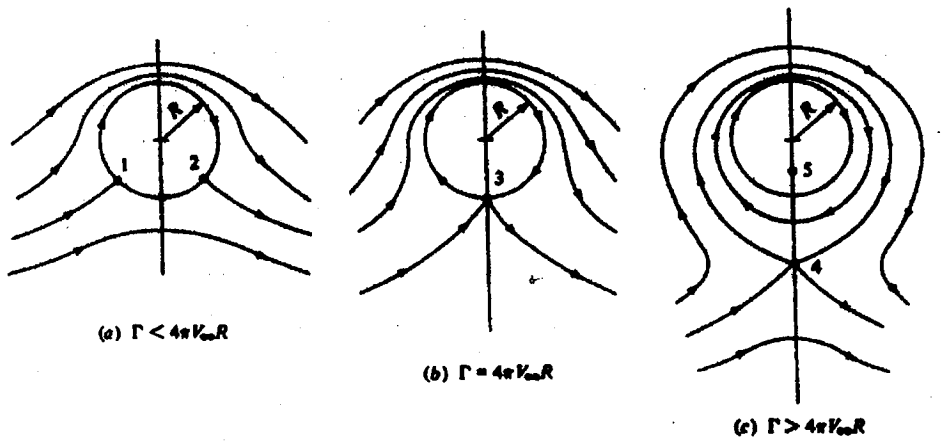

Figure 6-1 S tagnation points for the lifting flow over a circular cylinder (from Anderson, 2001).

Given the circulation around cylinder equal to $4\pi U_\infty R_{cyl}$, and the uniform flow coming from negative x axis direction, the flow around a rotating cylinder has one stagnation point on its envelope; see Fig. 6.2 for the flow field. The velocity distribution in polar system is given as follows:

$$U_r = U_\infty \cos\theta\left(1-\frac{R_{cyl}^2}{r^2}\right)$$
$$V_\theta = -U_\infty \sin\theta\left(1+\frac{R_{cyl}^2}{r^2}\right) - 2R_{cyl}U_\infty / r^2 \qquad (68)$$

Where U_∞ is the uniform flow velocity is set to 0.2, and R_{cyl} is the circular

cylinder radius, is equal to 0.5.

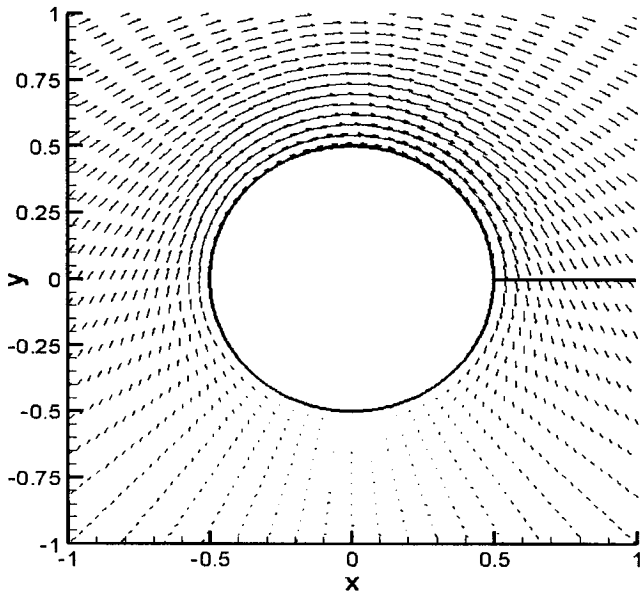

Figure 6-2 Background flow around rotating cylinder with one stagnation point on its envelope.

6.2 Computational Results

The interaction of a single vortex and that of a vortex street with a rotating cylinder were examined. The free-stream velocity U_∞ was kept equal to the constant value of 0.2. Small vortices were considered with core size equal to 0.04, and a circulation of 0.00005 and initially located at the horizontal centerline at the point $(-1.0,0.0)$..

6.2.1 Single vortex impingement into rotating cylinder

In this section, once again the prototype Taylor and Vatistas vortex models were taken into consideration.

The pressure isolines at times $t = 0.1$, and $t = 1.2$ are presented in Fig. 6.3. The sound pressure profiles appear alike to the ones of the vortex impingement on non-rotating cylinder, except that the assumed-symmetrical axis is rotated toward the upside surface of the cylinder by the convection effect of a mean flow. From its RMS distribution with respect to angle θ from the centerline, it is shown that the cylinder circulation does have a great impact on the sound strength and the directivity especially for Vatistas vortex. For Vatistas model, the sound strength is amplified, accompanied by an angular shift of the sound directivity. The sound strength has amplified more than two times as compared to its impingement on the non-rotating cylinder. For the Taylor vortex model, the changes of the lifting cylinder brings to the sound wave were marginally small. Note that for other initial locations of Taylor vortex, the sound may be amplified in a considered lifting flow compared to the flow about non-lifting cylinder.

However, the Kutta condition only applies at small angle of attack and also it does not establish immediately after deployment of multi-element airfoil, all the phenomena mentioned in Fig. 6.1 are possible to happen in reality. So to investigate the dynamics of change of directivity of sound with increase of circulation of flow around cylinder, the sound profiles corresponding to different cylinder circulation are presented in Fig. 6.5, and it is shown that the circulation of flow around cylinder have greater impact on the sound profile radiated by the Vatistas vortex, but have minor impact on the sound waves by the Taylor vortex. And the higher the circulation is, the stronger the sound wave

radiated and the further the sound directivity shifted.

6.2.2 A vortex street impingement into rotating cylinder

For the vortex street impingement case, due to the pressure built-up problem (that is, the time-averaged pressure may become non-zero), only the Vatistas vortex street was considered. The vortices are periodicly superimposed on the flow at the location $(-1.0,\pm D)$, see Fig 5.1. A high frequency vortex street at $f = 1/0.05 = 20$ and a low frequency vortex street with frequency $f = 1/0.50 = 2$ were chosen as the representatives of vortex chain for the current investigation.

The P_{rms} and P_{acous} distribution with respect to angle θ from the centerline are presented in Fig. 6.6. It was observed that the pressure build-up is negligibly small for the low frequencies, but not for the high frequencies. For the low frequency Vatistas vortex street, the sound is directed toward the upper half cylinder and the sound directivity emerges at an angle of $50°$ with the negative centerline. Notably, the minimum sound strength occurs at the angle of $100°$ with the centerline being in the lower half of the cylinder. For the high-frequency vortex street, the sound directivity becomes non-monotonic, which was also observed in the case of vortex street interaction with a non-rotating cylinder. Again, the sound wave has been amplified in comparison to the non-rotating cylinder case.

When a vortex street impinges into a stationary cylinder, a scaling law for the

sound wave strength related to the single vortex strength has been observed. This scaling law is also applicable to the sound wave generated by a vortex street interacting with a rotating cylinder (see Fig. 6.7). That is, if the RMS acoustic pressure is normalized by the vortex strength then individual curves will collapse into one curve.

The effect of core size and the vortex street distance on the produced sound were also investigated (see Figs 6.8 and 6.9). It was observed that the variation of the vortex core size or the vortex street distance brings almost no change to the sound wave strength or sound directivity.

6.3 Summary of Findings.

In this chapter, sound generation by a single vortex or vortex street impingement on rotating cylinder was investigated. For a single vortex case, the lifting flow about cylinder not only amplifies the sound strength but also shifts the sound directivity; it is also shown that the wave originated by impingement of Vatistas vortex is much more sensitive to the non-zero circulation of the mean flow.

For vortex street case, only Vatistas vortex street was investigated, two typical values of the frequency were chosen. For the low-frequency vortex street, the sound directivity occurs at around 50° from the centerline, while for the high-frequency vortex street, the sound directivity becomes non-monotonic.

In terms of scaling analysis, the present results are in qualitative agreement with

those obtained for a stationary cylinder. The RMS of acoustic pressure, was shown to be proportional to the vortex strength (circulation). The vortex core size and street distance have a minor effect on the radiated sound waves.

In summary, a spinning cylinder with one stagnation point on its envelope, amplifies the sound radiated by either a single vortex or a vortex street. The area of intense noise is shifted towards the upper surface of the cylinder. Nevertheless, the overall effects of vortex parameters on sound, for both unloaded and loaded airfoils, maintain their overall similarity.

$t = 0.1$

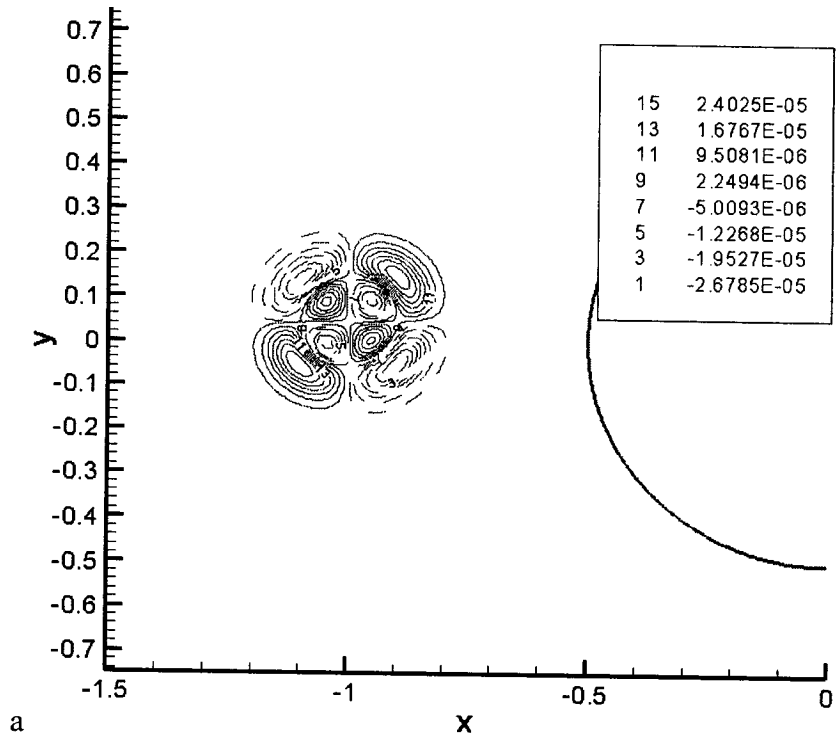
0.7
0.6
0.5
0.4
0.3
0.2
0.1
0
-0.1
-0.2
-0.3
-0.4
-0.5
-0.6
-0.7
y
-1.5
-1
-0.5
0
x
15 2.4025E-05
13 1.6767E-05
11 9.5081E-06
9 2.2494E-06
7 -5.0093E-06
5 -1.2268E-05
3 -1.9527E-05
1 -2.6785E-05

a

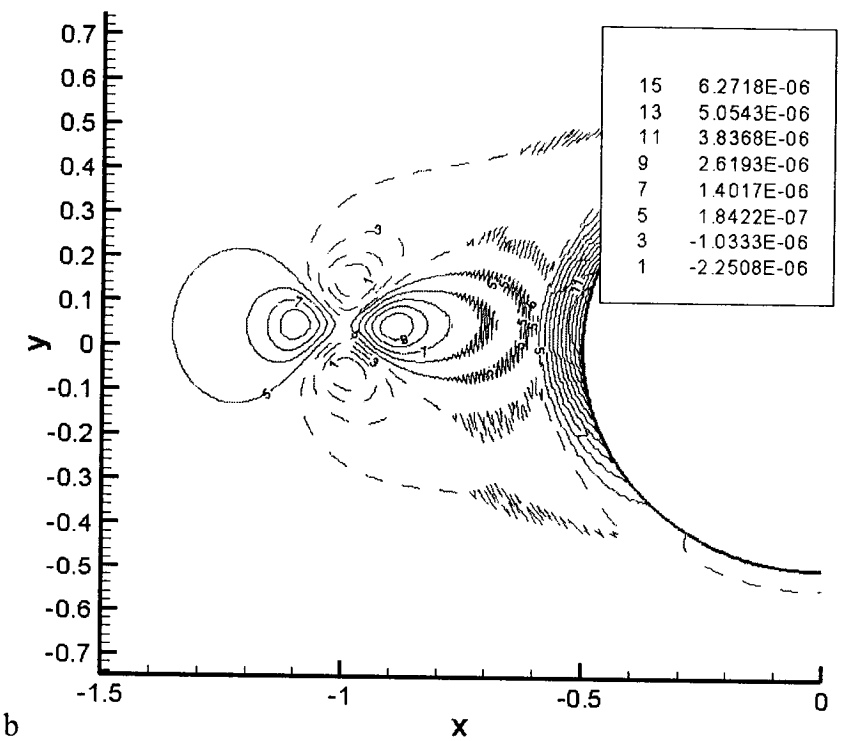
0.7
0.6
0.5
0.4
0.3
0.2
0.1
0
-0.1
-0.2
-0.3
-0.4
-0.5
-0.6
-0.7
y
-1.5
-1
-0.5
0
x
15 6.2718E-06
13 5.0543E-06
11 3.8368E-06
9 2.6193E-06
7 1.4017E-06
5 1.8422E-07
3 -1.0333E-06
1 -2.2508E-06

b

$t = 1.2$

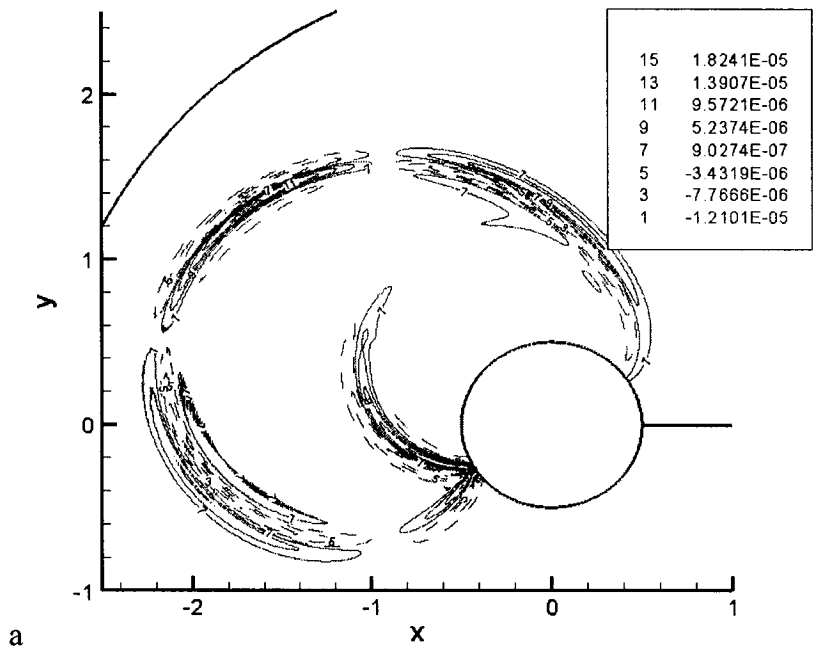

a

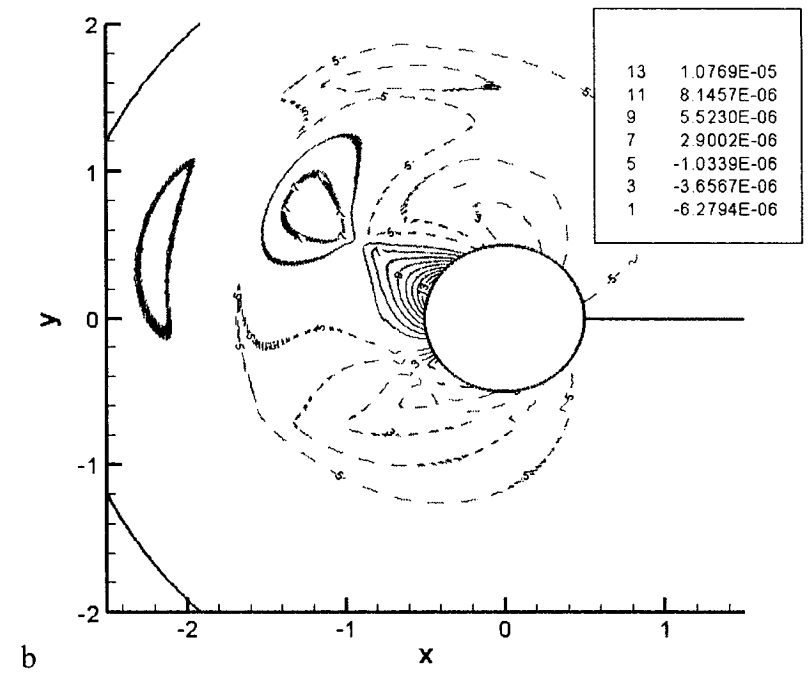

b

Figure 6-3 Distorting of the small vortex in the mean flow around a rotating cylinder, at times t=0.1 and $t = 1.2$. (a) the Taylor's vortex and, (b) the Vatistas's Vortex.

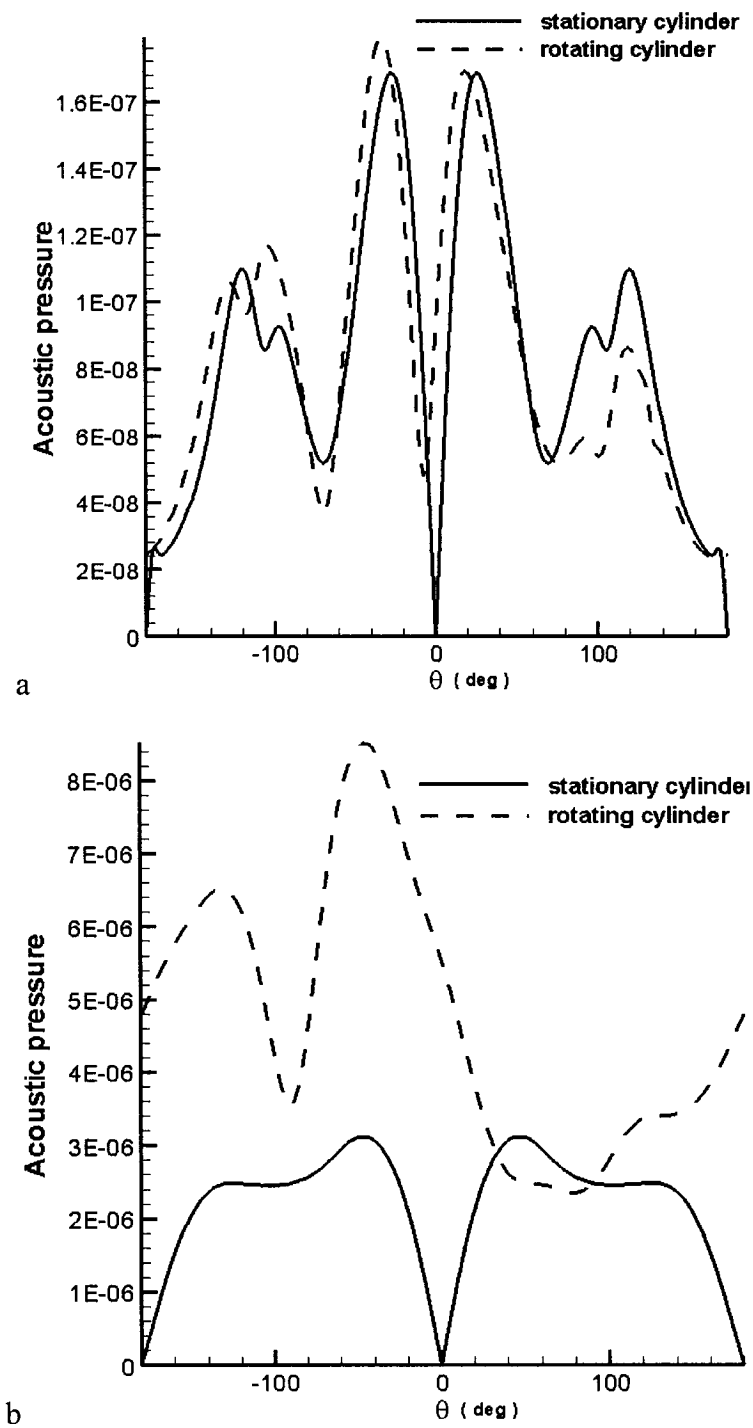

Figure 6-4 The RMS acoustic pressure distribution for rotating cylinder case. (a) the Taylor's vortex, (b) the Vatistas's vortex.

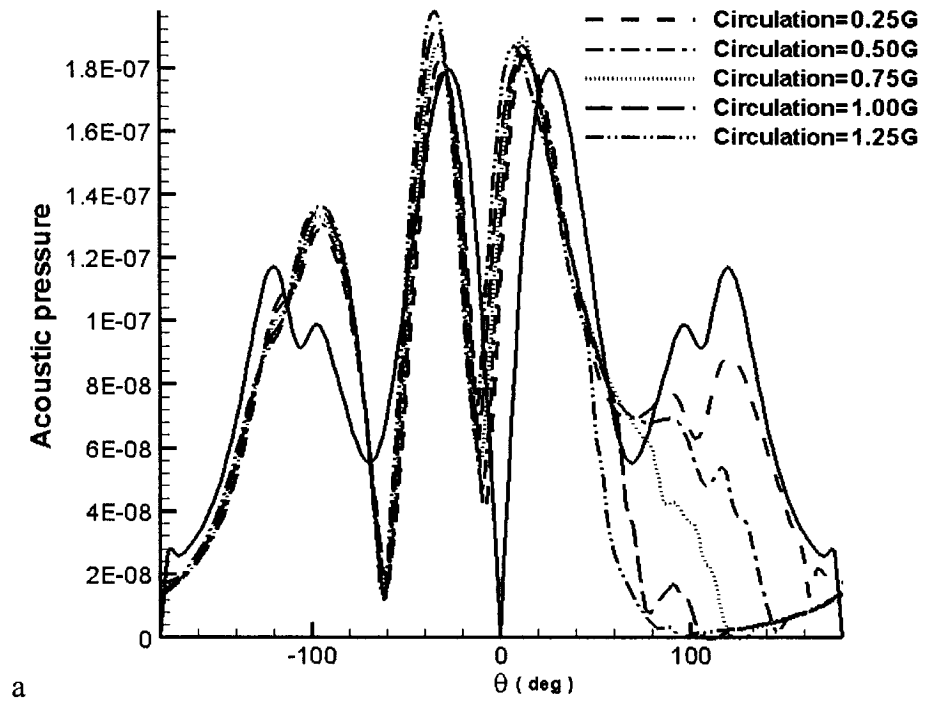

a

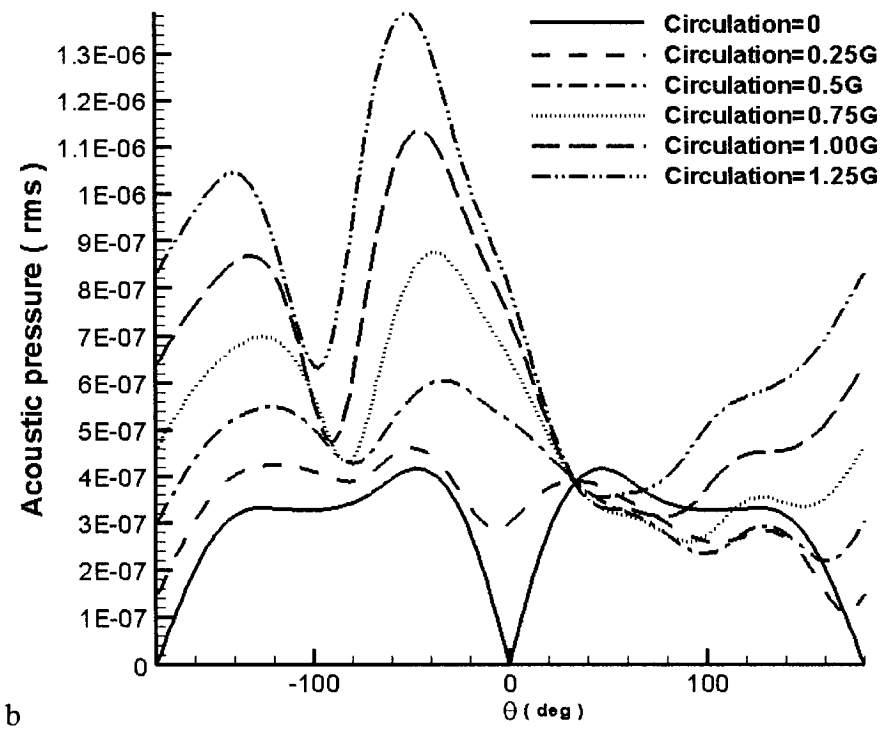

b

Figure 6-5 The RMS acoustic pressure distribution at different cylinder Circulation value: (a) the Taylor's vortex (b) the Vatistas's vortex.

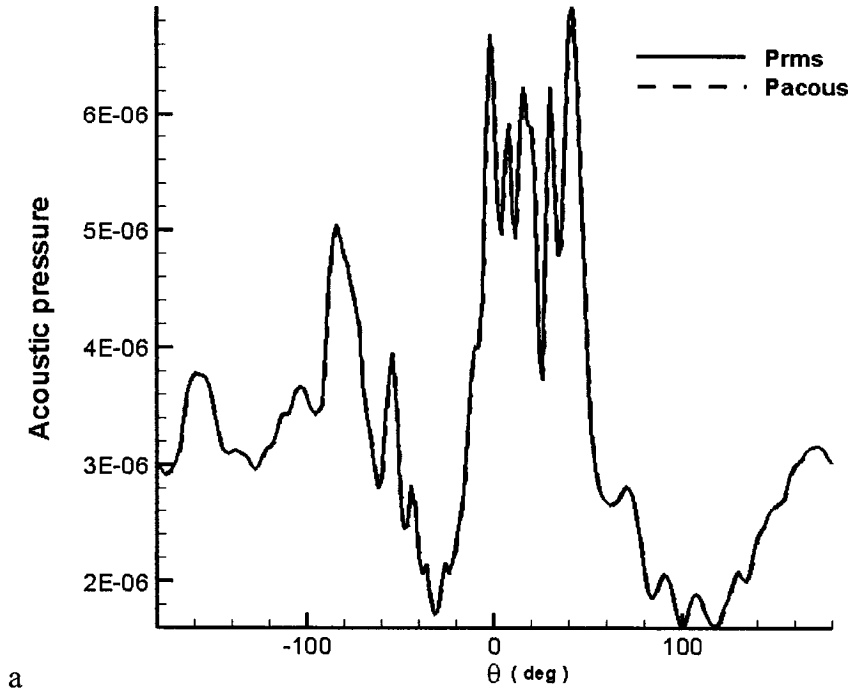

a

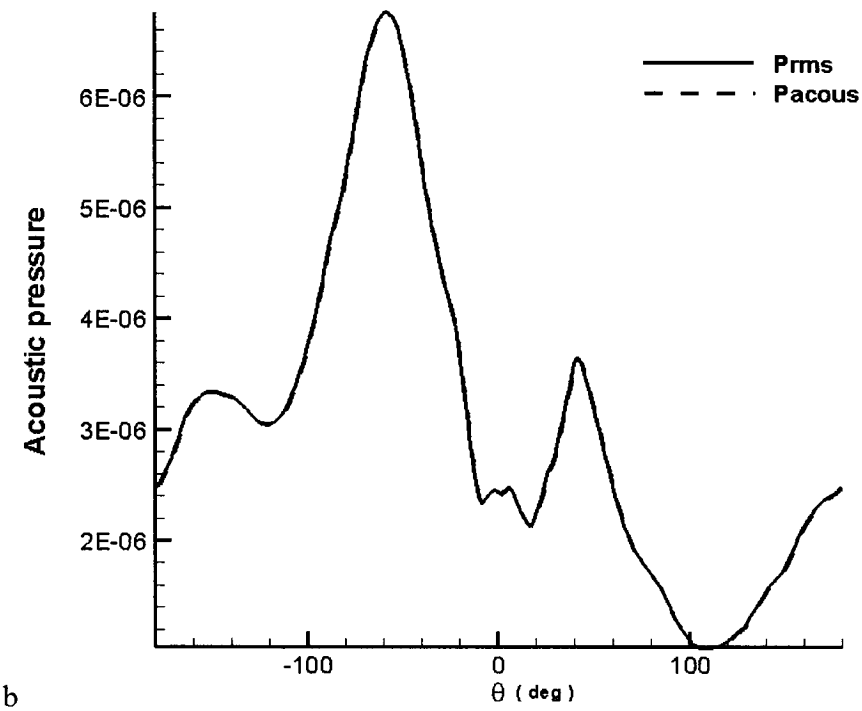

b

Figure 6-6 The RMS of acoustic pressure for Vatistas vortex street: (a) at frequency 1/0.05=20, (b) at frequency 1/0.5=2.

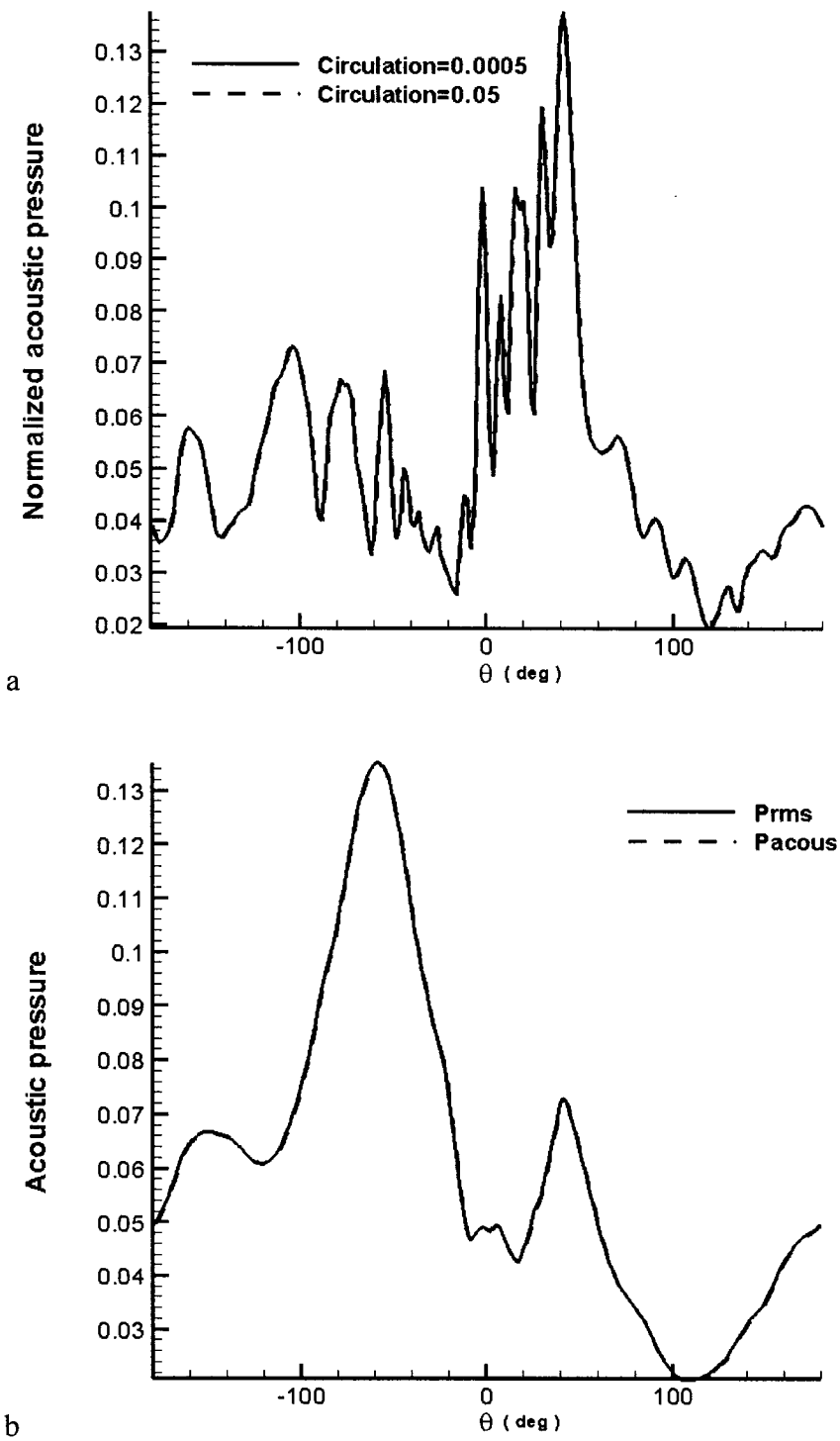

Figure 6-7 Normalized RMS (normalized by vortex strength) of acoustic pressure for Vatistas vortex street at frequency 1/0.5=2. Vortex street distance is set to 0.1.

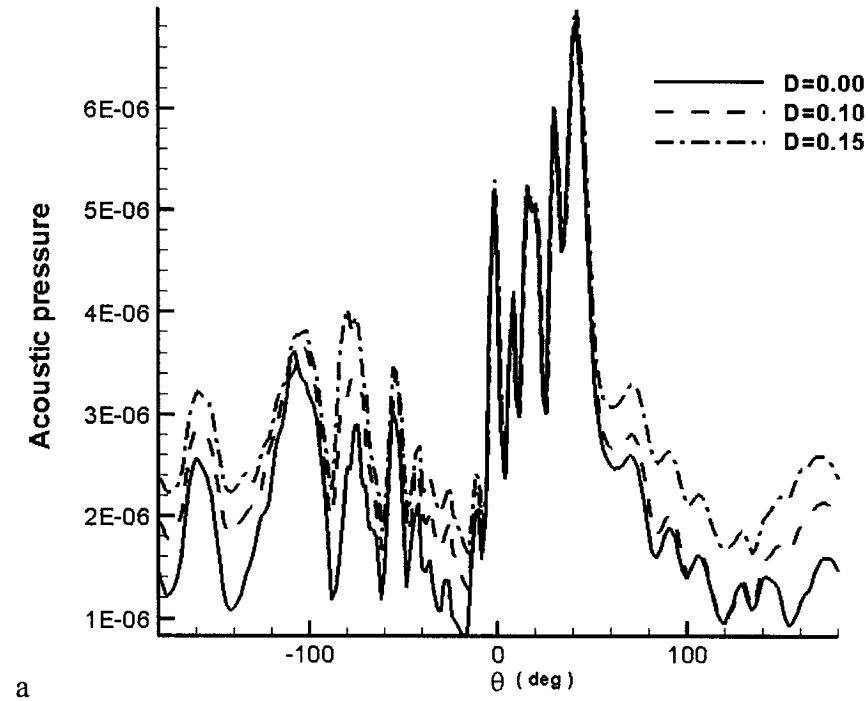

a

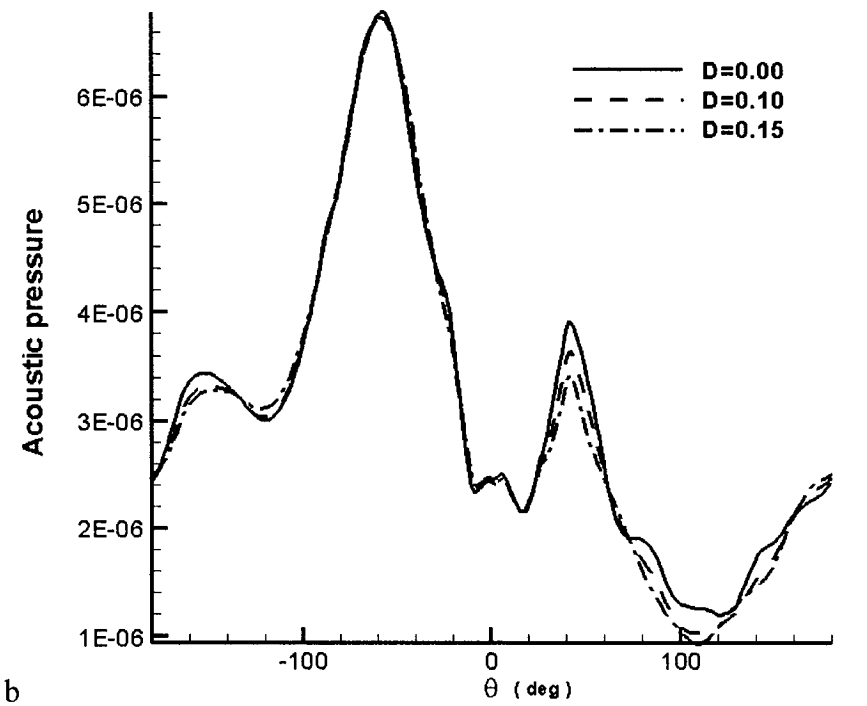

b

Figure 6-8 RMS of acoustic pressure for Vatistas vortex street: (a) at frequency 1/0.05=20, (b) at frequency 1/0.5=2.

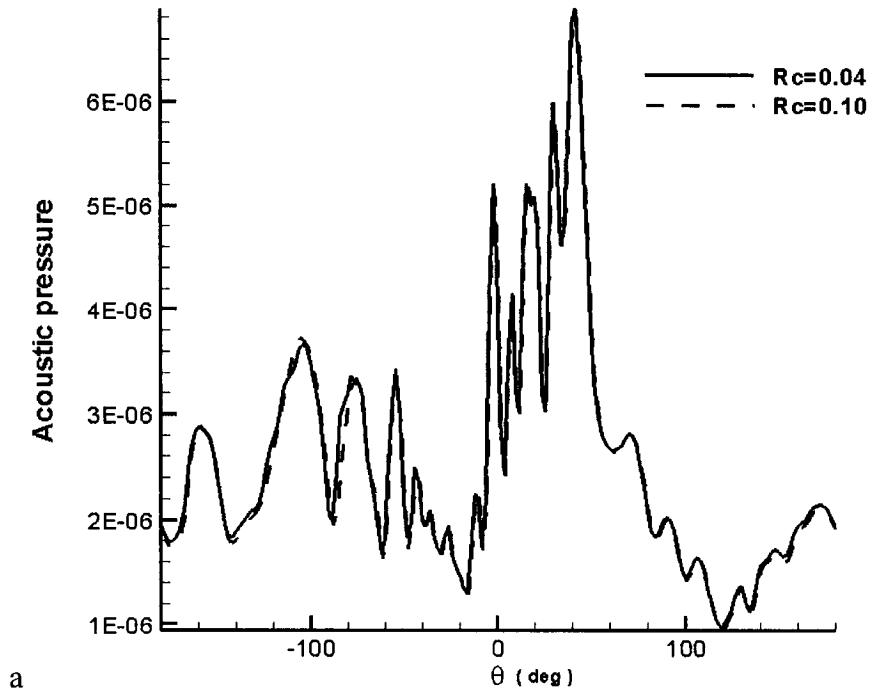

a

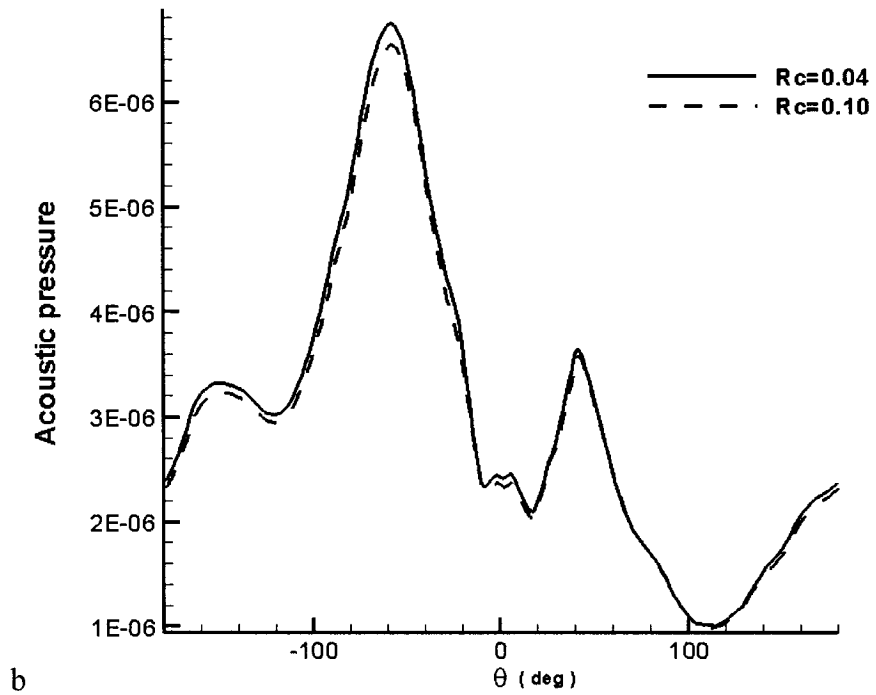

b

Figure 6-9 RMS of acoustic pressure for Vatistas vortex street at: (a) frequency 1/0.05=20, (b) frequency 1/0.5=2.Vortex street distance was set equal to 0.1.

Chapter VII

Acoustic Sources Trapped Between Two Cylinders

In this chapter, the propagation and scattering of sound generated by a spatially distributed axisymmetric acoustic source, between two rigid circular cylinders in still air (Case D-1) were considered and the computational results were compared with the available analytical solutions. Sound generation by vortex deformation in the mean flow parallel to the axis connecting centers of cylinders (Case D-2) and sound generation by vortex deformation in the flow perpendicular to the cylinders' centers axis (Case D-3) were investigated. These cases were taken as prototypes of sound generation by bodies in close proximity to each other, such as a multi-element airfoil or undercarriage gear. These cases provide a stringent test of the ability of high-order computational acoustics codes to handle increasingly complex geometries. In addition, this problem provides a demonstration of numerical robustness, long-time stability, and suitability of far-field radiation treatments in the presence of multiple scattering bodies.

7.1 Problem Setup

A schematic of the geometry is presented in Fig. 7.1. It consists of two cylinders of

unequal diameter (D_1, D_2) with a co-linearly located periodic acoustic source (Case D-1) or a single Taylor vortex disturbance equidistant from the center of each cylinder (Cases D-2 and D-3). The vortex parameters are given by: vortex core $R_c = 0.04$ and vortex strength $\Gamma = 0.0005$. In the Cartesian coordinate system centered on the source, the locations of the cylinders are given as (L, L_2)

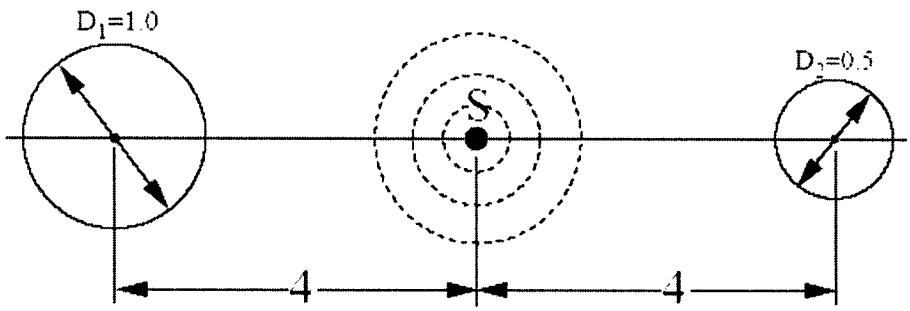

Figure 7-1 Geometry of acoustic scattering.

The ambient condition represents the case where there is no mean flow. The mass and momentum flux equations in the Cartesian coordinates are given as follows:

$$\begin{aligned}
&\frac{\partial \rho'}{\partial t} + \frac{\partial u'}{\partial x} + \frac{\partial v'}{\partial y} = 0 \\
&\frac{\partial u'}{\partial t} + \frac{\partial p'}{\partial x} = 0 \\
&\frac{\partial v'}{\partial t} + \frac{\partial p'}{\partial y} = 0 \\
&\frac{\partial p'}{\partial t} + \frac{\partial u'}{\partial x} + \frac{\partial v'}{\partial y} = S
\end{aligned} \tag{69}$$

To solve the linearized Euler equations describing the wave propagation from two

cylinders, various coordinate systems may be used including 1) Cartesian coordinate system, 2) polar coordinate system, and 3) bipolar coordinate system. Each of above-listed approaches has advantages and disadvantages. The Cartesian coordinate system works well with a perfectly matched layer (PML) at the boundaries, however, the boundaries of the cylinders do not coincide with the grid lines. For the polar coordinate system, one of cylinders coincides with the polar grid lines, but the second cylinder does not. In addition, the PML is less warranted with this system. For the bipolar coordinate approach, lines of the grid coincide with envelopes of the cylinders. The grid lines are clustered near the cylinder and become quite coarse in the far-field, which will greatly reduce the number of grid points needed, thus saving computer resources. The bipolar coordinate system has became more involved to implement because of required transformation of coordinates and integration of PML.

7.2 Bipolar system

The transforming relationships between coordinate variables ζ,η, and the x,y, variables in the Cartesian coordinate are:

$$x = \frac{a\sinh\eta}{\cosh\eta - \cos\xi}$$
$$y = \frac{a\sinh\xi}{\cosh\eta - \cos\xi} \qquad (70)$$

The Lame coefficients are obtained:

$$h_\xi = \frac{a}{\cosh\eta - \cos\xi}$$
$$h_\eta = \frac{a}{\cosh_\eta - \cos\xi} \tag{71}$$

The expressions for the gradient, divergence, and Laplace in terms of ζ,η are obtained as follows:

$$\nabla\phi = \frac{1}{h_\xi}\frac{\partial\phi}{\partial\xi}i_\xi + \frac{1}{h_\eta}\frac{\partial\phi}{\partial\eta}i_\eta$$
$$\nabla\cdot A = \frac{1}{h_\xi h_\eta}\left(\frac{\partial\left(h_\eta A_\xi\right)}{\partial\xi} + \frac{\partial\left(h_\xi A_\eta\right)}{\partial\eta}\right) \tag{72}$$
$$\Delta\phi = \frac{1}{h_\xi h_\eta}\left(\frac{\partial}{\partial\xi}\left(\frac{h_\eta}{h_\xi}\frac{\partial\phi}{\partial\xi}\right) + \frac{\partial}{\partial\eta}\left(\frac{h_\xi}{h_\eta}\frac{\partial\phi}{\partial\eta}\right)\right)$$

The following identities show that curves of constant ζ,η are circles in x,y space:

$$x^2 + \left(y - a\coth\xi\right)^2 = a^2\csc^2\xi$$
$$\left(x - a\coth\eta\right)^2 + y^2 = a^2\csc h^2\eta \tag{73}$$

where $0 < \zeta < 2\pi$ and $\eta_1 < \eta < \eta_2$. The limits η_1, η_2 and coefficient a are determined by the two cylinder location and radius as follows.

If a circle with radius r_1 is located at $(c_1,0)$, then another circle with radius r_2 is expected to be located at $(c_2,0)$ and the distance between them, i.e.,

$$c_2 - c_1 = d \tag{74}$$

Thus the following equations are obtained:

$$
\begin{aligned}
&a\coth\eta_1 = c_1 \\
&a\operatorname{csch}\eta_1 = r_1 \\
&a\coth\eta_2 = c_2 \\
&a\operatorname{csch}\eta_2 = r_2 \\
&c_2 - c_1 = d
\end{aligned}
\qquad (75)
$$

In this study, for case D-1 the two cylinders are located at a distance of 8. The right cylinder has a radius of 0.5, the left one 0.25. Substituting the values into the above equations gives:

$$
a = 3.980439, \quad c_1 = -4.01172 \quad c_2 = 3.98828, \quad \eta_1 = -2.771608, \quad \eta_2 = 3.461818 \qquad (76)
$$

For cases D-2 and D-3 the two cylinders are located at a distance of 2 units apart. The right cylinder has a radius of 0.5, the left one has a radius of 0.25. Substituting the values into the above equations, we have

$$
a = 0.847935, \quad c_1 = 0.984375, \quad c_2 = 1.015625, \quad \eta_1 = -1.298725, \quad \eta_2 = 2.079442 \qquad (77)
$$

Transforming the Linearized Euler Eq. 66 into bipolar coordinates, the equations became:

$$
\begin{aligned}
&\frac{\partial p'}{\partial t} = -\frac{1}{h_\zeta h_\eta}\left(\frac{\partial(h_\eta u')}{\partial\zeta} - \frac{\partial(h_\zeta v')}{\partial\eta}\right) - S \\
&\frac{\partial u'}{\partial t} = -\frac{\partial p'}{\partial\zeta}\frac{1}{h_\zeta} \\
&\frac{\partial v'}{\partial t} = -\frac{\partial p'}{\partial\zeta}\frac{1}{h_\eta} \\
&\frac{\partial \rho'}{\partial t} = -\frac{1}{h_\zeta h_\eta}\left(\frac{\partial(h_\eta u')}{\partial\zeta} - \frac{\partial(h_\zeta v')}{\partial\eta}\right)
\end{aligned}
\qquad , \qquad (78)
$$

where S is the acoustic source term. In the Case D-1, the time-dependent acoustic source term on the right-hand side of the energy equation is assumed axisymmetric and is written in the source-centered coordinate system as

$$S = \exp\left[-\ln 2 * \left\{\frac{x_S^2 + y_S^2}{b^2}\right\}\right] \sin(\omega t) , \tag{79}$$

where $\omega = 8\pi$ and $b = 0.2$

For Cases D-2 and D-3, the mean flow has velocity components U_ξ, U_η in bipolar system, the linearized Euler equations in bipolar system is given as:

$$\begin{aligned}
\frac{\partial p'}{\partial t} &= -\frac{1}{h}\left(\frac{\partial u'}{\partial \xi} + \frac{\partial v'}{\partial \eta}\right) - \frac{1}{h^2}\left(u'\frac{\partial h}{\partial \xi} + v'\frac{\partial h}{\partial \eta}\right) - \frac{1}{h}\left(\frac{\partial p'}{\partial \xi}U_\xi + \frac{\partial p'}{\partial \eta}V_\eta\right) \\
\frac{\partial u'}{\partial t} &= -\frac{1}{h}\frac{\partial p'}{\partial \xi} - \frac{1}{h}\left(U_\xi\frac{\partial u'}{\partial \xi} + V_\eta\frac{\partial u'}{\partial \eta} + u'\frac{\partial U_\xi}{\partial \xi} + v'\frac{\partial U_\xi}{\partial \eta} - \frac{2v'V_\eta}{h}\frac{\partial h}{\partial \xi} + \frac{u'V_\eta}{h}\frac{\partial h}{\partial \eta} + \frac{v'U_\xi}{h}\frac{\partial h}{\partial \eta}\right) \\
&\quad - \frac{p'}{h}\left(U_\xi\frac{\partial U_\xi}{\partial \xi} + V_\eta\frac{\partial U_\xi}{\partial \eta} - \frac{V_\eta^2}{h}\frac{\partial h}{\partial \xi} + \frac{U_\xi V_\eta}{h}\frac{\partial h}{\partial \eta}\right) \\
\frac{\partial v'}{\partial t} &= -\frac{1}{h}\frac{\partial p'}{\partial \eta} - \frac{1}{h}\left(U_\xi\frac{\partial v'}{\partial \xi} + V_\eta\frac{\partial v'}{\partial \eta} + u'\frac{\partial U_\eta}{\partial \xi} + v'\frac{\partial U_\eta}{\partial \eta} - \frac{2u'U_\xi}{h}\frac{\partial h}{\partial \eta} + \frac{v'U_\xi}{h}\frac{\partial h}{\partial \xi} + \frac{v'U_\eta}{h}\frac{\partial h}{\partial \xi}\right) \\
&\quad - \frac{p'}{h}\left(U_\xi\frac{\partial U_\eta}{\partial \xi} + V_\eta\frac{\partial U_\eta}{\partial \eta} + \frac{U_\xi V_\eta}{h}\frac{\partial h}{\partial \xi} - \frac{U_\xi^2}{h}\frac{\partial h}{\partial \eta}\right)
\end{aligned} \tag{80}$$

7.3 Mean Flow around Two Cylinders

The arrangement of the cylinders with respect to the free stream flow direction can be broadly classified as tandem (in-line, flow is parallel to the cylinders' centers line) or

transverse (side-by-side, the flow is perpendicular to the centers line). (Mittal et al. 1997)

The fluid dynamic interactions between the two stationary cylinders are sensitive to their relative arrangement (Zdravkovich 1977). If the cylinders are far apart, the flow around either of cylinders behaves as an isolated cylinder. Potential flow is assumed, and the background flow around the two cylinders may be analytically obtained in terms of stream function ψ by:

$$\psi = U_0\left(y - \frac{a^2 y}{(x-c_1)^2 + y^2} - \frac{b^2 y}{(x+c_2)^2 + y^2} \right) \tag{81}$$

The bipolar velocity components are:

$$\begin{aligned} U_\zeta &= \frac{1}{h_\eta}\frac{\partial \psi}{\partial \eta} \\ U_\eta &= \frac{1}{h_\zeta}\frac{\partial \psi}{\partial \zeta} \end{aligned}, \tag{82}$$

where ψ is the stream function, U_0 is the infinity uniform flow velocity. The variables c_1 and c_2 are the location center of the two cylinders, a,b are the corresponding radii of the cylinders, respectively, and x,y are the corresponding coordinates in the Cartesian plane.

If the cylinders are close to each other, no analytical solution is available. However, if the flow is assumed to be potential, then it must satisfy Laplace's equation. Therefore, it is possible to solve Laplace's equation numerically in terms of the potential function in

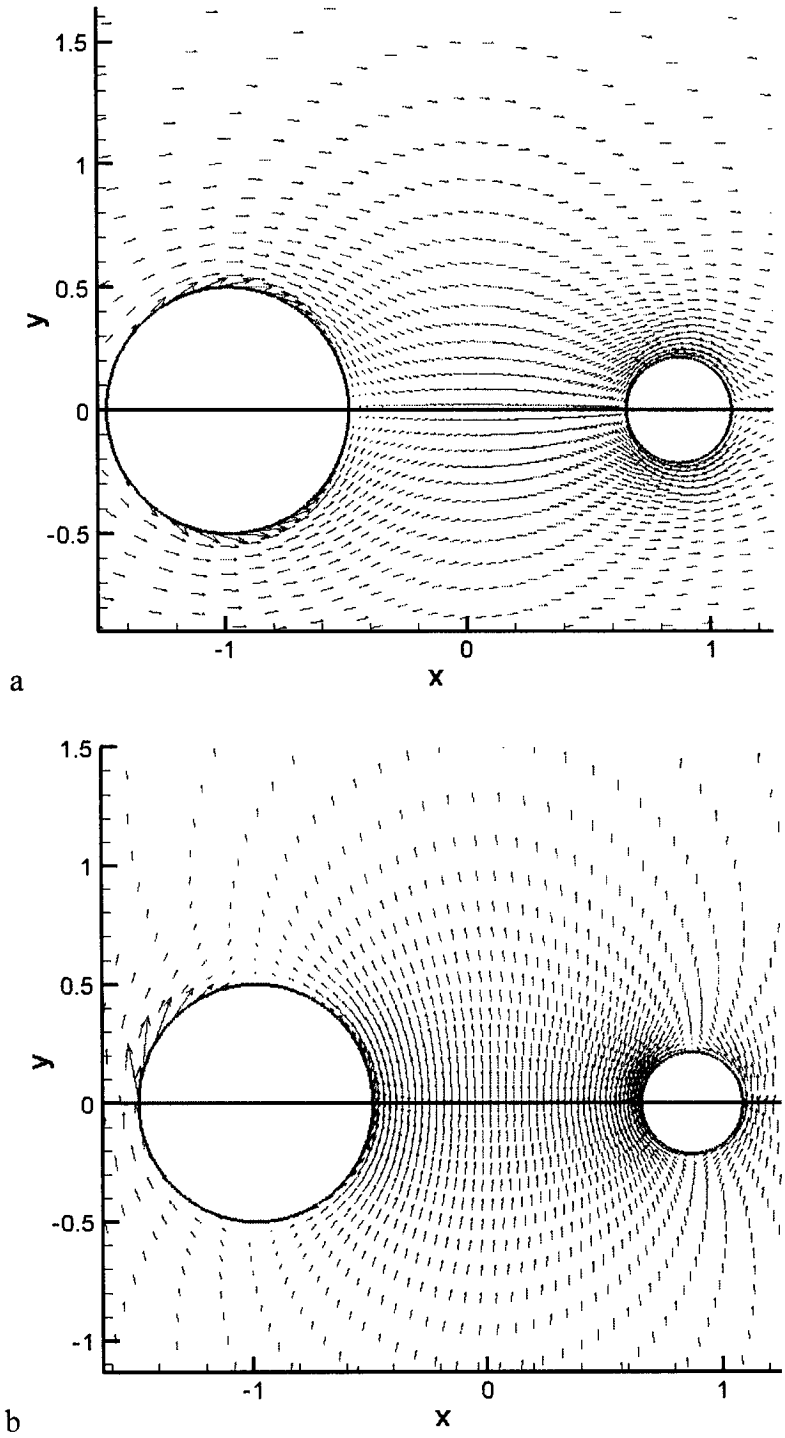

Figure 7-2 The flow field of mean flow around two cylinders: (a) parallel mean flow, (b) perpendicular mean flow.

bipolar system:

$$\nabla^2\phi = \frac{1}{h_\zeta h_\eta}\left(\frac{\partial}{\partial\zeta}\left(\frac{h_\eta}{h_\zeta}\frac{\partial\phi}{\partial\zeta}\right)+\frac{\partial}{\partial\eta}\left(\frac{h_\zeta}{h_\eta}\frac{\partial\phi}{\partial\eta}\right)\right)=0 \tag{83}$$

where $\zeta.\eta$ are the bipolar coordinates, and

$$U_\zeta = \frac{1}{h_\zeta}\frac{\partial\phi}{\partial\zeta}$$
$$U_\eta = \frac{1}{h_\eta}\frac{\partial\phi}{\partial\eta} \tag{84}$$

are the corresponding velocity components. Figs. 7.2 a and b show graphically the flow Cases D-2 and D-3, respectively.

7.4 Boundary Condition:

A schematic diagram of the computational domain for two circular cylinders in the bipolar system is given in Fig. 7.3. It is clear that the grids are clustered near the cylinder and greatly stretched in the far-field.

For the bipolar coordinate system, η_1,η_2 correspond to the left and right cylinder envelope, respectively. Furthermore, the non-penetrating solid boundary conditions are implemented. $\xi=0$ and $\xi=2\pi$ correspond to the centerline. Periodic boundary conditions are used for the disturbance components, i.e. $U_{\xi=0}=U_{\xi=2\pi}$, where $U=u',v',p'$ Discretization of spatial derivatives on the centerline is computed by second-order, one-sided finite differences.

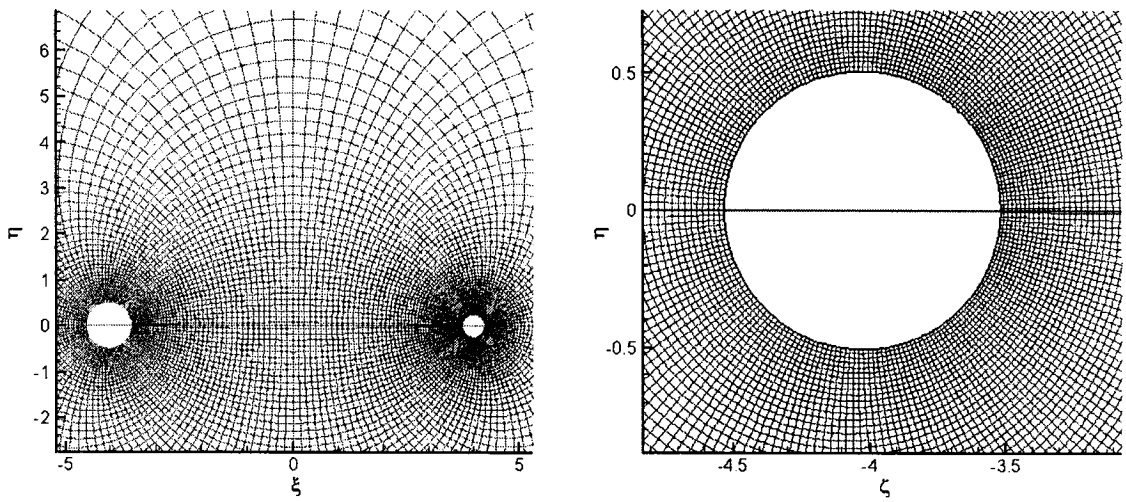

Figure 7-3 The schematic of computational domain.

A simple damping term in the far-field (so-called sponge layer) was employed as a simplified alternative to the perfect matched layer technique. Waves incident on this layer are damped, and reflections into the physical domain of interest are minimized using:

$$\frac{\partial \vec{u}}{\partial t} + A\frac{\partial \vec{u}}{\partial \zeta} + B\frac{\partial \vec{u}}{\partial \eta} + \sigma \vec{u} = 0 \qquad (85)$$

where the damping term $\sigma = 1.2$ is taken when $r \geq 6$, where r is the distance from the source center.

7.5 Results

For Case D-1, both a coarse mesh (300×300) and a fine mesh (600×600) were used for the computations. A conservative scheme that exactly satisfies the continuity equations, and a non-conservative scheme that satisfies continuity only for very fine

mesh size, were employed. The computations were performed up to $t = 42$, requiring a total running time of 1.5 hours for coarse mesh and 14 hours for the fine mesh on a modern unit station. The developed computer code was capable in handling curvilinear coordinates and the obtained results are in a very good agreement with the analytical solution of Visbal (2004). Both conservative and non-conservative schemes were able to predict accurately the sound directivity, when fine meshes were implemented.

For Cases D-2 and D-3, a single small Taylor vortex (vortex core $R_c = 0.04$ and a circulation of 0.00005), equidistant from the center of each cylinder is superimposed in the mean flow with a Mach number 0.2. A 300×300 grid and non-conservative scheme were used. The pressure isoline contour at time $t = 0.1$ and $t = 1.2$ are presented in Figs 7.7 and 7.8, respectively. The vortices were deformed in each case, and quadrupoles were observed at time $t = 0.1$. The pressures for the two cases at this time were almost at the same level. As the vortex has been convected with the mean flow, the vortex was further deformed and the sound wave was emerged from the quadruople, the wave reached the cylinder, reflected and refracted into the mean flow (see Fig 7.7s b and 7.8 b). It is worth noting that at time $t = 1.2$ the sound pressure level for Case D-3 is almost ten times larger than that for Case D-2 . For Case D-2, the closer the vortex moves to the downstream cylinder, the more it behaves like a vortex deforming in the flow around a single cylinder, which eventually impinges into the downstream cylinder. For Case D-3, the vortex convects with the mean flow and it will never impinge into either cylinder.

In Figs 7.9 and 7.10, the RMS acoustic pressure distribution on the cylinder surfaces (the integration time that is equal to $t = 3.0$ to allow that the sound wave propagate beyond the cylinder surface) are presented. For Case D-2, it is observed that the sound wave around the left cylinder is much stronger than for that around the right cylinder (almost ten times difference). For the left cylinder, the sound directivity occurs at around $\theta = 50°$ with the x positive axis (the origin is located at the left cylinder center). However, for the right cylinder, the sound directivity happens near the centerline (around $\theta = 10°$ with the x ne gative axis and the origin is located at the right cylinder). For Case D-3, the sound wave strengths on the two cylinders are at the same level. Asymmetry with the centerline was observed and obviously, the sound wave in the upper half cylinder is much stronger. For both cylinders, the sound directivity occurs at the line that connects cylinders' centers.

To investigate the sound directivity in the far-field, two test surfaces were chosen to present the angular distribution of the RMS of acoustic pressure. Surface A is the circle envelope with radius equal to 2.5, and surface B is the circle envelope with radius equal to 2.0. The centers of both test surfaces are located at the origin of the Cartesian coordinate system. For surface A, the RMS acoustic pressure integration time is given to $T = 5.0$; for surface B, the time is chosen to be 4.5 to guarantee that the sound wave reaches the testing surfaces.

The RMS of acoustic pressure distribution for Case D-2 and Case D-3 are

presented in Fig 7.11. For both cases, the RMS distribution on two testing surface turn out to be qualitatively same, which verified the reliability of the observed sound directivity. For Case D-2, the RMS of acoustic pressure is symmetrical with the centerline and two maxima were observed for the RMS of acoustic pressure, one at $50°$ from the positive x axis; and the other at $150°$. For Case D-3, an asymmetry was observed for the RMS acoustic pressure profile and stronger sound strength was observed in the upper side of the cylinders (to which direction the vortex moves with the mean flow), and the sound directivity occurs at its mid plane enterline, where the vortex originally located at.

7.6 Summary of Findings

The developed computer code was able of handling curvilinear coordinates and for the periodic acoustic pulse (Case D-1) a very good agreement with the analytical solution was obtained. Conservative scheme and non-conservative scheme both were found to be capable of good prediction of the sound directivity.

For vortex deforming in the flow around two cylinders' set-ups, tandem (Case D-2) and transverse (Case D-3) were investigated. It was found that the vortex trapped between transverse cylinders radiated much stronger noise than the vortex trapped between tandem cylinders. For Case D-2, the maximum disturbance pressure occurs at around $50°$ with the x posit ive axis on the left cylinder. For the right cylinder, the sound directivity occurs near the centerline (around $10°$ with the x neg ative axis). For

Case D-2, in the far-field, the RMS of acoustic pressure with respect to the centerline is symmetrical with the centerline and two maxima were observed for the RMS of acoustic pressure. For Case D-3, the sound wave in the upper half-plane cylinder is much stronger than that at the lower half-plane. For both cylinders, the sound directivity happens at the cylinders' centers connecting line. In the far-field, the sound directivity happens at in-between cylinders centerline.

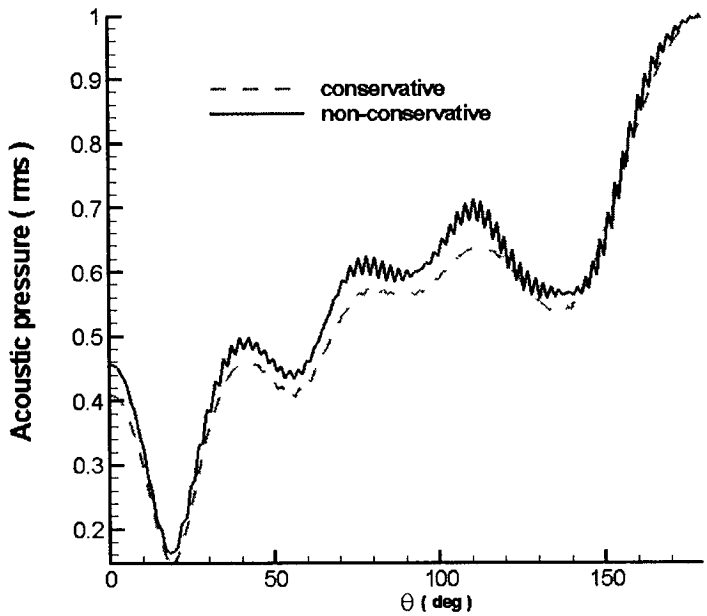

Figure 7-4 The RMS of acoustic pressure distribution on the right cylinder (computed on the coarse mesh (300×300) grid).

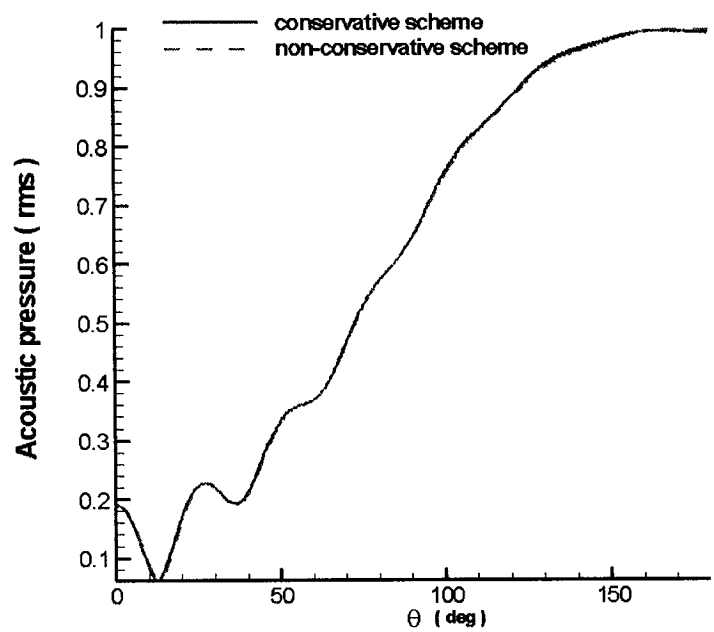

Figure 7-5 The RMS of acoustic pressure distribution on the right cylinder (computed with fine mesh (600×600) grid).

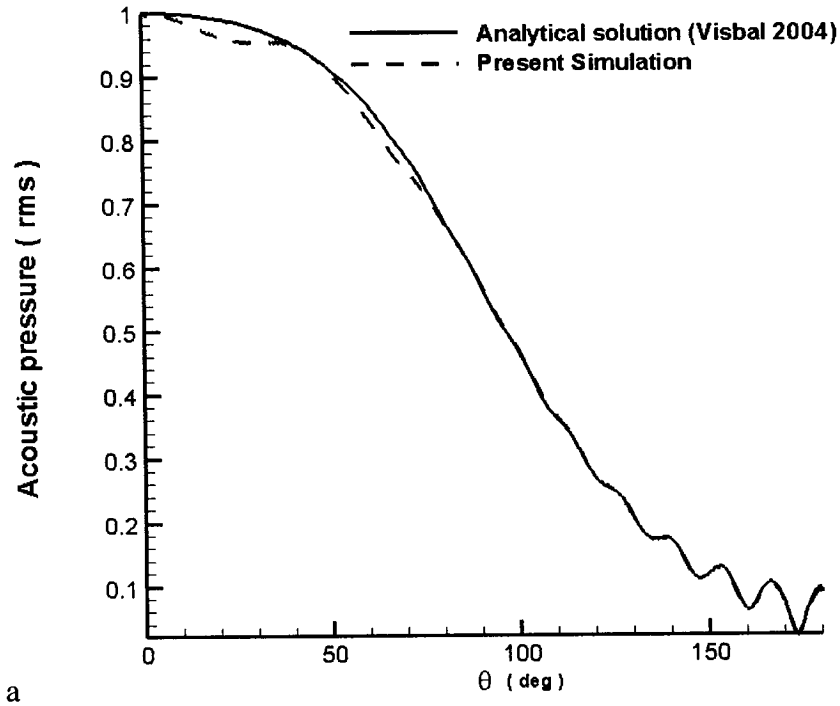

a

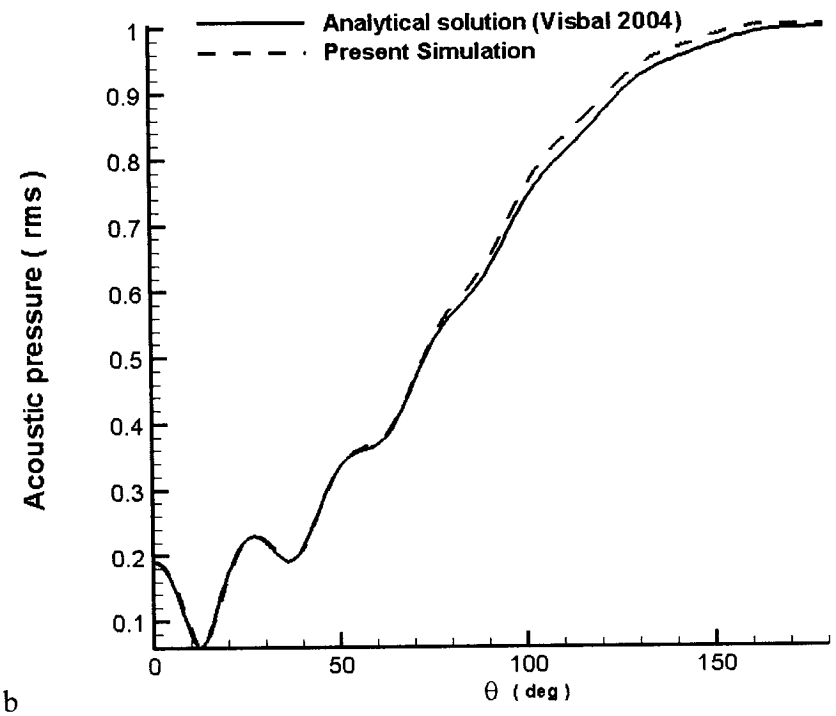

b

Figure 7-6 The RMS of acoustic pressure distribution on the upper half cylinder: (a) left cylinder, (b) right cylinder (solution on (600×600) grid).

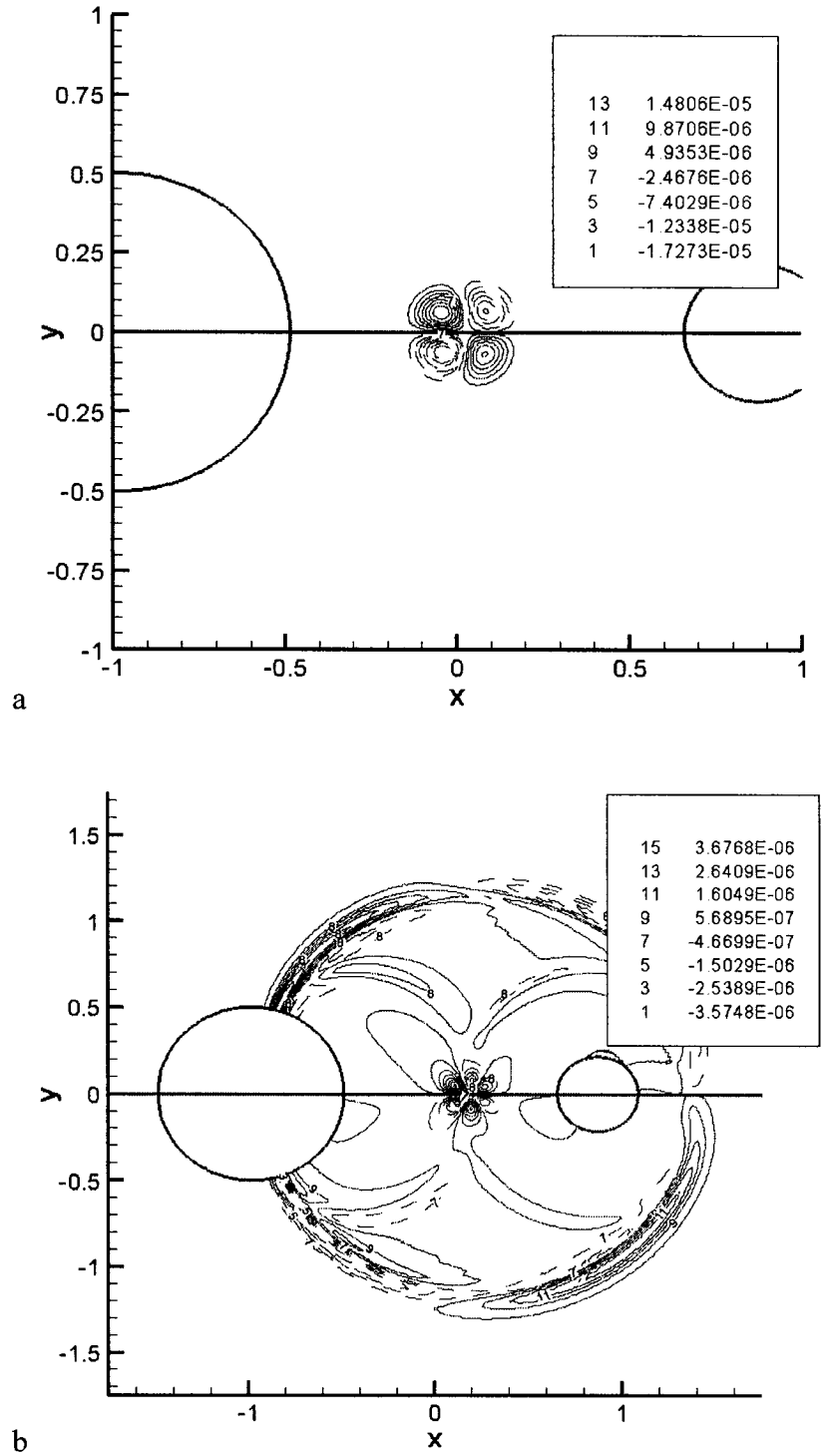

Figure 7-7 Unsteady pressure generated by the vortical disturbance that trapped between two cylinders (Case D-2) at times: (a) $t = 0.1$ and , (b) $t = 1.2$.

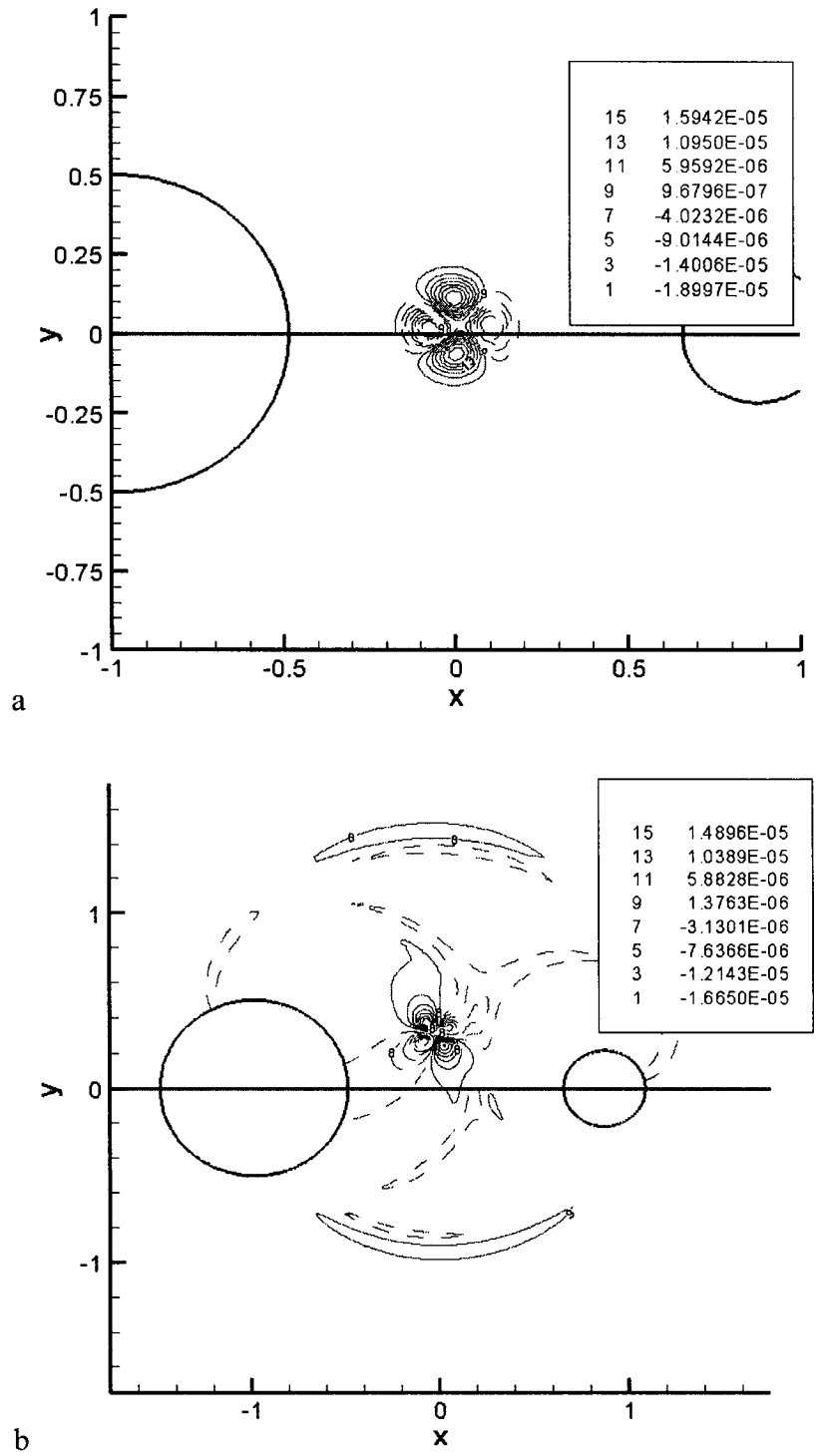

Figure 7-8 Unsteady pressure generated by the vortical disturbance that trapped between two cylinders (Case D-3) at times: (a) $t = 0.1$ and, (b) $t = 1.2$.

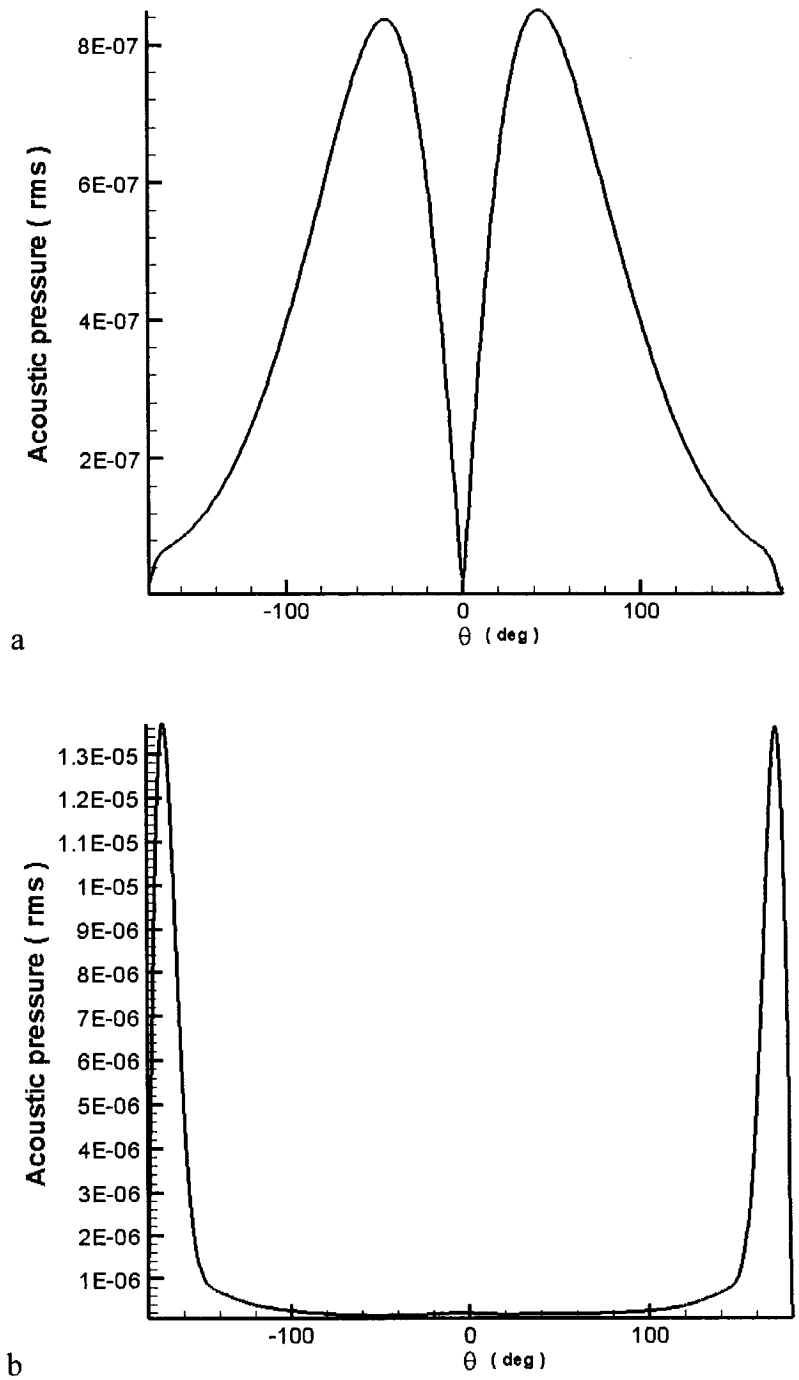

Figure 7-9 The RMS of acoustic pressure distribution on the cylinders (a) left cylinder and (b) –right cylinder, angle θ is measured from the negative x axis and the corresponding cylinder center, Case D-2.

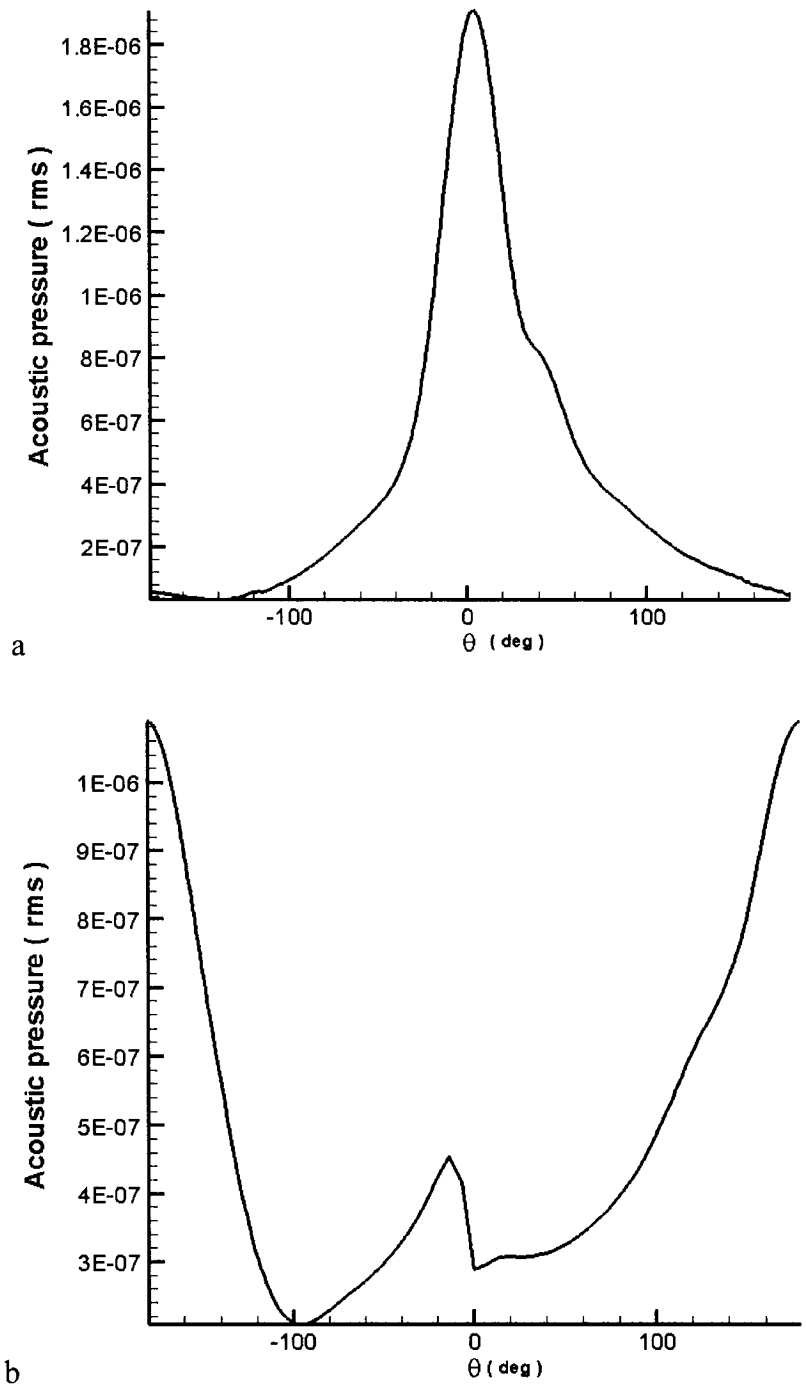

Figure 7-10 The RMS of acoustic pressure distribution along the cylinders (a) left cylinder and (b) right cylinder θ is measured from the negative x axis and the corresponding cylinder center , Case D-3.

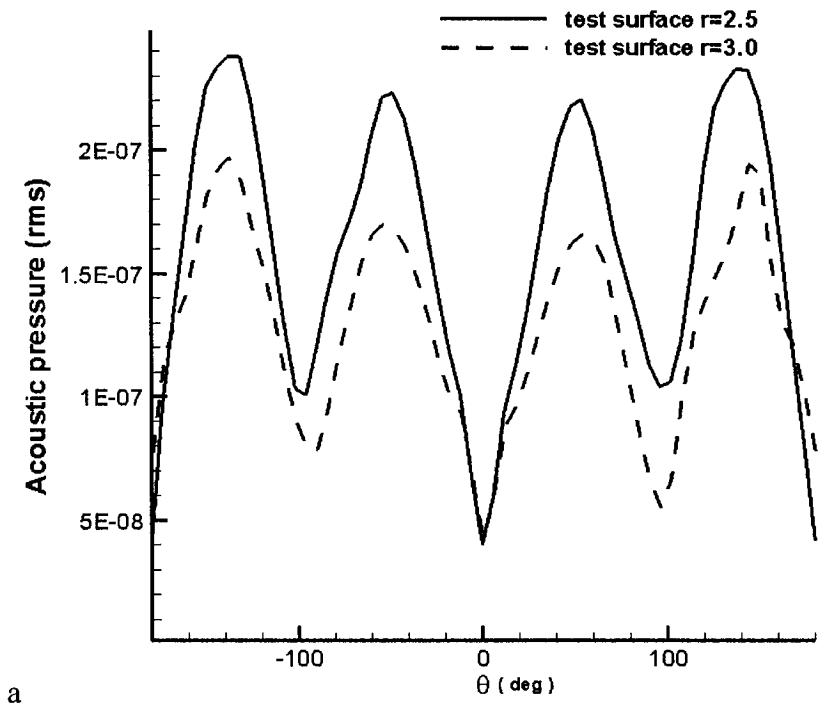

a

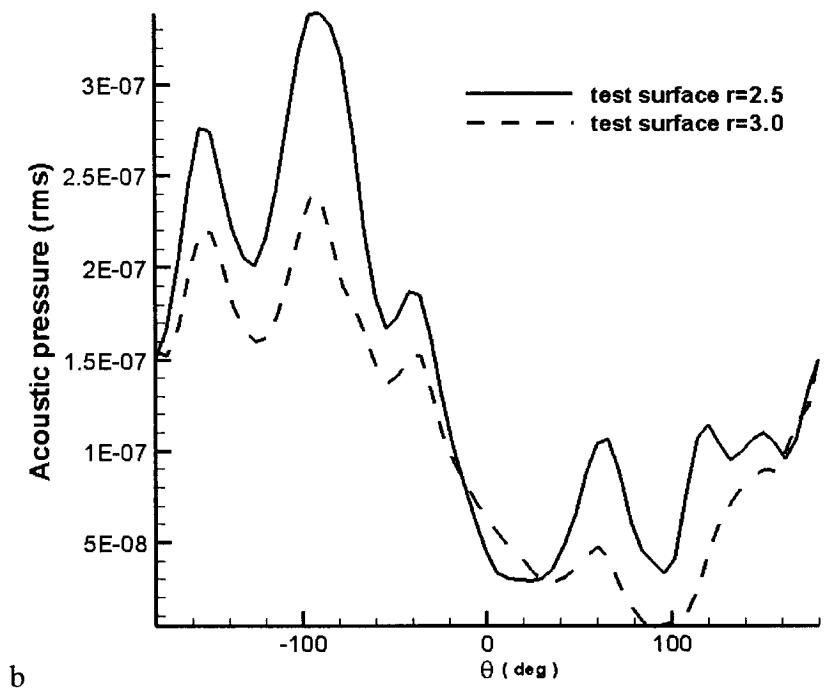

b

Figure 7-11 The RMS of acoustic pressure far-field distribution with angle θ from the positive x axis and measured from the origin: (a) Case D-2, (b) Case D-3.

CONCLUSIONS

The sound generated by vortical disturbances in a subsonic flow around solid surfaces, as obtained using different vortex velocity formulations, was investigated numerically. Errors associated with the discretization and boundary conditions were kept small using high-order schemes with accurate non-reflecting boundary conditions.

Stagnation flow on a flat plate, flow around a stationary and rotating cylinder, and that about two cylinders were taken as prototypes of real-world flows with strong gradients of mean pressure and velocity. Single and periodic vortices were also included. In addition, the effects of vortex core size, the street distance, street frequency, and the Mach number of the mean flow on sound generation and propagation were examined.

The sound strength was found to be proportional to the vortex strength. If the acoustic pressure was normalized by the vortex strength, then all the distinct acoustic pressure profiles were shown to collapse into single curve. The sound generated by vortex solid interaction, as well as its propagation, was found to be totally different between the two prototype vortex models. The core size and vortex street distance have minor influences on the acoustic pressure profile for sound waves radiated by the

Vatistas' vortex. Nevertheless, the change of the core size or the distance between the vortex rows significantly affected the sound pressure profile and directivity of a Taylor's vortex.

The effects of the non-linear terms on sound wave properties were also analyzed. These were found to increase with the vortex strength. A lifting cylinder would not only increase the wave amplitude but will also shift its directivity.

The vortex trapped between transverse cylinders radiated much stronger noise than the vortex trapped between tandem cylinders.

The developed codes can be used in the future as platforms to more elaborate software that will predict the noise generated by multi-element airfoils, and the undercarriage. Their implementation is expected reduce the need of costly, time consuming, wind tunnel and field experiments.

FUTURE WORK

Many areas of this analysis can be further explored to acquire a more complete understanding and prediction of the noise generated by parallel vortex-body interaction. Some of these areas are as follows:

1. The physical space of noise generation and propagation are split into three domains including: the boundary layer, the near-field and far-field. In this thesis, only near-field noise generation and propagation were investigated. The far-field noise prediction, which is important, should be examed in the future. The acoustic field radiated at the external boundary of the Euler domain, will become the entry data of a FW-H or Kirchhoff integration, which provides the noise radiated into the far-field.

2. For a sound wave, the strength, sound directivity and frequency are important characteristics. In this thesis, only the strength and sound directivity were investigated. The sound frequency can by analyzed using Fourier Transformation in the next step.

3. In this study, the background flow is analytically given as potential flow, a numerical solution of the Navior-Stokes equations or experimental data will be adopted as the

mean flow in the future.

4. In this study, inviscid background flow was assumed, and the turbulent, highly viscous boundary layer, which serves as a nursery of vortices was completely ignored. However, it has been pointed out (Lee & Bershader, 1991.), that viscousness may play an important role in sound generation by a vortex body interaction. A secondary vortex with opposite sign of vortices has been reported during a parallel vortex body interaction. This secondary vortex may encounter the original vortex, and have a great impact on the noise generation and propagation mechanism.

5. The acoustic source trapped between two cylinders is a very good prototype of sound generation by several bodies in close proximity to each other. However, in this study, only an acoustic source or a single vortex trapped between two cylinders was taken into consideration. The study on chain vortices interacting with a multi-body, which is a very good simulation of multi-element airfoil noise, was left to be investigated in the future. Furthermore, the periodic vortex was manually added in this study, which is naturally not physical. So, in the future when the investigation on a multi-body vortex street interaction is done, the chain vortices will be physically generated by the upstream cylinder, and come to interact with the downstream cylinder.

6. In this study, structured mesh was implemented. However the curvilinear and multi-body geometry of multi-element airfoil will restrict the use of structured

numerical grids and their generation. If the structured grids are taken, the curvilinear boundaries will not coincide with the grid lines. An unstructured grid system will be needed in the future, so as to be more flexible to deal with the curvilinear boundary.

7. This research is only applicable to a 2–D parallel vortex body interaction, an expansion to sound radiated by a full 3-D vortex body interaction and its propagation should be investigated in the future.

REFERENCES

Affes, H. & Conlisk, A. T., 1993, "Model for Rotor Tip Vortex-Airframe Interaction. Part 1: Theory," AIAA Journal, Vol.31, pp. 2263–2273

Affes, H., Conlisk, A. T., Kim, J. M. & Komerath, N. M., 1993, "Model for Rotor Tip Vortex-Airframe Interaction Part 2: Comparison with Experiment," AIAA Journal, Vol. 31, pp. 2274–2282

Affes, H., Xiao, Z. & Conlisk, A. T., 1994, "The Boundary-Layer Flow Due to a Vortex Approaching a Cylinder," Journal of Fluid Mechanics, Vol. 275, pp. 33–57

Affes, H., Xiao, Z., Conlisk, A. T., Kim, J. M. & Komerath, N. M., 1998, "Model for Rotor Tip Vortex-Airframe Interaction. Part 3: Viscous Flow on Airframe," AIAA Journal, Vol. 36, pp. 409–415

Atkins, H. L., 1991, "High-order ENO Methods for the Unsteady Compressible Navier-Stokes Equations," AIAA Paper No. 91–1557

Barker, S. J. & Crow, S. C., 1977, "The Motion of Two-Dimensional Vortex Pairs in a Ground," Journal of Fluid Mechanics, Vol. 82, pp. 659–671

Bayliss, A. and Turkel, E., 1980, "Radiation Boundary Conditions for Wave-like Equations," Communications on Pure and Applied Mathematics, Vol. 23, pp.707–725

Berenger, J. P., 1994, "A Perfectly Matched Layer for the Absorption of Electro-Magnetic Waves," Journal of Computational Physics, Vol. 114, pp.185–200

Bhagwat, M. J. and Leishman, J. G., 2002, "Generalized Viscous Vortex Model for Application to Free-vortex Wake and Aeroacoustics," Annual Forum of the American Helicopter Society, Montreal, Canada, June

Bi, N. & Leishman, J. G., 1990, "Experimental Study of Rotor/body Aerodynamic Interactions," Journal of Aircraft, Vol. 27, pp. 779–788

Bi, N., Leishman, J. G. & Crouse, G. L., 1993, "Investigation of Rotor Tip Vortex Interaction with a Body," Journal of Aircraft, Vol. 30, pp. 879–888

Brand, A., Komerath, N. M. & McMahon, H., 1989, "Results from Laser Sheet Visualization of a Periodic Rotor Wake," Journal of Aircraft, Vol.26, pp. 438–443

Brentner, K. S. & Farassat, F., 1994, "Helicopter Noise Prediction: the Current Status and Future Direction," Journal of Sound and Vibration, Vo. 170, No.1, pp.79–96

Burge, J. M., 1948, "A Mathematical Model Illustrating the Theory of Turbulence," Advances in Applied Mechanics, Vol. 1, pp. 171–199

Colonius, T., Lele, S. K. and Moin, P., 1993, "Boundary Conditions for Direct Computation of Aerodynamic Sound Generation," AIAA Journal, Vol. 31, No.9, pp. 1574–1582

Colonius, T., Lele, S. K. and Moin, P., 1994, "the Scattering of Sound Waves by a Vortex: Numerical Simulations and Analytical Solutions," Journal of Fluid Mechanics, Vol. 260, pp.271–298

Conner, D. A., and Wellman, J. B., 1991, "Hover Acoustic Characteristics of the XV-15 with Advanced Technology Blades," Proceedings of the AHS/RAeS Technical

Specialists Meeting on Rotorcraft Acoustics and Fluid Dynamics, Philadelphia, PA, October 15–16

Djambazov, G. S., Lai, C. H., and Koulis A. P., 1998, "Efficient Computation of Aerodynamic Noise," Contemporary Mathematics, Vol. 218, pp. 500–506

Dosanijh, D. S., Gasparek, E. P., and Eskinazi, S., 1962, "Decay of a Viscous Trailing Vortex," The Aeronautical Quarterly, Vol. 3, No.3, pp.167–188

Duncan, Than, and Yong, 1970, "Mechanics of Fluids," London, Edward Arnold Ltd. 2nd edition

Enquist, B. and Majda, A., 1977, "Absorbing Boundary Conditions for the Numerical Simulation of Waves," Mathematics of Computation, Vol. 31, No.139, pp. 629–651

Francescantonio, P. D., Casalino, D., 1999, "Green's Function Discretization Scheme for Sound Propagation in Non-Uniform Flows," AIAA Journal, Vol. 37, No. 10, pp. 1161–1173

Giles, M. B., 1990, "Non-reflecting Boundary Conditions for Euler Equation Calculations," AIAA Journal, Vol. 28, No. 12, pp. 2050–2058

Gee, K., Murman, S. M., Schiff L. B., 1995, "Computational Analysis of F/A–18 Tail Buffet," AIAA Paper 95–3440

Gervais, M., 2001, "Tiltrotor Blade-Vortex Interaction (BVI) Noise Control through Non-unique Longitudinal Force Trim," Presented at the Southeast Lichten Award Regional Competition of the American Helicopter Society, College Park, Maryland, January

Goldstein, M., 1976, Aeroacoustics, McGraw-Hill, New York

Gossler, A. A., & Marshall, J. S., 2001, "Simulation of Normal Vortex-cylinder Interaction in a Viscous Fluid," Journal of Fluid Mechanics, Vol. 431, pp. 371–405

Ham, M. D., 1974, "Some Preliminary Results from an Investigation of Blade-Vortex Interaction," Journal of American Helicopter Society, April, pp. 45–48

Ham, M. D., 1975, "Some Conclusions from an Investigation of Blade-Vortex Interaction," Journal of American Helicopter Society, Oct., pp. 26–31

Hardin, J. and Pope, D. S., 1992, "a New Technique for Aerodynamic Noise Calculation," Proceedings of the DGLRR/AIAA 14th Aeroacoustics Conference, pp. 448–456, Washington, DC

Harvey, J. K. and Perry, F. J., 1971," Flow Field Produced by Trailing Vortices in the Vicinity of the Ground," AIAA Journal, Vol. 9, pp.1659–1660

Higdon, R. L., 1987, "Numerical Absorbing Boundary Conditions of the Wave Equation," Mathematics of Computation, Vol. 49, No. 179, pp.65–90

Higdon, R. L., 1986, "Absorbing Boundary Conditions for Difference Approximations to the Multi-dimensional Wave Equation," Mathematics of Computation, Vol. 47, No 176, pp. 437–459

Howe, M. S., 1976, "The Influence of Vortex Shedding on the Generation of Sound Convected by Turbulence," Journal of Fluid Mechanics, Vol. 76, pp.711–740

Howe, M. S., 1995, "On the Force and Moment Exerted on a Body in an Incompressible Fluid with Application to Rigid Bodies and Bubbles at High and Low Reynolds

Numbers," the Quarterly Journal of Mechanics and Applied Mathematics, Vol. 48, pp. 401–426

Hu, F. Q., 1996, "On Absorbing Boundary Conditions for Linearized Euler Equations by a Perfectly Matched Layer," Journal of Computational Physics, Vol. 129, PP. 201–219

Hu, F. Q., Hussaini, M.Y., and Manthey, J.L., 1996, "Low-dissipation and Low-dispersion Runge-Kutta Schemes for Computational Acoustics," Journal of Computational Physics, Vol. 124, pp. 177–191

Hu, F. Q., 2001, "a Stable, Perfectly Matched Layer for Linearized Euler Equations in Unsplit Physical Variables," Journal of Computational Physics, Vol. 173, pp. 455–480

Inoue, O. and Hattori, Y., 1999, "Sound Generation by Shock-vortex Interactions," Journal of Fluid Mechanics, Vol.380, pp. 81–116

Inoue, O. and Hatakeyama, N., 2002, "Sound Generation by a two-dimensional Circular Cylinder in a Uniform Flow," Journal of Fluid Mechanics, Vol. 471, pp. 285–314

Israeli, M. and .Orszag, S., 1981, "Approximation of Radiation Boundary Conditions," Journal of Computational Physics, Vol. 41, No. 1, pp. 115–135

Iversen, J. D., 1976, "Correlation of Turbulent Trailing Vortex Decay Data," Journal of Aircraft, Vol. 13, No.5, May, pp. 338–342

JanakiRam, R. D. and Kham, H., 2000, "Prediction and Validation of Helicopter Descent Flyover Noise," Presented at the American Helicopter Society 56th Annual Forum, Virginia Beach, VA, May 2–4

Kandil, O. A., Sheta, E. F., and Massey, S. J., 1995, "Buffet Responses of a Vertical Tail in

Vortex Breakdown Flows," AIAA Paper, 95–3464

Keys, R. G., 1985, "Absorbing Boundary Condition for Acoustic Media," Geophysics, Vol. 50, pp. 892–902

Kitaplioglu, C. & Johnson, W. 2002, "Comparison of Full-scale XV-15 Blade-Vortex Interaction Noise Calculations with Wind Tunnel Data," Presented at the AMERICAN helicopter Society International Technical Specialist Meeting on Aerodynamics, Acoustics, and Test and Evaluation, San Francisco, CA, January 23–25

Krishnamoorthy, S., Gossler, A. A. and Marshall, J. S., 1999, "Normal Vortex Interaction with a Circular Cylinder," AIAA Journal, Vol. 37, pp.50–57

Kreiss, H.O., 1970, "Initial Boundary Value Problems for Hyperbolic Systems," Communications on Pure and Applied Mathematics, Vol. 23, pp. 277–298

Lamb, H., 1932, "Hydrodynamics," Cambridge University Press, Cambridge, UK

Lele, S. K., 1992, "Compact Finite Difference Schemes with Spectral-like Resolution," Journal of Computational Physics, Vol. 103, pp 16–42

Lee S., Bershader D., 1991, "An Experimental and Computational Study of 2-D Parallel Blade Vortex Interaction," AIAA Paper 91–3277

Lee S., and Bershader D., 1994, "Head-on Parallel Blade-Vortex Interaction," AIAA Journal, Vol. 32, pp.16–22

Lee, A., and Harris, D., 1979, "Hover Tests of the XV-15 Tilt Rotor Research Aircraft," AIAA Paper No. 79–0612

Lee, A., and Mosher, M., 1979, "An Acoustical Study of the XV-15 Tiltrotor Research Aircraft," AIAA paper No. 79–0612

Lighthill, M. J., 1952, "On Sound Generated Aerodynamically: I. General Theory," Proceeding of Royal Society, Vol. A221, pp.564–587

Lilley, G. M., 2001, "the Prediction of Airframe Noise and Comparison with Experiment," Journal of Sound and Vibration, Vol. 239, No. 4, pp. 849–859

Liu, S. R., Brieger, J. and Peryea, M., 1998, "Model Tiltrotor Flow Field/Turbulence Ingestion Noise Experiment and Prediction," the American Helicopter Society 54th Annual Forum, Washington, DC, May 20–22

Lockard, D. P., Brentner, K. S., and Atkins, H. L., 1995, "High-Accuracy Algorithms for Computational Aeroacoustics," AIAA Journal, Vol. 33, No. 2, pp. 246–251

Maisel, M., and Harris, D., 1981, "Hover Tests of the XV-15 Tiltrotor Research Aircraft," AIAA paper No. 81–2501

Marshall, J. S. & Yalamanchili, R., 1994, "Vortex Cutting By a Blade Part II: Computations of Vortex Response," AIAA Journal, Vol. 32, pp.1145–1150

Mayori, A., and Rockwell, D., 1994, "Interaction of A Streamwise Vortex with a Thin Plate: a Source of Turbulent Buffeting," AIAA Journal, Vol. 32, pp. 2022–2029

McAlister, K. W., and Tung, C., 1984, "Airfoil Interaction with an Impinging Vortex," NASA Technical Paper, 2273

McVeigh, M. A., 1985, "The V-22 Tilt-Rotor Large-Scale Rotor Performance/Wing Download Test and Comparison with Theory," 11th European Rotorcraft Forum,

London, England, Sept

Mittal, S., Kumar, V. and Raghuvanshi, A., 1997, "Unsteady Incompressible Flow Past Two Cylinders in Tandem and Staggered Arrangements," International Journal for Numerical Methods in Fluids, 25, pp. 1315–1344

Mosher, M., and Light, J. S., 1994, "Study of Noise on a Small-scale Hovering Tiltrotor," American Helicopter Society Technical Specialist Meeting, San Francisco

Mitchell, B. E., Lele, S. K. and Moin, P., 1995, "Direct Computation of the Sound for a Compressible Co-rotating Vortex Pair," Journal of Fluid Mechanics, Vol. 285, pp.181–202

Nakamura, Y., 1981, "Prediction of Blade Vortex Interaction from Measured Blade Pressure," AHS Seventh European Rotocraft Powered Lift

Oseen, C. W., 1912, "Uber Wirbelbewegune in einer reiben-den Flussigkeit," Journal of Mat. Astron. Fys., Vol. 7, pp. 14–21

Polark D., and George, A. R., 1998, "Flow Field and Acoustic Measurements from a Model Tiltrotor in Hover," Journal of Aircraft, Vol. 35, No. 6, pp. 921–929

Povitsky, A., 2000, "Acoustics of a stagnation flow near a rigid wall," Physics of Fluids, Vol. 12, No. 10, pp. 2595–2608

Povitsky, A., 2002, "Numerical Study of Wave Propagation in a Non-Uniform Compressible Flow," Physics of Fluids, Vol.14, No. 8, pp.2657–2672

Povitsky, A., Zheng, T. H., and Vatistas, G. H., 2004, "Effect of Vortex Profile on Sound Generation in a Non-uniform Flow," Mathematics and Computers in Simulations,

Vol.65, pp.447–468

Povitsky, A., Zheng, T. H. and Vatistas, G. H., 2003, "Numerical study on Propagation and Scattering by Two Cylinders," Proceedings of the 4th CAA Workshop on Benchmark Problems, Ohio Aerospace Institute in Cleveland, Ohio, U.S.A. Oct. 20-22, pp. 283–290

Rahier, G. and Delrieux, Y., 1997, " Blade-Vortex Interaction Noise Prediction Using a Rotor Wake Roll-up Model," Journal of Aircraft, Vol. 34, No.4, pp. 522–530

Ramasamy, M. and Leishman, G., 2004, "A Generalized Model for Transitional Blade Tip Vortices," 60th Annual Forum and Technology Display of the American Helicopter Society International, Baltimore, MD, June 7–11

Ramasamy, M. and Leishman, G., 2003, "The Interdependence of Straining and Viscous Diffusion Effects on Vorticity in Rotor Flowfields," Proceedings of the American Helicopter Society 50th Annual National Forum, Phoenix, Arizona, May 6–8

Rankine, W. J. M., 1858, Manual of Applied Mechanics, C.Griffen Co., London

Rizk, Y. M., and Gee, K., 1992, "Unsteady Simulation of Viscous Flow Field around F–18 Aircraft at Large Incidence," Journal of Aircraft, Vol. 29, pp. 986–992

Rizzetta, D.P., 1996, "Numerical Simulation of the Interaction between a Leading-Edge Vortex in a Vertical Tail," AIAA Paper, No. 96–2012

Rockwell, D., 1998 "Vortex-Body Interactions," Annual Review of Fluid Mechanics, Vol. 30, pp. 199–229

Rosenhead, L., 1930, "The Spread of Vorticity in the Wake behind a Cylinder,"

Proceedings of the Royal Society of London, Series A: Mathematical and Physical Science, Vol.127, pp. 73–76

Shen, W. Z. and Sorensen, J. N., 1999, "Comment on the Aeroacoustic Formulation of Hardin and Pope," AIAA Journal, Vol. 37, pp.141–143

Sheridan, P. F. and Smith, R. P., 1980, "Interactional Aerodynamics: a New Challenge to Helicopter Technology," Journal of American Helicopter Society, Vol. 25, pp. 3–21

Tung, C. Pucci, Caradonna, F. X., and Morse, H. A., 1983, "The Structure of Trailing Vortices Generated by Model Rotor Blades," Vertica, Vol. 7, pp. 33–43

Towfighi J, and Rockwell D., 1993, "Instantaneous Structure of Vortex Breakdown on a Delta Wing via Particle Image Velocimetry," AIAA Journal, Vol. 31, No. 6, pp.1160–1162

Straus J., Renzoni, P. and Mayle, R. E., 1988, "Airfoil Pressure Measurements during a Blade-Vortex Interaction and a Comparison with Theory," AIAA Paper 88–0669, Jan.

Tam, C. K. W., Webb, J. C. and Dong, Z., 1993, "A study of the Short Wave Components in Computational Acoustics," Journal of Computational Acoustics, Vol. 1, pp. 1–30

Tam, C. K.W., 1995, "Computational Aeroacoustics: Issues and Methods," AIAA Journal, Vol. 33, No. 10, pp. 1788–1796

Ta'asan, S. and Nark, D., 1995, "An Absorbing Buffer Zone Technique for Acoustic Wave Propagation," AIAA paper, 95–0146

Taylor, G. I., 1958, "On the Dissipation of Eddies," the Scientific Papers of Sir Geoffrey Ingram Taylor, Vol. 2, pp. 96–101

Thompson, K. W., 1987, "Time-Dependent Boundary Conditions for Hyperbolic Systems," Journal of Computational Physics, Vol. 6, No. 1, pp.65–90

Tucker, B., and Conlisk, A. T., 1992, "Massive Vortex Motion in the Presence of Solid Boundaries," Physics of Fluids A, Vol. 4, No. 2, pp.290–305

Vatistas, G. H., Kozel, V., and Mih, C. W., 1991, "A Simpler Model for Concentrated Vortices," Experiments in Fluids, Vol. 11, pp. 73–76

Vatistas, G. H., 1998, "New Model for Intense Self-Similar Vortices," Journal of Propulsion and Power, Vol. 14, No. 4, pp.462–469

Visbal, M. R., 1994, "Onset of Vortex Breakdown of a Pitching Delta Wing," AIAA Journal, Vol. 32, pp.1568–1575

Visbal, M. R., 1995, "Computational and Physical Aspects of Vortex Breakdown on Delta Wings," AIAA Paper, 95–0585

Visbal, M. R., 2003, "Comparison with Analytic Solution Category 2-Complex Geometry," Proceedings of the 4th CAA Workshop on Benchmark Problems, pp.457-460, Ohio Aerospace Institute in Cleveland, Ohio, U.S.A., Oct. 20–22

Wilder, M. C., Pesce, M. M., Telionis, D. P., Poling, D. R., Dadone L., 1990, "Blade-Vortex Interaction Experiments—Velocity and Vorticity Fields," AIAA Paper, 90–0030

Williams, F. J. E., and Hawkings, D. L., 1969, "Sound generated by Turbulence and Surfaces in Arbitrary Motion," Philosophical Transactions of the Royal Society, Vol. A264, No. 1151, pp. 321–342

Wittmer, K. S., and Devenport, W. J. 1996, "Turbulence Structure Resulting from a Perpendicular Airfoil-Vortex Interaction," AIAA Paper 96-2014, Presented at AIAA Fluid Dynamics Conference 27th, New Orleans

Wittmer, K. S., Devenport, W. J., Rife, M. C., and Gleghe, S. A. L., 1995, "Perpendicular Blade Vortex Interaction," AIAA Journal, Vol. 33, pp. 1667–1674

Wilder, M. C., Pesce, M. M., Telionis, D. P. Poling, D. R. and Dadone, L., 1990, "Blade-Vortex Interaction Experiments-Velocity and Vorticity Fields," AIAA Paper, No. 90–0030

Williamson, J., 1980, "Low Storage Runge-Kutta Schemes," Journal of Computational Physics, Vol.35, pp.48–56

Wilson, R.V., Demuren, A. O. and Carpenter, M., 1998, "High-order Compact Schemes for Numerical Simulation of Incompressible Flows," ICASE Report No. 98–13

Yasser Aboelkassem, 2003, "A Shared Similarity Relationship among Vortices," Master Thesis, Department of Mechanical Engineering, Concordia University, Montreal, Canada

Watson, W. R. and Zorumski, W. E., 1996, "Periodic Time Domain Nonlocal Nonreflecting Boundary Conditions for Duct Acoustics," NASA Technical Memorandum, No. 110230, Langley Research Center.

Ziada, S., and Rockwell D., 1982, "Vortex-Leading Edge Interaction," Journal of Fluid Mechanics, Vol.118, pp.79–107